NTNU – Trondheim
Norwegian University of
Science and Technology

Effects of Heat Treatment on the Ballistic Properties of AA6070 Aluminium Plates

Jens Kristian Holmen
Joakim Johnsen

Civil and Environmental Engineering
Submission date: June 2012
Supervisor: Tore Børvik, KT

Norwegian University of Science and Technology
Department of Structural Engineering

Department of Structural Engineering
Faculty of Engineering Science and Technology
NTNU- Norwegian University of Science and Technology

ACCESSIBILITY

OPEN

MASTER'S THESIS 2012

SUBJECT AREA:	DATE:	NO. OF PAGES: 193
Computational Mechanics	08 June 2012	18 + 150 + 25

TITLE:

Effects of Heat Treatment on the Ballistic Properties of AA6070 Aluminium Plates

BY:

Jens Kristian Holmen
Joakim Johnsen

SUMMARY:
The thesis includes a summary of important theory in the fields of impact engineering and plasticity theory, and a literature study is carried out on aluminium designations, alloying and heat treatment. The true stress-strain curves of aluminium alloy AA6070 in O-, T4-, T6-, and T7-configurations are identified by tensile tests where the behavior is continuously measured to fracture. The aluminium was delivered as 20 mm rolled plates; microstructural images and strain ratios are reported. Material constants are found by direct calibration and inverse modeling.

Ballistic tests are done in a laboratory using 7.62 mm APM2 bullets, 20 mm blunt projectiles and 20 mm ogival projectiles (CRH = 3). From these tests the ballistic limit curves and the ballistic limit velocities are found for all temper/projectile combinations. In the material tests it was shown that the O-temper is the most ductile temper and consequently almost no fragmentation takes place in the ballistic tests for this temper. The T6-temper proved to be brittle, and fragmentation was commonly seen in the ballistic tests. The degree of fragmentation is found to be of vital importance for the ballistic performance. The Cockcroft-Latham fracture criterion is implemented by using the plastic work to fracture. Numerical analyses are performed with the IMPETUS Afea Solver and LS-DYNA, with 3D-models and 2D axisymmetric models, respectively. Ballistic limit curves and the ballistic limit velocities are calculated on the basis of the numerical results and then compared to the experimental values. Limited sensitivity studies are conducted on mesh size, heat-expansion dependency, strain-rate dependency, etc. Overall the results from 2D axisymmetric models are found to be consistent with previous studies, and the 3D-analyses carried out with the IMPETUS Afea Solver gave some good results. The IMPETUS Afea Solver proved to be a user-friendly finite element program with some powerful features.

In addition to the numerical studies, a thorough derivation of the Cylindrical Cavity Expansion Theory (CCET) is given. Results from CCET are good for 7.62 mm APM2 bullets. A case-study where the ballistic performance is determined without conducting any experiments is also conducted. The results are promising, but less conservative than the original simulations, due to the inability to calibrate a fracture criterion. Some suggestions for further work within the field of impact engineering and the application of the finite element method are provided at the end of the thesis, followed by an appendix that includes graphical representations and photographs of the multiple material tests and program-codes written for use in the thesis.

RESPONSIBLE TEACHER:	Professor Tore Børvik.
SUPERVISORS:	Professor Tore Børvik and Professor Odd Sture Hopperstad
CARRIED OUT AT:	SIMLab, The Department of Structural Engineering, NTNU.

Institutt for konstruksjonsteknikk
Fakultet for ingeniørvitenskap og teknologi
NTNU- Norges teknisk- naturvitenskapelige universitet

TILGJENGELIGHET

ÅPEN

MASTEROPPGAVE 2012

FAGOMRÅDE:	DATO:	ANTALL SIDER: 193
Beregningsmekanikk	8. juni 2012	18 + 150 + 25

TITTEL:

Effekt av varmebehandling på ballistiske egenskaper av AA6070 aluminiumsplater

UTFØRT AV:

Jens Kristian Holmen
Joakim Johnsen

SAMMENDRAG:
Denne oppgaven inneholder sammendrag av aktuell teori innenfor fagfeltene støt, penetrasjon, plastisitetsteori og prossesering og varmebehandling av aluminiumslegeringer. Sann spenning-tøyningskurver til brudd for AA6070-O, -T4, -T6 og -T7 er funnet gjennom strekktester. Aluminiumen ble levert som 20 mm tykke plater. Mikrostrukturen til materialet er rapportert. Materialkonstanter er funnet gjennom direktekalibrering og gjennom inversmodellering.

I ballistiske tester har 7.62 mm APM2-kuler og 20 mm flate og ogivale prosjektiler (CRH=3) blitt brukt. Ballistiske kurver og ballistiske grenser er funnet for alle material/kurve-kombinasjoner. Temper O viste seg å være mest duktilt, og fragmentering av dette materialet var sjeldent, i motsetning til T6 som oppførte seg relativt sprøtt med mye fragmentering. Fragmentering viste seg å ha stor innvirkning på de ballistiske egenskapene. Cockcroft-Lathams bruddkriterium har blitt implementert i de fleste analysene med grunnlag i plastisk arbeid til brudd. I de numeriske analysene har IMPETUS Afea Solver og LS-DYNA blitt brukt i henholdsvis 3D analyser og 2D aksesymmetriske analyser. Ballistiske kurver og ballistiske grenser har blitt funnet fra alle numeriske analyser. Visse sensitivitetsanalyser har blitt utført. Resultatene fra de aksesymmetriske modellene er sammenlignbare med tidligere studier. 3D-analysene fra IMPETUS Afea Solver ga gode resultater og programmet var effektivt og brukervennlig.

En utledning av Cylindrical Cavity Expansion Theory er gitt, og resultatene er gode for APM2-kuler. Beregninger har også blitt gjort med materialegenskaper uten rot i eksperimentelle forsøk med lovende resultater. Til slutt kommer en utfyllende diskusjon og noen konklusjoner, etterfulgt av et vedlegg med grafer, bilder og MATLAB-script som har blitt brukt i oppgaven.

FAGLÆRER:	Professor Tore Børvik.
VEILEDERE:	Professor Tore Børvik og Professor Odd Sture Hopperstad
UTFØRT VED:	SIMLab, Institutt for konstruksjonsteknikk, NTNU.

Department of Structural Engineering
FACULTY OF ENGINEERING SCIENCE AND TECHNOLOGY
NTNU - Norwegian University of Science and Technology

MASTER'S THESIS 2012

for

Jens Kristian Holmen and Joakim Johnsen

Effects of Heat Treatment on the Ballistic Properties of AA6070 Aluminium Plates

The main objective of this study is to investigate the effect of heat treatment and consequently yield stress, strain hardening and ductility on the ballistic properties of 20 mm plates made from aluminium alloy AA6070. Both experimental and numerical studies are to be carried out.

The main topics in the research project will be as follows:

1. A 20 mm thick plate in AA6070 is produced at Hydro Aluminium Rolled Products.
2. Plates of dimension 300×300 mm^2 are cut from this larger plate. A minimum of four plates are required per temper (three for ballistic tests and one for material tests).
3. The plates are heat treated to four different tempers: O (annealed), T4 (naturally aged), T6 (peak strength) and T7 (over-aged). This will alter the yield stress, the strain hardening and the strain to failure of the alloy.
4. Uniaxial tensile tests are carried out for each temper; the data is used to identify the material properties in a constitutive relation and a failure criterion.
5. The plates are used in ballistic tests with three different projectile-types to determine the ballistic limit velocity as a function of tempering.
6. Numerical simulations of the impact tests using IMPETUS and LS-DYNA are carried out. The numerical results are compared to the experimental findings.

Supervisors: Professor Tore Børvik and Professor Odd Sture Hopperstad (NTNU).

The thesis must be written according to current requirements and submitted to the Department of Structural Engineering, NTNU, no later than June 11th, 2012.

NTNU, January 16th, 2012

Tore Børvik
Professor

Preface

This thesis was written in the spring of 2012 and submitted in partial requirement for the degree of Master of Science in Civil and Enviromental Engineering, with specilization in Computational Mechanics. The experimental work was funded and the problem statement was formulated by the Structural Impact Laboratory (SIMLab) at the Department of Structural Engineering at the Norwegian University of Science and Technology (NTNU).

Trondheim, June 8, 2012

Jens Kristian Holmen

Joakim Johnsen

Acknowledgements

A major part of the thesis is the numerical work carried out with the IMPETUS Afea Solver and we would like to emphasize the contribution of Dr. Lars Olovsson; he gave us an introduction to the solver, answered our questions throughout the semester and implemented new features in the solver to accomodate our needs.

The aluminium plates were processed by Hydro Aluminium in Bonn, Germany, and we would like to thank Dr. Olaf Engler and Dr. Simon Jupp, who in addition to providing the target plates gave us valuable information about the heat treatment and chemical composition of the material. With the help of Dr. Ole Runar Myhr we gained insight into new territories in material science, through his Nanostructural Model to predict stress-strain curves.

Mr. Tore Kristensen from SINTEF conducted the tensile tests and gave us an introduction to the laboratory procedure; we thank him for that. Dr. Ida Westermann provided metallurgical insight along with microstructual pictures of the aluminium plates.

Without the help from the excellent academic environment at SIMLab and the Department of Structural Engineering at NTNU the past spring would have been impossible to get through. Dr. Torodd Berstad implemented computer-solutions that were not readily available, made sure that the computer resources assigned to us worked properly and helped us with numerical issues in LS-DYNA. Start-up problems with LS-OPT was solved by Dr. Stéphane Dumoulin. Mr. Trond Auestad proved to be an irreplaceable resource for us: he guided us through every single ballistic test, provided high-speed video images and opened locked doors (literally); no task was too big or too small.

Dr. Michael J. Forrestal gave us access to his private notes regarding the Cylindrical Cavity Expansion Theory and this was imperative to the derivation of the elastic response equations.

Proofreading would have been a struggle without the help of Ms. Rachel Spiegel, who corrected grammatical errors and spelling mistakes.

Our colleagues Mr. Andreas Bjune Kjølseth and Mr. Terje Karlsen helped us with relevant and irrelevant issues through discussions in the office. We shared the coffee-making responsibility with them, and they provided valuable insight in modeling issues, given their experience with similar problems through work on their own master's thesis.

Lastly, the support and help of our supervisors Professor Tore Børvik and Professor Odd Sture Hopperstad through frequent informal correspondance and weekly meetings was integral to the beginning, follow-through and end result of our master's thesis. We thank them for sharing their experience in the fields of material science, finite element analyses, ballistic testing and impact dynamics in general. Professor Børvik in particular deserves gratitude for answering our questions day and night.

Abstract

The thesis includes a summary of important theory in the fields of impact engineering and plasticity theory, and a literature study is carried out on aluminium designations, alloying and heat treatment. The true stress-strain curves of aluminium alloy AA6070 in O-, T4-, T6-, and T7-configurations are identified by tensile tests where the behavior is continuously measured to fracture. The aluminium was delivered as 20 mm rolled plates; microstructural images and strain ratios are reported. Material constants are found by direct calibration and inverse modeling.

Ballistic tests are done in a laboratory using 7.62 mm APM2 bullets, 20 mm blunt projectiles and 20 mm ogival projectiles (CRH = 3). From these tests the ballistic limit curves and the ballistic limit velocities are found for all temper/projectile combinations. In the material tests it was shown that the O-temper is the most ductile temper and consequently almost no fragmentation takes place in the ballistic tests for this temper. The T6-temper proved to be brittle, and fragmentation was commonly seen in the ballistic tests. The degree of fragmentation is found to be of vital importance for the ballistic performance. The Cockcroft-Latham fracture criterion is implemented by using the plastic work to fracture. Numerical analyses are performed with the IMPETUS Afea Solver and LS-DYNA, with 3D-models and 2D axisymmetric models, respectively. Ballistic limit curves and the ballistic limit velocities are calculated on the basis of the numerical results and then compared to the experimental values. Limited sensitivity studies are conducted on mesh size, heat-expansion dependency, strain-rate dependency, etc. Overall the results from 2D axisymmetric models are found to be consistent with previous studies, and the 3D-analyses carried out with the IMPETUS Afea Solver gave some good results. The IMPETUS Afea Solver proved to be a user-friendly finite element program with some powerful features.

In addition to the numerical studies, a thorough derivation of the Cylindrical Cavity Expansion Theory (CCET) is given. Results from CCET are good for 7.62 mm APM2 bullets. A case-study where the ballistic performance is determined without conducting any experiments is also conducted. The results are promising, but less conservative than the original simulations, due to the inability to calibrate a fracture criterion. Some suggestions for further work within the field of impact engineering and the application of the finite element method are provided at the end of the thesis, followed by an appendix that includes graphical representations and photographs of the multiple material tests and program-codes written for use in the thesis.

Contents

Nomenclature

α_T	Heat expansion coefficient.
β	Metastable structure in Al-Mg-Si alloys.
β'	Metastable structure in Al-Mg-Si alloys.
β''	Metastable structure in Al-Mg-Si alloys.
χ	Taylor-Quinney coefficient.
δ_{ij}	Kronecker delta.
$\Delta\epsilon_{erode}$	IMPETUS: Limit for incremental change in the geometric strain.
$\dot{\epsilon}_p$	Plastic strain rate.
$\dot{\epsilon}_{0p}$	Reference plastic strain rate.
ϵ_A	Almansi strain.
ϵ_e	Engineering strain.
ϵ_f	Fracture strain.
ϵ_G	Green strain.
ϵ_l	True strain.
ϵ_p	Equivalent plastic strain.
ϵ_v	Volumetric strain.
$\epsilon_{lu,p}$	Plastic strain at incipient necking.
ϵ_{pf}	Equivalent plastic strain at fracture.
λ	Heat conductivity.
ν	Poisson's ratio.
ρ	Density.
σ'	Deviatoric stress.
σ_0	0.2% offset yield stress.
σ_1	Major principle stress.
σ_e	Engineering stress.
σ_t	True stress.
σ_u	Ultimate tensile strength.
σ_{eq}	Equivalent stress.
σ_{pt}	Peak true stress.
σ_{uc}	Ultimate compressive strength.
$\widetilde{\sigma}$	Theoretical material strength.
$\bar{\tau}_0$	Integrated shear strength.
τ_0	Shear strength.
θ_i	Hardening parameter in the SIMLab Metal Model.
A	Yield parameter in JC and Voce hardening laws.
a	Parameter in the Recht-Ipson model.
A_0	Reference cross section area.
a_B	Specimen radius at notch center (Bridgman analysis).
A_C	Current cross section area.
B	Material parameter JC hardening law.
n	Material parameter JC hardening law.
C	Parameter determining strain rate dependency.
C_i	Material parameter Voce hardening law.
C_p	Heat capacity.
D	Damage.
d	Current diameter.
d_0	Reference diameter.
d_p	Projectile diameter.
d_y	Current diameter y-direction.
d_z	Current diameter z-direction.
Δd	Diameter reduction.
E	Young's modulus.
F	Force.
F_s	Shear force.
h_t	Target plate thickness.
K	Bulk modulus.
L	Current length.
L_0	Reference length.
l_p	Projectile length.

m	Parameter determining temperature softening.
m_p	Mass of projectile.
m_{pl}	Mass of plug.
P	Pressure.
p	Hydrostatic pressure (EOS).
p	Parameter in the Recht-Ipson model.
Q_i	Material parameter Voce hardening law.
R	Radius of neck curvature.
r	Strain ratio (Investigation of anisotropy).
r_B	Radial coordinate (Bridgman-analysis).
T	Current temperature.
T^*	Homologous temperature.
T_0	Reference temperature.
T_m	Melting temperature.
T_r	Room temperature.
v_i	Initial velocity.
v_r	Residual velocity.
v_{bl}	Ballistic limit velocity.
W_c	Cockroft-Latham parameter.
d_p	Projectile diameter.
ΔK	Change in kinetic energy.
K_f	Final kinetic energy.
K_i	Initial kinetic energy.
$\vec{p}$	Linear momentum.
Q	Heat generation.
r_p	Radius of projectile.
$\vec{v}$	Velocity.
W	Total work.
W_g	Global work.
W_l	Local work.
W_p	Projectile work.
W_{el}	Elastic work.
W_f	Frictional work.

Nomenclature for CCET

α	$(c/c_d)^2$.
ϵ	Logarithmic strain.
ϵ	True strain.
ϵ_θ	Tangential strain.
ϵ_r	Radial strain.
$\epsilon_{1,2,3}$	Principal strain.
γ	Normalized radial cavity expansion velocity.
γ_n	Octahedral strain.
ν	Poisson's ratio.
ψ	Caliber Radius Head.
ρ_p	Projectile density.
ρ_t	Target plate density.
σ	True stress.
σ_0	Yield stress.
σ_θ	Tangential stress.
σ_r	Radial stress.
σ_s	Quasi-static stress required to open cavity.
σ_z	Stress in thickness direction.
$\sigma_{1,2,3}$	Principal stresses.
τ_n	Octahedral stress.
ξ	Normalized radial coordinate.
a	Projectile radius.
c	Plastic-elastic interface stress wave speed.
c_d	Elastic stress wave speed.
E	Young's modulus.
F_z	Force acting on projectile.
L	Projectile shank length.
l	Projectile nose length.
n	Strain-hardening exponent.
r	Radial coordinate.
S	Normalized radial stress.
s	Radius of curvature of projectile tip.
t	Time.
$\bar{u}$	Normalized particle displacement.
U	Normalized particle velocity.
u	Particle displacement.
V	Radial cavity expansion velocity.
v	Particle velocity.
v_i	Initial velocity.
v_r	Residual velocity.
V_z	Radial cavity expansion velocity in z-direction.
v_{bl}	Ballistic limit velocity.

Chapter 1

Introduction

Structures intended to protect against small-arms are often made of high-strength steel because of its combination of strength, hardness, high ductility, low price and good formability [16]. However, recent studies have indicated that high-strength aluminium alloys may have equally good or even better ballistic properties than steel when areal weight is taken into account. Other studies indicate that plates impacted by projectiles at various velocities and with various nose shapes are not only dependent on material strength, but also local ductility [22]. High-velocity perforation is an extremely localized process. The consequence being that structural materials with a balanced combination of strength and ductility in addition to good formability, under certain conditions, may be an equally good energy absorber during ballistic impact as special alloys, having high strength at the expense of ductility. Aluminium can through alloying and heat treatments obtain a great number of useful properties with respect to perforation resistance, possibly making aluminium a desirable material for small-arms protection.

In ordinary linear-elastic or elastic-plastic, quasi-static problems, the loads are applied slowly enough for the equilibrium equations to adequately describe the problem. When the duration of an applied load is short or the application of load is sudden, dynamic effects have to be considered [26]. These dynamic effects include inertia forces, material rate-dependency, stress wave propagation and stress wave reflection in addition to the nonlinearities already present [1]. A penetration problem makes matters even more complicated because sliding contact, stress triaxialities, temperature dependency, and localization and initiation of material failure have to be taken into account [15]. These factors combined make penetration problems interesting and challenging when it comes to both experimental work and numerical modeling. In real life design situations the number of material tests are often limited, so it is desirable to keep the number of variables in the problem to a minimum [16]. Thus another challenge is created: modeling the problem accurately with as few parameters as possible.

In this thesis a number of simple material tests have been performed to investigate the direct effect of heat treatment on the physical constants of the alloy, before ballistic impact experiments with three different projectile types in two different velocity ranges were carried out. Subsequent numerical analyses in both LS-DYNA and IMPETUS Afea are run to see how well they can predict the real physical behavior.

The thesis is split in four. There is an introductory part in Chapter 2, an experimental part in Chapter 3-5, numerical and analytical work in Chapter 6-10, and discussion and conclusions in Chapter 11-13. To give the reader an overview of what to expect from reading the different chapters, short summaries are given here:

Chapter 2, Theoretical background: Gives an introduction to the most important theory that is used in this thesis. It supplements the experimental and numerical work by providing background information on the subjects at hand. The sections on constitutive relations and aluminium in particular gave the writers of this thesis a broader knowledge base, and enhanced the understanding of the

challenges of designing protective structures.

Chapter 3, Material Tests: Describes the process of manufacturing and testing the materials at hand. Pictures of the specimens and the method to extract material constants from the experiments are also given.

Chapter 4, Ballistic Impact Experiments: 7.62 mm Bullets: Description of the experimental methods related to the ballistic tests using APM2 bullets, including the experimental results, pictures and ballistic limit curves.

Chapter 5, Ballistic Impact Experiments: 20 mm Projectiles: Describes the methods and equipment used to fire blunt and ogival projectiles. Pictures and results from the tests are posted including a comparison between the two different nose-shapes.

Chapter 6, Calibration of Material Models: The results obtained from the material tests are analyzed and calibrated. A direct method of curve fitting is described first, while an optimized way of guessing parameters and comparing numerical results obtained from a model and the true test results is given subsequently. Lastly, the calibrated parameters are put to use with an IMPETUS Afea Solver tensile test.

Chapter 7, Numerical Analysis: 7.62 mm Bullets: Prerequisites for succesful numerical analyses are stated, along with several simulations for each temper impacted by 7.62 mm APM2 bullets carried out with the IMPETUS Afea Solver. A limited sensitivity study is presented.

Chapter 8, Numerical Analysis: 20 mm Projectiles: Numerical analyses of all temper/20 mm projectile combinations are performed, 2D axisymmetric and 3D-models are used in LS-DYNA and IMPETUS Afea Solver, respectively.

Chapter 9, Analytical Methods: A full derivation of the Cylindrical Cavity Expansion Theory is presented, the theory is applied on the tempers at hand in this thesis, and the results are reported. A much simpler analytical model to be used for blunt projectiles is also given.

Chapter 10, The NaMo-Model: Material behavior is obtained solely from numerical work. These values are then used in numerical ballistic tests.

Chapter 11, Discussion: Clarification of choices made in the thesis, discussion and comparison of results both from this thesis and existing papers are given.

Chapter 12, Concluding Remarks: A short summary and assessment of results from the experimental and numerical work. Results are tabulated for later reference.

Chapter 13, Further Work: Suggestions for further work concerning the finite element method within the field of impact engineering are given.

Chapter 2

Theoretical background

2.1 Terminology

Structural impact is defined as the collision between two or more solids [60]. The interaction between the solids may be elastic, plastic, fluid or any combination of these. Many impact phenomena exist and they are influenced by e.g. impact angle, the geometric and material characteristics of target and projectile, and the striking velocity. Striking velocity is divided into regimes or ranges, spanning from the low-velocity range (< 25 m/s) to the hypervelocity regime (> 3000 m/s) [6]. For the former, many problems fall in the area of structural dynamics, while for the latter, energy dissipation occurs at such high rates that explosive vaporization of the materials colliding may happen. Our problem deals with velocities in the subordnance range ($25 - 500$ m/s) and the nominal ordnance range ($500 - 1300$ m/s); at these velocities response of the structure becomes secondary to the behavior of the material itself.

The study of motion, forces, and impact of free-flying projectiles, especially those accelerated from firearms or guns, are referred to as ballistics. Further, the science of ballistics is divided into three sub-categories: interior, exterior, and terminal ballistics. Interior and exterior ballistics are the studies of the motion and forces acting on an object when it is still inside the launcher and during free flight, respectively. Terminal ballistics describes the interaction between the object and target during impact.

Terminal ballistics is of most interest with regards to fortification, which may be defined as structures used for additional strengthening, especially in military defenses [12].

Penetration is defined as the entry of a penetrator (e.g. projectile) into any region of the target [6]. The penetration process can be described or classified as:

(a) perforation, when the penetrator passes through the target and maintains residual velocity,
(b) embedment, when the penetrator is stopped during contact with the target, and
(c) richochet, when the penetrator is deflected off the target without being stopped.

As for the penetration process, target thickness is classified by Backman and Goldsmith [6]. A target is:

(a) semi-infinite, if the penetration process does not influence the target's rear surface,
(b) thick, if the rear surface is influenced after substantial travel into the target,
(c) intermediate, if the rear surface exerts considerable influence on the deformation process during all (or nearly all) of the penetrator motion, and
(d) thin, if stress and deformation gradients throughout its thickness do not exist.

During impact materials may fail in a number of ways. The cause of fracture is governed by many variables, such as impact velocity, material properties, projectile geometry, target support, and the relative dimensions of the projectile and target. Fig. 2.1 is adapted from Backman and Goldsmith

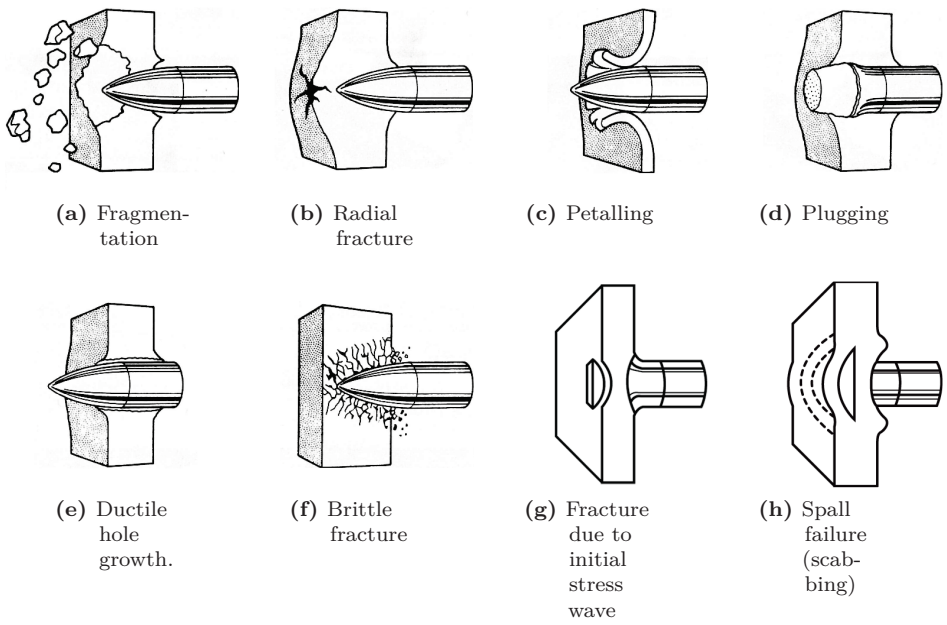

(a) Fragmentation **(b)** Radial fracture **(c)** Petalling **(d)** Plugging

(e) Ductile hole growth. **(f)** Brittle fracture **(g)** Fracture due to initial stress wave **(h)** Spall failure (scabbing)

Figure 2.1: Different failure modes in impacted plates [6, 60].

[6] and Zukas [60] and illustrates some dominant modes for thin and intermediate targets. It is important to remember that even if one of these modes dominates the failure process, they will often be accompanied by several other modes.

For high impact velocities brittle materials will fragment (Fig. 2.1a), while in ductile materials ductile hole growth dominates (Fig. 2.1e). Fracture due to an initial stress wave (Fig. 2.1g) which exceeds the ultimate compressive strength, σ_{uc}, may occur in weak, low-density targets, while hand radial fracture (Fig. 2.1b) is limited to materials whose tensile strength is substantially lower than their compressive strength, e.g. ceramics. Spalling (Fig. 2.1h) is fracture caused by the initial compressive stress wave being reflected as a tensile stress wave from the back of the target. Scabbing looks similar but is caused by deformations as opposed to stress waves and the fracture surface is determined by local inhomogeneities and/or anisotropies from e.g. rolling. Plugging is a consequence of adiabatic shearing, i.e. if the target is impacted by a blunt projectile; a cylindrical plug roughly the same diameter as the bullet will be set into motion by the projectile Fig. 2.1d. This causes large shear stresses around the moving plug, leading to failure. As the plug passes through the plate, heat is generated by the shear deformation, decreasing the material strength and leading to instability.

Petalling (Fig. 2.1c) is caused by high radial and circumferential tensile stresses after passage of the initial wave occuring near the lip of the penetrator. The forward motion of the plate material being pushed in front of the projectile produces bending moments. Inhomogeneities or planes of weakness in the target are the main sources of the deformation. This fracture mode is most frequently observed in thin plates struck by ogival or conical projectiles at relative low impact velocities, or by blunt projectiles near the ballistic limit velocity of the target. As the material in the bulge on the rear side of the plate is further deformed, the tensile strength will eventually be exceeded, leading to the characteristic star-shaped crack around the tip of the projectile. The segments are then pushed back by the continuing motion of the penetrator, leading to the formation of petals.

2.1.1 Ballistic Limit Velocity

Ballistic limit velocity, v_{bl}, is defined as the average of the highest projectile velocity suffering embedment and the lowest velocity of a perforating projectile. Several definitions exist; the army, protection, and

navy ballistic limits are the most significant [12]. The different ballistic limit definitions are illustrated in Fig. 2.2. The navy ballistic limit shown in Fig. 2.2c, is the most appropriate for our purpose.

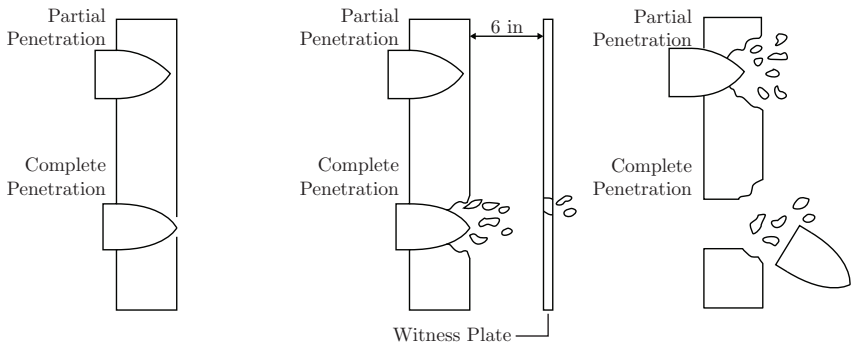

(a) Army ballistic limit **(b)** Protection ballistic limit **(c)** Navy ballistic limit

Figure 2.2: Different definitions of ballistic limit [6].

It is customary to plot a projectile's initial velocity against its residual velocity. Drawing a continuous line between these data-points gives the ballistic limit curve. This curve is often compared to the ballistic limit line which is the initial vs. residual velocity plotted for a target with zero thickness. Both are illustrated in Fig. 2.3.

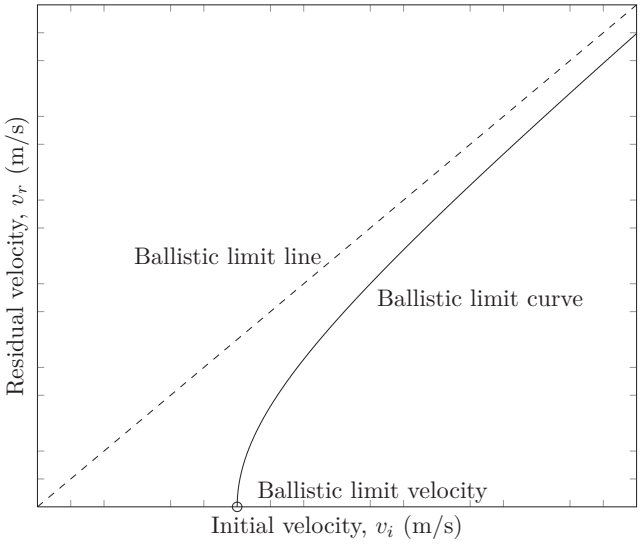

Figure 2.3: Ballistic limit curve, limit velocity, and limit line.

2.2 Mechanical Behavior of Metals

The behavior of materials when subjected to extreme loads, strain rates, and heat is highly nonlinear. The theory needed to describe these behaviors is too comprehensive to present thoroughly here, but some insight into the field is given in this section.

2.2.1 Strain Measures

Several strain measures exist, such as Green strain ϵ_G, Almansi strain ϵ_A, true strain ϵ_l, and conventional engineering strain ϵ_e. All strain measures have to satisfy the constraints of finite strains, namely predicting zero strain for rigid-body movement and reducing to the infinitesimal strain if the nonlinear terms are neglected. Additionally a good strain measure should be able to describe arbitrarily large strains, i.e. predict infinite negative strain for full compression ($\epsilon \to -\infty$ as $L \to 0$) and infinite strain for infinite elongation ($\epsilon \to \infty$ as $L \to \infty$) [46]. From Fig. 2.4 it can be seen that the only strain measure that fulfills these criteria is the true (logarithmic) strain, ϵ_l.

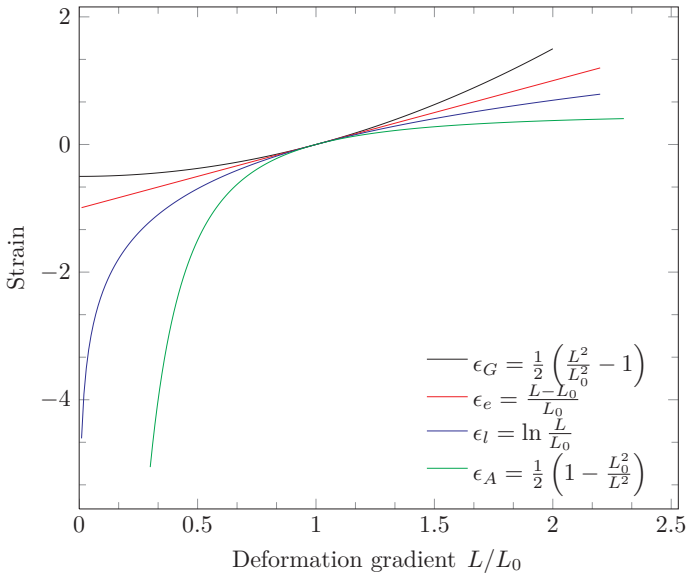

Figure 2.4: Comparison of the different strain measures.

In our material tests, the diameter reduction of the tensile specimen is measured along with the applied force. To calculate true strain we make use of the fact that the elastic strains in metals remain small, and that plastic deformation is incompressible [39], giving

$$A_0 L_0 = A_C L \tag{2.1}$$

$$A_0 = \frac{\pi}{4} d_0^2 \quad \text{and} \quad A_C = \frac{\pi}{4} d^2 \tag{2.2}$$

where A_0 and L_0 indicates reference dimensions and A_C and L are current dimensions. Inserting Eqs. (2.1) and (2.2) into the definition of logarithmic strain $\epsilon_l = \ln(L/L_0)$ we obtain

$$\epsilon_l = 2 \ln \frac{d_0}{d} \tag{2.3}$$

that states true strain as a function of diameter [35]. Because the applied force, F, and the current diameter, d, are known we can calculate the true stress

$$\sigma_t = \frac{F}{A_C} = \frac{4F}{\pi d^2} \tag{2.4}$$

2.2.2 The Effect of Nonuniformities of Stress at the Neck

Previously, the stress distribution throughout the tensile specimen has been assumed to be uniaxial; however, this is not the case in the region of the neck where the stress-state is triaxial.

First of all, it is necessary to define when necking occurs and the easiest interpretation stems from engineering stress-strain values (see Fig. 2.5b). Before necking, the required force to ensure elongation increases. When necking occurs the deformation localizes somewhere on the gauge, which means that elongation can take place at a lower level of applied force. Ergo, the point of neck initiation can be found by setting the derivative of the engineering stress ($\sigma_e = F/A$) equal to zero.

By using the relationship between engineering stress and true stress, $\sigma_e = \sigma_t e^{-\epsilon_l}$ we see that

$$\mathrm{d}\sigma_e = \mathrm{d}\sigma_t e^{-\epsilon_l} - \sigma_t e^{-\epsilon_l}\mathrm{d}\epsilon_l = (\mathrm{d}\sigma_t - \sigma_t \mathrm{d}\epsilon_l)\, e^{-\epsilon_l} = 0$$

This leads to the equation used in Fig. 2.5a

$$\frac{\mathrm{d}\sigma_t}{\mathrm{d}\epsilon_l} = \sigma_t \tag{2.5}$$

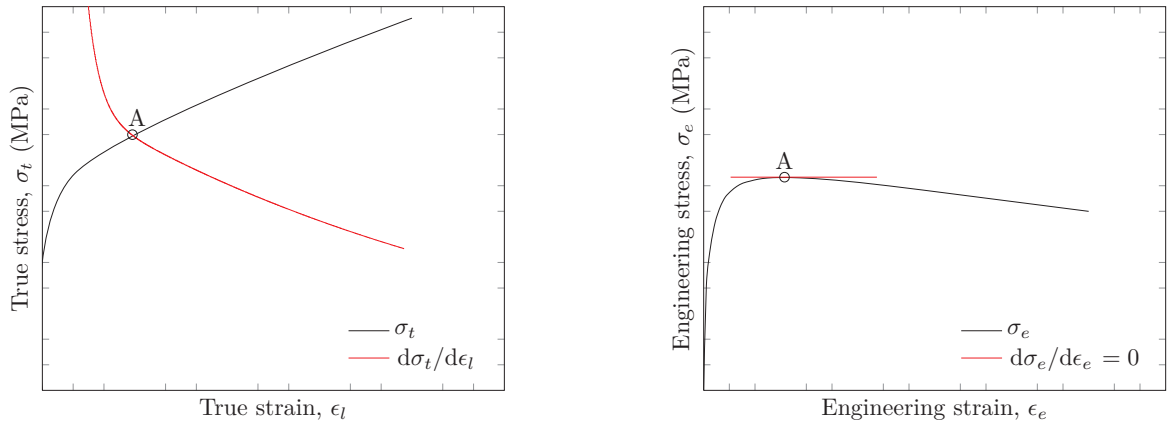

Figure 2.5: **(a)** Shows true stress-strain and how to find the point of incipient necking, **(b)** shows the same procedure only for engineering stress-strain.

We now need to account for the plastic flow contribution from shear stresses. This contribution can be measured by introducing an equivalent stress, σ_{eq}, e.g. the Von Mises equivalent stress.

$$\sigma_{eq} = \sqrt{\frac{3}{2}\sigma'_{ij}\sigma'_{ij}} \tag{2.6}$$

where $\sigma'_{ij} = \sigma_{ij} - \frac{1}{3}(\sigma_{kk}\delta_{ij})$ is the deviatoric stress tensor found by subtracting the hydrostatic stress from the stress tensor, δ_{ij} is the Kronecker delta [39].

Furthermore, the stress triaxiality at the neck may introduce errors in the laboratory measurements, because the hydrostatic contribution contaminates the results. In 1952 Bridgman carried out a mathematical analysis of the stress distribution at the neck, which enabled him to calculate the unpolluted longitudinal stress σ_z [11],

$$\frac{\sigma_z}{\sigma_{eq}} = 1 + \ln\left(\frac{a_B^2 + 2a_B R - r_B^2}{2a_B R}\right) \tag{2.7}$$

where a_B is the specimen radius at notch center, R the radius of the curvature of the neck, and r_B is the radial coordinate. Bridgman also obtained an expression for the average longitudinal stress

$$\frac{\sigma_{\overline{z}}}{\sigma_{eq}} = \left(1 + 2\frac{R}{a_B}\right)\ln\left(1 + \frac{a_B}{2R}\right) \tag{2.8}$$

which is the one used later in the thesis. This correction will decrease the stress magnitude after necking (examples can be seen in Fig. 6.1).

2.2.3 Rheological Model

For small strains aluminium behaves linear-elastically. However, in the case of large strains; strain rate and temperature dependency during plastic flow is introduced, thus making the aluminium behave as a thermoelastic-thermoviscoplastic material. We can describe this material behavior conveniently by springs, nonlinear dashpots and frictional elements in so called rheological models (see Fig. 2.6). In cases where work hardening is present, the resistance of the frictional elemens increase with plastic strain.

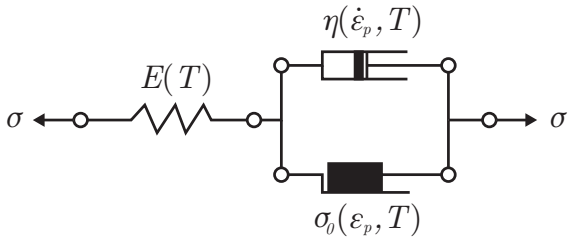

Figure 2.6: Rheological model for a thermoelastic-thermoviscoplastic material [39].

2.3 Constitutive Equations and Fracture Criteria

Models that describe material behavior, or constitutive equations, are used to relate stresses and strains experienced in a material during loading. Hooke's law (Eq. (2.9)) is a classic example of a constitutive equation; it applies to linear elastic material behavior.

$$\sigma = E\epsilon \tag{2.9}$$

where σ is the stress, E the Young's modulus, and ϵ the elastic strain. In impact dynamics more advanced material models are required in order to account for e.g. material nonlinearities, strain rate dependency, and temperature dependency. The Johnson-Cook model (JC) is an example of such a material model, the model is described in detail in Section 2.3.1.

However, the constitutive equation does not predict material failure. To do this a fracture criterion is needed; two fracture criteria are covered shortly in this section.

2.3.1 Johnson-Cook Strength Model

The JC flow stress model was first proposed in 1983 by Johnson and Cook [42]. It is an empirical viscoplastic model where the von Mises flow stress is given as a function of equivalent plastic strain, strain rate and temperature.

$$\sigma_{eq} = [A + B\epsilon_p^n][1 + C\ln\dot{\epsilon}_p^*][1 - T^{*m}] \tag{2.10}$$

where A, B, n, C and m are material constants, ϵ_p is the equivalent plastic strain, $\dot{\epsilon}_p^* = \dot{\epsilon}_p/\dot{\epsilon}_{0_p}$ is the dimensionless plastic strain rate given by plastic strain rate $\dot{\epsilon}_p$ and reference plastic strain rate $\dot{\epsilon}_{0_p}$. The homologous temperature $T^* = (T - T_r)/(T_m - T_r)$ is given by the current material temperature T, room temperature T_r and the material's melting temperature T_m.

In Eq. (2.10) term 1 represents stress as a function of strain, term 2 takes strain rate into account, and finally term 3 captures the effect of temperature softening. It is worth noticing that the logarithmic term may cause trouble if the plastic strain rate $\dot{\epsilon}_p^*$ becomes smaller than 1, to accommodate this problem one may augment term 2, to obtain the Modified Johnson-Cook model (MJC)

$$\sigma_{eq} = [A + B\epsilon_p^n][1 + \dot{\epsilon}_p^*]^C[1 - T^{*m}] \tag{2.11}$$

The strain hardening in Eq. (2.11) follows the power law. This law has been found to better describe steel than aluminium [14]. Therefore it is necessary to introduce Voce work-hardening:

$$R(\epsilon_p) = \sum_{i=1}^{j} Q_i \left(1 - e^{-C_i \epsilon_p}\right) \quad \text{where} \quad j \in \mathbb{N} \tag{2.12}$$

where Q_i and C_i are material parameters, j is typically 1, 2 or 3. By inserting Eq. (2.12) into Eq. (2.11) we obtain:

$$\sigma_{eq} = [A + \sum_{i=1}^{j} Q_i \left(1 - e^{-C_i \epsilon_p}\right)][1 + \dot{\epsilon}_p^*]^C [1 - T^{*m}] \tag{2.13}$$

As a consequence of the high plastic strain rate, adiabatic heating will occur [13]. The change of temperature in the material can be calculated from

$$\Delta T = \int_0^{\epsilon_p} \chi \frac{\sigma_{eq} \mathrm{d}\epsilon_p}{\rho C_p} \tag{2.14}$$

in which ρ is the material density, C_p the specific heat, and χ the Taylor-Quinney coefficient, representing the fraction of plastic work converted into heat (typically 0.9 in metals [36]).

2.3.2 The Cockcroft-Latham Fracture Criterion

This fracture criterion was proposed by Cockcroft and Latham in 1968 [24]. It takes into account the magnitude of the highest normal stress present in the material, i.e. the major principal stress. In addition to this the criterion is dependent on the developed plastic strain.

$$W_c = \int_0^{\epsilon_{pf}} \langle \sigma_1 \rangle \, \mathrm{d}\epsilon_p \tag{2.15}$$

where W_c is the plastic work per unit volume, σ_1 is the major principal stress, ϵ_p is the equivalent plastic strain and ϵ_{pf} is the equivalent plastic strain at fracture. Assuming that fracture will not occur in compression, the value $\langle \sigma_1 \rangle = 0$ if $\sigma_1 < 0$ and $\langle \sigma_1 \rangle = \sigma_1$ if $\sigma_1 \geq 0$. Considering the dependency on both stress and strain, the criterion is robust with respect to strain rate and temperature. High temperature gives low strength and high ductility while high strain rate gives high strength and low ductility, this in turn makes the plastic work (W_c) approximately constant which is integral for a fracture criteron in high velocity impact dynamics [16].

The simple calibration and the ease of which Cockcroft-Latham can be implemented in finite element codes (e.g. LS-DYNA and the IMPETUS Afea Solver) are both strong arguments for the use of this fracture criterion. The results have been shown to be promising, however limitations arise with the description of stress triaxialities [28].

2.3.3 The Johnson-Cook Fracture Criterion

Although the Cockcroft-Latham failure criterion somewhat indirectly deals with strain rate and temperature by "coincidence", the Johnson-Cook criterion from 1985 directly incorporates dependency on temperature, strain rate and strain path, thus making calibration more cumbersome.

The JC-criterion is more extensive than the CL-criterion, and it reads

$$\epsilon_f = (D_1 + D_2 \exp(D_3 \sigma^*)) \left(1 + D_4 \ln \dot{\epsilon}_p^*\right) (1 + D_5 T^*) \tag{2.16}$$

where D_1, D_2, D_3, D_4 and D_5 are material constants. The damage evolution is described by:

$$D = \sum \frac{\Delta \epsilon_p}{\epsilon_f} \tag{2.17}$$

Failure occurs when $D \geq 1$.

Several other fracture criteria exists, although they have not been looked into in this thesis. More on this can be found in Dey's Dr.ing. thesis [28].

2.4 Adiabatic Shear Bands

In many of the analyses performed in this thesis, adiabatic conditions are assumed. For velocities in the ranges we study, this is an adequate assumption. Especially for blunt projectiles, localized plastic deformation in the form of narrow shear bands, so-called adiabatic shear bands can be seen. They occur because of rapid heating and give intense plastic shear deformation. Due to their microscopic size of up to just a few hundred microns, the elements to be used in finite element analyses have to be very small. This is particularly important for the blunt projectile impacts because this ballistic configuration is very susceptible to plugging which is often initiated by shear banding. The shear banding process is not fully understood, and a thorough investigation of the phenomenon has been deemed outside the scope of this thesis. However, adiabatic shear bands have been the focus in past research and more information can be found in the works of Bai and Dodd 1992 [7], and Wright 2002 [58].

2.5 The Recht-Ipson Model

Originally proposed by Recht and Ipson in 1963, this equation predicts the residual velocity by using the ballistic limit velocity, mass of the projectile, mass of the plug created and the initial velocity (or a selection of these). The standard model uses conservation of momentum and the impulse-momentum law to find an equation that is valid for thin plates impacted by blunt, practically undeformable projectiles that cause plug ejection [12]:

$$v_r = \left[\frac{m_p}{m_p + m_{pl}}\right] \left(v_i^2 - v_{bl}^2\right)^{1/2} \tag{2.18}$$

where v_r is the residual projectile velocity, v_i is the initial projectile velocity, v_{bl} is the ballistic limit velocity, m_p is the projectile mass and m_{pl} is the mass of an ejected plug. If no plug is ejected, but the material is pushed aside and compressed, Eq. (2.18) reduces to

$$v_r = \left(v_i^2 - v_{bl}^2\right)^{1/2}. \tag{2.19}$$

A generalization of this equation was proposed by Lambert in 1978 [60]:

$$v_r = a\left(v_i^p - v_{bl}^p\right)^{1/p}. \tag{2.20}$$

where a and p are empirical constants that are fitted to experimental data points (for example in Fig. 4.12) by using the method of least squares to create continuous lines. If $a = 1$ and $p = 2$, Eq. (2.19) is obtained, a and p can also take on other values which makes Eq. (2.20) able to describe the ballistic limit curve for more complex fracture types.

The definition for thin plates used in this thesis is

$$\frac{h_t}{l_p} < 0.5 \quad \text{and} \quad \frac{h_t}{d_p} < 0.5 \tag{2.21}$$

where h_t is the plate thickness, l_p is the projectile length and d_p is the projectile diameter [12].

2.6 Aluminium

Aluminium in its pure form is widely recognized as a light and ductile metal with a density of 2700 kg/m^3 and it exhibits good corrosion resistance due to its oxide coating. Although it takes large amounts of energy to produce aluminium from scratch, recycling is very effective, and requires only 5% of the original enery [40]. Pure aluminium has a yield strength of $15 - 20$ MPa [41], but by introducing alloying elements and by heat treating the alloy one can refine the properties of aluminium to fit a number of needs without compromising the weight advantage aluminium has over e.g. steel.

2.6.1 Microstructure

As almost all metals, aluminium is made up entirely of crystals in which atoms are packed in regular three-dimensional patterns [4]. Aluminium atoms take on a three-dimensional structure called face-centered cubic (f.c.c), because it gives aluminium its minimum energy. Magnesium on the other hand, takes on the close-packed hexagonal (c.p.h) structure, while for instance iron will be body-centered cubic (b.c.c). By breaking the metal down to a unit-cell, i.e. the smallest repeated construction of aluminium, it can be seen that the atoms in a f.c.c.-structured crystal are placed at the corners of a cube, and at the face centers of that same cube (Fig. 2.7a). The atom-arrangement is not necessarily isotrope, which means that the different directions can have different physical properties. The ideal strength, $\widetilde{\sigma}$, is the theoretical limit of how strong a material can get. This strength is found to be $\widetilde{\sigma} \approx E/15$ [4], however, a material never reaches this theoretical limit due to several imperfections: e.g. dislocations. Plastic deformation is mainly determined by dislocation movement, for f.c.c. aluminium, dislocations glide on the closely packed {111} planes. These planes can be defined by the atoms in three corners for which the connecting lines form diagonals on each cube face.

Initiation and progression of dislocation movement can be inhibited by different strengthening mechanisms. For metals it is important to increase the resistance opposing the motion of dislocation by work hardening, solution hardening, precipitation hardening or grain size hardening [47]. Work hardening results from the interaction of several dislocations that accumulate in the material and obstruct one another, this can be recognized from a rapidly rising yield stress. Solution hardening is a way of roughening up the slip planes by introducing alloying elements into the aluminium matrix, success criteria for this is to find alloying elements with high solubility and high atomic misfit to create local tensile and compressive strains. The practical significance of precipitation hardening will be covered in Section 2.6.3, but in principle precipitates are small and hard particles that obstruct dislocation motion, see Figs. 2.7b and 2.7c. The dislocation can either cut through the precipitate or bow around it. Large precipitates force the precipitates to bow around, which implies that closely spaced, large precipitates provide the greatest hardening. Grain size hardening takes advantage of the fact that reduced grain size leads to increased strength, but this will not be covered in this thesis. These four hardening mechanisms can be assumed to be additive [4], so in practice more than one hardening mechanism adds to the overall strength.

2.6.2 Alloying

Alloying elements that can be used to improve the mechanical behavior of aluminium are numerous; ranging from copper to zinc, and each element brings new and possibly useful properties to the alloy [41]. The high strength-to-weight ratio makes aluminium alloys interesting in the fabrication of protective structures, while it creates a large demand in for instance the automotive and the aerospace industry. The Aluminum Association has created a system to identify and separate the different alloys, for wrought alloys a four-digit system is used [41]. The notation reads: AAxxxx, where the x's are numbers. The first number denotes the major alloying elements (see Table 2.1), the second number denotes modifications from the original alloy while the two last numbers separate the alloys from each other.

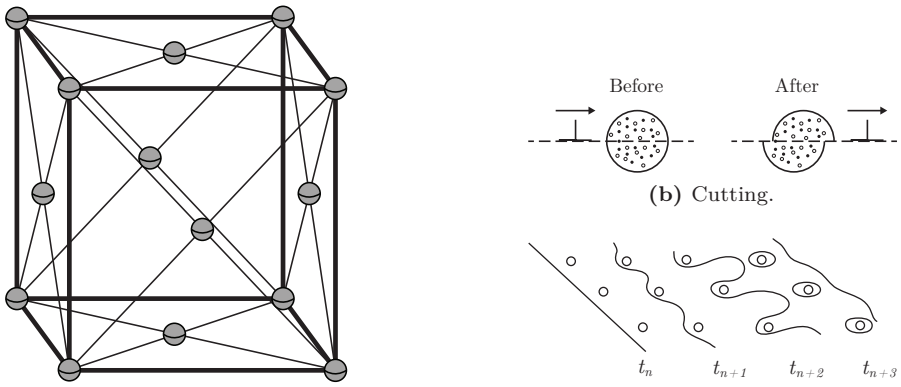

(a) Unit cell. **(b)** Cutting. **(c)** Bowing

Figure 2.7: **(a)** A unit cell for a face-centered cubic material, **(b)** a dislocation cutting through a precipitate [5] and **(c)** a dislocation bowing around precipitates [53].

Table 2.1: Properties of the different alloys in the AA-system [34, 41, 47].

	Alloying elements		
Alloy series	**Major**	**Minor**	**Properties**
1xxx	Commercially pure aluminium		Low strength; excellent formability, weldability and corrosion resistance.
2xxx	Cu	Mg, Mn, Si ++	High strength, good fatigue properties. Heat treatable.
3xxx	Mn	Mg	Ductile and weldable.
4xxx	Si		Brittle.
5xxx	Mg	Cr	Medium strength, good formability, excellent corrosion resistance under marine conditions.
6xxx	Mg and Si	Mn and Cr	High strength, formability, weldability and excellent corrosion resistance. Heat treatable.
7xxx	Zn	Mg, Cu, Cr ++	Very high strength, poor corrosion resistance. Heat treatable.
8xxx	Sn	Li	Low weight, good fatigue properties and increased stiffness.
9xxx	Series not used		

2.6.3 Heat Treatment

The process of heat treatment is thoroughly described by the American Society for Metals [34]. A selection of the important subjects is given here. The manipulation of aluminium alloys through heat treatment can drastically change the behavior of the alloy itself. Among the wrought alloys only the 2xxx, 6xxx and 7xxx series are heat treatable. In many alloys the contents of soluble elements in the aluminium are higher than that of equilibrium at room temperature, they are what we call super-saturated. As for temper designations, they are denoted with a letter and sometimes numbers after the alloy designation, i.e. AAxxxx-Lxx, where L is a letter describing the treatment type, and the two last x's are sub-designations to more accurately describe the process. The letters mean the following:

F **As fabricated:** No special control over thermal conditions is applied.

O **Annealed:** Wrought products annealed to produce the lowest strength temper.

W **Solution heat treated:** Unstable temper used for alloys that age spontaneously at room temperature.

T **Thermally treated to produce stable tempers:** With or without strain hardening.

Annealing is a process where aluminium (or any other metal) is heated up to a temperature well below the eutectic point and kept there to restructure the microstructure that has been altered by e.g. cold-rolling, making the specimen more ductile and with a lower strength than before, for example to retain formability. Solution heat treatment is used to solute as much of an alloying element into the aluminium as possible, meaning that the aluminium often must be heated to around the eutectic temperature to reach max solubility. To trap the solutes in the aluminium matrix and to obtain the desired supersaturated solution, rapid cooling takes place in a process known as quenching.

Immediately after quenching the aluminium can be formed or straightened with relative ease before some form of aging can take place. Natural aging is aging at temperatures around room temperature and artificial aging is aging at temperatures well above what can be described as room temperature. Often an artificially aged alloy will have higher yield strength, but it will be less ductile than the same naturally aged alloy [47]. (This can also be seen later in this thesis in Fig. 3.11b.) The aging duration may also affect the properties of aluminium: overaging is known to reduce tensile and yield strengths compared to alloys aged shorter, on the other hand stress-corrosion cracking resistance may increase.

To convey some of the possibilities within heat treatment the different thermally treated tempers under the T-designation are explained below. These are the definitions given by the American Society for Metals [34]:

O Rolled and formed, then moderately heated to retain crystal structure and ductility.

T1 Cooled from an elevated-temperature shaping process and naturally aged to a substantially stable condition. Not cold worked afterwards.

T2 Same as T1, but cold worked before aging.

T3 Solution heat treated, cold worked and naturally aged to a substantially stable condition. Cold worked after solution heat treatment to increase strength.

T4 Solution heat treated and naturally aged to a substantially stable condition. Not cold worked after solution heat treatment.

T5 Cooled from elevated-temperature shaping process, then artificially aged. Not cold worked afterwards.

T6 Solution heat treated, artificially aged to reach peak strength. Not cold worked after solution heat treatment.

T7 Solution heat treated, cold worked and then artificially aged. This temper is over-aged.

T8 Solution heat treated, cold worked and artificially aged.

T9 Solution heat treated, artificially aged and then cold worked.

T10 Cooled from elevated-temperature shaping process, cold worked and then artificially aged.

A schematic overview of the tempering process is shown in Fig. 2.8. Solution heat treatment takes place at around 500 °C, annealing takes place roughly between 250 °C and 500 °C, while the aging process occurs in the range between 150 °C and 220 °C [34].

To make an alloy susceptible to age-hardening, at least one of the alloying elements has to have a significantly lower solubility in aluminium at low temperatures than at the eutectic temperature [47]. When a supersaturated solid solution is formed after quenching, the alloying elements are frozen in place along with vacancies. As already seen, the strength of aluminium greatly depends on the nature and size of the precipitates. Figs. 2.7b and 2.7c depict how dislocations can pass the precipitates, the cutting stress increase with aging time, while the bowing stress decrease with aging time. These two

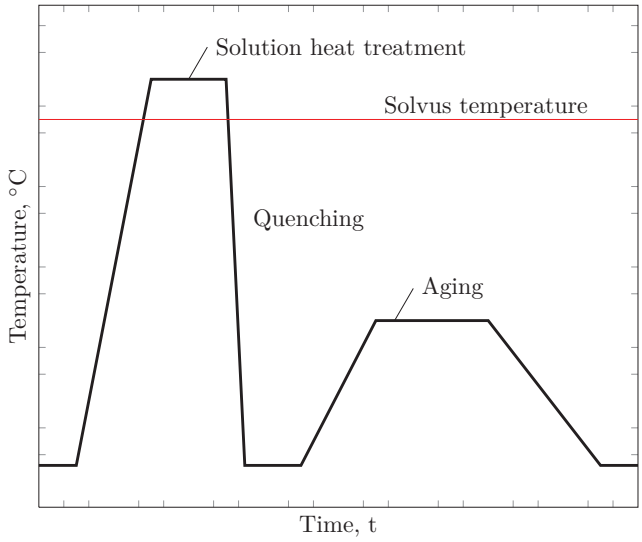

Figure 2.8: A qualitative plot on how to heat-treat an aluminum alloy [47].

effects are mutualy exclusive, so a peak stress alloy needs to be aged until bowing stress approximately equals the cutting stress (or a little further). If an alloy is aged longer than this, the precipitates will grow bigger and farther apart, i.e. bowing will take place, and the strength is reduced (Fig. 2.9) [5].

To obtain these dislocation motion inhibiting precipitates, the particles from the supersaturated solid solution has to merge. Throughout the aging, a simplified way of looking at the previously described process through classical nucleation theory is (N is number of precipitates and $\overline{r}$ is the mean radius):

Nucleation	$\rightarrow$	**Growth**	$\rightarrow$	**Coarsening**
N increase		N constant		N decrease
$\overline{r}$ constant		$\overline{r}$ increase		$\overline{r}$ increase

In real life these processes will not necessarily happen succesively, but they might overlap and happen at the same time [50].

Fig. 2.9 also show the different precipitation stages as the aging time increase: α(ssss) $\rightarrow$ GP zones $\rightarrow$ $\beta'' \rightarrow \beta' \rightarrow \beta$ [49]. α(ssss) is the supersaturated solid solution, GP zones are spherical clusters with unknown structure and β'', β' and β are differently shaped precipitates oriented in different directions with different chemical composition that affect the strength of the material in different ways [49, 29]. β'' and β' are metastable structures, while β is the stable equilibrium configuration.

Another important factor that has to be taken into account when designing a heat treatment is the occurance of precipitate free zones (PFZs). A PFZ is a region near the grain boundaries which is depleted of precipitates. Wide PFZs are undesirable because they affect the mechanical strength of materials in a negative way. Methods of narrowing the PFZ includes lowering the aging temperature to reduce the critical vacancy concentration needed for precipitates to nucleate, or simply by increasing the vacancy concentration [47]. Because PFZs are softer than the rest of the matrix, they are susceptible to strain localization, i.e. fractures can initiate and take place along the grain boundaries [55].

2.6.4 The 6xxx-series

In this study the ballistic performance of the AA6070 alloy is examined, the specific alloy will be covered in Section 3.1. In general the 6xxx-series has high strength, formability, weldability and

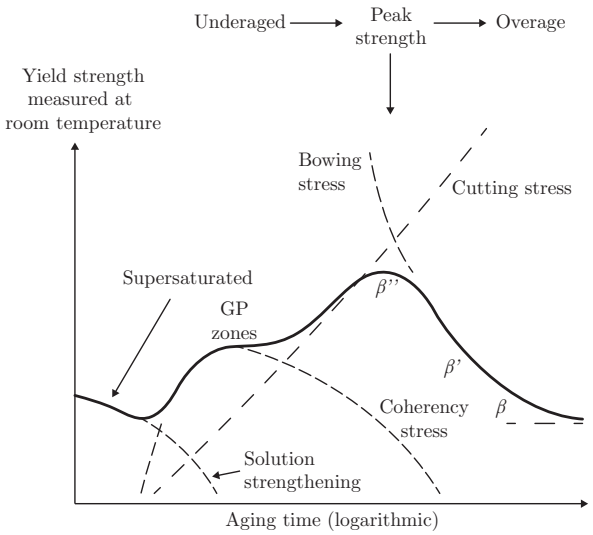

Figure 2.9: Schematic of how yield strength evolve during aging, adapted from Ashby-Jones [5].

corrosion resistance (see Table 2.1). The main alloying elements are usually silicon and magnesium, and they contribute to the high strength of the material while minor alloying elements like copper, calcium, chromium, cadmium, lead and manganese may be added for properties such as grain size stabilization, toughness and machinability [47]. The 6xxx-series can (in the same fashion as the 2xxx-series and the 7xxx-series, see Table 2.1) be thermally treated through precipitation hardening, this strengthens the material by inhibiting the dislocation movement that takes place inside the material. A variety of properties can be obtained by different amounts of silicon and magnesium and by giving the material different heat treatments. An example of chemical composition of the AA6070 found in the literature can be seen in Table 2.2 [34].

Table 2.2: The nominal chemical components in AA6070 using wt-%.

Silicon (Si)	**Magnesium (Mg)**	**Manganese (Mn)**	**Copper (Cu)**	**Aluminium (Al)**
1.30 %	0.80 %	0.70 %	0.28 %	Balance

2.7 Impetus Explicit Solver

IMPETUS Afea Solver is a non-linear finite element solver specifically created to predict large deformations under extreme loading conditions [2]. IMPETUS can be run on graphic processing units (GPUs), this can drastically reduce the computational time, due to its surperiority in processing large blocks of data in parallel, compared to regular central processing units (CPUs) [25].

The software package features several modules, including a welding module (WELDSIM), a Discrete Particle module, and a module to model fluids (Smoothed Particle Hydrodynamics); the Finite Element module with an explicit solver has been used in this thesis. Advantages of this module are: one contact algorithm (penalty) and no elements with zero-energy-modes. In addition to this, IMPETUS features higher order elements that can handle large deformations, e.g. the 64-node cubic hexahedron element displayed in Fig. 2.10 [3]. A user friendliness combined with a powerfull post-processor, makes working with the IMPETUS Afea Solver very effective.

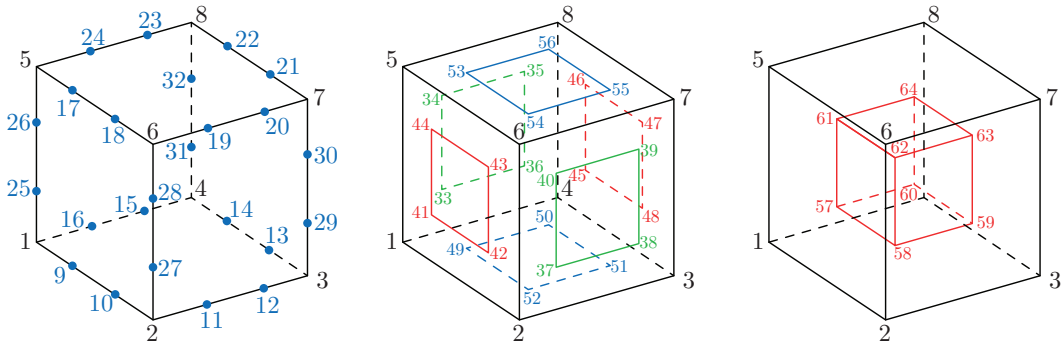

Figure 2.10: The 64-node cubic hexahedron element implemented in IMPETUS Afea.

Chapter 3

Material Tests

3.1 Material Processing

The processing of the aluminium that was used in all of the material and ballistic tests in this thesis was done by Hydro Aluminium in Bonn, Germany. The chemical components are tabulated in Table 3.1, as well as the nominal values taken from the literature [34]. According to the manufacturer the material is recrystallized due to the solution heat treatment, meaning that the initial structure of all tempers should be virtually stress free [34].

Table 3.1: The actual and nominal chemical components in AA6070 using wt-%. Concentrations not listed are less than 0.01 wt-%.

	Si	**Mg**	**Mn**	**Cu**	**Fe**	**Al**
Real values	1.38 %	1.23 %	0.54 %	0.26 %	0.22 %	Balance
Nominal values	1.30 %	0.80 %	0.70 %	0.28 %	-	Balance

All material provided to us has been DC-cast (direct chill) to a thickness of 126 mm, machined to 103 mm, homogenized at 550 °C for 4 hours then hot-rolled to a thickness of 20 mm. Subsequently, the following heat treatment took place to create the different tempers:

O 90 min at 560 °C (+5 °C) → water quench → 24 h at 350 °C → slow cooling.
T4 90 min at 560 °C (+5 °C) → water quench
T6 90 min at 560 °C (+5 °C) → water quench → 64 h at 160 °C (+5 °C) → slow cooling.
T7 90 min at 560 °C (+5 °C) → water quench → 8 h at 200 °C (+5 °C) → slow cooling.

The heat treatment process described above for the O-temper deviates from the process found in the literature. After the wrought process the aluminum should immediately be soft annealed, not solution heat treated and water quenched before annealing. However, the extended heat treatment given to the O-temper plates after quenching should provide sufficient over-aging to get to the soft state, ensuring that the properties of the O-temper at hand are practically identical to a normal O-temper, despite the different heat treatment. The level of alloying elements in the AA6070 is high, and it effectively has the maximum Mg-Si level before the primary particles are precipitated from the melt.

3.2 Experimental Work

The tensile tests were carried out at NTNU (the Norwegian University of Science and Technology) by SINTEF (The Foundation for Scientific and Industrial Research). The tensile specimens (Fig. 3.1), were mounted in a Dartec M 1000RK 20kN universial servohydraulic test machine (Fig. 3.2a). To be

able to obtain accurate true stress-strain values all the way to fracture, an AEROEL XLS 13XY Laser Micrometer (Fig. 3.2b) was used to measure the diameter reduction in the thickness direction (z) and the in-plane direction (y) at the point of the minimum cross section. The laser device was placed on a mobile frame to ensure that the measurements were taken at the exact point of the neck. A total of 36 individual tensile tests were carried out on four different tempers of the AA6070 aluminium alloy to investigate the significance of heat treatment. Different test orientations were also used. Three tests were carried out on each temper/test orientation-combination; these combinations are described in Table 3.2. All specimens were tested with a speed of 1.2 mm/min which gives an initial strain rate of 0.0005 s^{-1} over the 40 mm parallel length (Fig. 3.1).

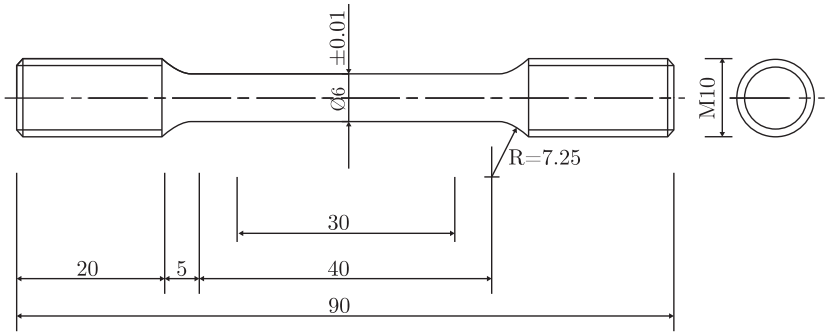

Figure 3.1: Geometry of the tensile specimen, all dimensions in mm.

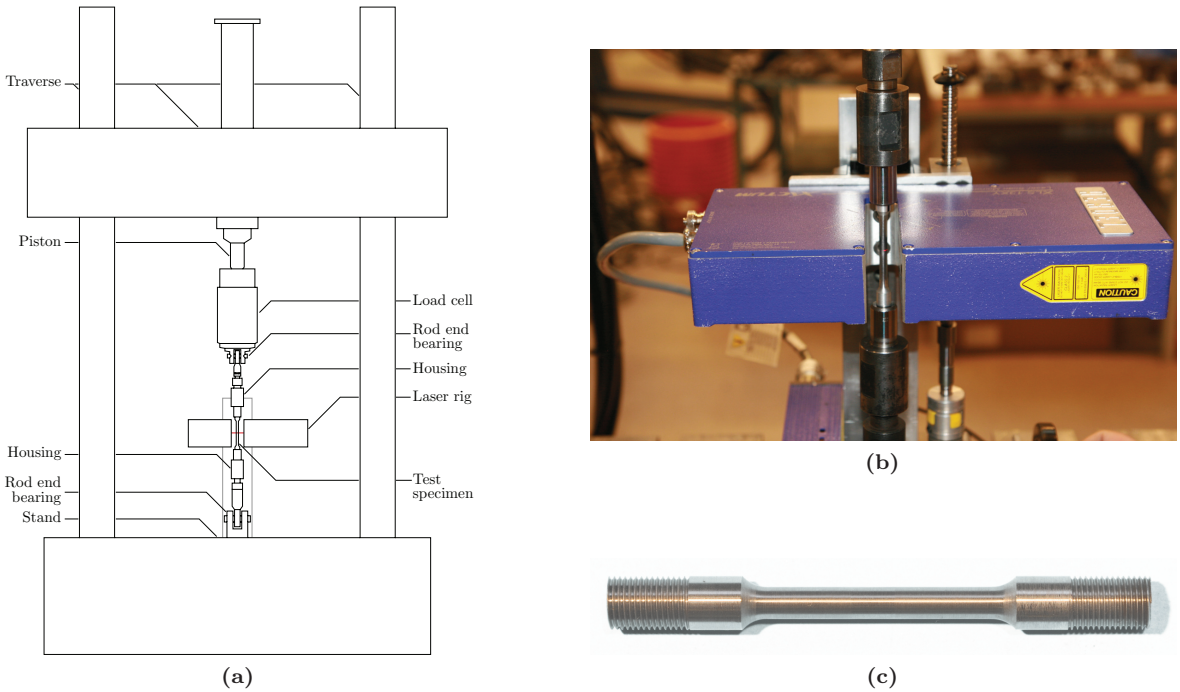

Figure 3.2: **(a)** shows the schematics of the servohydraulic test machine used for the tensile tests, **(b)** the laser rig used to continously measure diameter reduction, and **(c)** a test specimen pre-testing.

It must be mentioned that the diameter at the midpoint of all the tensile tests was made marginally smaller than the diameter outside the midpoint to make sure that necking initiated at that midpoint.

This made measuring the diameter reduction significantly easier without compromising test results. Even after the diameter reduction was done, the homogeneous O-temper proved difficult to test due to the relatively low yield stress and high ductility which made the area of the specimen shrink rapidly and stepwise, not in a smooth continous motion that was the case for the other tempers.

Table 3.2: Organization of the tensile tests performed. Highlighted entries display the median fracture strain and are viewed as typical curves to represent the specified temper/test-orientation combination.

Temper	Test orientation	Test name		
AA6070-O	0°	***O-0-1***	O-0-2	O-0-3
	45°	O-45-4	***O-45-5***	O-45-6
	90°	O-90-7	O-90-8	***O-90-9***
AA6070-T4	0°	T4-0-1	T4-0-2	***T4-0-3***
	45°	T4-45-4	***T4-45-5***	T4-45-6
	90°	T4-90-7	***T4-90-8***	T4-90-9
AA6070-T6	0°	T6-0-1	T6-0-2	***T6-0-3***
	45°	T6-45-4	***T6-45-5***	T6-45-6
	90°	***T6-90-7***	T6-90-8	T6-90-9
AA6070-T7	0°	T7-0-1	***T7-0-2***	T7-0-3
	45°	T7-45-4	***T7-45-5***	T7-45-6
	90°	T7-90-7	***T7-90-8***	T7-90-9

3.3 Experimental Results

The experimental data presented in this section is a result of the 36 tensile tests described in Section 3.2. Due to the sheer volume of tensile data gathered for this paper, it is structured such that each temper is treated individually. This makes it easier to identify the representative material test and to extract the useful material properties before a comparison is given to clarify the differences and similarities between the tempers. For the rest of the thesis, the yield stress, σ_0, is defined as the stress that gives 0.2% plastic strain (i.e. $\sigma_{0.2}$) unless otherwise specified.

3.3.1 Initial Data Processing

In the following sections we will present results from the material tests conducted for AA6070-O, AA6070-T4, AA6070-T6 and AA6070-T7.

AA6070-O

The nine tensile tests performed on the AA6070-O temper proved to have a low yield stress of about 50 MPa for all orientations. The graphs in Appendix B reveal that the tests taken in the same orientation behave almost identically with only small variations in fracture strain. The values from tests O-0-1, 0-45-5 and O-90-9 (Table 3.2 and Appendix B) have been chosen to represent the material behavior in the three test orientations because they exhibit the median fracture strain, ϵ_f. The fracture strains for these tests are 0.79, 0.76 and 0.65 for test orientations 0°, 45° and 90° respectively. Fig. 3.8a displays a direct comparison of the typical curves in the different orientations. The curves look relatively similar, as expected for a homogeneous O-temper (see Section 2.6.3). The yield stress and the hardening behavior do not vary with test orientation, but it is worth noting that

(a) O-0°

(b) O-45°

(c) O-90°

Figure 3.3: O-temper specimens post fracture.

(a) T4-0°

(b) T4-45°

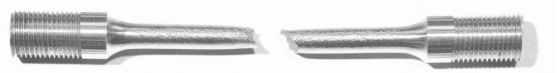

(c) T4-90°

Figure 3.4: T4-temper specimens post fracture.

(a) T6-0°

(b) T6-45°

(c) T6-90°

Figure 3.5: T6-temper specimens post fracture.

(a) T7-0°

(b) T7-45°

(c) T7-90°

Figure 3.6: T7-temper specimens post fracture.

the fracture strains in the 45° and 90°-directions are about 82% and 96% of that in the rolling direction.

Investigation of the pictures after fracture (Fig. 3.3) reveals that the O-temper experiences a somewhat ductile fracture with a large neck in all test orientations, the well-known cup-and-cone mode is present. However, in some of the specimens the fracture modes resemble shear fracture. Shear failures in tensile specimens can be interpreted as instabilities, i.e. the plastic work to failure W_c might be severely underestimated [11]. This is, however, not discussed further in this thesis.

AA6070-T4

The nine tensile tests performed on AA6070-T4 showed that the yield stress is about 186 MPa for all orientations. Tests taken with the same orientation behave very similarly (Appendix B). The curves T4-O-3, T4-45-5 and T4-90-8 (Table 3.2 and Appendix B) exhibit the median fracture strain in each direction and are chosen as typical curves for the temper/test-orientation combination. The anisotropy in plastic flow is minor, but the fracture strains, ϵ_f, are 0.52, 0.45 and 0.39 for the 0°- ,45°- and 90°-orientations respectively, so the variation is significant. In other words: $\epsilon_{f,45^\circ}$ is 87% of $\epsilon_{f,0^\circ}$ and $\epsilon_{f,90^\circ}$ is 75% of $\epsilon_{f,0^\circ}$ (Fig. 3.8b). The T4-temper does not have a distinct yield point, hence the transition from elastic to plastic behavior is smoother than for the other tempers, see Fig. 3.11b.

In the post fracture photos in Fig. 3.4c, some necking can be seen. But for the most part, evidence of shear failure mechanisms are present. Especially the tensile specimen shown in Fig. 3.4b (the 45°-direction) exhibits a typical shear failure, a plane oriented 45° compared to the length of the rod.

By inspecting the true stress-strain curve in Fig. 3.8b closely, we can observe distinct serrations in the plastic area. These serrations may indicate presence of the Portevin-Le Chatelier effect (PLC). The phenomenon is closely related to a negative strain rate sensitivity, and has been known to take place in Al-Mg-Si-alloys under quasi-static conditions [48]. Riley et al. [56] found that the critical strain at incipient serrated yield is increased by aging, and for aging-times longer than 6 h at 180 °C serrated yielding was not observed. The AA6070-T4 has only been naturally aged and could in theory be susceptible to PLC. However, examining the true strain-time curve in Fig. 3.7a does not give a clear answer of whether PLC is present or not, since the curve for the T4-temper does not exhibit a distinct stair-shape unless the axes are scaled down (Fig. 3.7b) [9].

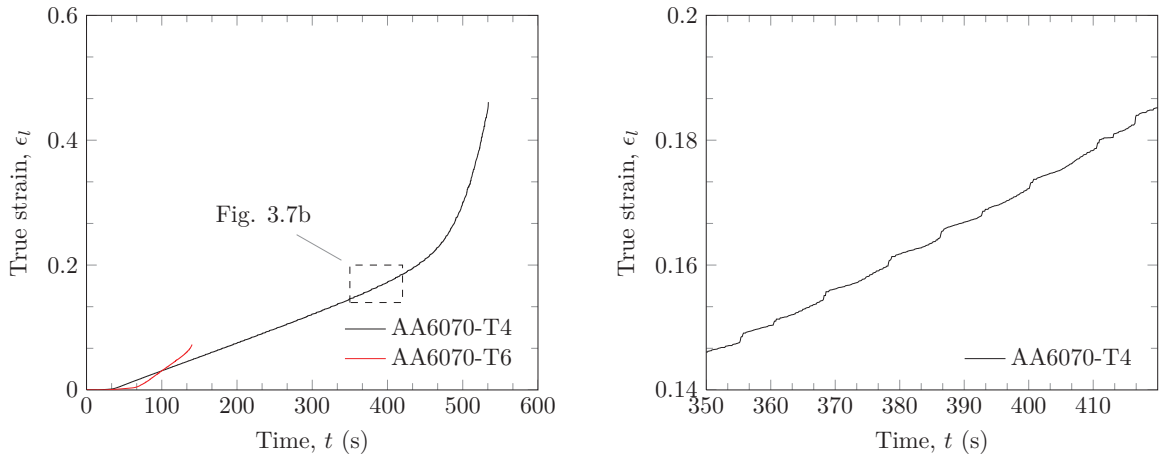

Figure 3.7: **(a)** True strain plotted against time for T4 and T6 in the 45°-orientation. **(b)** True strain plotted against time for T4 late in the hardening process in the 45°-orientation.

In the post-fracture photos of the T4-temper it can be seen that the surface in and around the neck has been roughened and looks wrinkled. This can sometimes be seen in coarse grained materials subjected to stretching, bending or other types of cold working; and has previously been observed in other 6xxx aluminium alloys [34, 44]. The surface texture indicates orange peeling that for tensile tests can produce an unsmooth appearence that can act as initiation sites for strain localization [59]. It is important to note that both orange peeling and PLC are strain-rate dependent phenomena and that the hypothetical presence of these will not affect the ballistic properties of the material.

AA6070-T6

The AA6070-T6 temper displays a high yield stress, σ_0, of about 380 MPa. But this compromises the fracture strain which is 0.26, 0.068 and 0.044 for 0°, 45° and 90° respectively. The curves T6-0-3, T6-45-5 and T6-90-7 exhibit the median fracture strain and will be refered to as typical curves. The fracture strain for the 90°-orientation tests vary somewhat (Fig. B.2i), but not enough to cause mistrust in the test results. The anisotropy in plastic flow is minor in the T6-temper, but the fracture strain for the 45°-orientation is only 27% of that in the 0°-orientation, thus revealing a huge difference. The fracture strain in the 90°-orientation is even lower: it is only 17% of the value from the 0°-orientation (Fig. 3.8c). This is a high-strength temper, but this strength has seemingly been achieved at the

expense of ductility and isotropy in the fracture strain.

AA6070-T7

The experiments conducted on the over-aged AA6070-T7 show that the tests conducted in the same test-orientation behave very similar (Appendix B), so the typical curves with the median fracture strain are T7-0-2 with $\epsilon_f = 0.32$, T7-45-5 with $\epsilon_f = 0.14$ and T7-90-8 with $\epsilon_f = 0.13$ (Fig. 3.8d). The anisotropy in plastic flow is almost negligible for this temper too (Fig. 3.8d), but anisotropy is very large in fracture strain. $\epsilon_{f,45^\circ}$ and $\epsilon_{f,90^\circ}$ is 44% and 40% of that for the 0°-orientation. Although the strength is not as high as in the T6-temper and the ductility is not as low, the T7-temper can be said to display high strength and low ductility (Fig. 3.11b).

Pictures of the fractured T6 and T7 tensile specimens (Figs. 3.5 and 3.6) confirm what the experiment data indicates: that the failure is somewhat brittle. Necking is only visible in the specimen taken in the rolling direction, and all fracture surfaces are jagged, indicating a swift propagating fracture.

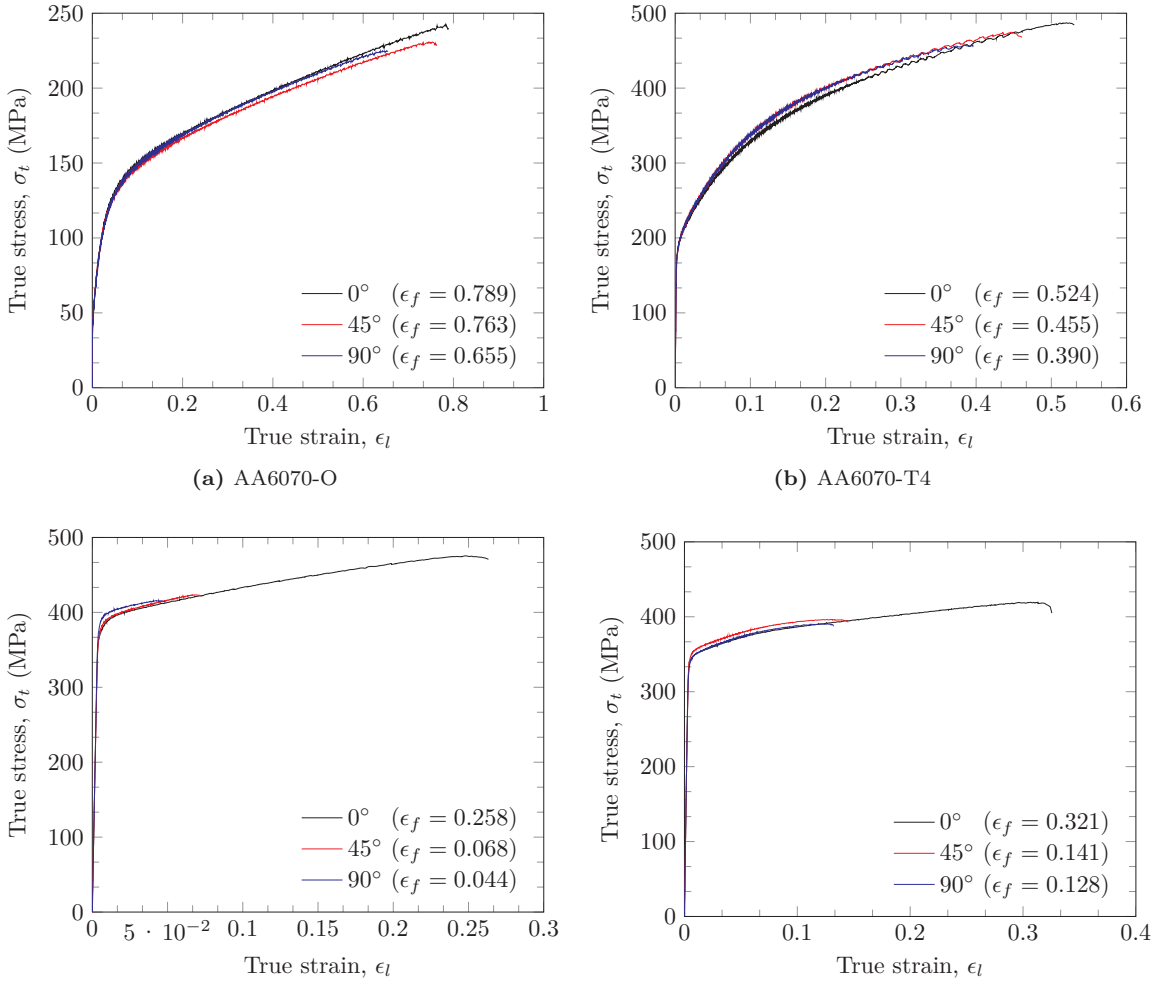

(a) AA6070-O **(b)** AA6070-T4

(c) AA6070-T6 **(d)** AA6070-T7

Figure 3.8: Typical true stress-strain curves for **(a)** AA6070-O **(b)** AA6070-T4 **(c)** AA6070-T6 **(d)** AA6070-T7.

3.3.2 Microstructure

Photographs of the microstructure of the O- and T6-tempers were provided by SIMLab (Figs. 3.9 and 3.10). The following notation is used: x denotes the rolling direction, y denotes the in-plane direction and z denotes the thickness direction. The grains are large, and the structure is recrystalized for both tempers indicating that heat treatment does not change the structure of the material on a large scale.

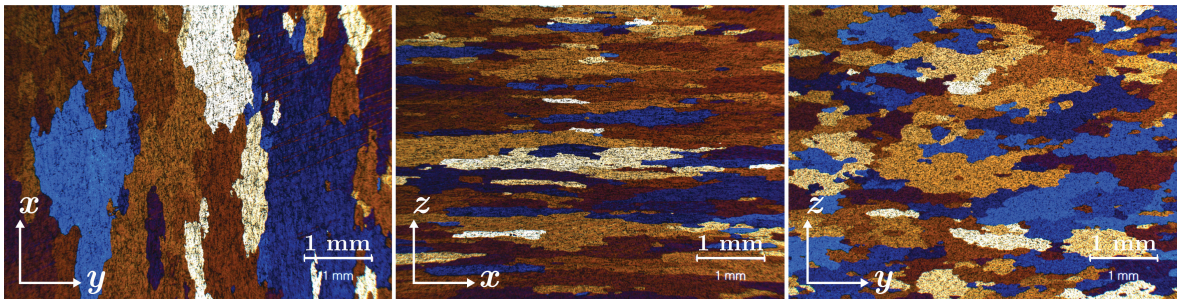

Figure 3.9: Microstructure of AA6070-O where x denotes the rolling direction, y denotes the in-plane direction and z denotes the thickness direction.

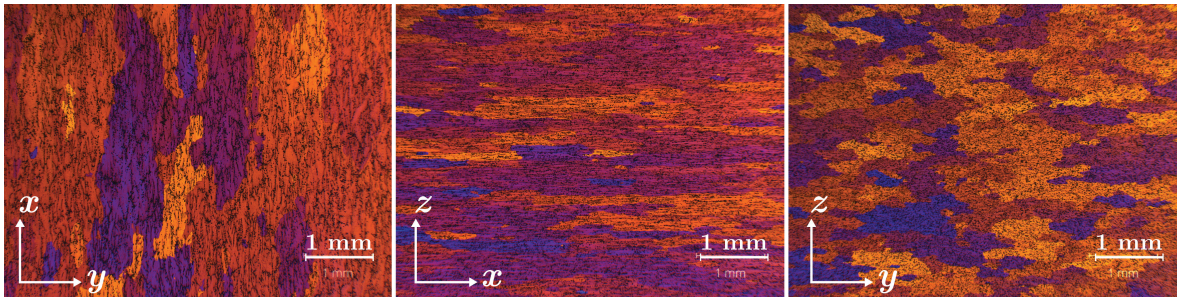

Figure 3.10: Microstructure of AA6070-T6 where x denotes the rolling direction, y denotes the in-plane direction and z denotes the thickness direction.

3.3.3 Material Data Comparison

The 36 different uniaxial tensile tests done in 3 different orientations on the 4 tempers resulted as seen in Section 3.3.1 in 12 representative test results. One for each temper/test-orientation combination. From these we can draw conclusions regarding the material behavior and the impact different heat treatments can have on properties like the 0.2% yield stress (σ_0), plastic flow, and fracture strain, ϵ_f. Table 3.3 gives an overview over these properties including the parameter in the Cockcroft-Latham fracture criterion, W_c, which is taken as the area under the true stress-plastic strain curve to fracture:

$$W_c = \int_0^{\epsilon_{pf}} \sigma_t \mathrm{d}\epsilon_p \tag{3.1}$$

General trends in the material test data include that the annealed O-temper is significantly more ductile than the others. The fracture strain in the rolling direction is more than three times as high as for the T6-temper, while the 90°-orientation-fracture strain is about 15 times as high. This proves that the anisotropy is more evolved in the T6-temper than in the O-temper. The yield stress relationships are the opposite of the fracture strain, supporting the teachings of introductory material courses in universities that to obtain high ductility one must sacrifice strength, and vice versa (Table 3.3, Fig. 3.11b).

Fig. 3.12c show that yield stress (σ_0) is independent of test orientation. True peak stress (σ_{pt}) on the other hand is slightly orientation-dependent (Fig. 3.12d); this can be caused by the reduced ductility in 45° and 90° that might create an upper bound that makes the material go to fracture before it can utilize its full capacity. By inspecting Figs. 3.12a and 3.12b we see that both W_c and fracture strain decrease when the test-orientation-angle increases; this is more distinct for the brittle tempers T6 and T7 where the 45°- and 90°-orientations give much smaller values (less then half) of the rolling direction. These results indicate that particles decide the fracture strain, a process that does not change with heat treatment, and it is normal that fracture strain decreases with increasing angle for particle induced fractures [38].

As expected the naturally aged T4-temper has a lower yield stress than the artificially aged T6- and T7-tempers. The T6-configuration gives the peak strength, while the over aged T7-temper has reduced both yield and tensile strength in comparison to obtain other properties, see Section 2.6.3

Table 3.3: Material data for typical AA6070 material tests.

Temper & orientation		σ_0 (MPa)	W_c (MPa)	σ_u (MPa)	σ_{pt} (MPa)	ϵ_f
AA6070-O	0°	50.5	151	139	243	0.789
	45°	51.0	142	136	231	0.763
	90°	50.0	118	138	225	0.655
AA6070-T4	0°	186.5	211	320	487	0.524
	45°	185.5	180	328	474	0.455
	90°	187.0	150	328	457	0.390
AA6070-T6	0°	372.5	115	393	475	0.258
	45°	379.0	29	396	423	0.068
	90°	387.0	19	399	416	0.044
AA6070-T7	0°	341.0	128	354	419	0.321
	45°	346.0	55	360	396	0.141
	90°	340.0	49	356	391	0.128

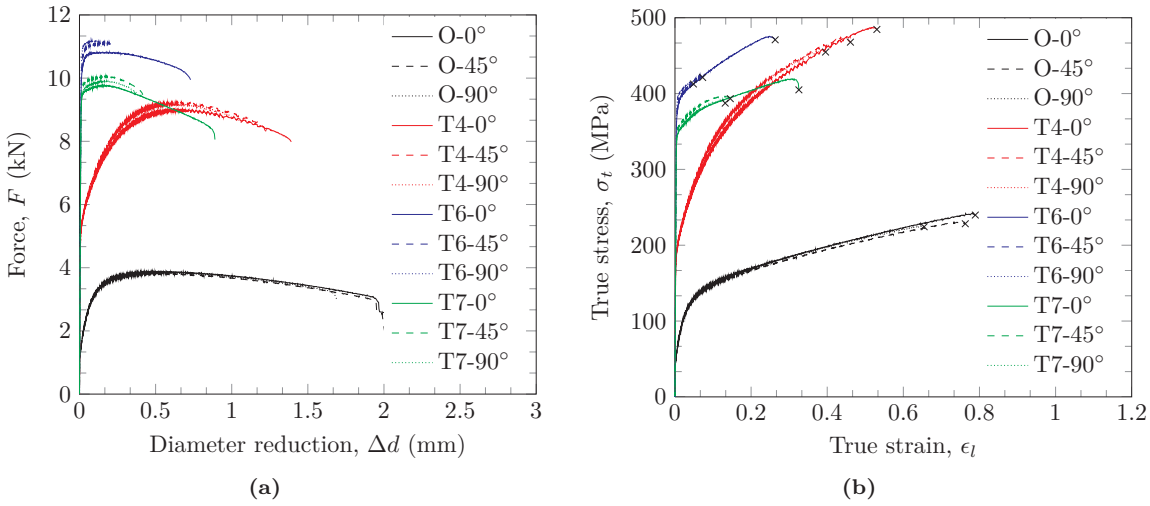

(a) **(b)**

Figure 3.11: **(a)** Measured load-diameter reduction curves and **(b)** true stress-strain curves for the typical curves of all tempers and test orientations (The black crosses depict fracture strain, ϵ_f).

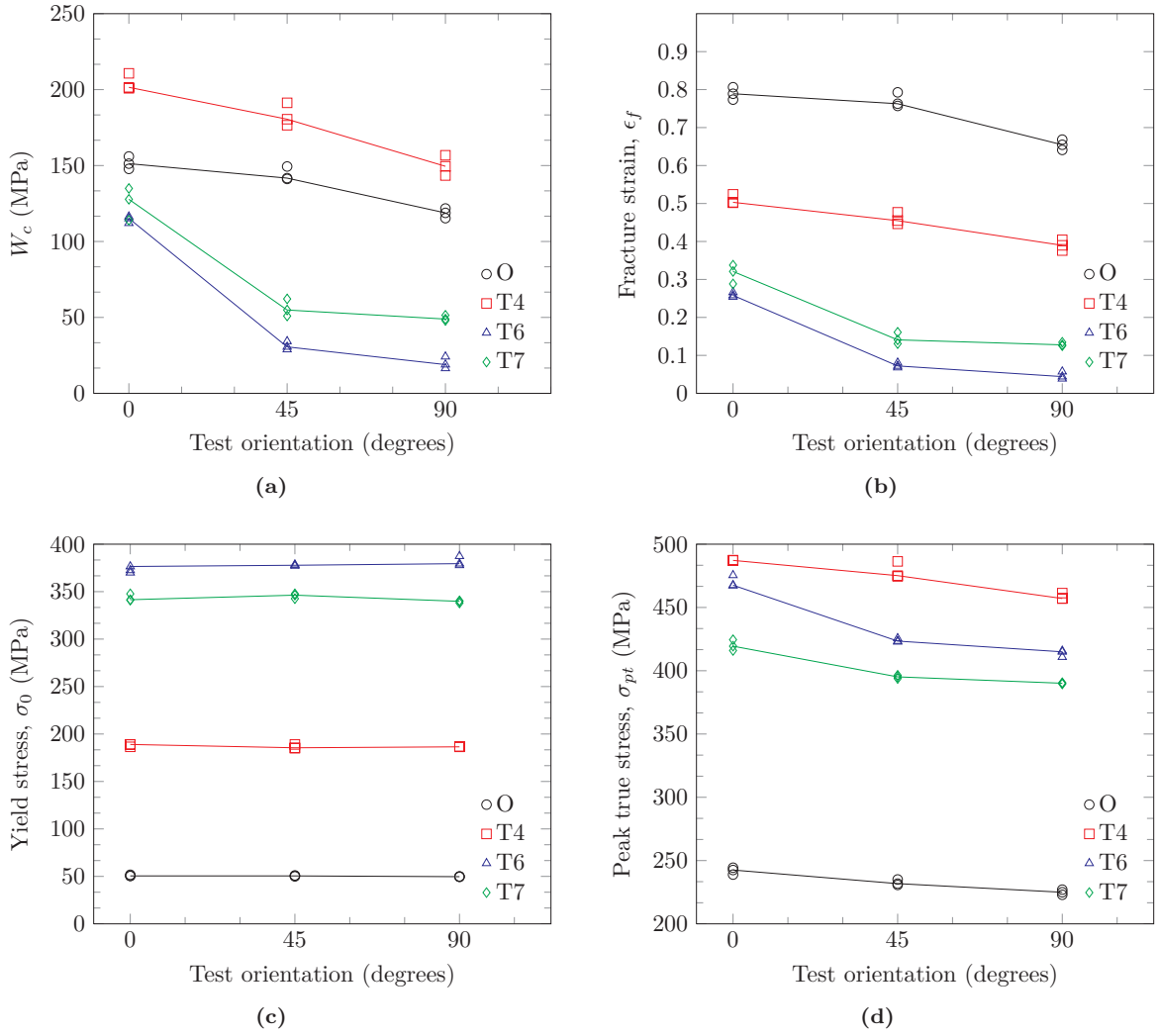

Figure 3.12: **(a)** The Cockcroft-Latham failure parameter ,W_c, **(b)** the fracture strain, ϵ_f, **(c)** Yield stress, σ_0 and **(d)** peak true stress, σ_{pt}, as functions of test orientation for all tensile tests.

3.3.4 Investigation of Anisotropy

A further investigation of anisotropy is required to understand how the materials behave in the directions perpendicular to the tensile direction. As described in Section 3.2 the diameter reduction in two directions were measured at the point of the smallest diameter throughout the experiment. This indirectly gave us access to the current diameter value since the initial diameter was known. The strain ratio, r, gives an apt description of the material behavior perpendicular to the tensile direction. It is defined as

$$r = \frac{\epsilon_y}{\epsilon_z} = \frac{\ln(d_y/d_0)}{\ln(d_z/d_0)} \tag{3.2}$$

where ϵ_y is the true strain and d_y is the current diameter in the longitudinal direction of the plate, ϵ_z is the true strain and d_z is the current diameter in the thickness direction of the plate; d_0 is the initial diameter [22]. The strain ratios are given in Table 3.4, while the dependency of test-orientation is displayed in Fig. 3.13. The definition in Eq. (3.2) is not used directly to find the r-values: these are found by fitting the ϵ_y and ϵ_z-values plotted in Fig. 3.14 to a linear function using the `polyfit`-command in MATLAB. To validate linear relationship between ϵ_y and ϵ_z it is satisfactory to inspect the curves in Fig. 3.14. It is known that $r = 1$ for isotropic materials, for all our the temper/test-orientation combinations $r < 1$, so it is clear that there is some anisotropy in the plastic flow.

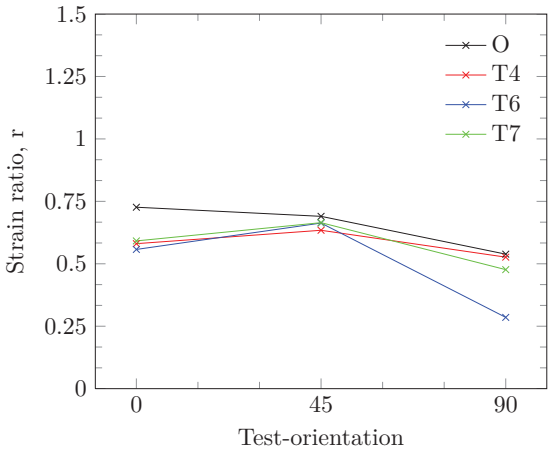

Figure 3.13: Strain ratio plotted against test-orientation.

Table 3.4: Strain ratios for each temper/test-orientation.

	0°	**45°**	**90°**
AA6070-O	0.7265	0.6900	0.5385
AA6070-T4	0.5806	0.6342	0.5266
AA6070-T6	0.5575	0.6631	0.2854
AA6070-T7	0.5916	0.6647	0.4766

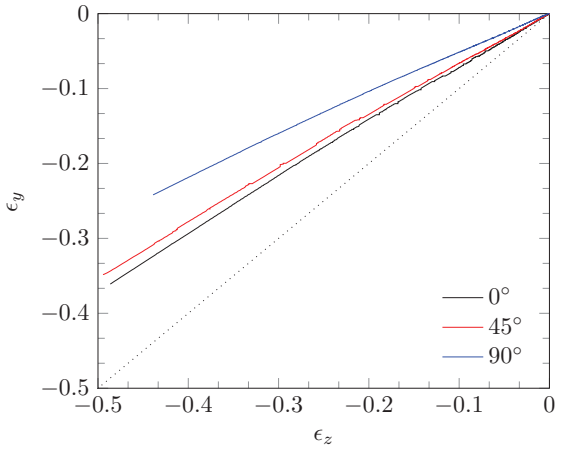

(a) AA6070-O

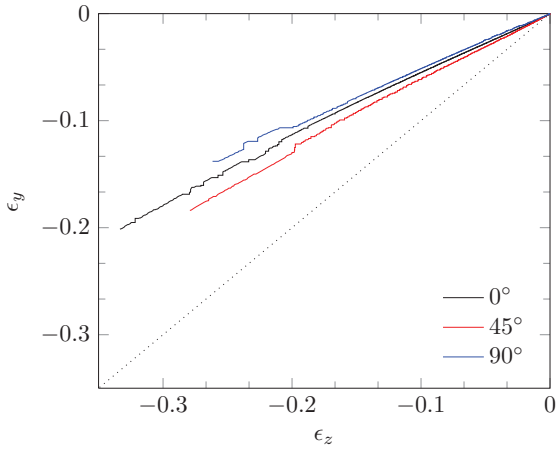

(b) AA6070-T4

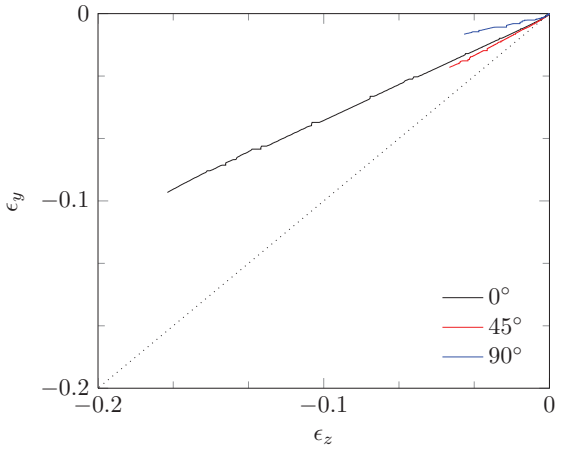

(c) AA6070-T6

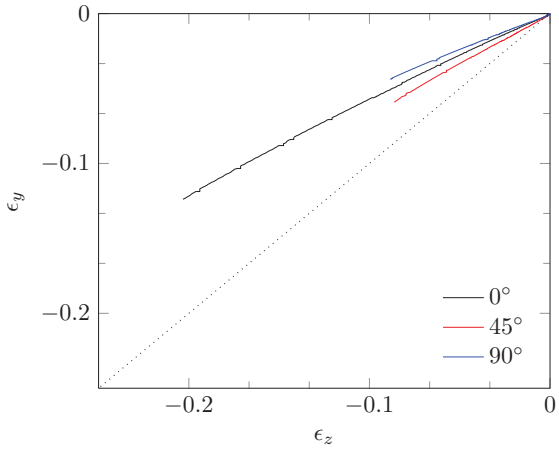

(d) AA6070-T7

Figure 3.14: Strain in the longitudinal (y) and thickness-direction (z) plotted against each other. The slopes are the respective strain ratios.

Chapter 4

Ballistic Impact Experiments: 7.62 mm Bullets

4.1 Experimental Work

The ballistic impact experiments were conducted in a ballistic rig at the Norwegian University of Science and Technology (NTNU) where 7.62 mm APM2 bullets were fired from a smooth-bore Mauser gun inside a protective tank (Fig. 4.1a). A remote trigger was used in all of the experiments (Fig. 4.2c), and the high-speed camera (Fig. 4.2b) initiated when the bullet passed through a metal sheet fastened infront of the hole in Fig. 4.2d. To adjust the velocity of the projectiles fired from the gun, the amount of gun-powder was varied from test to test. There is no one-to-one relation between the amount of gun-powder and velocity, especially when a small amount of gun-powder is used. This makes it difficult to obtain the exact same velocity for two different experiments.

The projectile used was, as mentioned, a 7.62 mm APM2 bullet. This projectile consists of three parts: an outer casing made of brass, a hardened steel core, and a lead tip. Bullet dimensions and composition is illustrated in Fig. 4.1b.

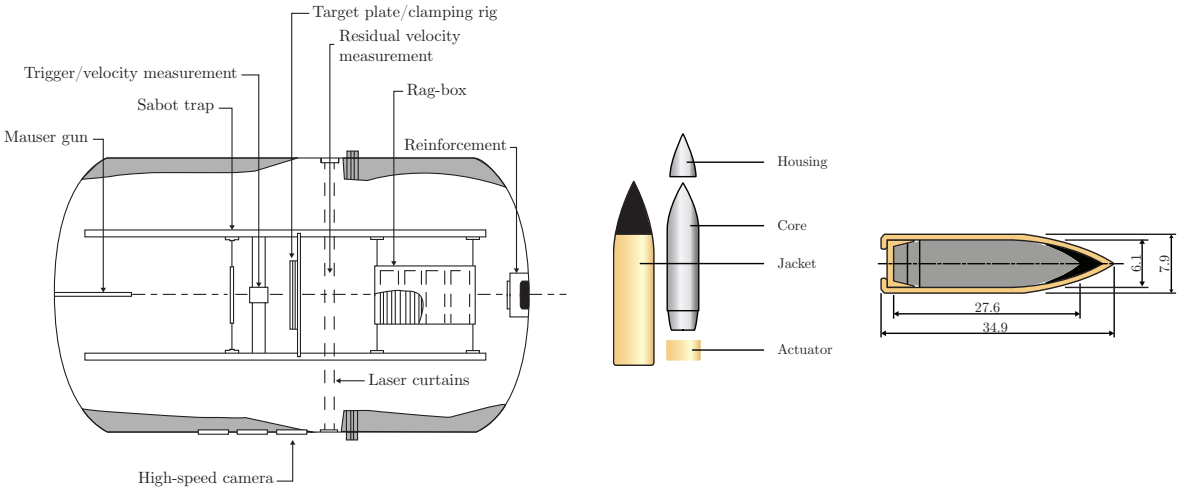

(a) Schematic of the setup for impact experiments, adapted from Børvik et al. [21]

(b) Composition and geometry of the 7.62 mm APM2 bullet.

Figure 4.1: (a) Experimental setup, and **(b)** APM2 bullet composition.

The objective of the experiments was to obtain the ballistic limit curve and the ballistic limit velocity, in practice this was done by firing projectiles at the target plates at different velocities (Fig. 4.2a). The target plates were clamped at the top and at the bottom, thus approximating fixed supports (this will be discussed later in the thesis, see Section 11.2). The first shot at each temper was always fired at maximum velocity, typically around 900 m/s, before lowering the amount of gunpowder to reduce the velocity for the subsequent shots. Penetration during high-speed impact is widely recognized to mostly affect the plate material locally, not globally [12]. This can be verified by inspecting the high-speed videos from the experiments. Taking this into account, each plate was used several times. Between each shot the plate was rotated and/or translated to make sure that the bullet hit previously undamaged material. To get an accurate approximation of the ballistic limit velocity, six to nine shots had to be fired at each plate.

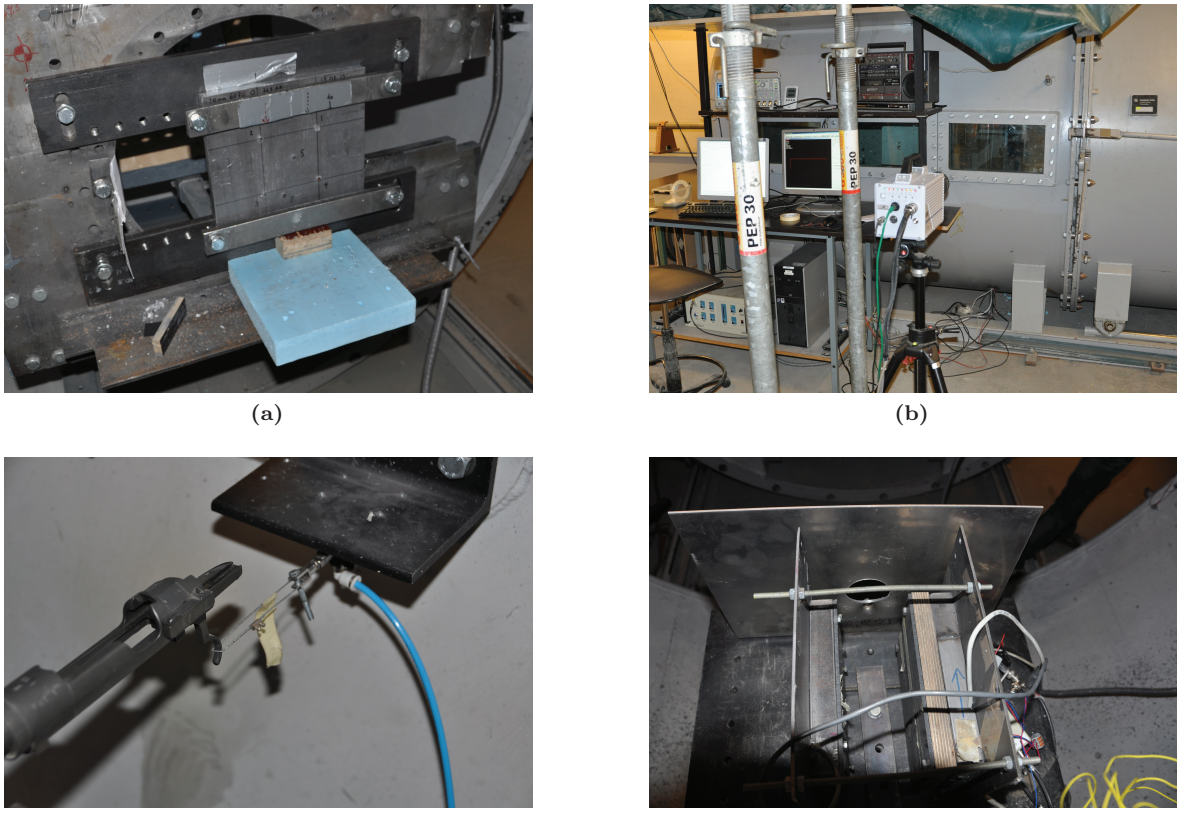

(a) **(b)**

(c) **(d)**

Figure 4.2: **(a)** The 300×300 mm^2 target plate attached to the clamping rig, **(b)** the high-speed camera, **(c)** the remote trigger, and **(d)** the device to trigger the high-speed camera.

4.2 Experimental Results

The inital and residual velocities were measured on the laboratory computer by utilizing pictures from the high-speed camera. Results from all the tests can be viewed in Table 4.1 below.

Table 4.1: Tabulated results from ballistic impact experiments on 20 mm thick aluminium plates of four different tempers using 7.62 mm APM2 bullets.

Temper	**Test**	**Gunpowder** (g)	v_i (m/s)	v_r (m/s)	**Comment**
AA6070-O	1	full	899.9	824.1	OK
	2	35.0	658.3	505.7	OK
	3	30.0	549.3	415.5	OK
	4	25.0	433.7	-	No result given.
	5	25.0	431.9	263.2	OK
	6	20.0	344.6	0.0	OK
	7	22.0	377.0	165.4	OK
AA6070-T4	1	full	894.3	779.2	OK
	2	35.0	604.4	340.8	OK
	3	30.0	520.6	117.3	OK
	4	28.0	470.0	0.0	OK
	5	29.5	509.4	62.3	OK
	6	29.0	514.5	32.1	OK
	7	28.5	503.3	0.0	OK
AA6070-T6	1	full	902.8	741.3	OK
	2	40.0	662.1	377.8	OK
	3	37.0	645.9	336.2	OK
	4	35.0	614.5	293.1	OK
	5	30.0	537.1	0.0	OK
	6	32.0	561.7	0.0	OK
	7	33.0	581.8	169.8	Struck very close to test 3.
	8	33.0	622.8	311.6	The projectile split in half.
	9	32.5	588.8	199.4	OK
AA6070-T7	1	full	900.6	770.1	OK
	2	35.0	657.3	418.1	OK
	3	30.0	538.3	122.4	OK
	4	29.0	509.9	0.0	OK
	5	29.5	527.6	0.0	OK
	6	32.5	586.6	276.9	OK

Close-ups of both entry and exit holes can be seen in Fig. 4.3. It is clear that the bullet holes are mainly circular, indicating isotropic material behavior during impact. This is as expected, seeing that our materials exhibit little anisotropic behavior during plastic flow.

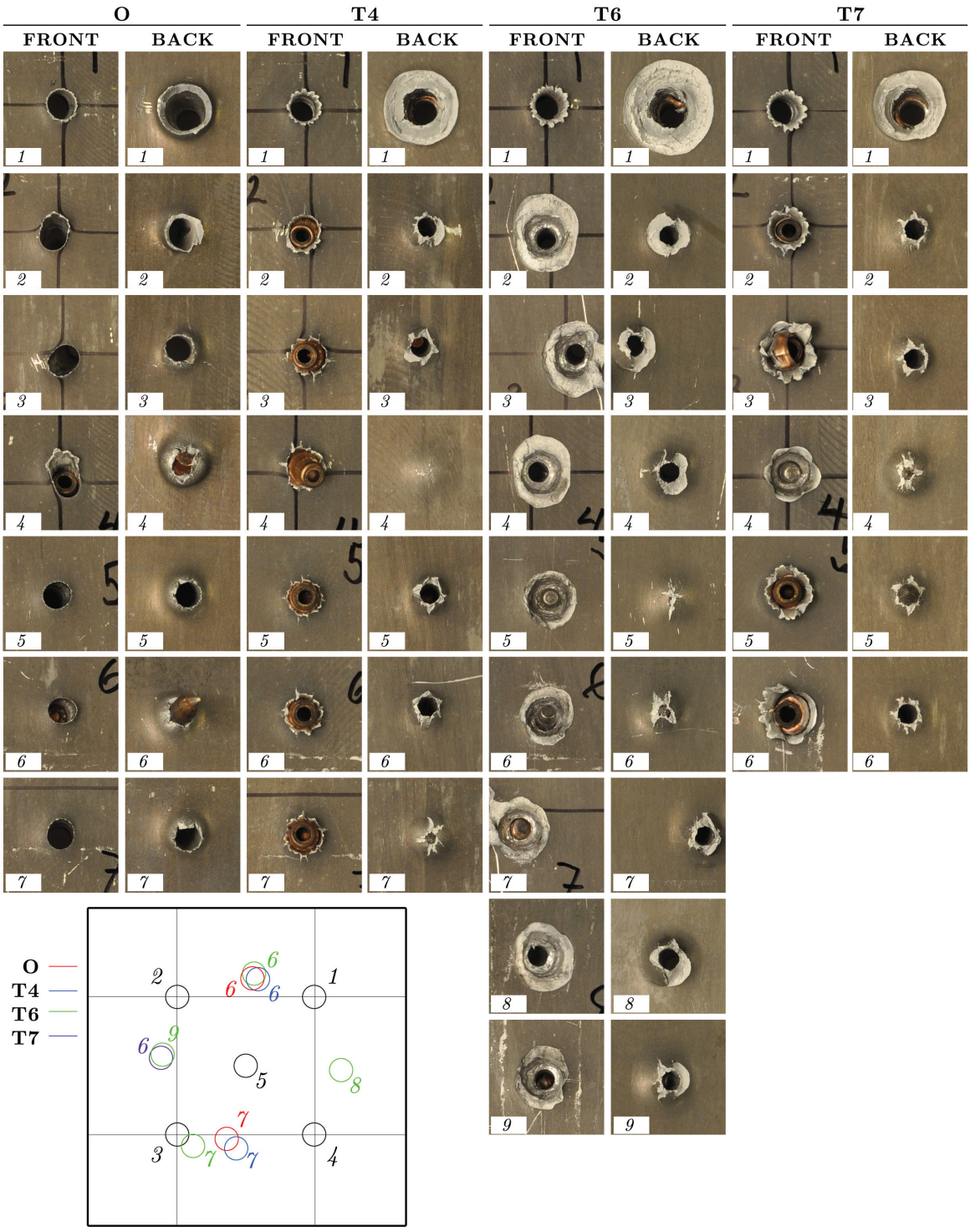

Figure 4.3: Close-ups of bullet holes, and indication of impact point.

4.2.1 O-temper

As seen from Figs. 4.3 and 4.4, AA6070-O fails predominantly by ductile hole growth, which is characterized by thickening of the metal around the circumference of the hole. The observed behavior was more or less expected for a relatively homogeneous material as an annealed aluminium. It also

corresponds well with the shape of the true stress-strain curves obtained from the material tests (see Fig. 3.8a), showing that the O-temper exhibits high ductility, and almost no anisotropic behavior in plastic flow.

(a) Front **(b)** Back

Figure 4.4: Impacted AA6070-O plates.

Fig. 4.5 shows a time-lapse of the high-speed video from the perforation process. Fig. 4.5a shows penetration for a stock bullet, i.e. maximum velocity in Table 4.1. This results in some fragmentation of the metal at the rear of the plate. The brass jacket enclosing the steel core of the APM2 bullet survived in this test. A time-lapse of impact no. 7 can be seen in Fig. 4.5b. The initial velocity is considerably lower in this test, and we have less (almost no) fragmentation. Inspection of holes $2-6$ in Fig. 4.3 confirm that no fragmentation takes place in the O-temper for these velocities. However, small indications of petalling is seen.

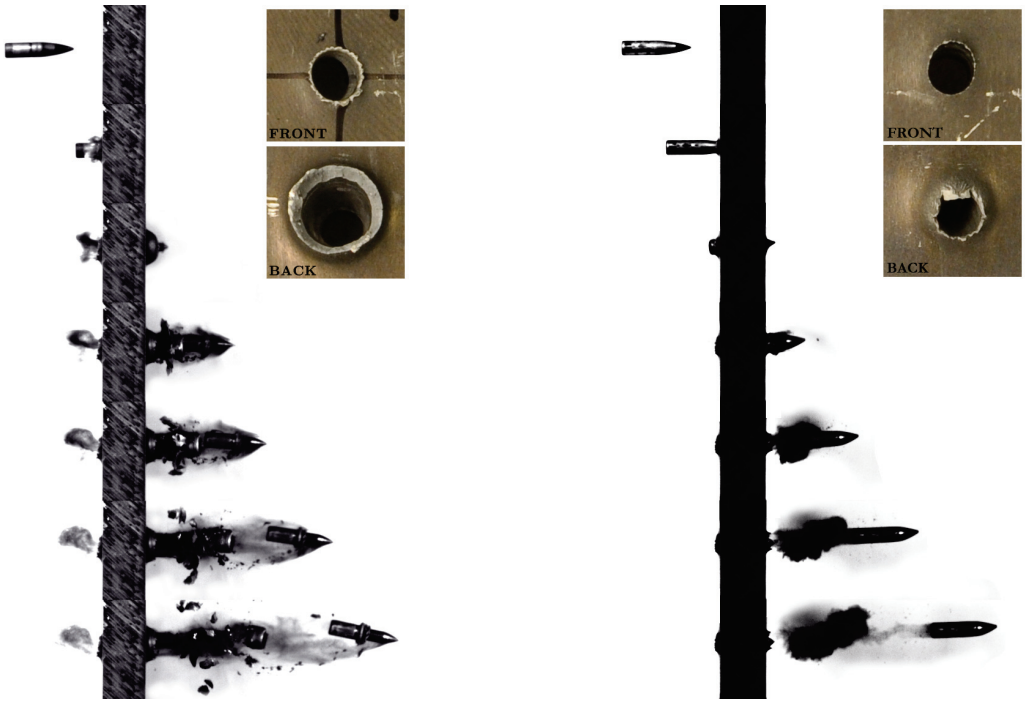

(a) $v_i = 899.9$ m/s, $v_r = 824.1$ m/s, impact no. 1 in Fig. 4.3.

(b) $v_i = 377.0$ m/s, $v_r = 165.4$ m/s, impact no. 7 in Fig. 4.3.

Figure 4.5: Time-lapse of high-speed video showing the perforation of a 20 mm thick AA6070-O plate by an APM2 bullet.

4.2.2 T4-temper

From Figs. 4.3 and 4.6 we observe that the T4-temper, in the same manner as the O-temper, suffers ductile hole growth. We can also observe some degree of petalling for holes $2, 3$, and 6. For the highest velocity test, i.e. impact no. 1, it can be seen that as the projectile exits the rear, relatively large chunks of the plate are ejected - indicating a scabbing failure. The diameter of the affected area is approximately two times that of the projectile. Overall the material behaves as we anticipated, seeing that the T4-temper lies between the T6-temper (high yield strength) and the O-temper (high ductility).

(a) Front **(b)** Back

Figure 4.6: Impacted AA6070-T4 aluminium plates.

In Fig. 4.7 the perforation processes of impacts no. 1 and 3 are illustrated. Fig. 4.7a clearly show the scabbing failure mode. The only remaining part of the projectile post-impact is the steel core for all impact velocities.

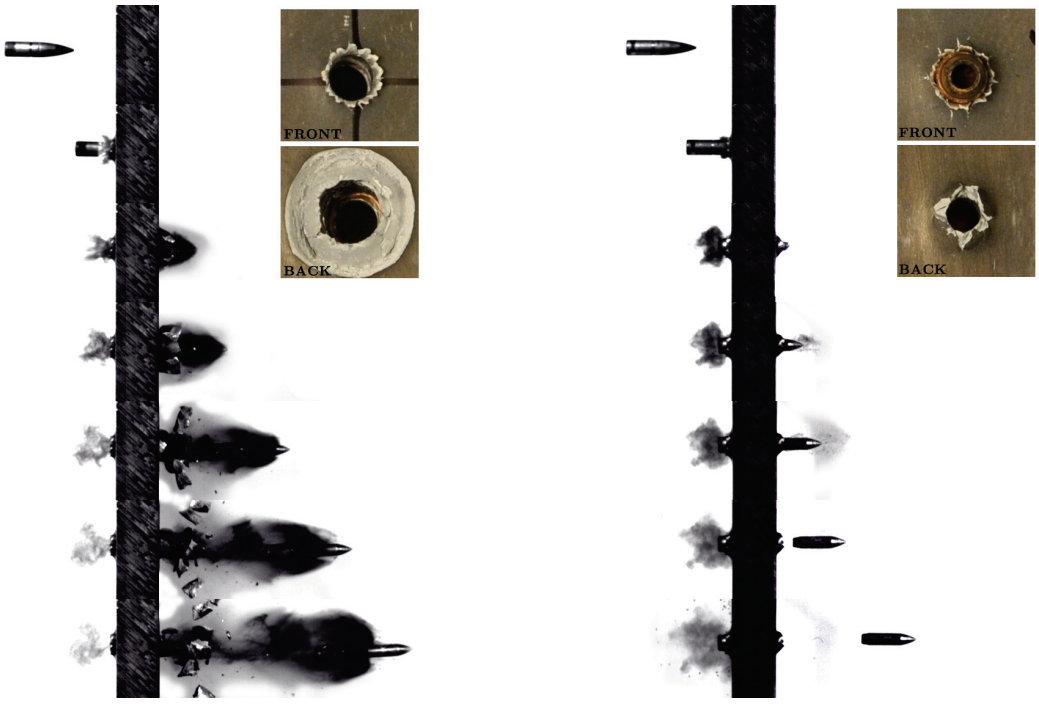

(a) $v_i = 894.3$ m/s, $v_r = 779.2$ m/s, impact no. 1 in Fig. 4.3.

(b) $v_i = 509.4$ m/s, $v_r = 62.3$ m/s, impact no. 3 in Fig. 4.3.

Figure 4.7: Time-lapse of high speed video showing the perforation of a 20 mm thick AA6070-T4 plate by an APM2 bullet.

4.2.3 T6-temper

The T6-temper exhibits the highest yield strength and the lowest fracture strain (see Fig. 3.11b). This brittle uniaxial tensile behavior reveals itself in the ballistic tests through a high degree of fragmentation (see Fig. 4.3). It is worth noticing that as the impact velocity decreases, the front-side fragmentation increases, albeit fragmentation on the rear side is still present. Shot no. 7 and 3 struck so close to each other (see Fig. 4.8) that we considered the results untrustworthy, explaining the high number of shots fired at the T6-temper.

(a) Front **(b)** Back

Figure 4.8: Impacted AA6070-T6 aluminium plates.

A time-lapse of the perforation processes of impacts no. 1 and 4 (see Table 4.1) can be seen in Fig. 4.9. Here the transition from rear side fragmentation exclusively, to a combination of front- and rear-side fragmentation is clearly illustrated.

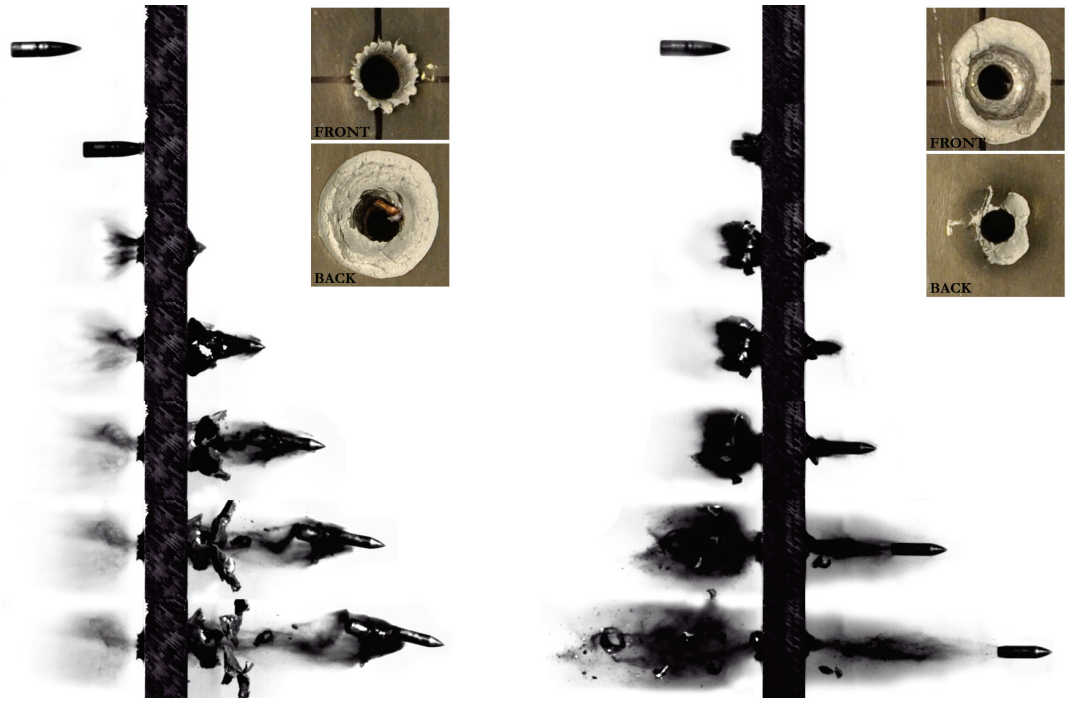

(a) $v_i = 902.8$ m/s, $v_r = 741.3$ m/s, impact no. 1 in Fig. 4.3.

(b) $v_i = 614.5$ m/s, $v_r = 293.1$ m/s, impact no. 4 in Fig. 4.3.

Figure 4.9: Time-lapse of high speed video showing the perforation of a 20 mm thick AA6070-T6 plate by an APM2 bullet.

4.2.4 T7-temper

The T7-temper lies between T6 and T4 considering yield strength, but has a strain hardening gradient similar to the O-temper. The ballistic limit velocity was deemed accurate after six shots. We see the same fracture modes as previously mentioned for the T4-temper, i.e. fragmentation for the highest velocity, and petalling for lesser projectile velocities (see Fig. 4.3).

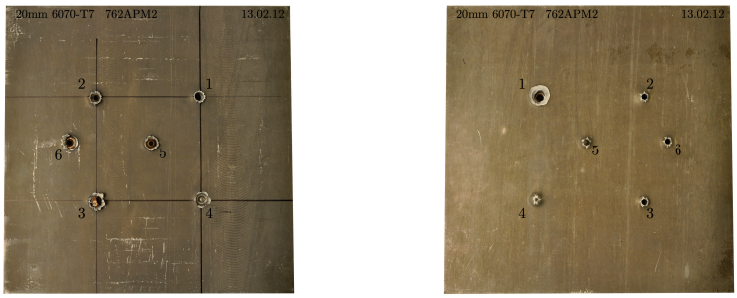

(a) Front **(b)** Back

Figure 4.10: Impacted AA6070-T7 aluminium plates.

In Fig. 4.11a the fragmentation of the rear side of the aliminium plate is evident, in addition we observe that the housing, jacket and actuator is peeled off after perforation for all velocities.

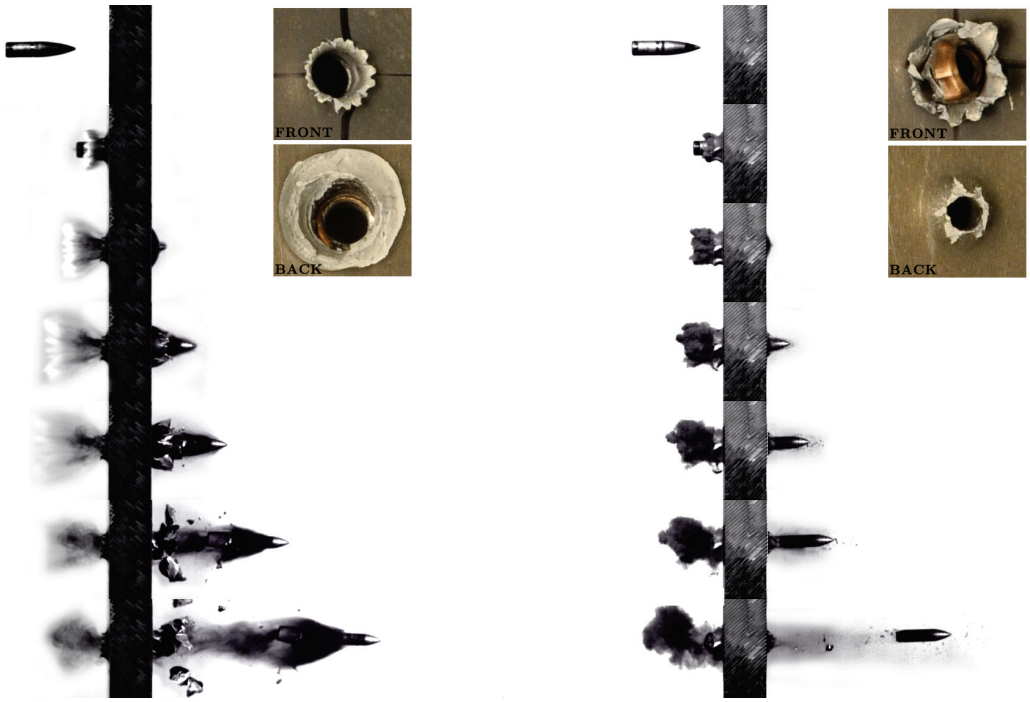

(a) $v_i = 900.6$ m/s, $v_r = 780.1$ m/s, impact no. 1 in Fig. 4.3.

(b) $v_i = 538.3$ m/s, $v_r = 122.4$ m/s, impact no. 3 in Fig. 4.3.

Figure 4.11: Time-lapse of high speed video showing the perforation of a 20 mm thick AA6070-T7 plate by an APM2 bullet.

4.2.5 Determination of the Ballistic Limit Curve

Although only a limited number of tests were carried out, the ballistic limit curve and the ballistic limit velocity can still be found. The initial projectile velocity (v_i) and residual projectile velocity (v_r) given in Table 4.1 are plotted as a scatter in Fig. 4.12, and the ballistic limit curve is predicted by using the Recht-Ipson model described in Section 2.5. In this case, it is assumed that no plug is ejected, but the bullet can sustain deformation. Thus by keeping $a = 1$ and varying p the fitted lines in Fig. 4.12 are found by using Eq. (2.20).

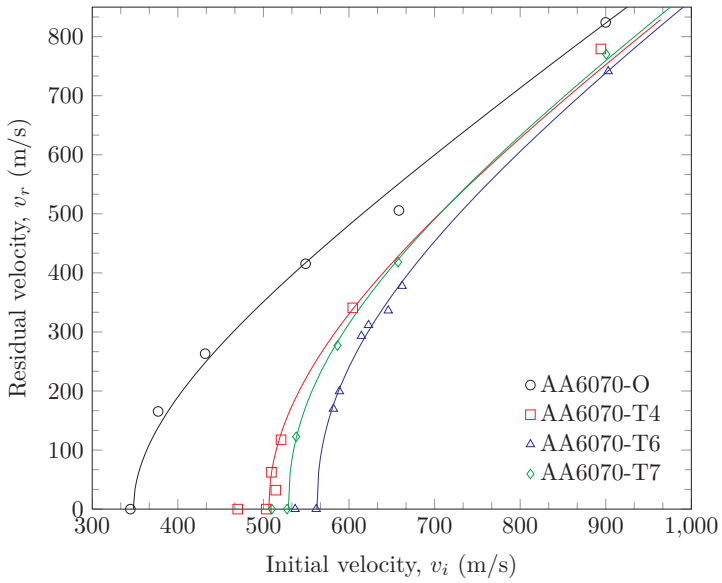

Figure 4.12: Initial versus residual velocity curves for the four tempers.

Table 4.2 shows the ballistic limit velocities from the ballistic tests using 7.62 mm APM2 bullets along with some material parameters and the Recht-Ipson parameters a and p. By plotting the ballistic limit velocity against σ_0 (Fig. 4.13a) and area under the stress-strain curve (Fig. 4.13b) we can see how these parameters affect v_{bl}.

Table 4.2: Comparison of some ballistic velocity limits of 20 mm aluminium plates impacted by 7.62 mm APM2 projectiles. Material data is taken from the rolling direction. The a and p parameters used in the Recht-Ipson equation to obtain the solid lines in Fig. 4.12 are also given.

Designation	v_{bl}	σ_0	σ_u	ϵ_f	**Parameters**	
	(m/s)	(MPa)	(MPa)		a	p
AA6070-O	348	50.5	139	0.84	1	1.94
AA6070-T4	506	186.5	320	0.53	1	2.05
AA6070-T6	563	372.5	393	0.26	1	2.21
AA6070-T7	529	341.0	354	0.32	1	2.20
AA5083-H116 [18]	492	244.0	325	0.16	1	2.14
AA7075-T651 [31]	628	520.0	582	0.11	1	2.17

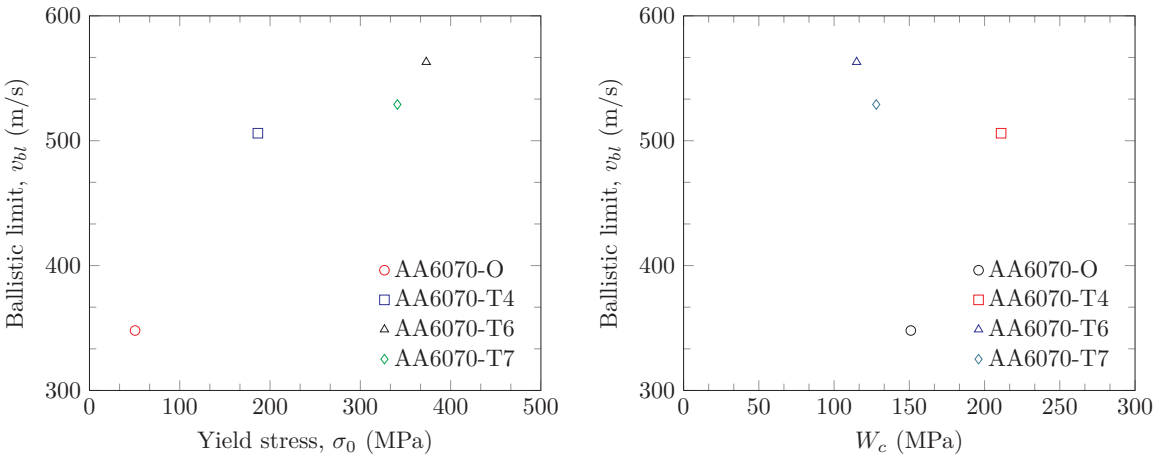

Figure 4.13: Ballistic limit plotted against **(a)** the yield stress of the tempers in the rolling direction and **(b)** the area under the true stress-strain curves of the tempers in the rolling direction.

4.3 Images of Target Plate Cross Sections

In this section, images of some target plate cross sections are given. AA6070-O and AA6070-T6 have been chosen for cutting.

For the O-temper plate, the maximum velocity impact was chosen. From the high-speed video images we could observe no fragmentation at the front of the plate, but many small fragments were knocked loose from the back of the plate Fig. 4.5a. In the cross-section picture Fig. 4.14 it is clearly seen that ductile holegrowth is the dominating, no sign of delamination can be seen.

The four cross-section pictures of the T6-temper plate are taken from experiments where the velocities vary from below the ballistic limit velocity all the way to the maxiumum velocity test. The fracture shape varies from excessive fragmentation at the front of the plate and none in the back, to no fragmentation at the front to excessive fragmentation at the back. High speed gives delamination of the target and fragmentation (Fig. 4.15a). For the lower velocities Figs. 4.15b and 4.15c we see that delamination takes place, but the fragments have not been blasted away.

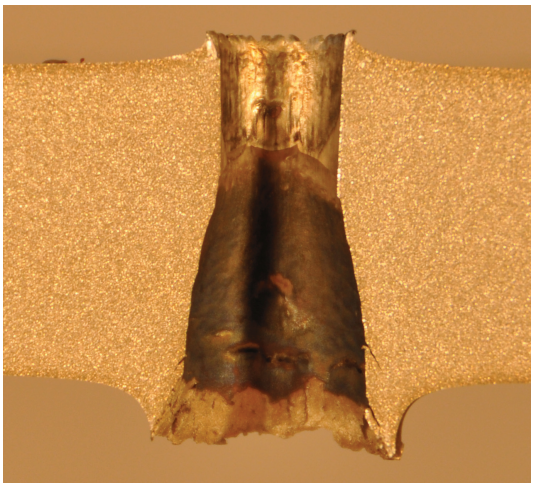

Figure 4.14: Cross section of AA6070-O perforated by a 7.62 mm APM2 bullet. $v_i = 899.9$ m/s and $v_r = 824.1$ m/s

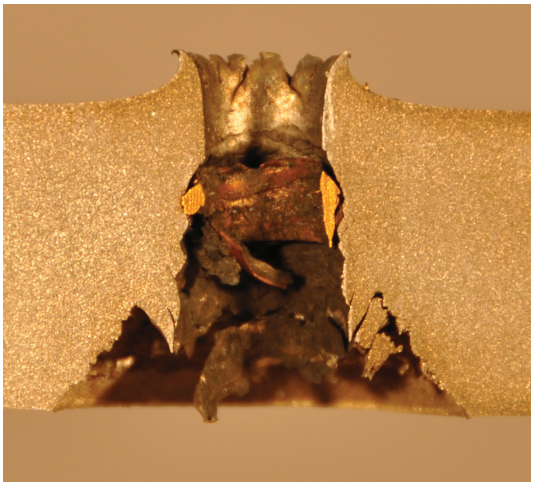

(a) $v_i = 902.8$ m/s and $v_r = 741.3$ m/s

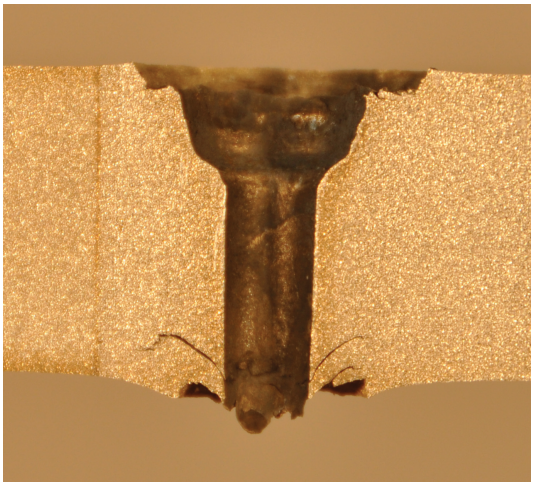

(b) $v_i = 662.1$ m/s and $v_r = 377.8$ m/s

(c) $v_i = 588.8$ m/s and $v_r = 199.4$ m/s

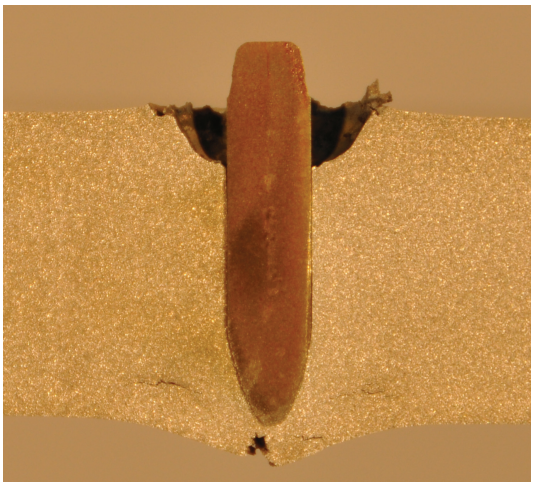

(d) $v_i = 537.1$ m/s and $v_r = 0.0$ m/s

Figure 4.15: Cross sections of AA6070-T6 perforated by 7.62 mm APM2 bullets.

4.4 Prediction of the Ballistic Limit Velocity

As it can be seen in Fig. 4.13b the area under the true stress-plastic strain curve gives virtually no information about the ballistic limit velocity of this aluminium alloy. And although earlier studies done on steel has shown a linear relationship between stress at 0.02% plastic strain and ballistic limit velocity [16], the relationship between yield stress and ballistic limit velocity can for this aluminum alloy be described as pseudo-linear at best (see Fig. 4.13a). The T4-temper is the definite outlier, it exhibits no distinct yield point and a steep hardening curve; considering this we want to investigate if stress at another level of plastic strain can be decisive for the ballistic limit velocity. Fig. 4.16 displays the ballistic limit velocity versus stress for a selection of plastic strain values. It is seen that the graph becomes more linear at increasing plastic strain, until a plastic strain of 15% (σ_{15}), where it starts to diverge from a straight line.

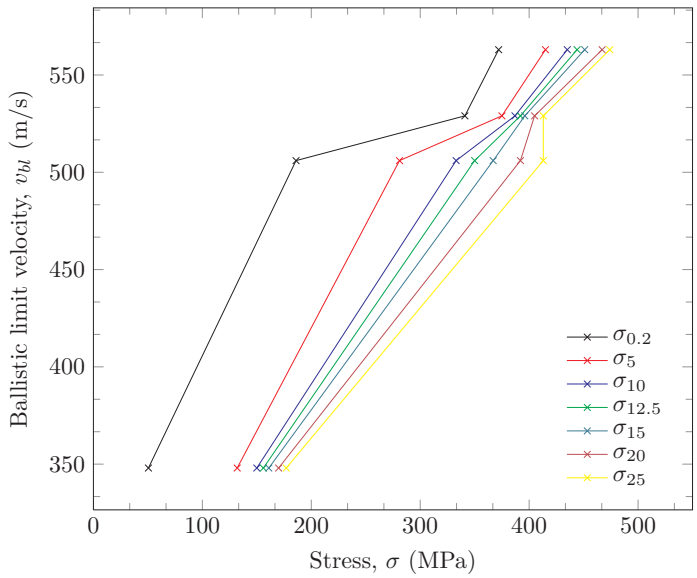

Figure 4.16: The relationship between ballistic limit velocity and stress at different amount of plastic strain (subscripts in %-values).

The same method is tried out on five different steel tempers; Armox 560T, Domex Protect 500, Hardox 400, Weldox 700E and Weldox 500E, from Børvik et al. [16] and on the two aluminium tempers AA5083-H116 and AA7075-T651. The internal variation of the shape of the hardening part of the true stress-strain curves is not as big as for the AA6070-tempers, but the yield stresses vary alot, see Fig. 4.17.

Fig. 4.18a is a plot showing the ballistic limit velocity against the yield stress at different %-values of plastic strain for the steels. Some important material parameters are given in Table 4.3. Regrettably the 2x6 mm configuration of the steel plates is not the same as the 20 mm plates we have investigated in this thesis. However, the principle of predicting the ballistic limit velocity is the same. Inspection of Fig. 4.18a shows that a linear relationship between v_{bl} and yield stress at different plastic strains does not exist in the steel plates, except for $\sigma_{0.2}$ as it was pointed out in the study itself [16].

Fig. 4.16 is augmented with AA5083-H116 and AA7075-T651 to create Fig. 4.18b, and the linear relationship does not reveal itself here either. Thus the hypothesis has to be refused.

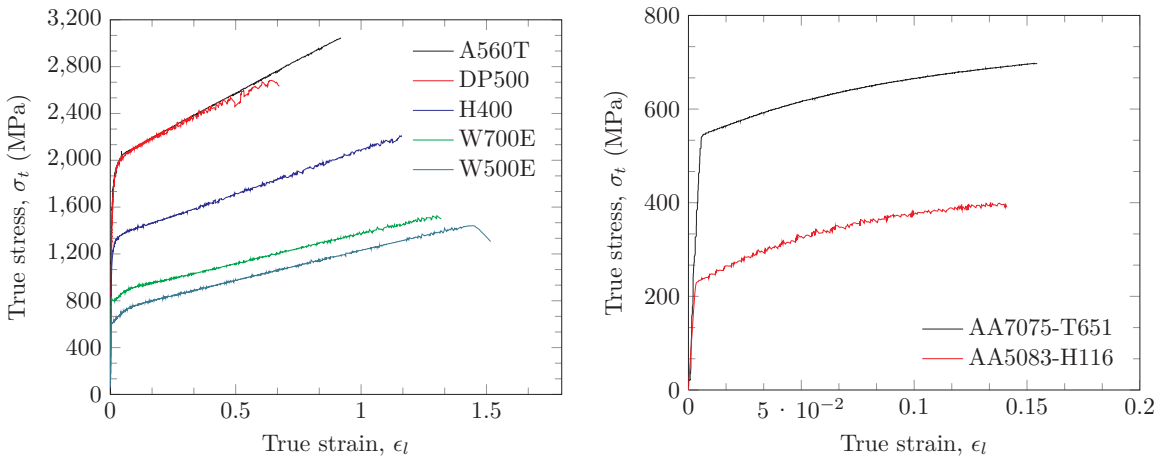

(a) **(b)**

Figure 4.17: True stress-strain graphs for **(a)** different steel tempers and **(b)** two aluminium tempers. Note the different axis-scales used.

Table 4.3: Comparison of the ballistic velocity limits of some 2x6 mm steel plates impacted by 7.62 mm APM2 projectiles. Material data is taken from Børvik et al. [16]. The a and p parameters that can be used in the Recht-Ipson model are also provided.

Designation	v_{bl} (m/s)	σ_0 (MPa)	ϵ_f	**Parameters** a	p
Weldox 500E	624	605	1.52	1	2.20
Weldox 700E	674	819	1.32	1	2.40
Hardox 400	741	1148	1.16	1	2.00
Domex Protect 500	837	1592	0.67	1	2.10
Armox 560T	871	1711	0.92	1	1.50

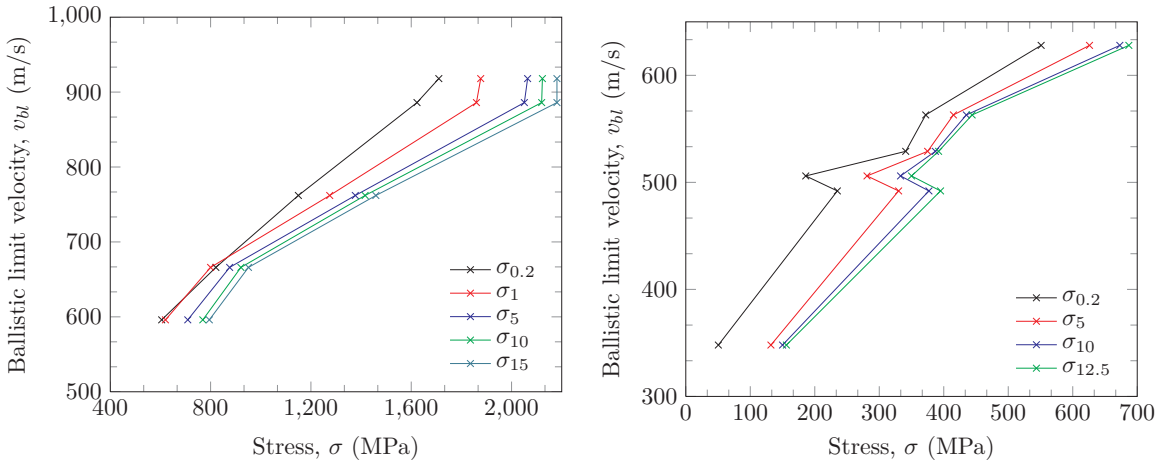

(a) Steel **(b)** Aluminium

Figure 4.18: The relationship between ballistic limit velocity and stress at different amounts of plastic strain (subscripts in %-values).

Chapter 5

Ballistic Impact Experiments: 20 mm Projectiles

5.1 Experimental Work

The experimental procedure employed for the 20 mm blunt and ogival steel projectiles is similar to the procedure used for the 7.62 mm APM2 bullets in Chapter 4. The same ballistic rig at the Norwegian University of Science and Technology was used, however the smooth bore Mauser gun was replaced by a light gas-gun shown in Fig. 5.1. The principle behind the light gas-gun is simple: a pressure gradient is created, and when it reaches a specific value, a membrane ruptures, in turn accelerating the projectile. The projectile geometry is shown in Fig. 5.3a.

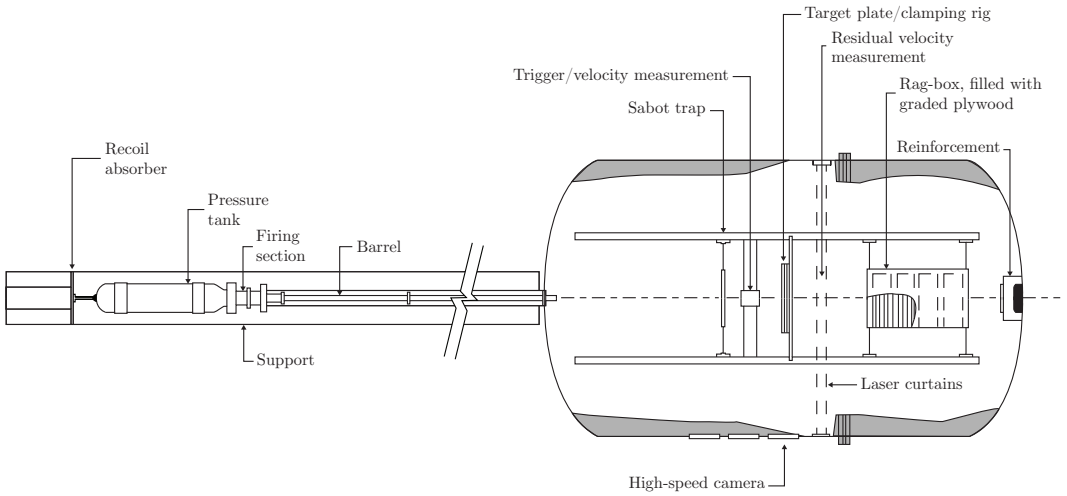

Figure 5.1: The ballistic rig used for experiments on blunt and ogival steel projectiles.

Oxygen is used to create the pressure difference needed to accelerate the projectile to the desired velocity. The firing mechanism consists of two pressure chambers, and the firing barrel; the latter will not be pressurized. These three chambers are separated by two mylar membranes designed to withstand certain pressure-levels. The gas-gun is loaded by filling pressure chamber 1 and 2 to about half the value of the pressure needed to obtain the desired velocity (P_2, see Fig. 5.2). When this value is reached, chamber 2 is sealed and chamber 1 is filled to the firing-level (P_1, see Fig. 5.2). The gun fires when chamber 2 is depressurized rapidly to create a pressure-gradient large enough to break the mylar membranes and fire the projectile. It is important that the barrel is extended into the impact chamber to prevent imperfections in the straightness of the barrel, ensuring a minimum impact angle (pitch) of the projectile as it impacts the target plate [14].

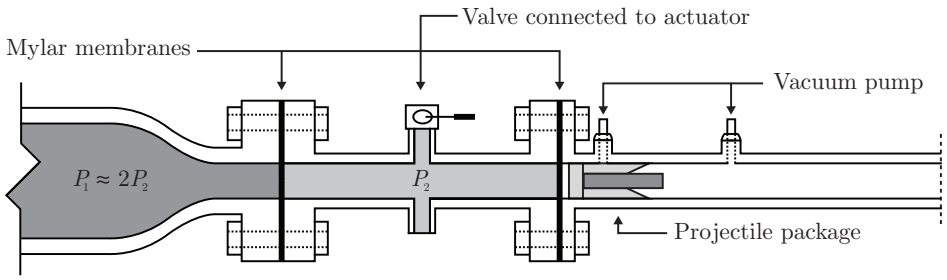

Figure 5.2: Detailed picture of the light gas-gun.

Pictures and nominal geometry of the two projectile types are shown in Fig. 5.3, where the nominal weight of both the blunt and the ogival projectiles is 0.197 kg. The projectile material is hardened Arne tool steel with a nominal yield stress $\sigma_0 = 1900$ MPa, fracture strain of about 2.15% and elastic modulus $E = 204000$ MPa [20]. The ogival projectile has a caliber radius head (CRH) equal to 3.

A five piece hard shell and four pieces of styrofoam makes a nine piece sabot, seen in Fig. 5.4. This device is used to ensure that the projectile, which is relatively small compared to the barrel, is accelerated in a satisfactory way. The sabot is stopped by a sabot trap, preventing the sabot from entering the area of sensitive equipment.

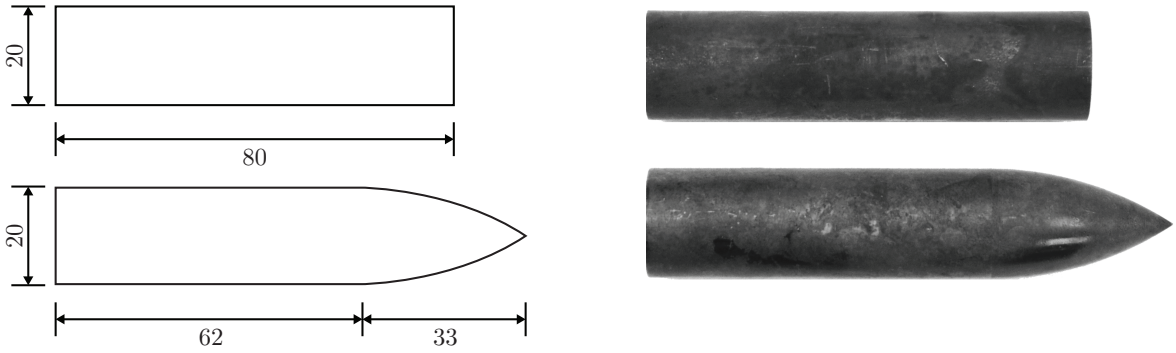

Figure 5.3: **(a)** Projectile geometry and **(b)** the blunt and ogival (CRH = 3) projectiles.

The 300×300 mm^2 target plates are identical to the one shown in Fig. 4.2a, however, only one shot is fired at each plate. The firing velocity used for the blunt projectiles was 200 m/s, and 250 m/s for the projectiles with an ogival nose shape. Two additional experiments were performed on the T6-temper using blunt projectiles; the firing velocities were 250 m/s and 300 m/s.

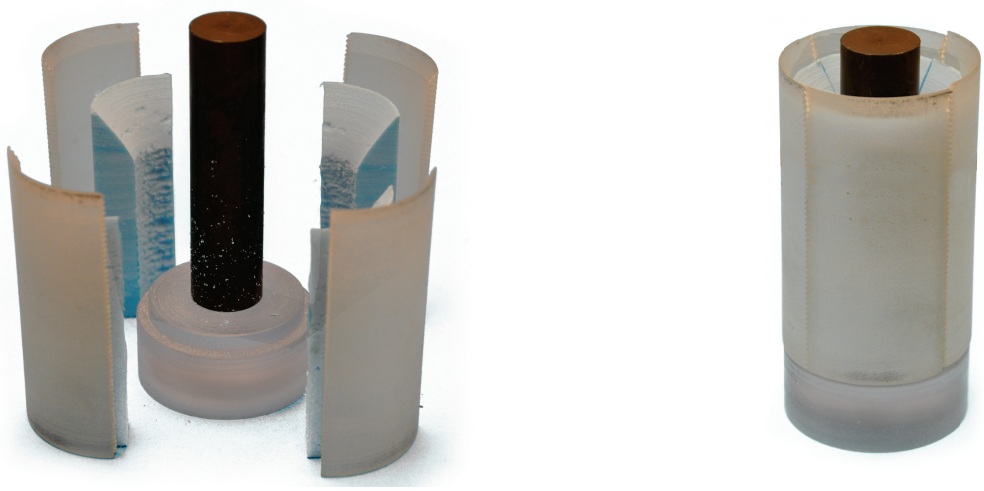

(a) Disassembled sabot. **(b)** Assembled sabot.

Figure 5.4: The sabot used to ensure good acceleration conditions.

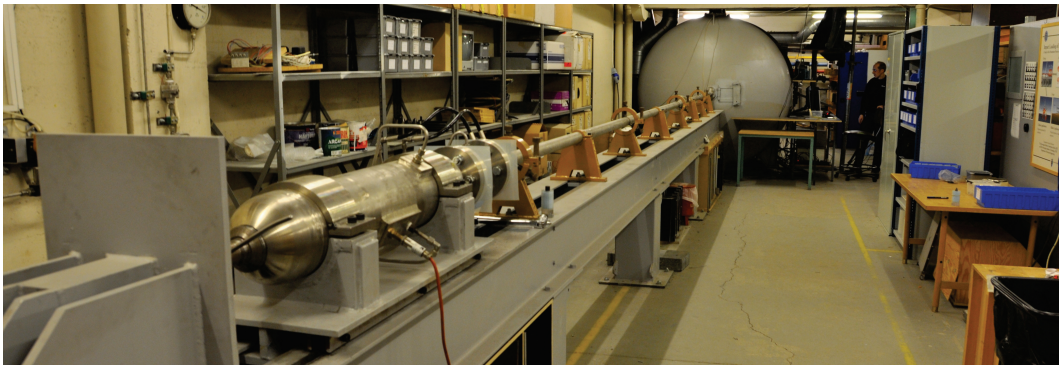

Figure 5.5: Gas-gun, barrel and impact chamber.

5.2 Experimental Results

The results from the ballistic impact experiments performed on the aluminium plates using 20 mm blunt and ogival steel projectiles are tabulated in Tables 5.1 and 5.2 and displayed in Figs. 5.7 and 5.11. The ballistic limit curves are calculated on the basis of the Recht-Ipson-model. Because the number of available data-points is small, the curves are constructed by estimating the ballistic limit velocity, v_{bl}. For the blunt projectiles it is assumed that the projectile is rigid and that a shear plug is ejected from the plate; the mass of the plug (m_{pl}) is used to calculate p. For the ogival projectiles it is assumed that the projectile is rigid and that only plastic deformations take place in the aluminium plate [12].

In the estimation of v_{bl} for the blunt projectile $p = 2$ and m_{pl} is taken from Table 5.1

$$v_{bl} = \left(v_i^2 - \left[\frac{m_p + m_{pl}}{m_p} \right]^2 v_r^2 \right)^{1/2} \tag{5.1}$$

and for the ogival projectile $p = 2$ and $a = 1$:

$$v_{bl} = \left(v_i^2 - v_r^2 \right)^{1/2} \tag{5.2}$$

In both cases, Eq. (2.20) is used to construct the curves.

5.2.1 Blunt Projectiles

For blunt projectiles, the results from the impact experiments with $v_i \approx 200$ m/s show that the T4-temper has the lowest residual velocity of $v_r = 84.3$ m/s. Applying Eq. (5.1) gives us $v_{bl} = 175.7$ m/s for AA6070-T4 in this specific test configuration. Then the T7-temper follows with $v_{bl} = 166$ m/s. The T6-temper, which displays the highest yield strength, has an estimated ballistic limit velocity, $v_{bl} = 162$ m/s, while for the O-temper $v_{bl} = 157$ m/s. These results are tabulated in Table 5.3 and indicate that the ballistic performance of aluminium is not necessarily just strength dependent. By investigating the high-speed video images (Fig. 5.12) and the post-impact photos of the plates (Fig. 5.6a), it is evident that the O-temper experiences no fragmentation whatsoever. The plug ejected from the plate is the heaviest one measured of all the experiments (see Table 5.1). The T4-temper ejects a plug, though not as intact as the one from the O-temper plate. Some fragmentation is observed after penetration from the backside of the plate. In the two mentioned tempers, a bulge of significant size can be seen at the back of the plate before a plug is ejected and penetration occurs, while the T6-temper has only a small bulge that can be seen before some petalling and excessive fragmentation from the rear side of the plate occurs. Similarly, the T7-temper only exhibits a small bulge, but the plug-ejection process is cleaner and a minimum of fragmentation is observed, about the same amount as for T4.

Fig. 5.6a reveals that the T6-temper experiences a completely different failure mode compared to the three other tempers. This can help explain why fracture of quasi-brittle aluminium alloys in this velocity range can not only be predicted by the yield stress. The post-perforation pictures of the plugs are shown in Fig. 5.6b. Note that the missing plug (T6-2) is in Dr. Brandtzæg's (Hydro Aluminium) possesion.

Table 5.1: Tabulated results from ballistic impact experiments on 20 mm thick aluminium plates of 4 different tempers using blunt steel projectiles.

Temper	**Test**	**Pressure** (bar)	$\boldsymbol{v_i}$ (m/s)	$\boldsymbol{v_r}$ (m/s)	$\boldsymbol{m_p}$ (g)	$\boldsymbol{m_{pl}}$ (g)	**Comment**
AA6070-O	1	9.1	186.5	95.3	196.44	13.54	OK
AA6070-T4	1	9.1	196.5	84.3	196.46	11.62	OK
AA6070-T6	1	25.0	300.2	232.8	196.82	10.16	OK
	2	15.0	246.8	177.8	196.80	11.44	OK
	3	9.1	198.9	120.9	197.36	12.64	m_p from post impact.
AA6070-T7	1	9.1	197.2	98.6	196.52	13.02	m_p from post impact.

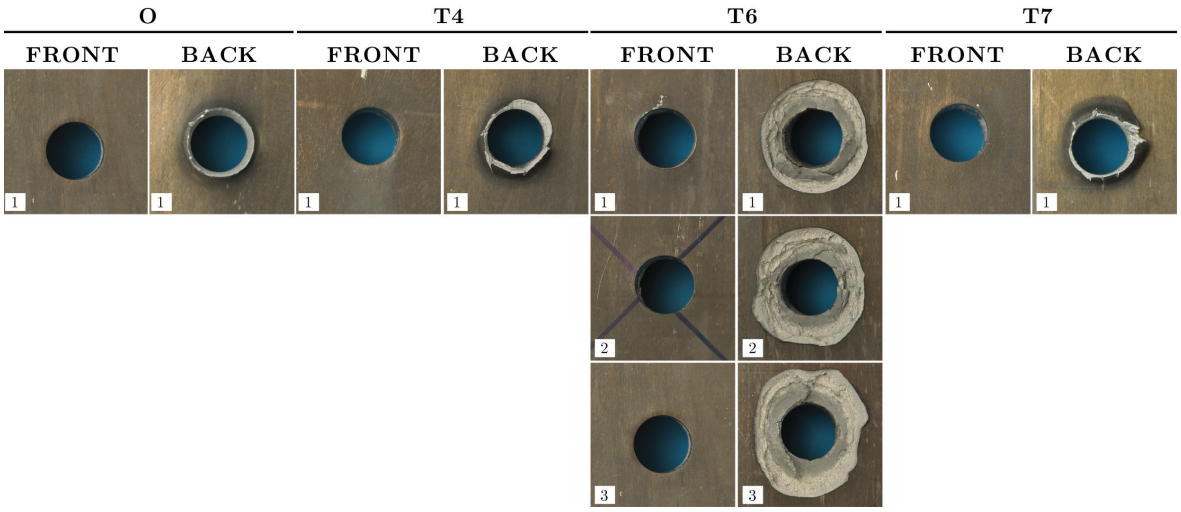

(a)

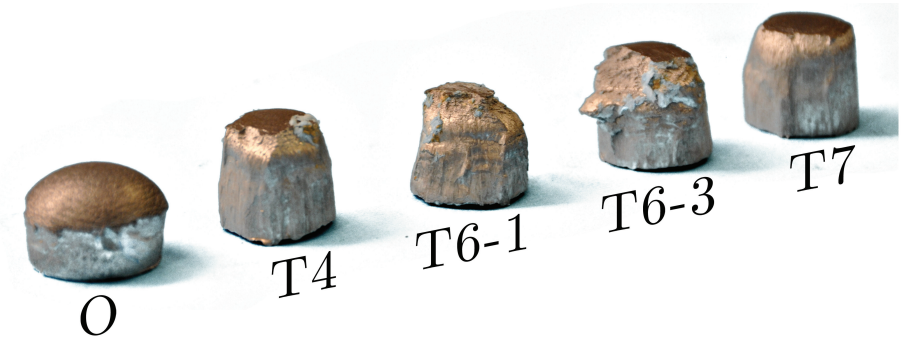

(b)

Figure 5.6: Close-up of bullet holes and plugs after impacts suffered from blunt projectiles.

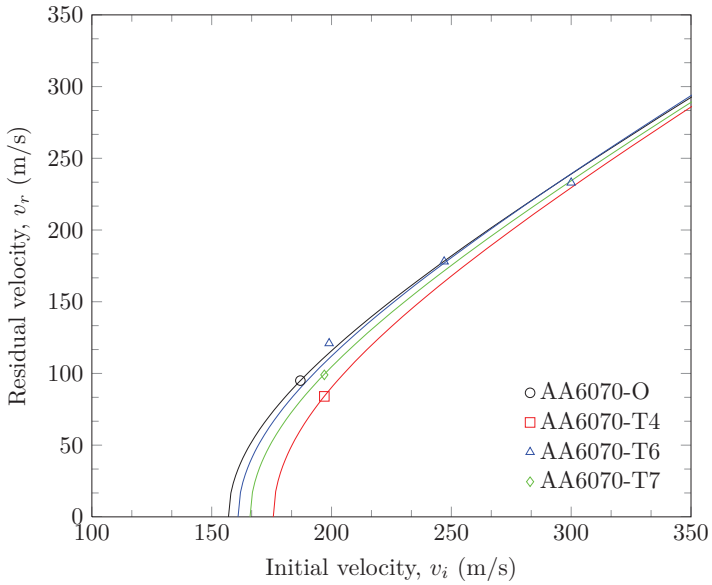

Figure 5.7: The ballistic limit curves from the experiments carried out with blunt projectiles.

5.2.2 Ogival Projectiles

The experiments done with ogival projectiles produced some interesting results. At the chosen firing velocity of $v_i = 250$ m/s we almost managed to capture the ballistic limit velocity experimentally with only one shot for the T4- and T7-tempers: $v_r = 18$ m/s for the T4-temper and $v_r = 39$ m/s for the T7-temper. The ballistic "ranking" for the heat treatments relative to each other is about the same for experiments with ogival noses as with blunt noses: the estimated ballistic limit velocities are 247 m/s, 246 m/s, 222 m/s and 187 m/s for T7-, T4-, T6- and the O-temper respectively.

The projectile that penetrates the O-temper has a slight pitch when it makes contact with the plate, but the effect of this small angle is questionable [6]. No fragmentation takes place at the front side of the plate at impact, and no fragments are ejected from the rear side for the O-temper. Some petalling can be observed and plastic deformation of the plate some distance away from the hole itself can also be seen.

In the case of the T4-temper, Fig. 5.8 and the high-speed video images reveal petalling at perforation (Fig. 5.13b); hardly any fragments can be seen. This experiment hit very close to the ballistic limit velocity, with a residual velocity of 18 m/s.

The T6-temper fragmented at the front during initial impact and on the back side at perforation; this can easily be seen in Figs. 5.8 and 5.13c. As for the blunt projectiles, the ballistic performance of the T6-temper in the case of ogival projectiles cannot be predicted from yield stress alone. T6 experiences fragmentation and delamination to a degree the more ductile tempers do not.

The response of T7 resembles the T4-temper when the curves are compared in Fig. 5.11. But when the close-ups of the bullet holes are compared in Fig. 5.8. It can be seen that T7 looks like a hybrid of T4 and T6, with a response just ductile enough to prevent excessive fragmentation.

Table 5.2: Tabulated results from ballistic impact experiments on 20 mm thick aluminium plates of four different tempers using ogival steel projectiles.

Temper	Test	Pressure (bar)	v_i (m/s)	v_r (m/s)	Comment
AA6070-O	1	15.0	248.2	163.0	Some global deformation observed.
AA6070-T4	1	15.0	246.5	18.2	OK
AA6070-T6	1	15.2	247.4	107.6	OK
AA6070-T7	1	15.0	250.0	39.4	OK

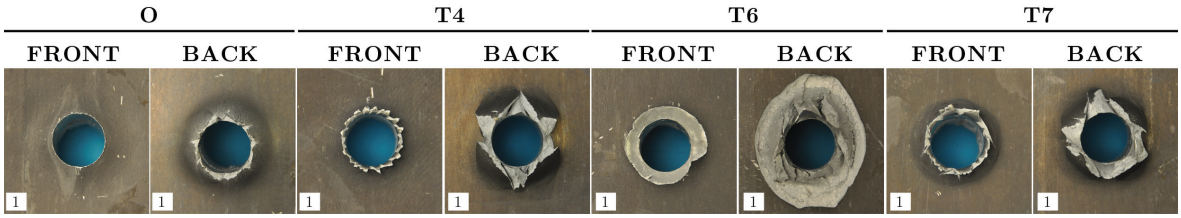

Figure 5.8: Close-ups of bullet holes after impacts suffered from ogival projectiles.

Fig. 5.9 shows cross-sections of AA6070-O and AA6070-T6. No fragmentation and no delamination can be seen for the O-temper in Fig. 5.9a where ductile holegrowth clearly dominate. In Fig. 5.9b classic delamination followed by excessive fragmentation can be observed.

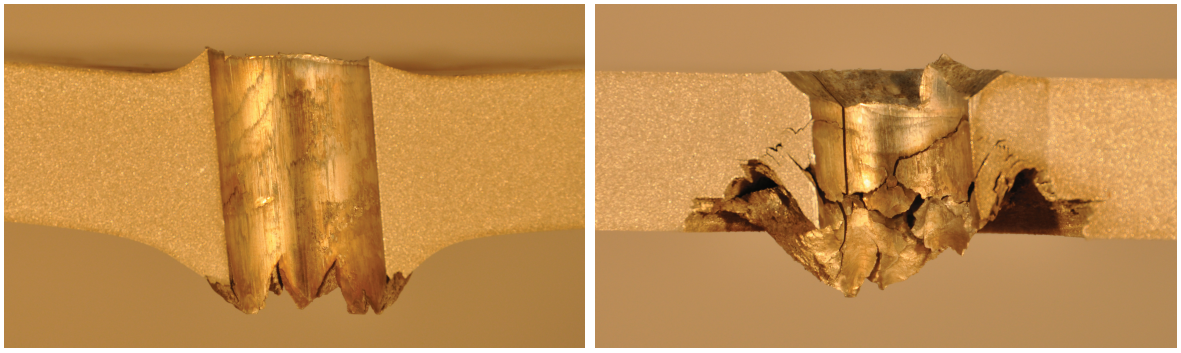

(a) AA6070-O, $v_i = 248.2$ mm and $v_r = 163.0$ mm

(b) AA6070-T6, $v_i = 247.4$ mm and $v_r = 107.6$ mm

Figure 5.9: Pictures of cross-sections of the target plates perforated by 20 mm ogival projectiles.

The microstructure of delamination is covered by Pedersen et al. [55]. Apparently the precipitate free zones are of vital importance in the development of the delamination: they provide space for the fracture to propagate along the grain boundarys (see Fig. 5.10b). When the material cannot sustain the force any longer, the material breaks off in a transgranular fracture (see Fig. 5.10a).

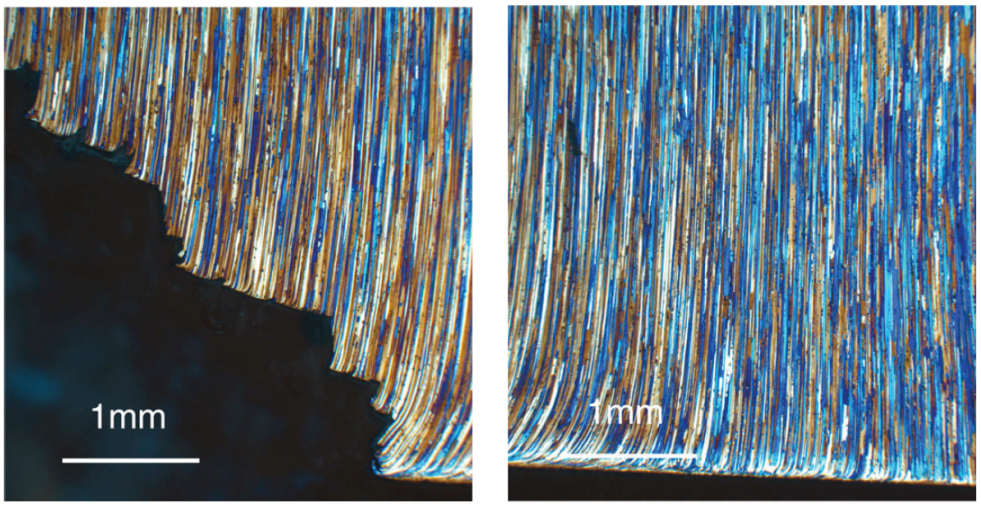

(a) Framentation area.

(b) Penetration channel.

Figure 5.10: Optical micrographs of AA7075-T651 [55].

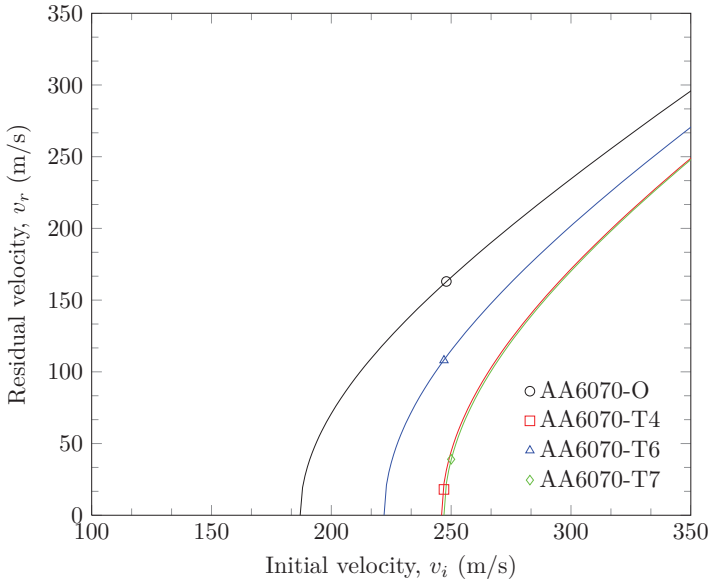

Figure 5.11: The ballistic limit curves from the experiments carried out with ogival projectiles.

5.3 Comments and Comparison

Figs. 5.7 and 5.11 reveal that the ballistic limit curves are slightly more heat-treatment sensitive when it comes to impacts with ogival projectiles as opposed to blunt projectiles. The figures also show that the target plates can withstand hits with higher velocity when ogival projectiles are used compared to blunt projectiles. In addition to this, the conclusion from Børvik et al. [22] is confirmed for both blunt and ogival nose projectiles: ballistic resistance can not be solely based on the yield stress. Further comments and discussion about the fragmentation process for the hardened 20 mm steel projectiles can be found in Chapter 11.

Table 5.3: Tabulated experimentally determined ballistic limit velocites for 20 mm blunt and ogival projectiles.

Temper	$v_{bl,\mathrm{BLUNT}}$ (m/s)	$v_{bl,\mathrm{OGIVAL}}$ (m/s)
AA6070-O	157.0	186.9
AA6070-T4	175.7	246.3
AA6070-T6	162.0	222.1
AA6070-T7	166.0	246.9

(a) AA6070-O

(b) AA6070-T4

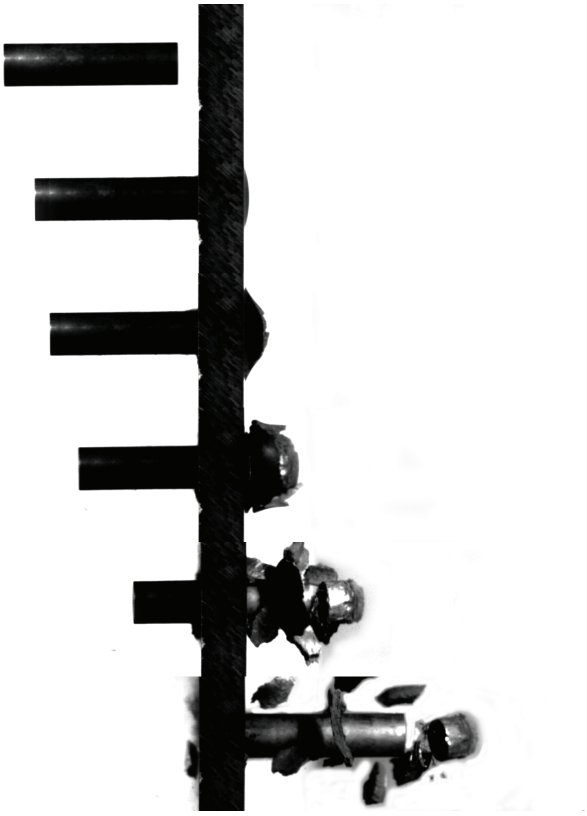

(c) AA6070-T6

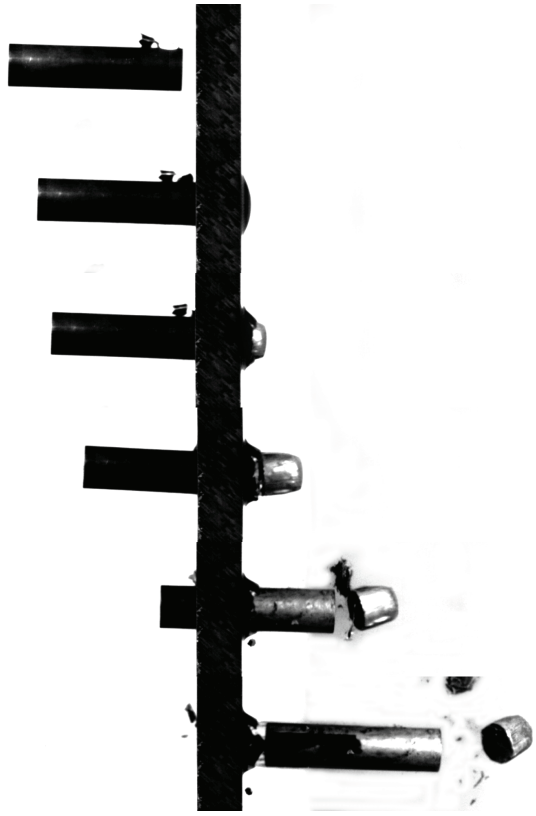

(d) AA6070-T7

Figure 5.12: Time-lapse for the aluminium plates penetrated by blunt projectiles.

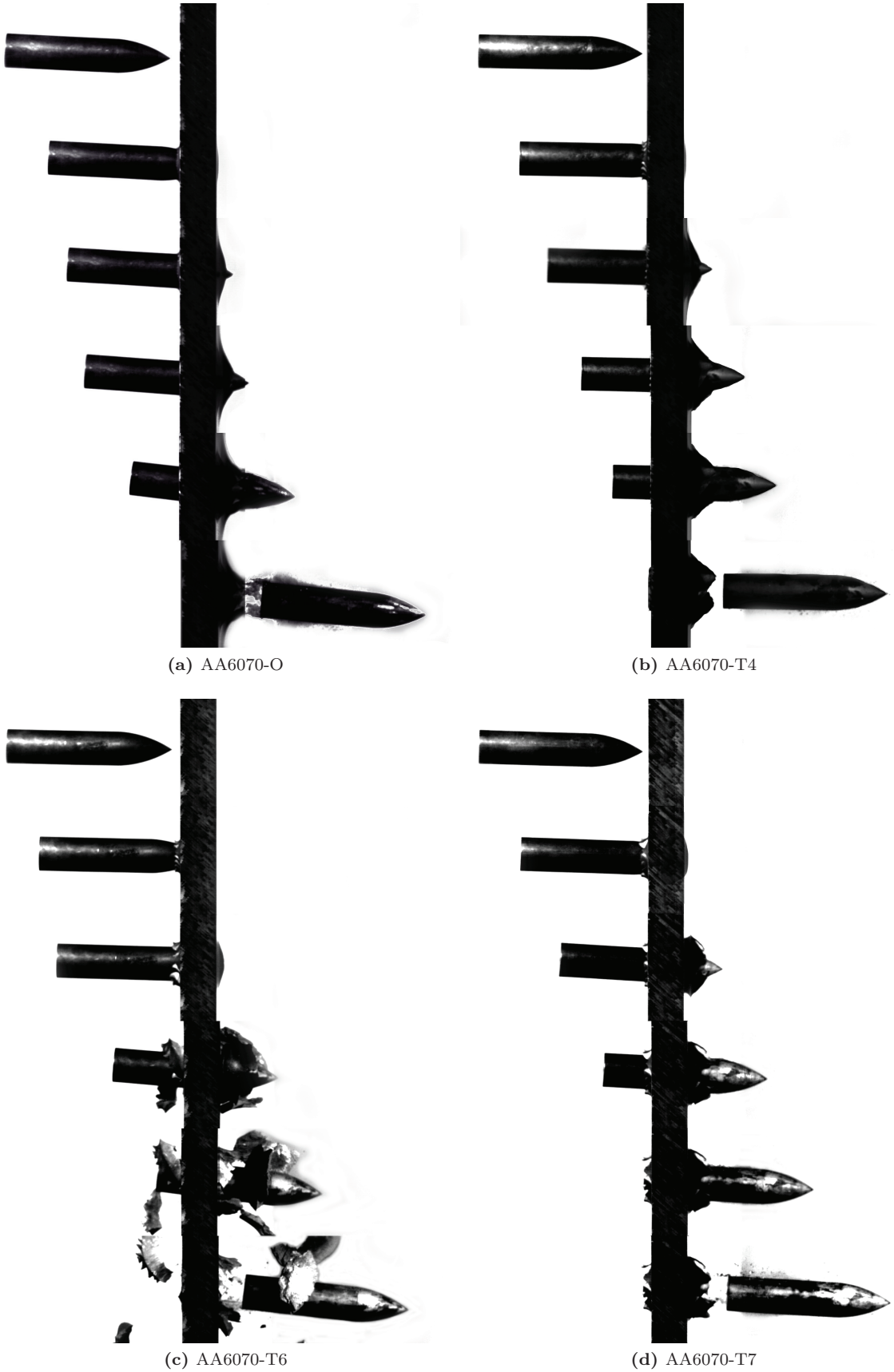

(a) AA6070-O **(b)** AA6070-T4

(c) AA6070-T6 **(d)** AA6070-T7

Figure 5.13: Time-lapse for the aluminium plates penetrated by ogival projectiles.

Chapter 6

Calibration of Material Models

6.1 Direct Calibration

Two calibration methods were used: direct calibration from material data obtained from laboratory test, and an inverse modeling method simulating the tensile test in LS-DYNA. The direct calibration method is covered first.. In addition to this, a purely numerical way of predicting the material behavior is discussed in Chapter 10.

As a consequence of necking, stress triaxiality is introduced in the specimen. To remove the hydrostatic stress-component from the test data, a Bridgman correction of the measured true stress-strain curve is required before calibration of the material parameters can be done [13]. The Bridgman correction needs a_B/R as an input parameter, where a_B is the specimen radius and R is the curvature radius of the neck. These values were not measured in the laboratory tests so it is necessary to make use of an empirical expression proposed by Le Roy et. al [13]:

$$\frac{a_B}{R} = 1.1\left(\epsilon_p - \epsilon_{lu,p}\right) \quad \text{for} \quad \epsilon_p > \epsilon_{lu,p} \tag{6.1}$$

where ϵ_p is the equivalent plastic strain, and ϵ_{lu_p} is the equivalent plastic strain at incipient neck. $\epsilon_{lu,p}$ is calculated by checking where the gradient of the true stress-strain curve is equal to the true stress, i.e.

$$\frac{\mathrm{d}\sigma_t}{\mathrm{d}\epsilon_l} = \sigma_t \tag{6.2}$$

Since the measured data from the tensile test is a set of data points it is impossible to apply Eq. (6.2) directly because the discontinuities cause the gradient to change dramatically between each data point. This is solved by curve fitting a two term Voce law (Eq. (2.12)) to the material data to obtain a continuous differentiable function. It is worth noticing that the last 20 data-points of the target curve is weighted higher relative to the preceding data-points, to make sure that the gradient of the regression line matches the gradient of the data from the laboratory tests. Also note that the Levenberg-Marquardt algorithm is implemented [45].

After calculating $\epsilon_{lu,p}$, a Bridgman correction of the true stress-strain curve is done, before fitting both the Voce law and the Power law to this curve. In Fig. 6.1 the regression process is illustrated for various tempers in the rolling direction.

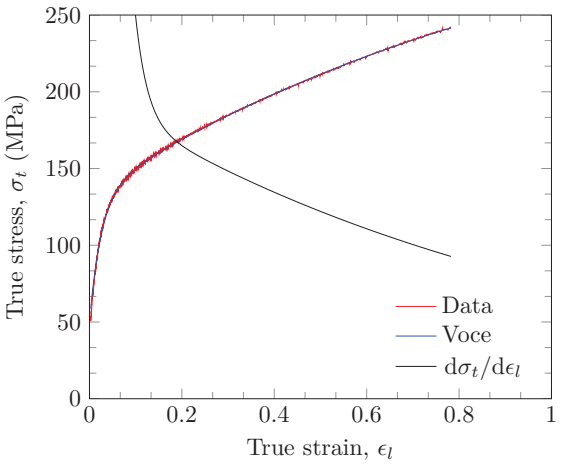

(a) AA6070-O-0°

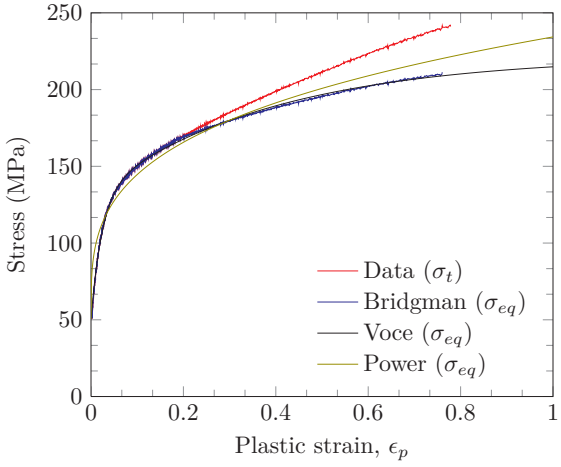

(b) AA6070-O-0°

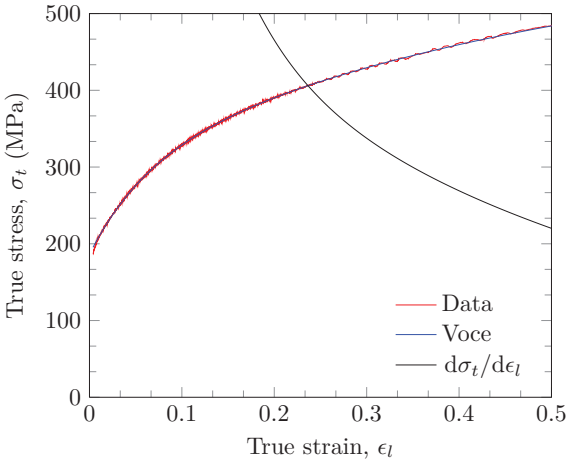

(c) AA6070-T4-0°

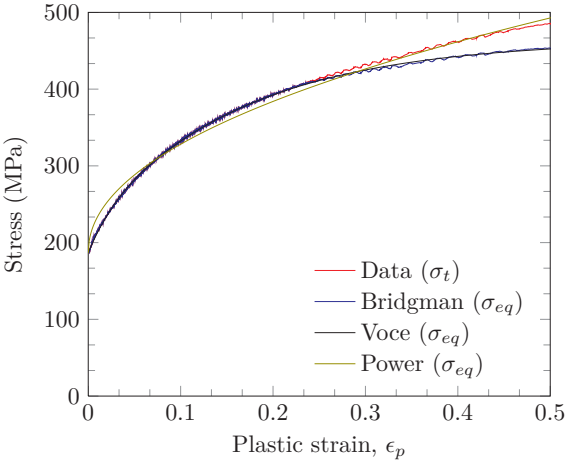

(d) AA6070-T4-0°

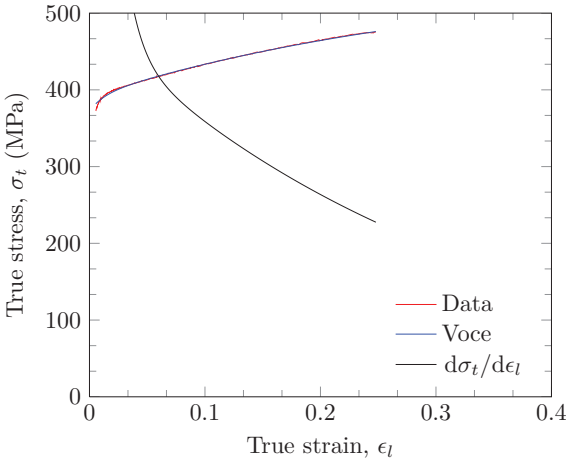

(e) AA6070-T6-0°

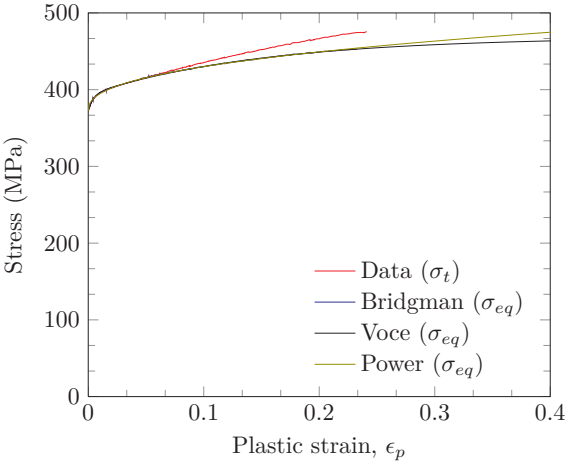

(f) AA6070-T6-0°

Figure 6.1: Continues...

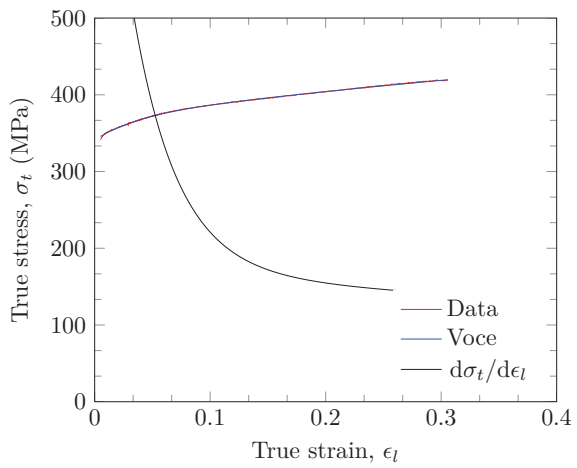

(g) AA6070-T7-0°

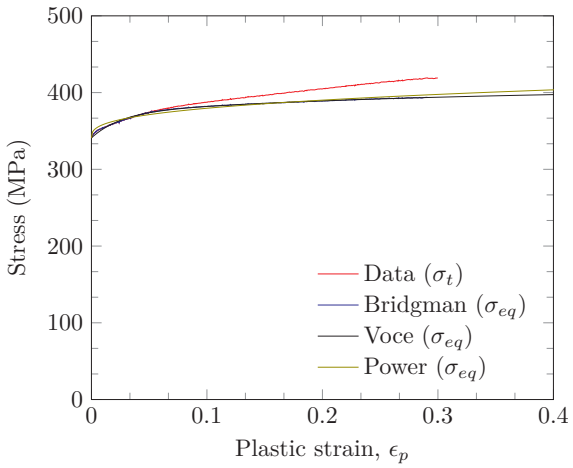

(h) AA6070-T7-0°

Figure 6.1: **(a)**, **(c)**, **(e)** and **(g)** show the first regression and the determination of $\epsilon_{lu,p}$, **(b)**, **(d)**, **(f)** and **(h)** show the Bridgman corrected true stress and the final calibration of both the Voce, and the Power work-hardening law for tempers O, T4, T6, T7 in the rolling direction.

The material parameters for use in the MJC constitutive relation with Power law hardening and Voce law hardening are given in Table 6.1. Furthermore, the MATLAB-script used for direct calibration and material parameters for all the plate directions are given in Appendix C.1.

Table 6.1: Material parameters for MJC with Power law hardening and Voce law hardening in the rolling direction.

Temper	$\boldsymbol{A}$ (MPa)	$\boldsymbol{B}$ (MPa)	$\boldsymbol{n}$	$\boldsymbol{C_1}$	$\boldsymbol{C_2}$	$\boldsymbol{Q_1}$ (MPa)	$\boldsymbol{Q_2}$ (MPa)	$\boldsymbol{\epsilon_{lu,p}}$
AA6070-O	50.5	183.82	0.290	2.58	41.45	90.35	80.35	0.188
AA6070-T4	186.5	426.96	0.479	6.06	40.70	240.19	37.30	0.231
AA6070-T6	372.5	150.55	0.417	217.66	6.78	20.98	75.07	0.054
AA6070-T7	341.0	86.00	0.349	38.89	3.21	32.45	33.06	0.047

6.2 Inverse Modeling

The direct calibration method often provide satisfactory results [14], but a_B/R has been approximated from Eq. (6.1) and might be somewhat inaccurate. To validate (or improve) the material model parameters, several successive analyses can be done on the same model. By changing the material-input-parameters from analysis to analysis, different responses are obtained, which in turn can be compared to a target curve where the best fit obviously has the best material-input-parameters.

In practice this can be done by using an optimization tool that changes the desired parameters based on different algorithms. The design optimization package LS-OPT with an interface to the explicit finite element code LS-DYNA has been used in this thesis [27]. For the target curve the force-diameter reduction curve is used because it is, in fact, the original data obtained in the laboratory tests. Please note that no additional manipulations (e.g. weighing or deletion of points) of the experimental data sets are performed. Firstly, a LS-DYNA-model of the tensile specimen has to be created, where the parameters found in the direct calibration are used as initial guesses. LS-OPT then reads this LS-DYNA keyword-file, and on the basis of this file does several iterations (runs the mentioned keyword-file) while changing only the desired parameters (A, C_1, C_2, Q_1 and Q_2) to obtain the solution with the smallest mean square error between the target curve and the computed force-diameter reduction curve.

The inverse modeling process is carried out based on the results from the tensile tests performed in the rolling direction. This is done because, by inspection of the stress-strain curves in Figs. 3.8a to 3.8d, the plastic flow is almost identical in the three different directions, meaning if the material model is valid for the most ductilie direction it also describes the more brittle directions well enough as long as a fracture criterion is not part of the optimization. To make sure that the optimization process is not mesh sensitive, LS-OPT is run with different element sizes: a coarse mesh with 0.5 mm elements in the necking region and a finer mesh with 0.25 mm elements in the necking region. Due to the high number of analyses that have to be run during each optimization, the models are axisymmetric (Fig. 6.2). The optimizations are done using MJC with mainly the two term Voce hardening rule, where A, C_1, C_2, Q_1 and Q_2 can be defined as variables that can be changed to obtain the best fit. 15 iterations are done with the coarse mesh for each optimization to ensure convergence while only 10 iterations are done for the fine mesh.

The two term Voce hardening rule has been implemented using the material card *MAT_107, element formulation type 15: axisymmetric solid - volume weighted, a smooth loading curve and hourglass control.

(a) Element size: 0.5 mm

(b) Element size: 0.25 mm

Figure 6.2: The different meshes used for the LS-OPT optimization

Improving the values for A, C_1, C_2, Q_1 and Q_2 from the direct calibration is not a trivial task, and LS-OPT demands much processing power, 15 iterations that each include 10 runs of the axisymmetric model takes alot of time. But after some trial and error a few success criteria revealed themselves. Firstly, a cut-of-criterion has to be established, i.e the `*TERMINATE_NODE` card in LS-DYNA that terminates the analysis when a maximum diameter reduction has been reached so analysis time is not wasted and it facilitates a better fit to the target curve. Secondly, a tight solution range should be defined for the variables so that the program will not start to search for a local mean square error

minimum instead of a global mean square error minimum. This is of particular importance if initial values that already give a good fit are avaliable. Thirdly, adjustments may be necessary during an iteration process; the narrow ranges might have to be expanded or variables (e.g. A) have to be held constant. To adjust the input variables to do "manual iterations" might be cumbersome due to the amount of data produced, but it is very benificial for the final results.

Table 6.2: The material model parameters for the two-term Voce hardening rule obtained through optimization in LS-OPT.

Temper	**Mesh**	$\boldsymbol{A}$ (MPa)	$\boldsymbol{C_1}$	$\boldsymbol{C_2}$	$\boldsymbol{Q_1}$ (MPa)	$\boldsymbol{Q_2}$ (MPa)	**MSE** Final	**MSE** Initial
AA6070-O	Coarse	38.80	4.00	56.89	88.17	79.51	$2.39 \cdot 10^{-5}$	$3.38 \cdot 10^{-4}$
		Good results after 8 iterations. Excellent convergence.						
	Fine	38.26	4.39	60.21	88.63	77.44	$3.02 \cdot 10^{-5}$	$3.80 \cdot 10^{-4}$
		Good results, hardly deviates from the coarser mesh.						
AA6070-T4	Coarse	172.72	6.52	80.57	247.72	35.60	$6.15 \cdot 10^{-5}$	$2.37 \cdot 10^{-4}$
		Good results after 10 iterations. Excellent convergence.						
	Fine	172.88	6.43	75.22	247.70	36.67	$6.16 \cdot 10^{-5}$	$2.36 \cdot 10^{-4}$
		Excellent results, very stable solution.						
AA6070-T6	Coarse	350.00	185.92	7.70	30.12	72.82	$9.36 \cdot 10^{-4}$	$1.84 \cdot 10^{-3}$
		Difficult to obtain convergence, solution slightly unstable.						
	Fine	352.76	207.96	8.04	22.5	78.48	$9.60 \cdot 10^{-4}$	$1.83 \cdot 10^{-3}$
		Difficult to obtain convergence. Parameters different from coarse mesh.						
AA6070-T7	Coarse	292.47	317.16	10.00	55.34	31.07	$5.95 \cdot 10^{-4}$	$1.79 \cdot 10^{-3}$
		Behavior of T7 makes fitting to the target curve difficult.						
	Fine	293.40	362.24	9.95	57.73	35.04	$5.89 \cdot 10^{-4}$	$1.77 \cdot 10^{-3}$
		Difficult to describe the transition between elastic and plastic domain.						

All optimizations show that every hardening parameter, including yield stress (A) has to be included in the analysis to obtain the best fit. Table 6.2 shows the optimized values, together with a short note, and the mean square error between the target curve and the computed curve for each case. Fig. 6.6 gives a graphical representation of the results.

The O-temper gave excellent results both in direct calibration and after using LS-OPT, the force-diameter reduction does not display an abrupt transition between elastic and plastic behavior, so the two-term Voce hardening law can be fitted with ease. The same applies for the T4-temper, where the fit also is excellent. A typical screenshot from the LS-OPT viewer section shows how Q_1 converges from the directly calibrated values to the optimized values for T4 is shown in Fig. 6.3 and how the optimal force-diameter reduction curve approaches the target curve is shown in Fig. 6.5a. It is evident from this figure that a good solution is reached after about eight iterations. The T6- and T7-tempers on the other hand, are not as easy to fit. A converged solution is harder to obtain, and the fit is not as good; this can be seen when Figs. 6.6a to 6.6d are compared to Figs. 6.6e to 6.6h. Typical convergence can be seen in Fig. 6.4. Although the fit of the T6-temper is excellent, the convergence is not as smooth as for O and T4; this can be due to the previously mentioned abrupt change between elastic and plastic domain. The T7-temper was the hardest to fit: both convergence and fit is notably poorer than for the rest of the tempers. A particular problem area is the corner seen in Fig. 6.6g. The target curve displays three distinct domains, one elastic where the slope of the curve is steep, then a corner where a gentler, but still positive slope follows. After a second

corner the force-diameter reduction curve gets a negative slope. The two-term Voce hardening rule seem to be having difficulties describing this curve exactly, but fairly good approximations are obtained.

Additional information to be taken from Table 6.2 is that a mesh with mainly 0.25 mm elements does not give results that are vastly different from the mesh with mainly 0.50 mm elements, indicating that the axisymmetric LS-DYNA model is not particularly mesh sensitive for this problem. Furter testing could be done on this, however the material parameters seem good enough to use in the ballistic simulations.

Seeing that the T7-fit is poor, the SIMLab metal model that includes a three term Voce hardening rule is also applied in LS-OPT. The computational time now increase because seven parameters have to be optimized instead of the previous five parameters. The isotropic hardening rule is implemented in LS-DYNA by SIMLab [37]:

$$R(\epsilon_p;\dot{\epsilon}_p) = \sum_{i=1}^{3} Q_{Ri}(\dot{\epsilon}_p)\left(1-\exp(-\frac{\theta_{Ri}}{Q_{Ri}(\dot{\epsilon}_p)})\epsilon_p\right) \tag{6.3}$$

Results from this optimization are shown as dashed lines in Figs. 6.6g and 6.6h, where it can be seen that the force-diameter reduction curve is estimated with a smoother shape that resembles the target curve slightly better than a two term Voce. The equivalent stress-plastic strain curve differs slightly from the two term curve in the beginning, but is almost identical afterwards. However, if strain values after ϵ_f are considered, one can see that the dashed curve does not saturate. The three term Voce hardening rule values that are calibrated directly and the optimized values are given in Table 6.3

Table 6.3: Directly calibrated and inverse modeled material parameters for SIMLab Metal Model for AA6070-T7.

Method	$\boldsymbol{A}$ (MPa)	$\boldsymbol{Q_1}$ (MPa)	$\boldsymbol{Q_2}$ (MPa)	$\boldsymbol{Q_3}$ (MPa)	$\boldsymbol{\theta_1}$ (MPa)	$\boldsymbol{\theta_2}$ (MPa)	$\boldsymbol{\theta_3}$ (MPa)	**MSE**
Dir. Cal.	341.00	3.74	433.31	34.45	3637.34	50.40	977.00	$17.35 \cdot 10^{-4}$
Optimized	318.59	3.45	333.95	40.38	2867.26	63.68	2000.00	$7.93 \cdot 10^{-4}$

Some things are worth noting about the results that are displayed in Fig. 6.6. Since all the true stress-plastic strain curves are given for values of plastic strain from 0 to 1, i.e. further than experimental fracture we can get an impression of the values the finite element code will extrapolate from the input values. This is especially important for the O-temper (Fig. 6.6b), where it is evident that the true stress-plastic strain curve based on direct calibration has a gradient, while the curve based on LS-OPT values does not have a gradient. This discrepancy can occur due to the approximations done by using Le Roy's relation Eq. (6.1) and by Bridgman correcting. However, the importance of this in penetration problems is questionable [14]. All the directly calibrated curves lie higher than the optimized curves in Figs. 6.6a, 6.6c, 6.6e and 6.6g, which also indicate that the approximations done through the Bridgman analysis are somewhat inaccurate.

All the algorithms and possiblilites in LS-OPT have not been employed in this thesis, so further effort regarding the optimization process might give better results. For example, a procedure where a fixed number of equally spaced data points from the true stress-strain curve is promising [14]. However, optimizing takes up a considerable amount of time, and it is doubtful that further tweaking of parameters will have a large impact on the final results in a penetration analysis. In the following chapters, the optimized values with two term Voce hardening calculated using a coarse mesh in LS-OPT are used (Table 6.2).

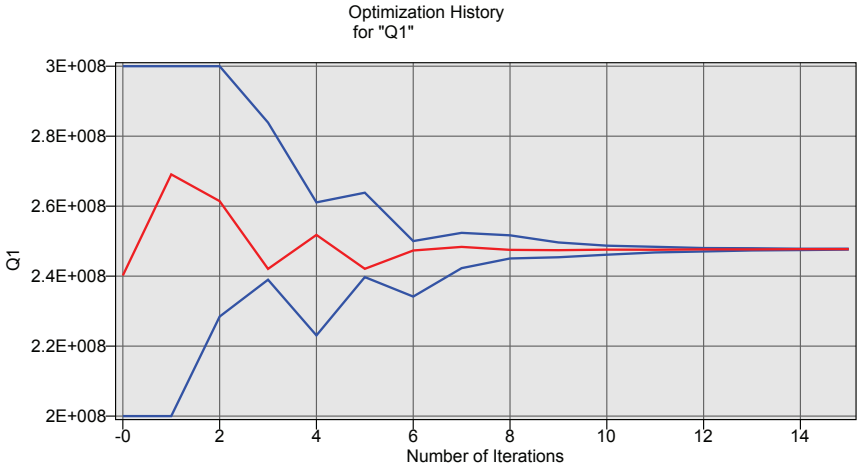

Figure 6.3: Screenshot from LS-OPT showing how Q_1 converges very well for the T4-temper.

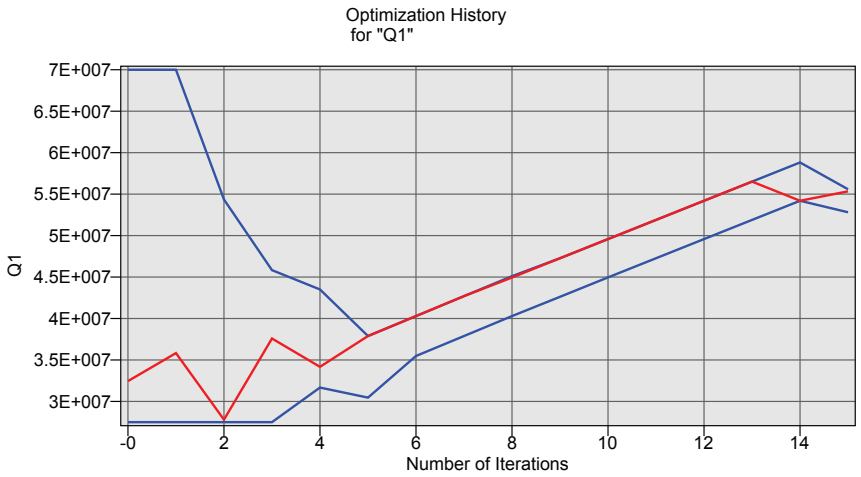

Figure 6.4: Screenshot from LS-OPT showing how Q_1 has problems converging for the T7-temper.

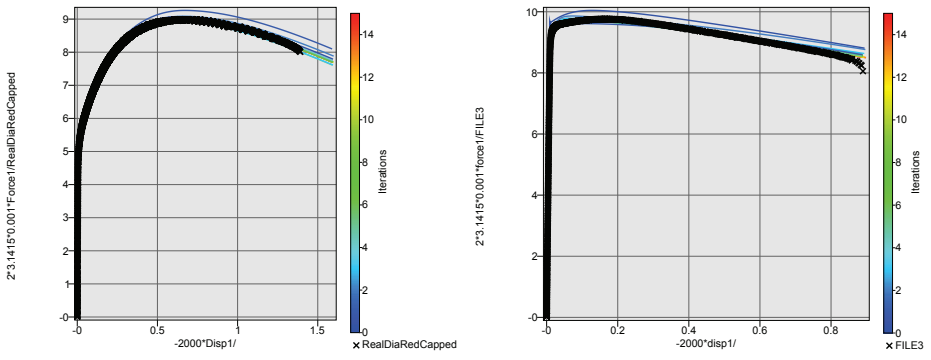

(a) **(b)**

Figure 6.5: Screenshot from LS-OPT showing how the fit to the target curve converges for **(a)** AA6070-T4 and **(b)** AA6070-T7.

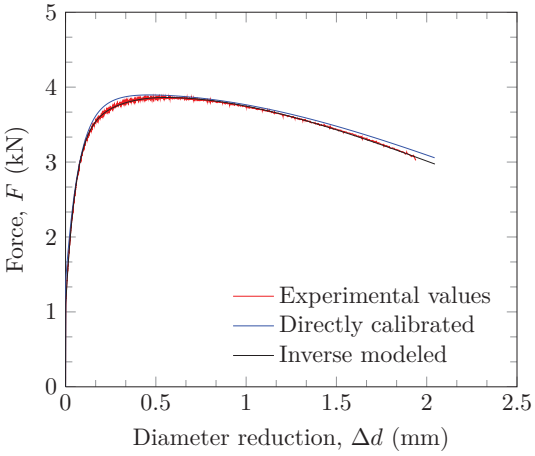

(a) AA6070-O-0°

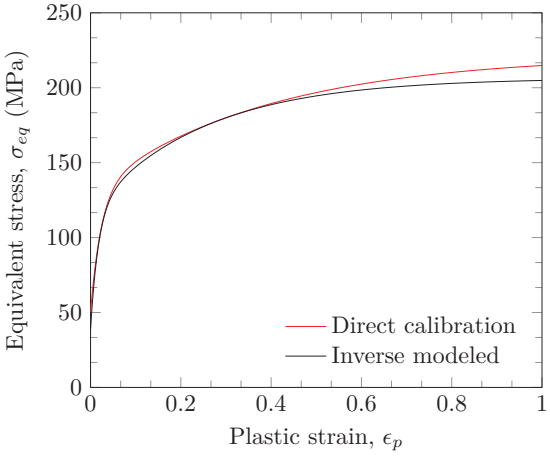

(b) AA6070-O-0°

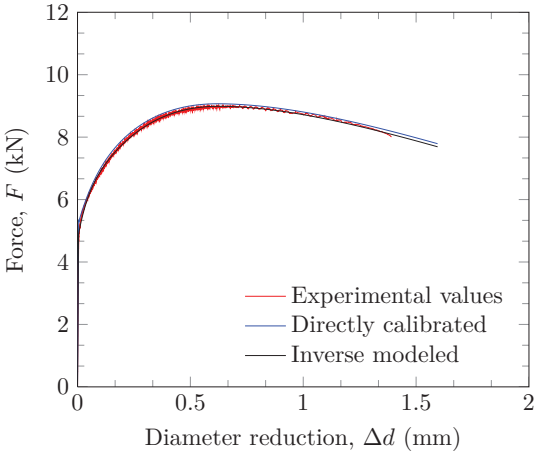

(c) AA6070-T4-0°

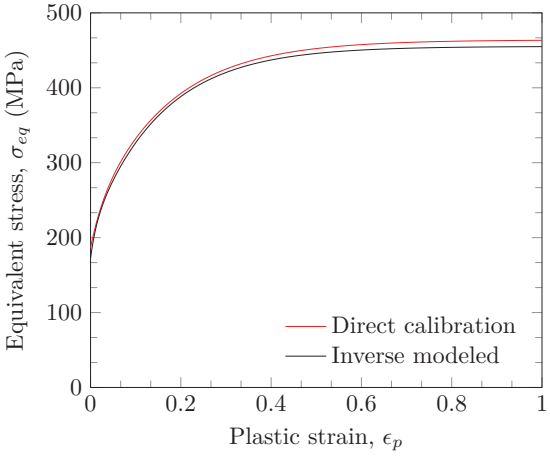

(d) AA6070-T4-0°

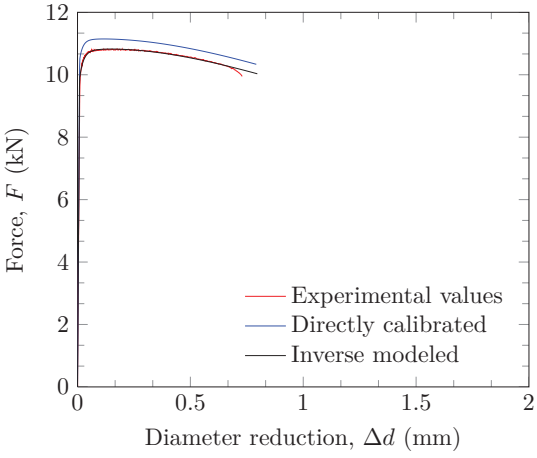

(e) AA6070-T6-0°

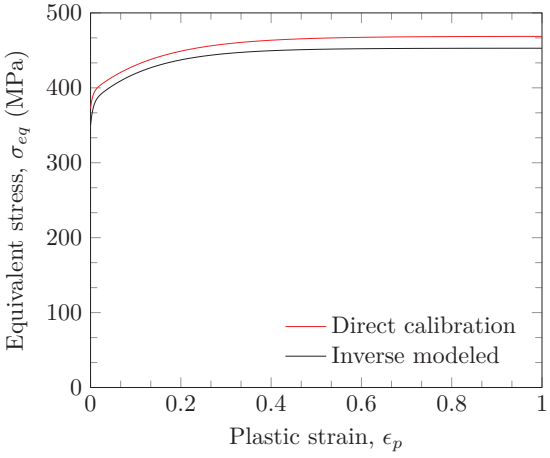

(f) AA6070-T6-0°

Figure 6.6: Continues...

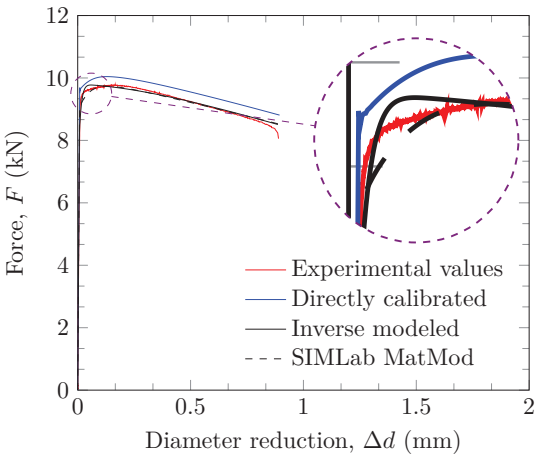

(g) AA6070-T7-0°

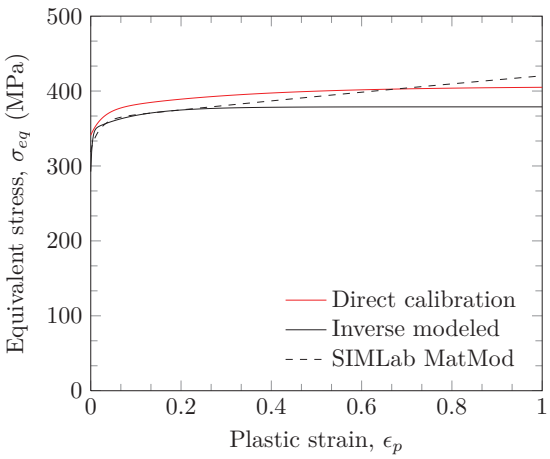

(h) AA6070-T7-0°

Figure 6.6: **(a)**, **(c)**, **(e)** and **(g)** show the force-diameter reduction curves from inverse modeling compared to experimental values and values obtained using the material parameters from direct calibration, while **(b)**, **(d)**, **(f)** and **(h)** show the equivalent stress-strain curve from the inverse modeling process compared to the Bridgman-corrected true stress-strain curve fitted to the experimental data for all tempers in the rolling direction.

6.3 Material Model Validation

To be absolutely sure that the material models that were calibrated in Sections 6.1 and 6.2 are correct, a tensile experiment is recreated and analysed using the IMPETUS finite element code. This code is to be used to solve the penetration problems in addition to LS-DYNA, so it is of interest to see how the results from IMPETUS compare to the experimental values.

The tensile tests are run with the 64-node cubic hexahedra elements described in Section 2.7. Needless to say, the mesh is 3D and it is shown in Fig. 6.7. It is desirable to copy the exact quasi-static conditions from the real experiments, however it requires a lot of computational time in explicit solvers. To remedy this, mass scaling is used and the tensile speed has been increased tenfold. After controlling that the kinetic energy is significantly (several orders of magnitude) smaller than the internal energy of the tensile specimen the alterations were found to be reasonable.

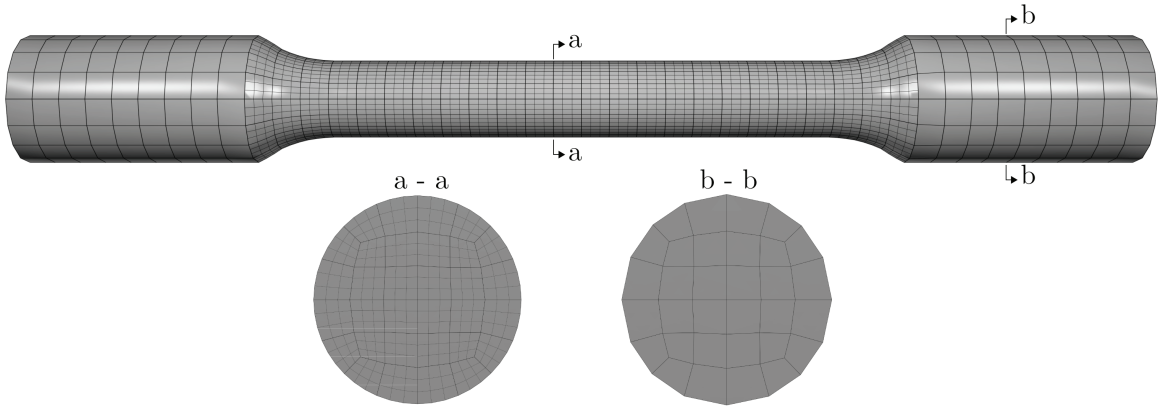

Figure 6.7: Mesh used for validation of the IMPETUS Afea Solver.

The Modified Johnson-Cook constitutive relation with Voce hardening stated in Eq. (2.13) is implemented and used. To be able to get results that are comparable to the real test data the diameter reduction at the neck and the applied force is reported and plotted. The true stress-strain curve shown in Fig. 6.8b has been calculated from

$$\epsilon_l = 2\ln(\frac{d_0}{d_0 - \Delta d}) \tag{6.4}$$

$$\sigma_t = \frac{4F}{\pi\left(d_0 - \Delta d\right)^2} \tag{6.5}$$

where F is the applied force, d_0 is the initial diameter and d is the current diameter.

By inspecting Fig. 6.8b it is seen that the material parameters obtained using LS-OPT on the axisymmetric LS-DYNA model (Fig. 6.2) in Section 6.2 gave decent results when used in a 3D IMPETUS model. The Cockcroft-Latham fracture criterion has also been implemented in some of the analyses. In general the failure takes place slightly too early, but all in all the results are satisfactory.

It is not guaranteed that a single node hits the exact point of the neck, especially when a mesh this coarse is used, see Fig. 6.9b. So the discrepancy late in the analyses can be blamed on the fact that the true displacement cannot be measured, but only approximations that will give smaller diameter reductions. Among the four tempers, the error for the O-temper was the largest, probably due to its ductility. To mend the error found because of the coarse mesh, the displacements were interpolated in the neck to investigate the effect of neck-localization, see Fig. 6.9b. The result of this can be seen

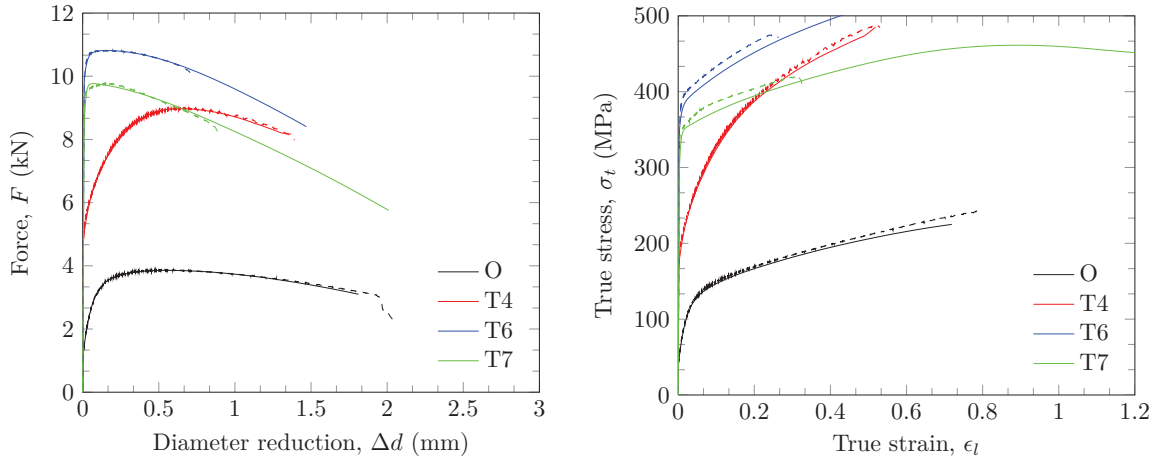

(a) **(b)**

Figure 6.8: **(a)** Force-diameter reduction plot and **(b)** true stress-strain. Where the results from IMPETUS are displayed as solid lines and experimental data is dashed.

in Fig. 6.9a where a linear approximation turns out to give too much reduction in diameter, while a quadratic interpolation gives too little reduction in diameter. These two were averaged to get the best solution.

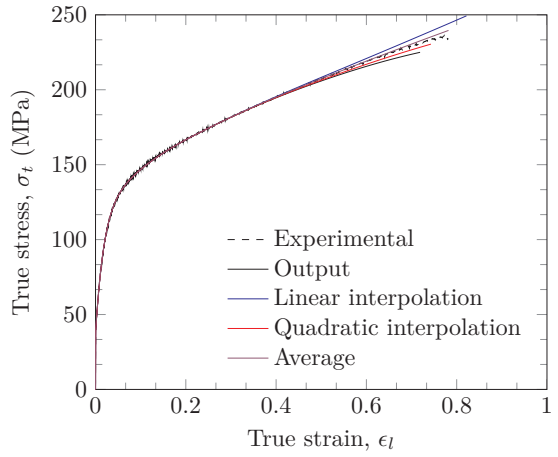

(a) True stress-strain curves for AA6070-O calculated from different interpolation types.

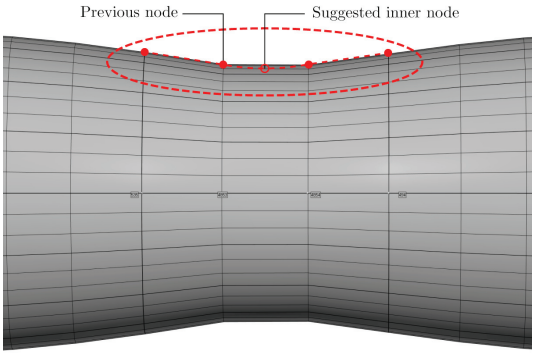

(b) Close-up of the neck in a typical IMPETUS analysis.

Figure 6.9: Numerical exercise to improve the results.

Chapter 7

Numerical Analysis: 7.62 mm Bullets

7.1 Prerequisites for Numerical Analyses

Before we can conduct a finite element analysis three prerequisites have to be in place:

(1) a constitutive relation,
(2) a fracture criterion, and
(3) an equation of state (EOS).

The constitutive relation and the fracture criterion have already been chosen: the Modified Johnson-Cook (MJC) material model (see Section 2.3.1) and the Cockcroft-Latham (CL) fracture criterion (see Section 2.3.2). But the third point has not yet been discussed; an equation of state provides a mathematical relation between two or more state variables, in this case the relationship between hydrostatic pressure and volumetric strain. Impact velocities in this thesis are generally fairly moderate, so it is reasonable to assume a linear relationship between pressure and volumetric strain. Thus our equation of state reads:

$$p = -K\epsilon_v + K\alpha_T(T - T_0) \tag{7.1}$$

where p is the hydrostatic pressure, K the bulk modulus, ϵ_v the volumetric strain, α_T the heat expansion coefficient, T the current temperature, and T_0 is the reference temperature. Note that when heat expansion is neglected, the last term in Eq. (7.1) disappears. The effect α_T has on the numerical results is investigated in Section 7.2.4.

The need for a non-linear EOS is discussed by Børvik et. al [23]. In this paper results are obtained in agreement with Zukas et al. [60], namely that the EOS is of secondary importance for solid-solid impacts in the $500 - 2000$ m/s velocity range.

7.2 Impacts with 7.62 mm APM2 Bullets Analyzed in IMPETUS

The explicit finite element code IMPETUS Afea Solver was used to carry out simulations of the ballistic experiments performed with 7.62 mm APM2 bullets. Initially, our intention was to model the complete APM2 bullet shown in Fig. 4.1b, but we had to reconsider due to the lack of energy conservation, specifically for low initial velocities. This problem is thoroughly covered in Section 7.2.2 and Section 7.2.4. The bulk of the analyses were run with only the steel core of the APM2 bullet, which in a physical perspective is a decent approximation since the hard steel core is the most significant component with regards to perforation [31].

7.2.1 Procedure

The basic input-file we used in this thesis is an adaptation of an input-file based on a paper by Forrestal et al. [31], but some alterations have to be mentioned. The Voce hardening law has been implemented instead of the Power law because of its ability to describe the hardening in the AA6070-tempers. This is

done through the *MAT_PWL-card by calling Eq. (2.12) through *FUNCTION. Material parameters for the plate are taken from the inverse modeled values in Table 6.2 and Table 3.3. The *PROP_DAMAGE_CL-card is active to invoke Cockcroft-Latham fracture.

Inspection of the high-speed images from the experimental work show that in general, the steel core of the APM2 bullet remains practically undeformed, hence it was chosen to model the projectile as a rigid body to save some computational time. The aluminium plate was modeled with the MJC constitutive relation with Voce work-hardening as mentioned. The symmetry of the problem has been exploited modeling only half of the projectile and plate. In addition the plate-size was reduced by including only a partition (80×80 mm^2) of the plate. No boundary conditions were introduced, this is considered viable because there are large differences in projectile and aluminium plate mass [23]. Linear elements were used in the peripheral parts of the plate, while higher-order 64-node cubic elements were used in the region of the plate undergoing large deformations. The mesh which is provived by Dr. Olovsson and used with the IMPETUS Afea Solver can be seen in Fig. 7.1b.

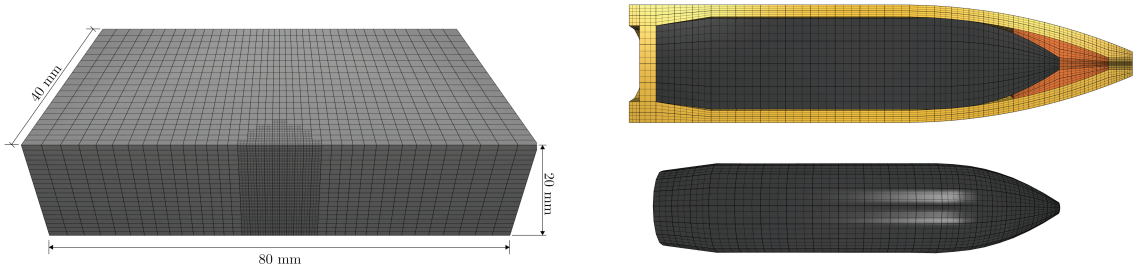

(a) Mesh of the aluminium plate.

(b) Mesh of the APM2 bullet and steel core

Figure 7.1: Illustration of mesh used in IMPETUS. **(a)** shows the aluminium target plate with 8-node linear elements in the periphery and 64-node cubic elements in the impact area (two times the radius of the bullet). In **(b)** the bullet composition with its mesh is shown. All elements are 64-node cubic elements.

In the simulations described, the IMPETUS Afea Solver deals with element damage in three ways, where point (3) removes the element completely:

(1) The CL fracture criterion removes an element's shear strength when the damage parameter $D = (1/W_c) \int_0^{\epsilon^p} \max(0, \sigma_1) \mathrm{d}\epsilon_p$ reaches 1, more on this in Section 2.3.2. Note that the element still exhibits compressive strength.

(2) When the temperature reaches the melting temperature ($T = 893$ K for aluminium) the yield strength drops to zero.

(3) Elements are eroded when the critical time step Δt_{cr} of the element drops below a user-defined value, in this case $3.0 \cdot 10^{-9}$ s unless otherwise stated.

Contact is imperative in impact and perforation problems. The IMPETUS Afea Solver uses penalty contact where the contact surfaces, if specified, are updated as elements erode; this method is used in this thesis. One of the downsides with the penalty method as opposed the Lagrange multiplier method is that the analyst has to choose a penalty number. In IMPETUS, we can define an absolute value for the penalty stiffness factor and the code then accounts for the contact stiffness and reduces the time-step to ensure numerical stability [2]. For our thesis the penalty number was set to $-1 \cdot 10^{15}$, meaning that a penetration of 0.001 mm gives a contact pressure of 1 GPa.

General material constants used for the current materials can be found in Table 7.1. Material constants for the brass jacket, the lead filling, and the steel core of the APM2 bullet are taken from Børvik et al. [23].

Table 7.1: Physical material constants for the MJC constitutive relation [23].

Material	E (MPa)	ν	ρ (kg/m^3)	C_p (J/kg K)	χ	T_r (K)	T_m (K)	m	$\dot{\epsilon}_{0_p}$	C
Aluminium	70 000	0.30	2700	910	0.9	293	893	1.0	$5.0 \cdot 10^{-4}$	0.001
Steel core[a]	210 000	0.33	7850	452	0.9	293	1800	1.0	$5.0 \cdot 10^{-4}$	0.0
Brass jacket	115 000	0.31	8520	385	0.9	293	1189	1.68	$5.0 \cdot 10^{-4}$	0.01
Lead filling[b]	10 000	0.42	10 660	124	0.9	293	760	1.0	$5.0 \cdot 10^{-4}$	0.1

[a] Modeled as rigid, only ρ is used. [b] Wrong Young's modulus in [23].

7.2.2 Troubleshooting

The mentioned difficulties regarding the energy balance when modeling the complete APM2 bullet has been of major concern. It proved to be especially problematic when the initial velocity of the bullet was low. Energy balance is one of the few ways an explicit element analysis can be validated, and a deviation in energy ratio of more than 5% is undesirable [14]. In Fig. 7.2 different energy outputs from the IMPETUS Afea Solver are plotted. The two pictures on the right-hand side show snapshots of the model at two points in time where significant changes in the total energy are observed. The first point at time $t \approx 0.034$ ms is where energy conservation fails. After this time the total energy suffers a monotonic increase until the end of the simulation.

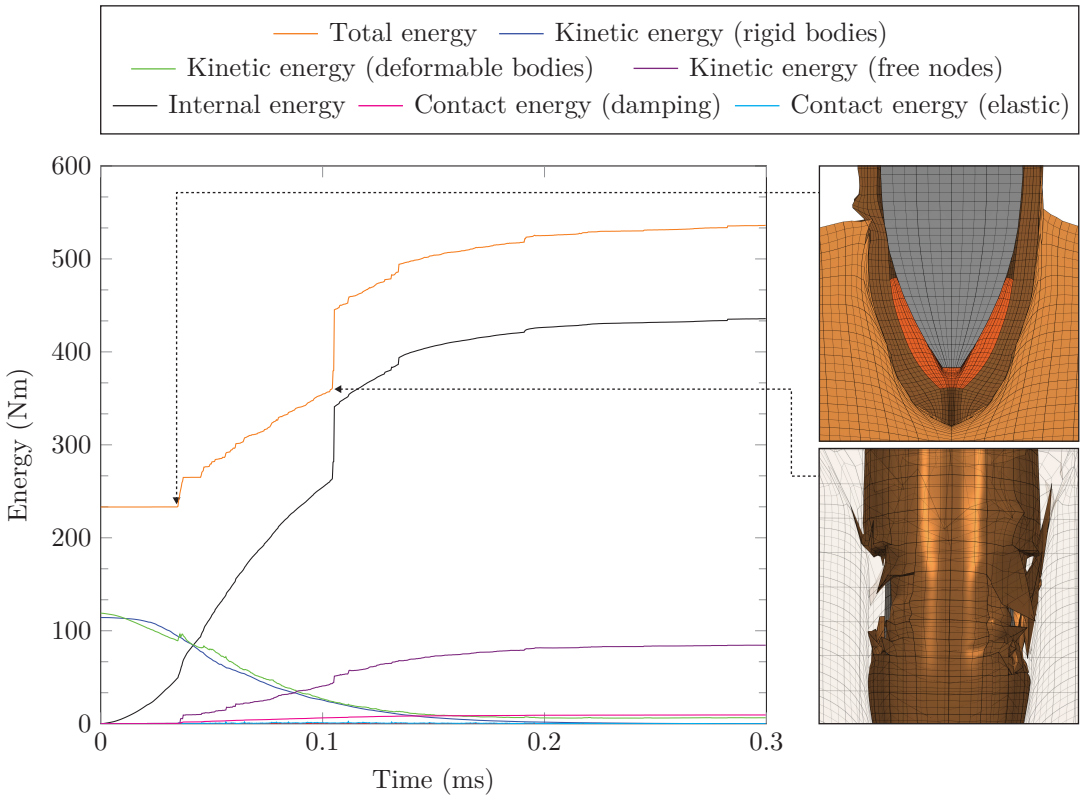

Figure 7.2: Energy conservation problem when modeling the complete APM2 bullet.

The first attempt to resolve the energy conservation issues in Fig. 7.2 involved decreasing the time step scaling factor (tfac) in IMPETUS from 0.9 to 0.3. This action would determine if the issue could have come from a numerical error caused by large time steps. The resulting energy plot in Fig. 7.3 shows that this is not the case. The peak total energy when tfac = 0.9 is roughly 533 Nm, while for tfac = 0.3 the peak total energy increased to about 3500 Nm. The sudden jumps in internal and consequently total energy are discontinuities that need resolving.

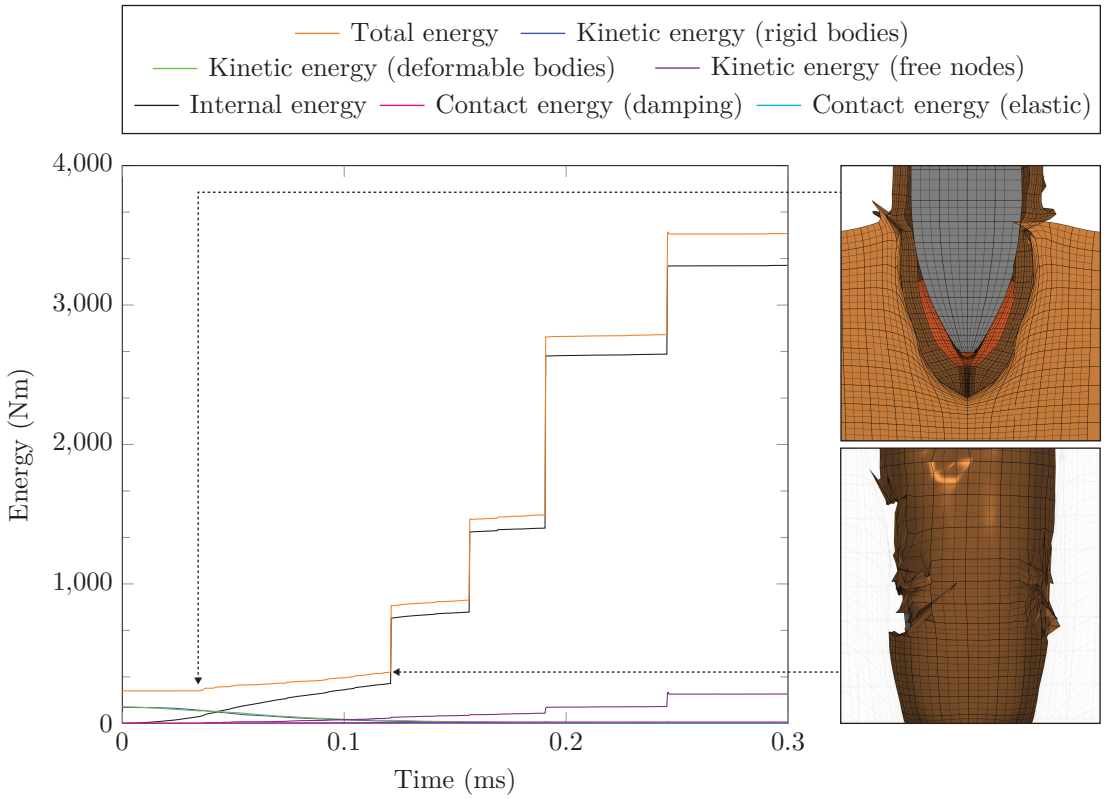

Figure 7.3: Energy conservation problem when modeling the complete APM2 bullet, after adjusting the time step scaling factor from 0.9 to 0.3.

According to Olovsson [52], energy balance problems may be caused by elements about to be inverted. A built-in feature in the IMPETUS Afea Solver proved to be a suitable measure against inverted elements: checking the incremental change in the geometric strain of each element. If the incremental change, $\Delta\epsilon$, in an element exceeds a user-defined limit, this specific element should be eroded, thus ensuring energy conservation. New simulations of the initial model with tfac = 0.9 were run with $\Delta\epsilon_{\text{erode}} = 0.5$ and $\Delta\epsilon_{\text{erode}} = 1.0$ and the corresponding energy balance plots are shown in Fig. 7.4.

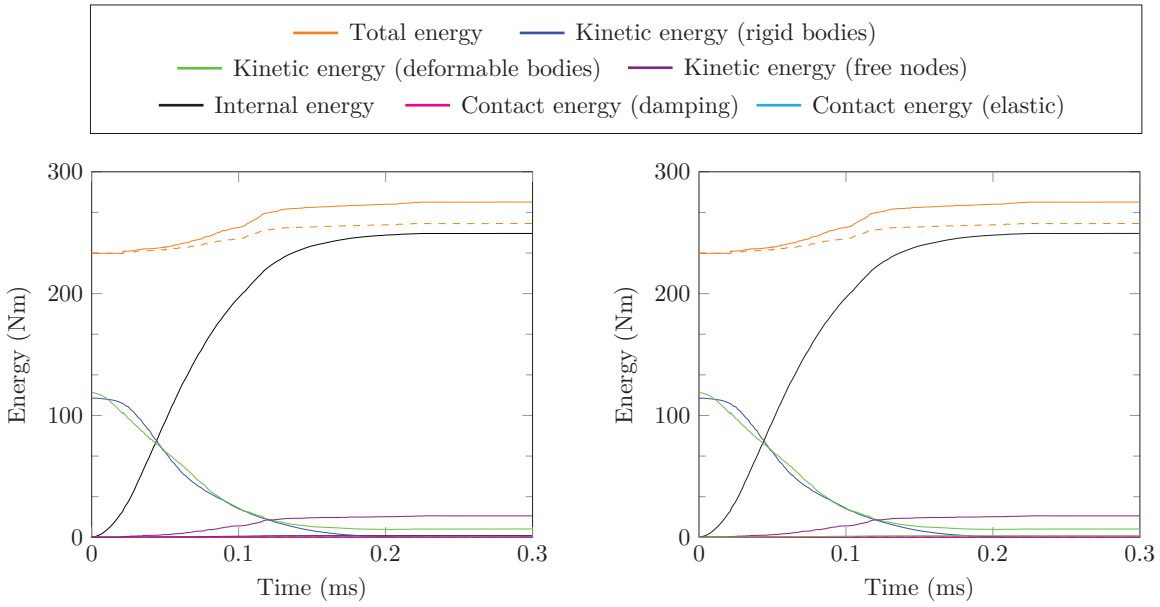

(a) $\Delta\epsilon_{\text{erode}} = 1.0$ **(b)** $\Delta\epsilon_{\text{erode}} = 0.5$

Figure 7.4: Energy balance plots from IMPETUS, the dashed lines describe the total energy when kinetic energy from free nodes and leaked blast particles (eroded energy) is excluded.

From inspection of Fig. 7.4 it appears that we still do not have satisfactory energy conservation, although the improvement is significant. Adding up all the energy contributions for the case with $\Delta\epsilon_{\text{erode}} = 1.0$ gives an 18% increase in the total energy, and a 10.5% increase when eroded energy is excluded. As seen from Fig. 7.4b no notable effect can be seen from changing $\Delta\epsilon_{\text{erode}}$ from 1 to 0.5. It seems that for the time being, eroded elements might tamper with the energy calculations, however it is important to emphasize that the numerical results are not affected, as shown in Fig. 7.5 where the effect of enabling $\Delta\epsilon_{\text{erode}}$ for the T6-temper with initial velocity $v_i = 900.6$ m/s is shown. The difference in residual velocity is minor, while the difference in energy ratio is huge. These results indicate that the problem in the IMPETUS Afea Solver is a small glitch rather than a detrimental error.

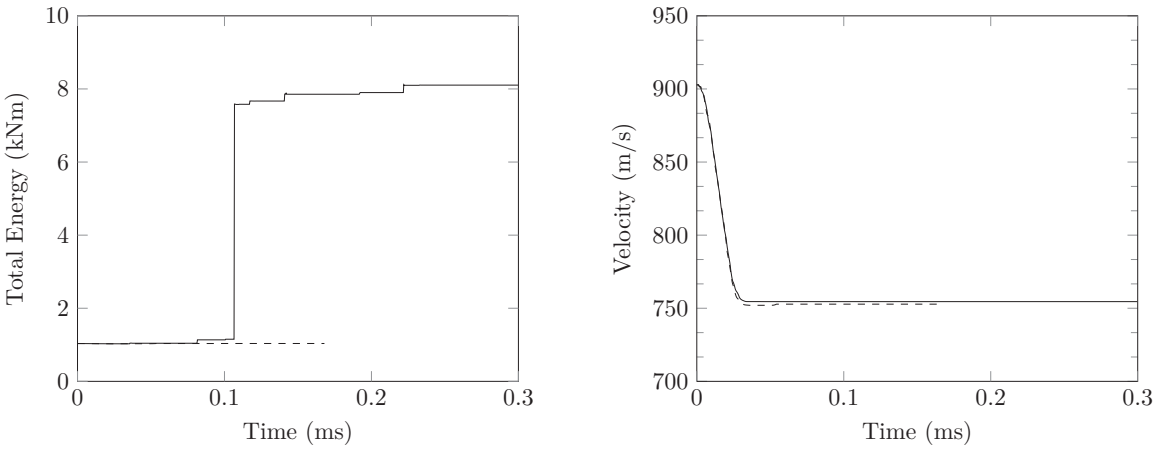

(a) **(b)**

Figure 7.5: Dashed lines are from analyses with $\Delta\epsilon_{\text{erode}} = 1$. Solid lines from analyses without this flag enabled. **(a)** shows total energy and the effect of enabling $\Delta\epsilon_{\text{erode}}$, **(b)** shows that the velocity of the projectile is not affected (only the steel core is modeled).

For comparative reasons, two energy plots for the T6-temper are shown in Fig. 7.6. Only the rigid steel core was used. In Fig. 7.6a with $v_i = 902.8$ m/s, $\Delta\epsilon_{\text{erode}} = 1$ to ensure appropriate energy balance. In Fig. 7.6b with $v_i = 430.0$ m/s the default value $\Delta\epsilon_{\text{erode}} = 1 \cdot 10^{20}$ was used. This is a clear indication that energy conservation in IMPETUS is slightly problematic at this point in time, but that the results regarding e.g. residual velocity can be trusted.

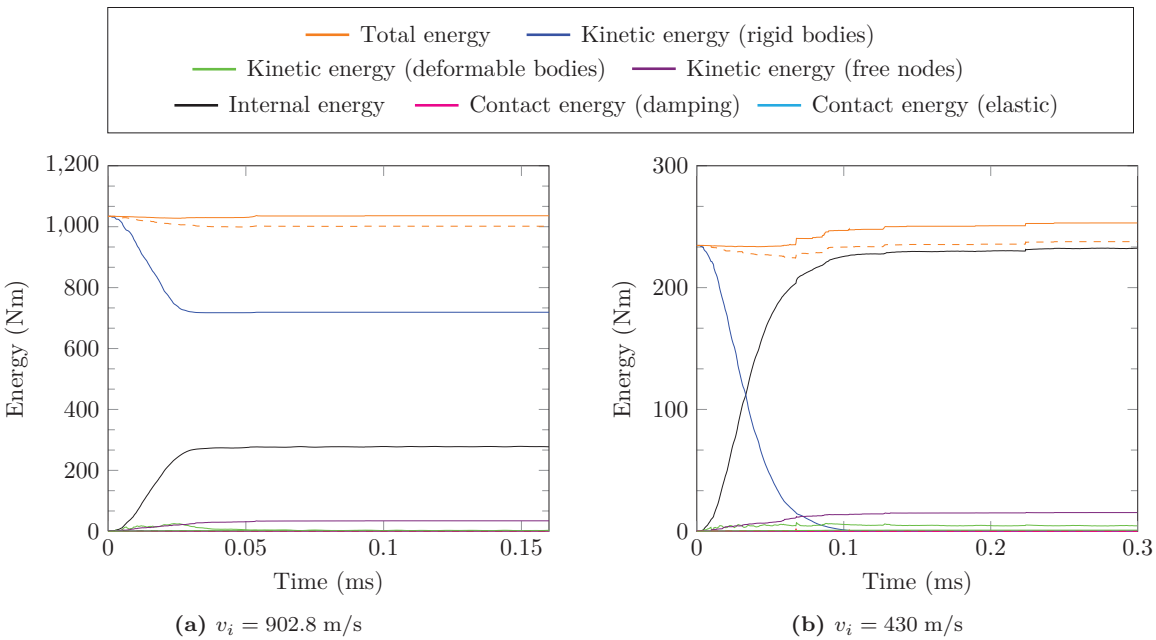

(a) $v_i = 902.8$ m/s **(b)** $v_i = 430$ m/s

Figure 7.6: Energy balance plots from IMPETUS for the T6-temper, with only the hardened steel core modeled. With initial velocity **(a)** $v_i = 902.8$ m/s and **(b)** $v_i = 430.0$ m/s. The dashed lines describe the total energy without eroded energy.

7.2.3 Results

The time-lapses in Fig. 7.7 show the perforation process for the O-temper with two different initial velocities and the T4-temper with two different initial velocities. Fragmentation has proven to be difficult to capture in the simulations, so we can only observe slight differences between the perforation processes of the two tempers. This can also be seen in the images of the bullet holes in Figs. 7.9 and 7.10. The pictures from the simulations also show that only a small part of the plates are affected by the penetration and perforation of the APM2 bullets, in Fig. 7.7 we can see that the area of the target plates with severe plastic strains is a region with a diameter just over two times the diameter of the projectile.

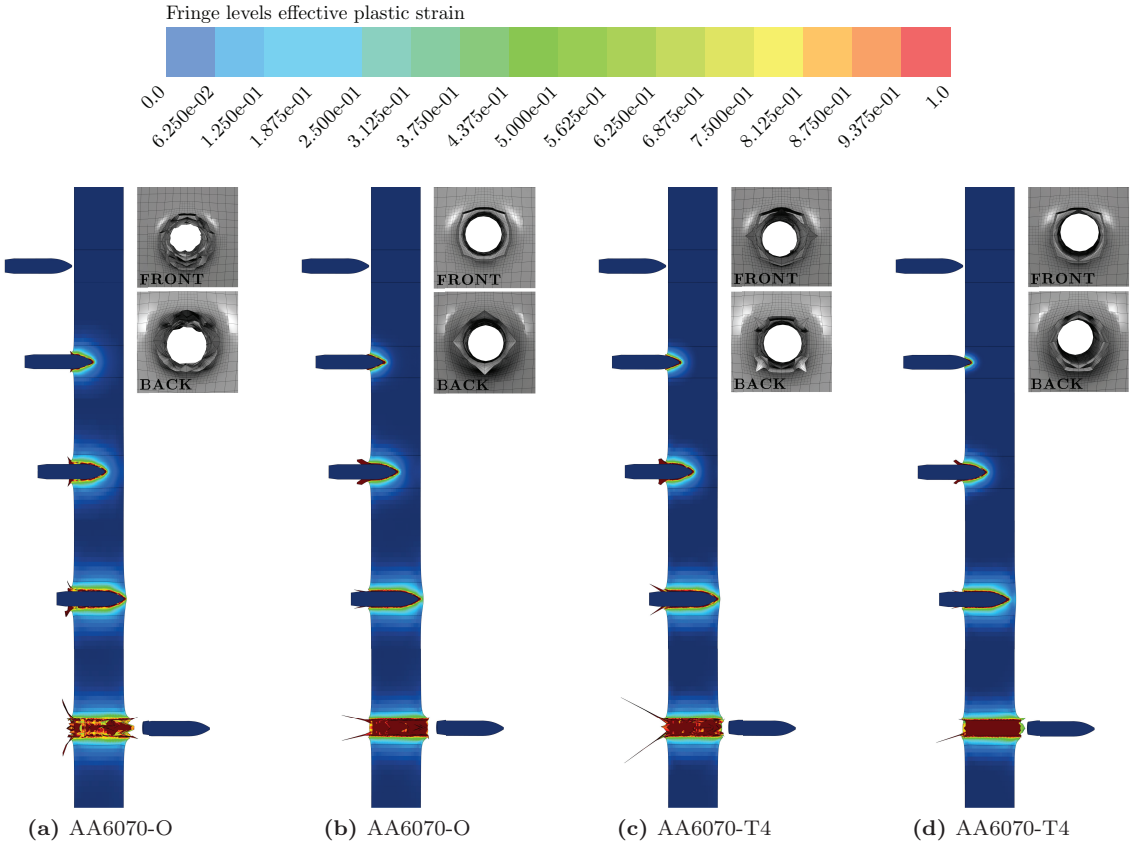

(a) AA6070-O **(b)** AA6070-O **(c)** AA6070-T4 **(d)** AA6070-T4

Figure 7.7: **(a)** and **(b)** are time-lapses for the O-temper with $v_i = 899.9$ m/s, $v_r = 834$ m/s, and $v_i = 377$ m/s, $v_r = 230.5$ m/s, respectively. **(c)** and **(d)** the T4 temper with $v_i = 894.3$ m/s, $v_r = 769$ m/s, and $v_i = 509.4$ m/s, $v_r = 266$ m/s, respectively.

For the T6- and T7-tempers time-lapses can be seen in Fig. 7.8 and the behavior is similar to that of the O- and T4-tempers: highly localized strains and small differences regarding the penetration process betwees the two tempers. Figs. 7.11 and 7.12 display more excessive element distortion that may indicate a more violent penetration process for T6 and T7 compared to O and T4.

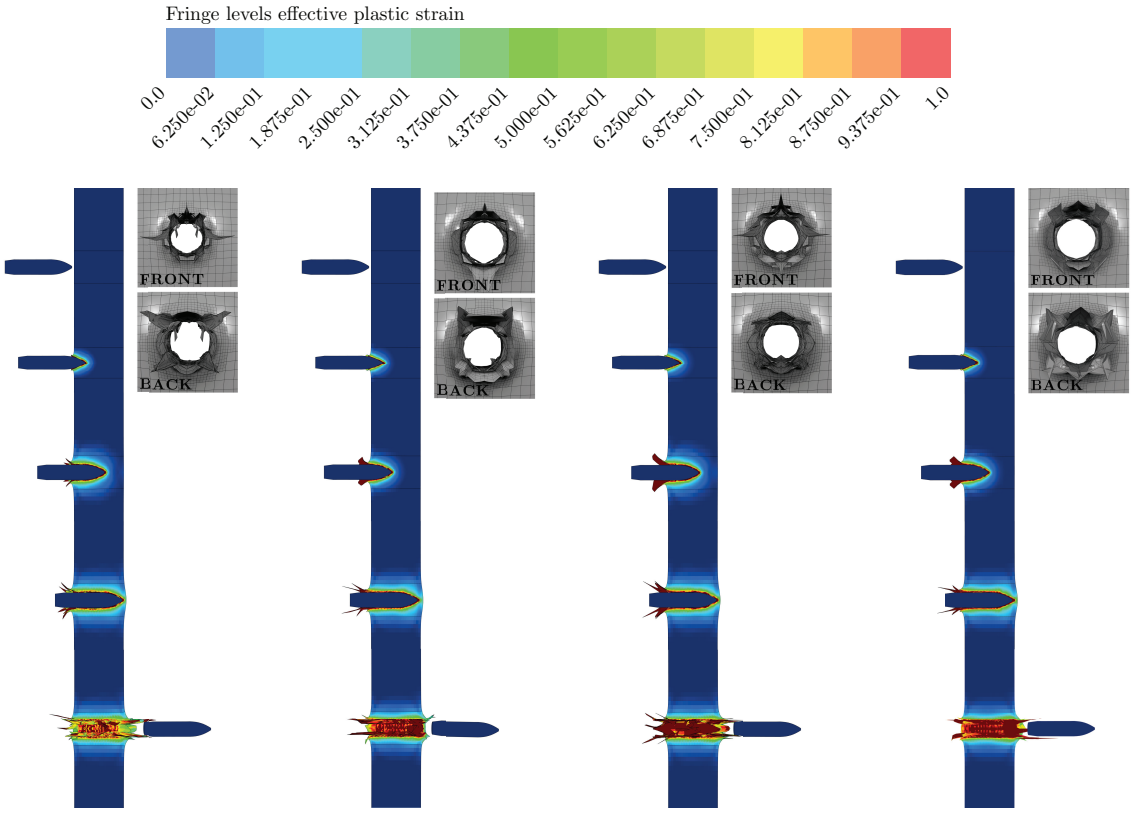

(a) AA6070-T6 **(b)** AA6070-T6 **(c)** AA6070-T7 **(d)** AA6070-T7

Figure 7.8: **(a)** and **(b)** are time-lapses for the T6-temper with $v_i = 902.8$ m/s, $v_r = 754$ m/s, and $v_i = 614.5$ m/s, $v_r = 395$ m/s, respectively. **(c)** and **(d)** the T7 temper with $v_i = 900.6$ m/s, $v_r = 764$ m/s, and $v_i = 538.3$ m/s, $v_r = 374$ m/s, respectively.

Closer inspection of Figs. 7.9 to 7.12 show that the number of eroded elements in the target plates are higher for simulations with high initial velocities than for simulations with low initial velocities. This can be seen on the lip around the exit holes; the lip is bigger for lower impact velocities suggesting less element erosion. Counting the remaining cubic hexahedra elements in each of the figures confirms this assumption.

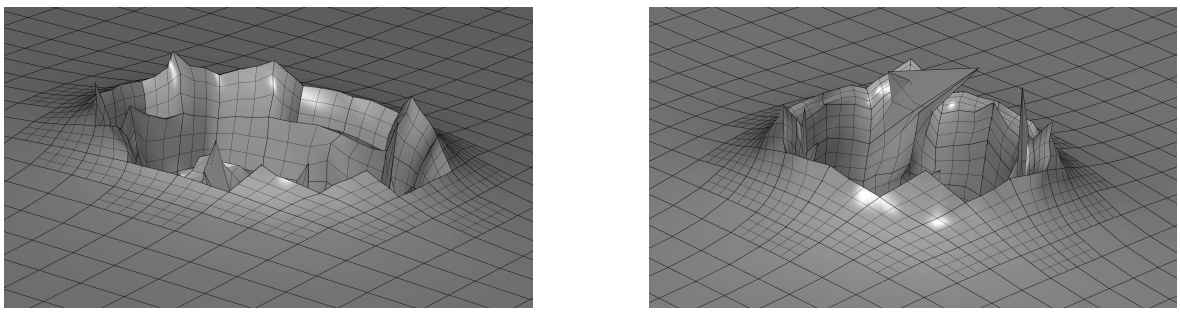

(a) Front AA6070-O **(b)** Back AA6070-O

Figure 7.9: Continues...

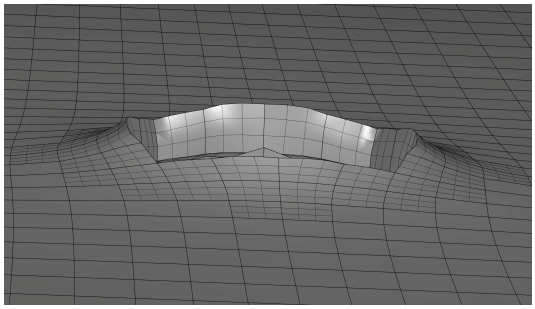

(c) Front AA6070-O

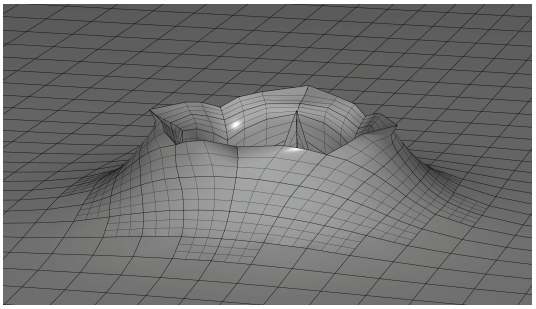

(d) Back AA6070-O

Figure 7.9: Close-ups of entry and exit holes for the O-temper from IMPETUS. In **(a)**-**(b)** $v_i = 899.9$ m/s, $v_r = 834$ m/s, **(c)**-**(d)** $v_i = 377$ m/s, $v_r = 230.5$ m/s.

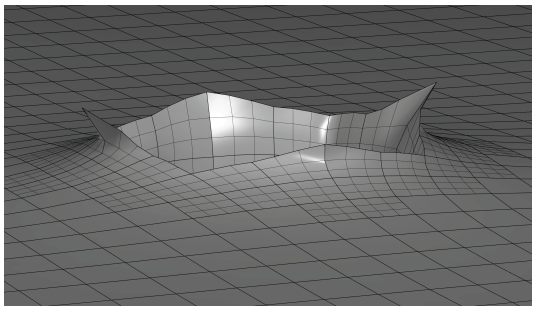

(a) Front AA6070-T4

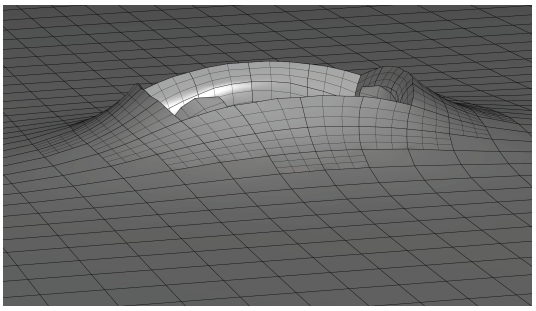

(b) Back AA6070-T4

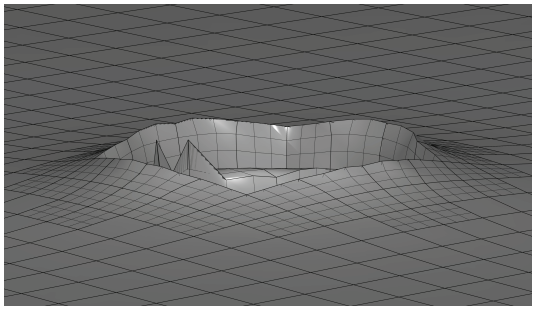

(c) Front AA6070-T4

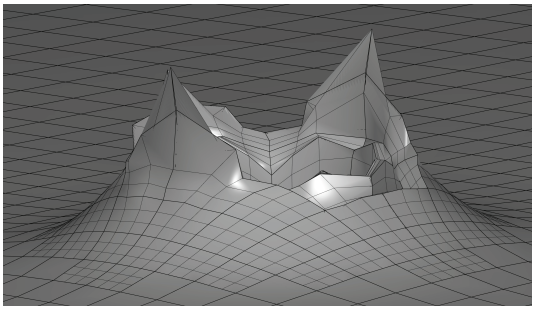

(d) Back AA6070-T4

Figure 7.10: Close-ups of entry and exit holes for the T4-temper from IMPETUS. In **(a)**-**(b)** $v_i = 894.3$ m/s, $v_r = 769$ m/s, **(c)**-**(d)** $v_i = 509.4$ m/s, $v_r = 266$ m/s.

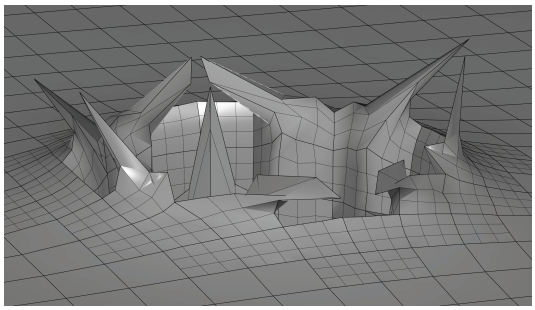

(a) Front AA6070-T6

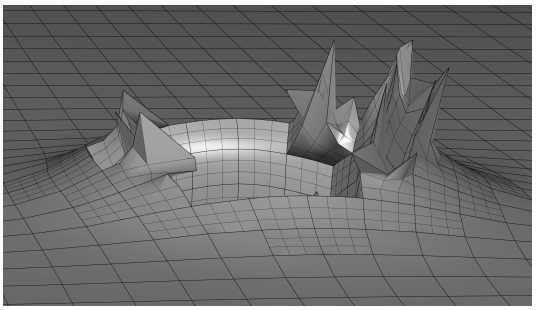

(b) Back AA6070-T6

Figure 7.11: Continues...

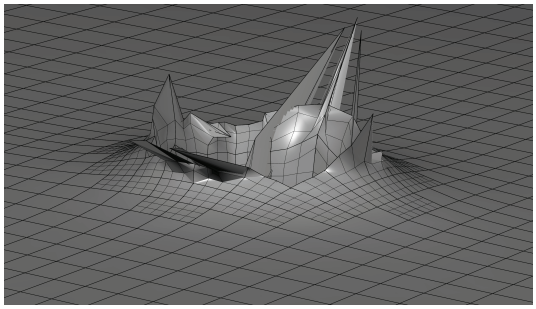

(c) Front AA6070-T6

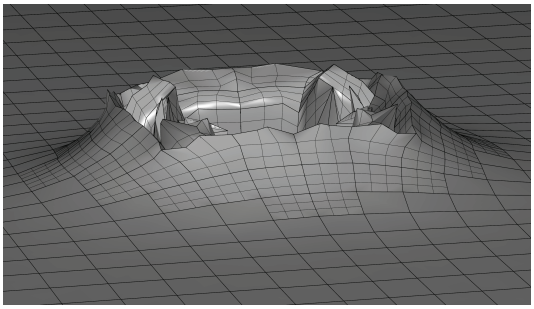

(d) Back AA6070-T6

Figure 7.11: Close-ups of entry and exit holes for the T6-temper from IMPETUS. In **(a)**-**(b)** $v_i = 902.8$ m/s, $v_r = 754$ m/s, **(c)**-**(d)** $v_i = 614.5$ m/s, $v_r = 395$ m/s.

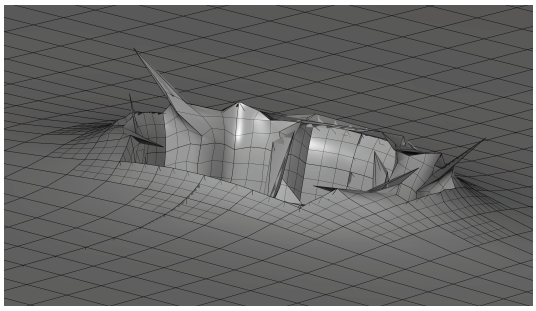

(a) Front AA6070-T7

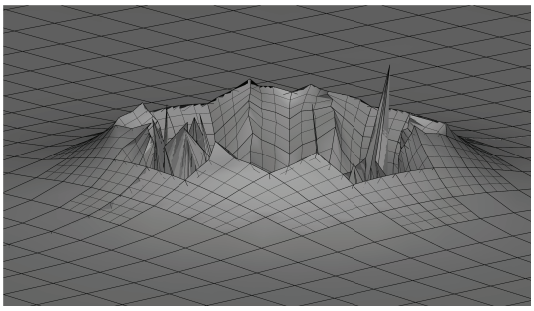

(b) Back AA6070-T7

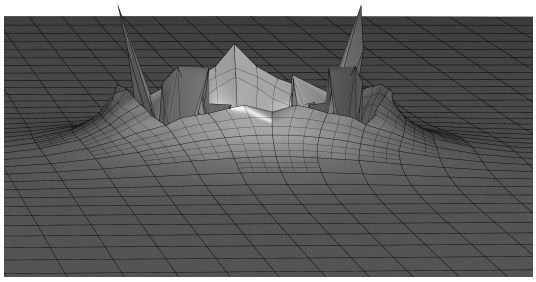

(c) Front AA6070-T7

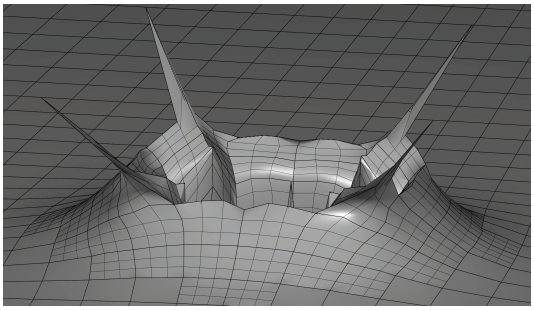

(d) Back AA6070-T7

Figure 7.12: Close-ups of entry and exit holes for the T7-temper from IMPETUS. In **(a)**-**(b)** $v_i = 900.6$ m/s, $v_r = 764$ m/s, **(c)**-**(d)** $v_i = 538.3$ m/s, $v_r = 374$ m/s.

To gain further insight in the processes taking place near the bullet hole, we selected an element close to the cavity for closer analysis. The element is marked in red in Fig. 7.13. Values for damage, plastic strain rate, plastic strain and temperature were found for both high and low initial velocity simulations of the O-temper plates; and compared to each other in Fig. 7.14. We see that all parameters are higher for higher impact velocities, causing the behavior illustrated in Figs. 7.9 to 7.12.

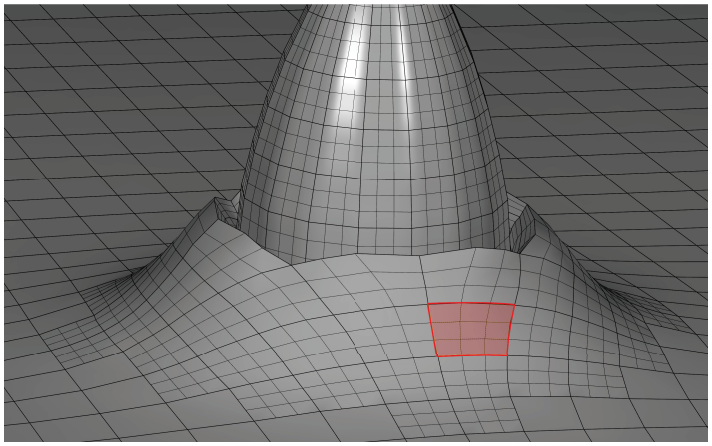

Figure 7.13: Selected element used for comparison of history variables.

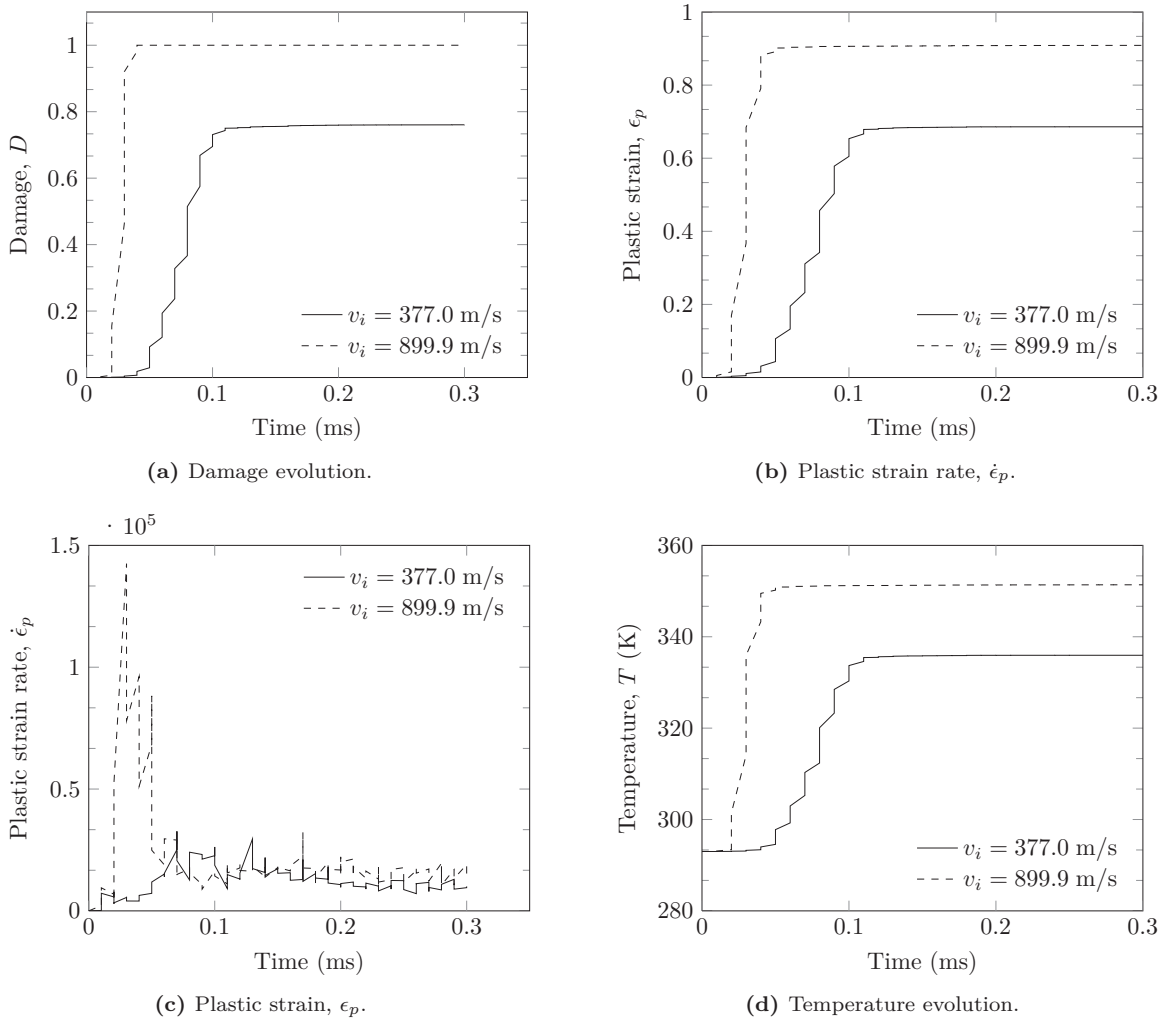

(a) Damage evolution.

(b) Plastic strain rate, $\dot{\epsilon}_p$.

(c) Plastic strain, ϵ_p.

(d) Temperature evolution.

Figure 7.14: Plots of different history variables for the element marked in Fig. 7.13.

Regardless of the energy balance issues and the increased computational time of simulations with the full APM2 bullet; we are interested in checking if IMPETUS can accurately capture the deformation of the APM2 bullet and the peeling of the brass jacket. Analyses were conducted for all tempers with $v_i \approx 900$ m/s, where the post perforation screenshots were compared to the post perforation photos taken from the high-speed videos. The results are given in Fig. 7.15 where it can be seen that IMPETUS captures the deformation and peeling process very well. The brass jacket is completely removed from the steel core after perforation of the T4-, T6- and T7-temper target plates, and it is still attached to the steel core after perforation of the O-temper. This is consistent with the high-speed video images from the experiments. Time-lapse of the perforation process with the complete APM2 bullet is shown in Fig. 7.16, the same timelapse with only the steel core is shown in Fig. 7.17.

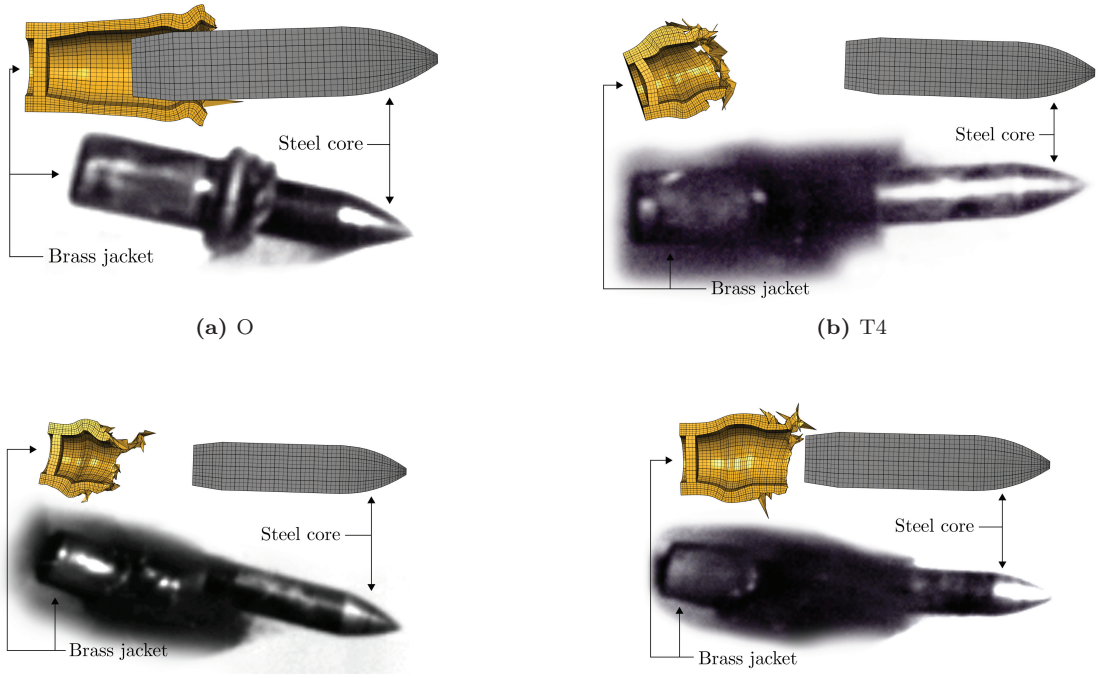

(a) O **(b)** T4

(c) T6 **(d)** T7

Figure 7.15: Comparison of APM2 bullet after perforation. All the pictures and screenshots are from the maximum velocity tests ($v_i \approx 900$ m/s).

The final results from a long series of simulations are presented as ballistic limit curves in Fig. 7.18. We observe that all the analyses are conservative with regards to experimental results, i.e. the ballistic limit velocity is underestimated for each temper. The numerical results are in satisfactory agreement with experimental values, with a maximum deviation from experimentally determined ballistic limit velocity of 17.1% for the T7-temper, and a minimum deviation of 13.5% for the T4-temper, see Table 7.2. All ballistic curves in Fig. 7.18 are curve fitted with the Recht-Ipson model, where $a = 1$ and the values for p obtained from the respective experimental results (Table 4.2).

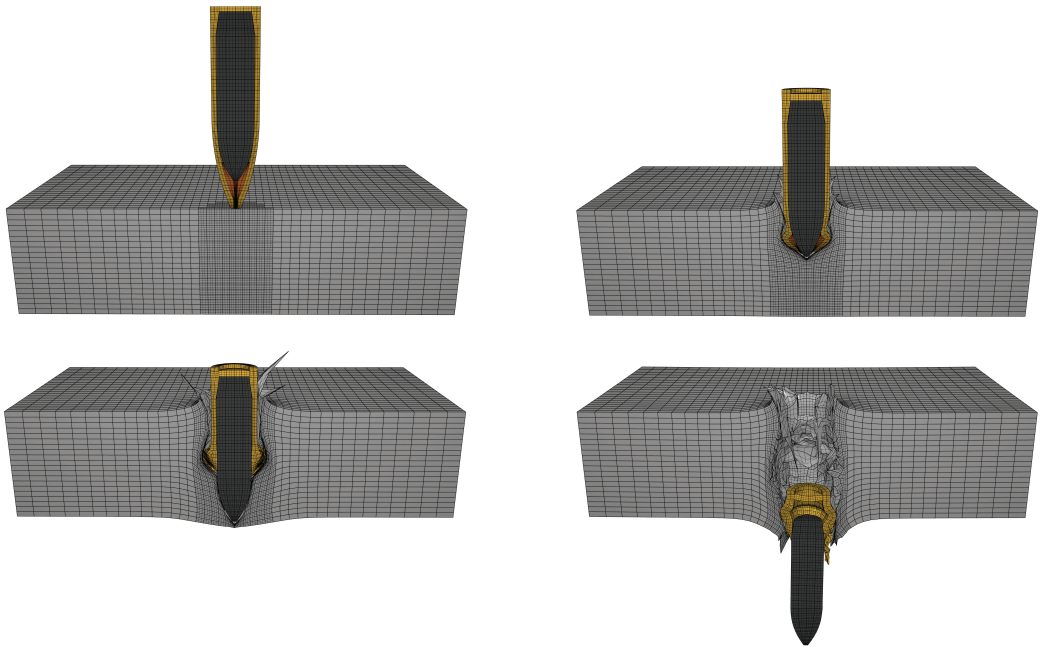

Figure 7.16: Perforation of the AA6070-T6 with the entire bullet, $v_i = 902.8$ m/s and $v_r = 783.5$ m/s.

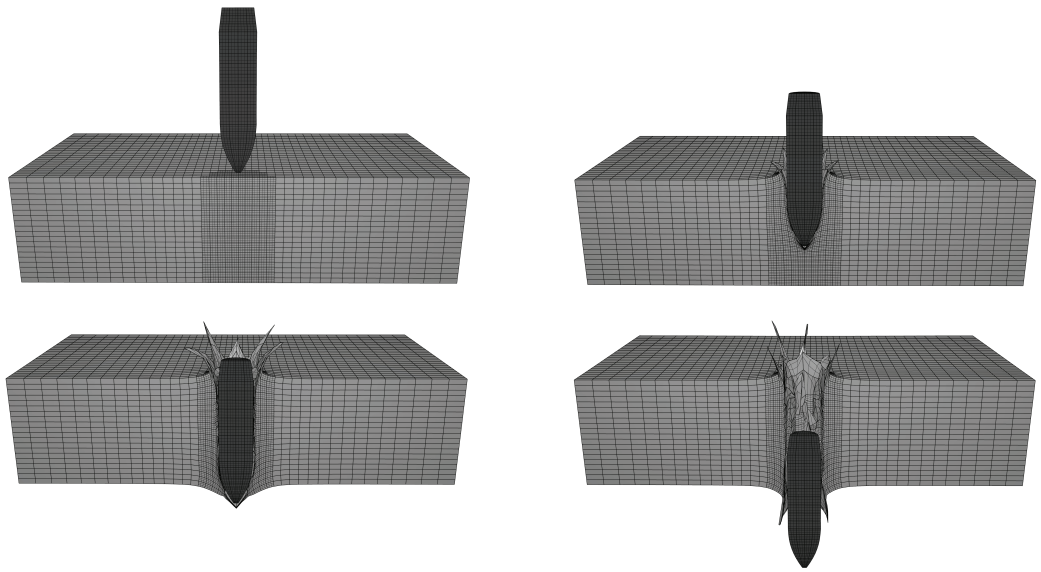

Figure 7.17: Perforation of the AA6070-T6 with the steel-core only, $v_i = 902.8$ m/s and $v_r = 754.0$ m/s.

Table 7.2: v_{bl} for 7.62 mm APM2 steel core projectiles from experiments and IMPETUS-analyses.

Temper	$v_{bl,\mathrm{EXP}}$ (m/s)	$v_{bl,\mathrm{IMPETUS}}$ (m/s)	Deviation
AA6070-O	348.0	296.0	14.9%
AA6070-T4	506.2	438.1	13.5%
AA6070-T6	562.5	480.6	14.6%
AA6070-T7	529.1	438.3	17.1%

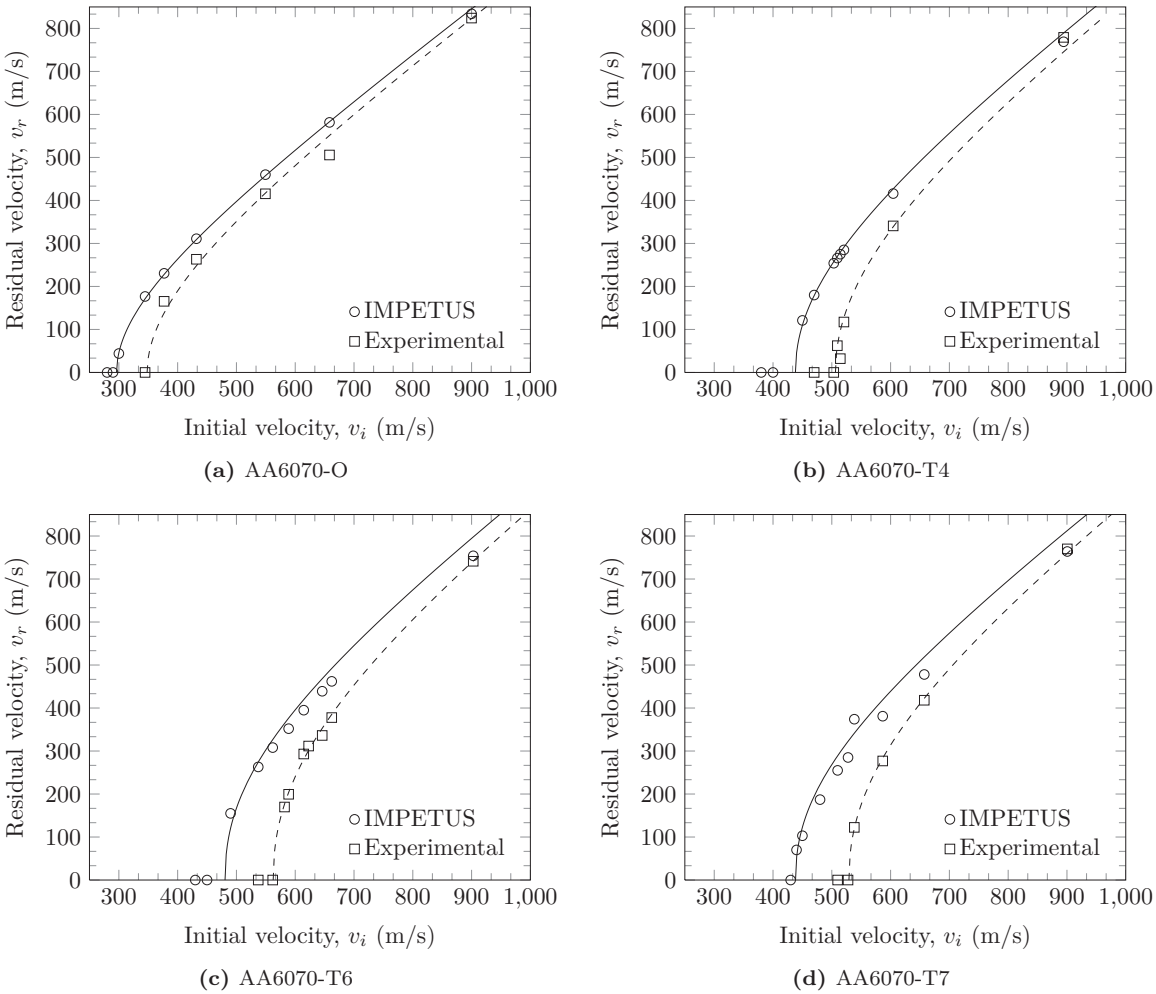

(a) AA6070-O **(b)** AA6070-T4

(c) AA6070-T6 **(d)** AA6070-T7

Figure 7.18: Ballistic limit curves from the numerical simulations in IMPETUS compared to the experimental values,

7.2.4 Sensitivity Studies

The effect of changing input variables like mesh, rigidness of the projectile and material model parameters can in some cases be of numerical significance, and it is important to understand if better solutions are available through different choices. Computational efficiency is also a factor in explicit numerical simulations, and cannot be overlooked. By checking the residual velocities of the bullets after perforation in each simulation, we get an indication of the accuracy of the numerical analyses. A quantitative measure on the computational time on the other hand is hard to obtain seeing that simulations have been run on both CPUs and a GPU. However, a feel of the computer-effort each analysis requires can give an indication of whether the alteration is worth the extra time or not. Unless otherwise specified the sensitivity studies are performed on AA6070-O, with an initial velocity $v_i = 549.3$ m/s. In the ballistic experiments this initial velocity/temper-combination had a residual velocity $v_r = 415.5$ m/s.

Mesh

The bulk of the numerical simulations carried out with the 7.62 mm APM2 bullets were run with 20 cubic hexahedra elements over the thickness, this was also done with satisfactory results by Børvik et al. [23]. To see if a sufficient number of elements are used, we created five meshes in addition to the basic one and simulated impacts on O-temper plates in models that were identical, apart from the mesh. Numbers of elements over the thickness for the five new meshes are: 7, 10, 30, 40 and 50 elements. In Fig. 7.19 the results from the study can be seen, tabulated values in Table 7.3. It appears that the solution has not yet converged completely, although convergence is probably obtained for most practical purposes [14]. Since this is a viscoplastic model implemented in an explicit finite element code with small timesteps, we assume that we have uniqueness in our solutions, i.e. the mesh sensitivity is most likely not pathological [8].

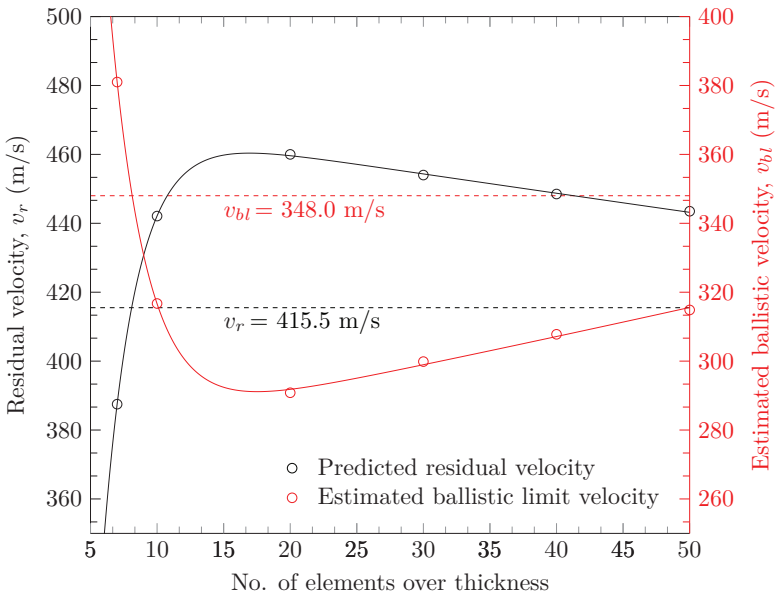

Figure 7.19: The effect of element size on the residual- and ballistic limit velocity on AA6070-O target plates, impacted by 7.62 mm APM2 bullets.

Table 7.3: Numerical results from the mesh sensitivity study on AA6070-O with 7.62 mm APM2 bullets, $v_i = 549.3$ m/s. Experimentally determined values: $v_r = 415.5$ m/s and $v_{bl} = 348.0$ m/s

	Elements over the thickness					
	7	**10**	**20**	**30**	**40**	**50**
v_r (m/s)	387.5	442.1	460.0	454.0	448.5	443.5
v_{bl} (m/s)	381.0	316.7	290.8	299.9	307.8	314.9

Projectile

To avoid numerical problems and to decrease computational time, the reported results in Section 7.2.3 come from simulations run with only the steel core of the APM2 bullet, not including the housing, jacket or actuator (Fig. 7.1b). This is a simplification of the physical problem, and a study was done to see whether this simplification changed the results. To get a basis of comparison, numerical simulations were run for all shots fired on the AA6070-O temper; additionally the maxium velocity tests on the three other tempers were also simulated. The results regarding the O-temper test series can be seen in Fig. 7.20 and the values for the maximum velocity simulations are tabulated in Table 7.4.

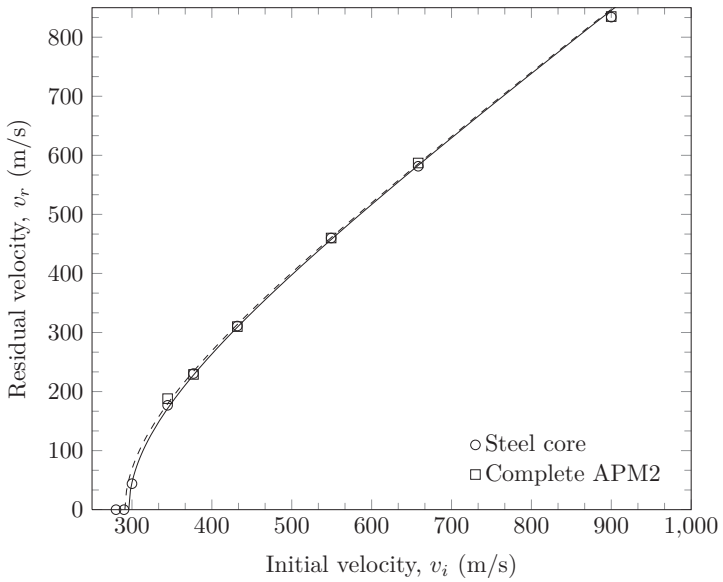

Figure 7.20: Comparison of numerical values of initial and residual velocity for the AA6070-O temper, struck by the complete 7.62 mm APM2 bullets and steel core only.

Table 7.4: Comparison of initial and residual velocity for all tempers, struck by 7.62 mm APM2 bullet. The last column states if modeling the complete bullet is an improvement compared to modeling only the steel core.

Temper	v_i (m/s)	$v_{r,\mathrm{EXP}}$ (m/s)	$v_{r,\mathrm{CORE}}$ (m/s)	$v_{r,\mathrm{COMPLETE}}$ (m/s)	**Improvement?**
AA6070-O	899.9	824.1	834.0	835.0	No
AA6070-T4	894.4	779.2	769.0	785.0	Yes
AA6070-T6	902.8	741.3	754.0	783.5	No
AA6070-T7	900.6	770.1	764.0	794.9	No

The change in residual velocities and ballistic limit velocity are minimal for AA6070-O when including housing, jacket and acutator for the APM2 bullet. The difference for the other tempers is slightly larger, but no significant improvement can be seen. Evidently, modeling the complete APM2 bullet does not justify the increase in computational time.

Rigid Steel Core vs. Johnson-Cook Steel Core

The numerical analyses throughout Section 7.2 features a rigid steel core. A limited study was done to see how incorporating deformability in the bullet would change the results. The Johnson-Cook constitutive relation was appointed to the steel core, and a simulation was run. Material parameters can be found in Table 7.1 and in Børvik et al. [23].

The new simulation with the Johnson-Cook constitutive relation implemented for the steel core resulted in a residual velocity $v_r = 454.0$ m/s, in comparison the rigid steel core had a residual velocity of $v_r = 460.0$ m/s. The measured residual velocity was $v_r = 415.5$ m/s, so in fact the error is reduced by 13.3% when the JC-constitutive relation is included. Accuracy-wise it would be advantageous to include a JC-core.

MJC-Parameters, m and C

Temperature dependency was not a part of any of the experiments, so to investigate the effect of temperature softening: a limited numerical study of the value of the homologous temperature exponent m is carried out (Fig. 7.21b). The results can be seen in Fig. 7.21a. It is evident that m has limited influence on the residual velocity. The biggest difference in residual velocity is between the analyses where $m = 1$ and $m = 2$, the deviation is small: only 0.74%, indicating that penetration problems with adiabatic conditions are almost independent of m, and that $m = 1$ is a sensible choice.

The strain rate sensitivity, C, was not investigated in the material experiments. So the strain rate sensitivities of AA6070-O, -T4, -T6 and -T7 are in this thesis based on experience. Simulations with $C = 0.001$ and $C = 0.01$ were done. Setting $C = 0.001$ in MJC resulted in a residual velocity $v_r = 460$ m/s. A strain rate parameter $C = 0.01$, i.e. a more strain rate dependent material, gave $v_r = 445.4$ m/s. In other words: the error in residual velocity compared to the experiment ($v_r = 415.4$ m/s) was reduced by 32.8% when C was set to 0.01 instead of 0.001, thus results of penetration simulations can be said to be strain rate sensitive. Nevertheless, previous studies have shown that $C = 0.01$ is too high [15, 22, 17, 14], so $C = 0.001$ is used throughout the thesis.

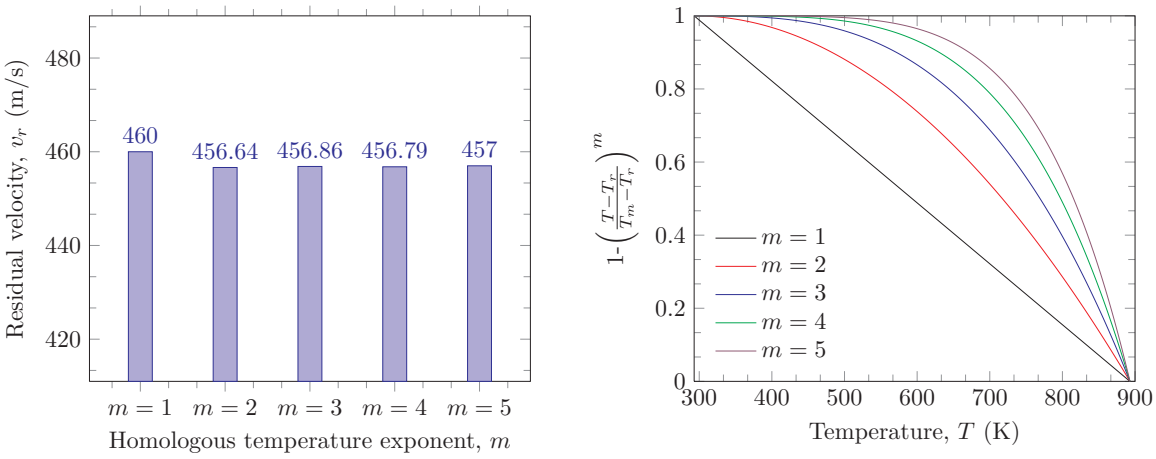

(a) **(b)**

Figure 7.21: Effect of adjusting homologous temperature exponent m. **(a)** shows the results from IMPETUS, **(b)** shows value of temperature softening term as a function of temperature.

Effect of α_T in the Equation of State

As mentioned in Section 7.1: α_T has been neglected. The effect of α_T on the hydrostatic pressure p in the linear equation of state, Eq. (7.1), was investigated by setting $\alpha_T = 2.3 \cdot 10^{-5}$ K^{-1} and simulating AA6070-O with $v_i = 549.3$ m/s. The analysis yielded $v_r = 459$ m/s, compared to $v_r = 460$ m/s when $\alpha_T = 0$. Hence only a minimal improvement can be seen when α_T is included.

Boundary Conditions

The localized behavior of impact allows for ways to save computational resources. On that basis, only a partition of the target plate was modeled in IMPETUS, seen in Fig. 7.1a. Simulations from Børvik et al. [23] showed that the big differences in plate mass and the APM2 bullet made boundary conditions unnecessary. To investigate this assumption a sensitivity study of the different boundary conditions and whether they influence the residual velocity of the rigid steel core of the APM2 bullet was carried out. Results can be seen in Fig. 7.22 and the investigated boundary conditions are shown in Fig. 11.4.

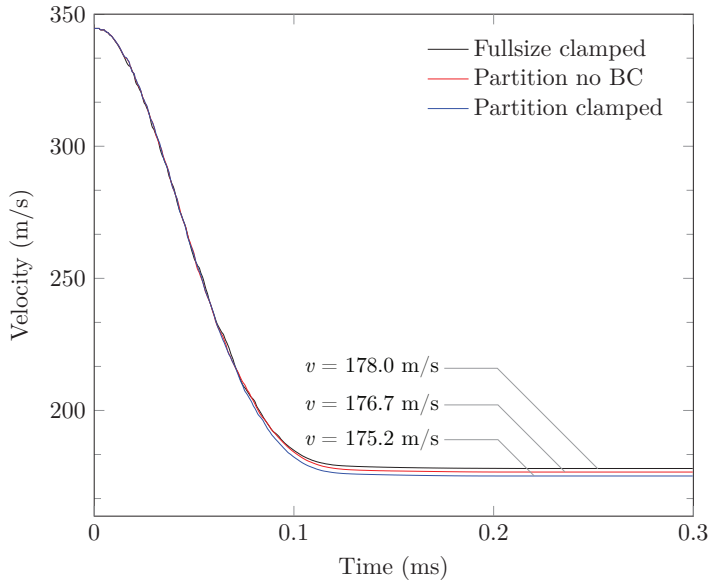

Figure 7.22: Effect of boundary conditions on the velocity of the rigid steel core of the APM2 bullet in IMPETUS.

For the partitioned plate configuration, effects of boundary conditions are seen to be small. Compared to the seemingly most physical numerical model (fullsize plate, clamed top and bottom edges), modeling only a partition of the target plate without boundary conditions gives the best results with a deviation of 0.8%.

Chapter 8

Numerical Analysis: 20 mm Projectiles

8.1 Impacts with 20 mm Blunt Projectiles Analyzed in IMPETUS

The experiments performed with the 20 mm blunt projectiles revealed penetration modes that differed from the ones seen in the experiments carried out with 7.62 mm APM2 bullets and 20 mm ogival projectiles. It is of interest to investigate the ability of the IMPETUS Afea Solver to describe the phenomena seen in the experiments. The results from the 3D-model created for IMPETUS will not only be compared to the experimental values, but also to those from a 2D axisymmetric model created for LS-DYNA (see Section 8.2). No previous simulations from IMPETUS were found regarding shear banding and plugging; so considerable time was spent creating the model and making it run smoothly.

8.1.1 Procedure

The mesh of the plate and projectile were both made in Abaqus CAE since IMPETUS does not feature a pre-processor. Alteration of the mesh was done in MATLAB in order to convert the text file into a format supported by IMPETUS (see script in Appendix G). The mesh used in the analyses can be seen in Fig. 8.1. Because the expected failure mode in the blunt nose simulations is shear banding, the average element size in the area of interest has to be small. The mesh features 60 elements over the thickness, i.e. $\Delta x = 0.33$ mm while $\Delta y = \Delta z = 0.5$ mm. Half the plate is modeled, and a symmetry-plane is introduced to represent the second half of the plate. With the large number of elements present in the analyses, the computational effort is large, hence only a small number of analyses are run. We have recreated the experimental data-series with the same intitial velocities, additional simulations with 200 m/s are also carried out.

The projectile is modeled as rigid. For the plate the material card `*MAT_PWL` with MJC and Voce-hardening is used; the material parameters are the same as those used in Section 7.2. The Cockcroft-Latham fracture criterion is activated in all the analyses, and elements are mainly eroded on the basis of Cockcroft-Latham material failure. The `*PROP_THERMAL`-card is active, meaning that the thermal properties of the aluminium are taken into account; the card ensures that the yield stress becomes zero when the melting temperature is reached. It must be mentioned that to ensure numerical stability elements on the verge of being inverted are eroded as well.

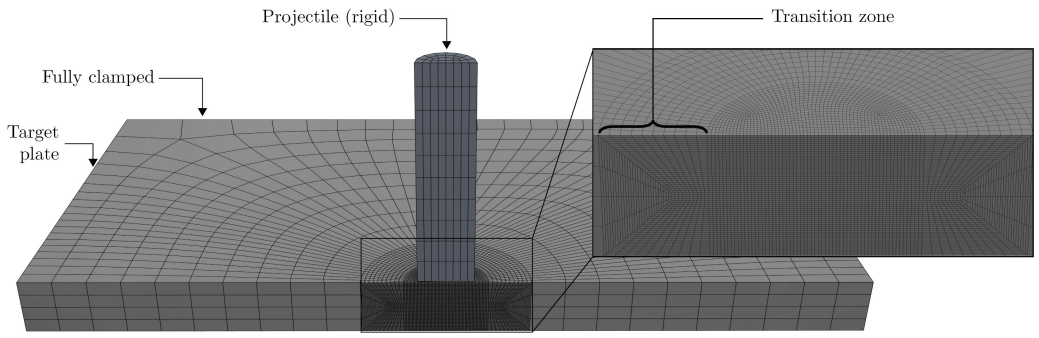

Figure 8.1: Mesh of target plate and blunt projectile used in IMPETUS.

8.1.2 Results

From Fig. 8.5 it is clear that the residual velocities obtained from the 3D-simulations in IMPETUS are very close to the experimental results. The ballistic limit curves are calculated by setting $p = 2$ and a equal to the experimentally determined value. The deviation in ballistic limit velocity is less than 1% for T4 and T6, and just about 5% for T7. The O-temper however, deviates by 20% (Table 8.1). Fig. 8.6 show that the shear zone propagates ahead of the projectile as expected. The O-temper gets a large plastic zone, while the three other tempers have smaller plastic zones. The figures are comparable, fracture-mode-wise, to the time-lapses in Fig. 5.12. It can also be seen that the plugs for the four tempers, seen in Fig. 8.3, get shapes that resemble the real plugs in Fig. 5.6b. The plug ejected from the O-temper in IMPETUS has a flattened shape, consistent with the real plug, T6 and T7 give plugs where some of the material towards the backside of the plate is missing, also consistent with the experimental results.

Fig. 8.4 gives a good indication of how well the simulations can capture the fragmentation observed in the testing. Practically no fragmentation is seen in AA6070-O, some small to medium fragments can be seen in T4 and T7, and many large fragments are seen in T6. Comparing this to the high-speed video images from the experiments (Fig. 5.12) show that the 3D-simulations capture fragmentation to some extent. The full penetration process for the T6-temper with $v_i = 200$ m/s can be seen in Fig. 8.2.

Although the mesh sensitivity of the 3D-simulations with blunt projectiles is not investigated in this theis, a study by Børvik et al. [22] have shown that the results are mesh dependent, and the promising results shown in this section may be somewhat coincidental. Further comments on this can be found in Chapter 12.

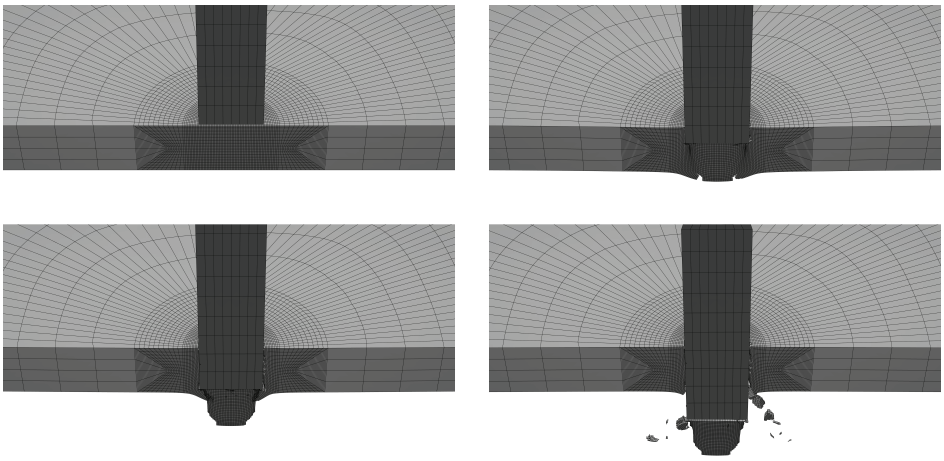

Figure 8.2: Illustration of the penetration process for AA6070-T6 with $v_i = 200$ m/s and $v_r = 111.5$ m/s.

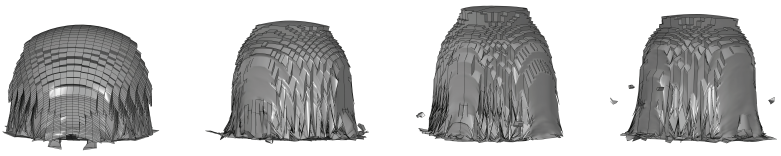

Figure 8.3: Post-perforation screenshots of the plugs ejected from the plates in IMPETUS, $v_i = 200$ m/s in all cases.

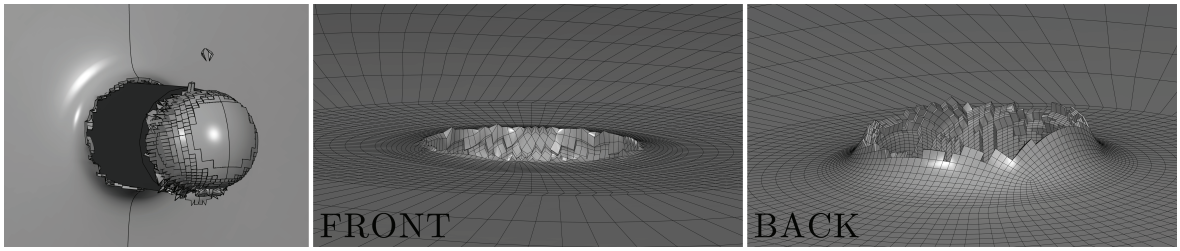

(a) AA6070-O, $v_i = 186.5$ m/s, $v_r = 129.4$ m/s.

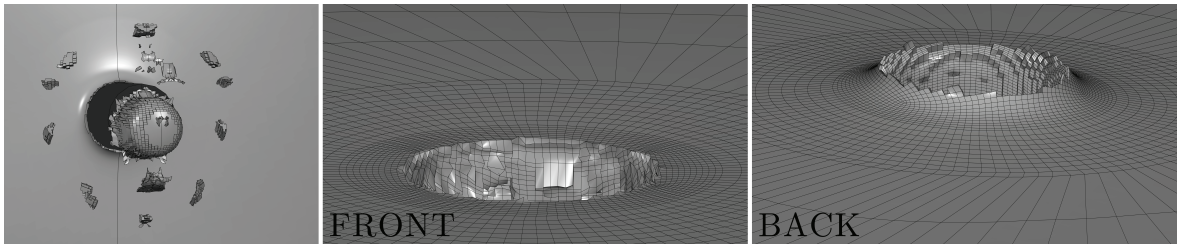

(b) AA6070-T4, $v_i = 196.5$ m/s, $v_r = 89.0$ m/s.

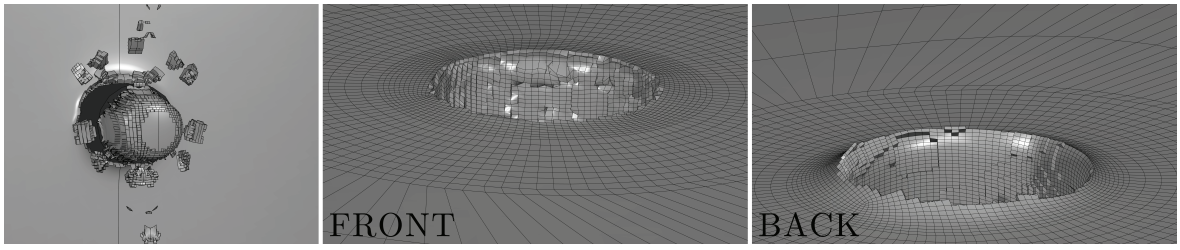

(c) AA6070-T6, $v_i = 198.9$ m/s, $v_r = 110.3$ m/s.

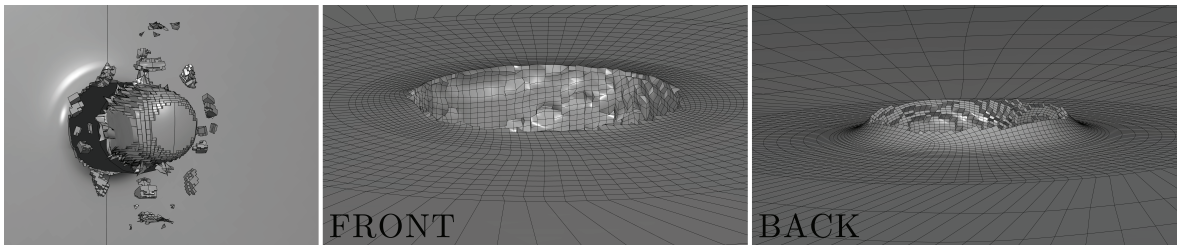

(d) AA6070-T7, $v_i = 197.2$ m/s, $v_r = 112.3$ m/s.

Figure 8.4: Screenshots from IMPETUS reflected about the symmetry-axis showing post-perforation images, the entry holes and the exit holes respectively.

Table 8.1: v_{bl} for 20 mm blunt projectiles from experiments and IMPETUS-analyses.

Temper	$\boldsymbol{v_{bl,\mathrm{EXP}}}$ (m/s)	$\boldsymbol{v_{bl,\mathrm{IMPETUS}}}$ (m/s)	**Deviation**
AA6070-O	157.0	124.7	20.6%
AA6070-T4	175.7	174.5	0.7%
AA6070-T6	162.0	161.5	0.3%
AA6070-T7	166.0	157.5	5.1%

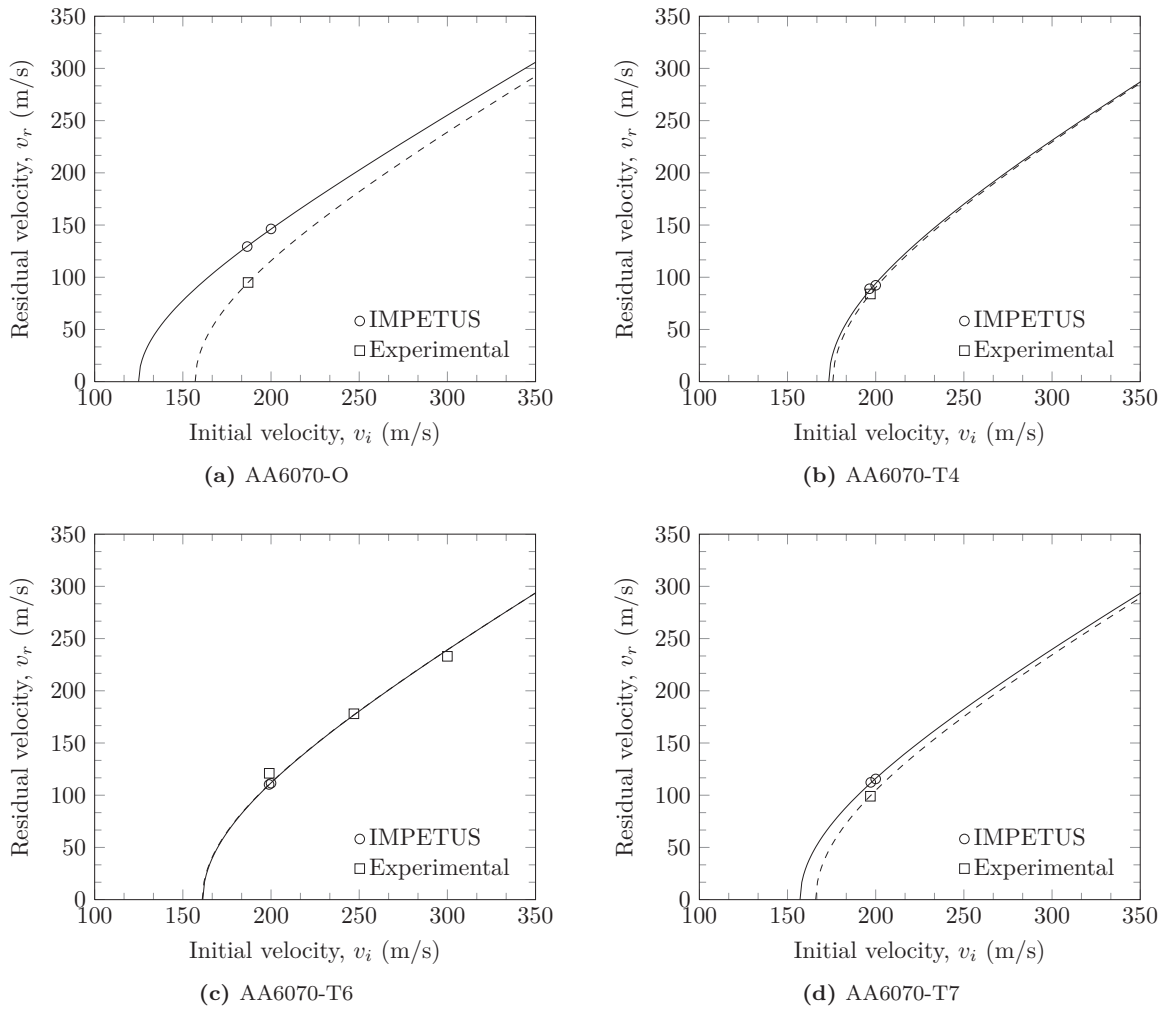

(a) AA6070-O

(b) AA6070-T4

(c) AA6070-T6

(d) AA6070-T7

Figure 8.5: Ballistic limit curves for blunt projectiles from IMPETUS compared to experimental values.

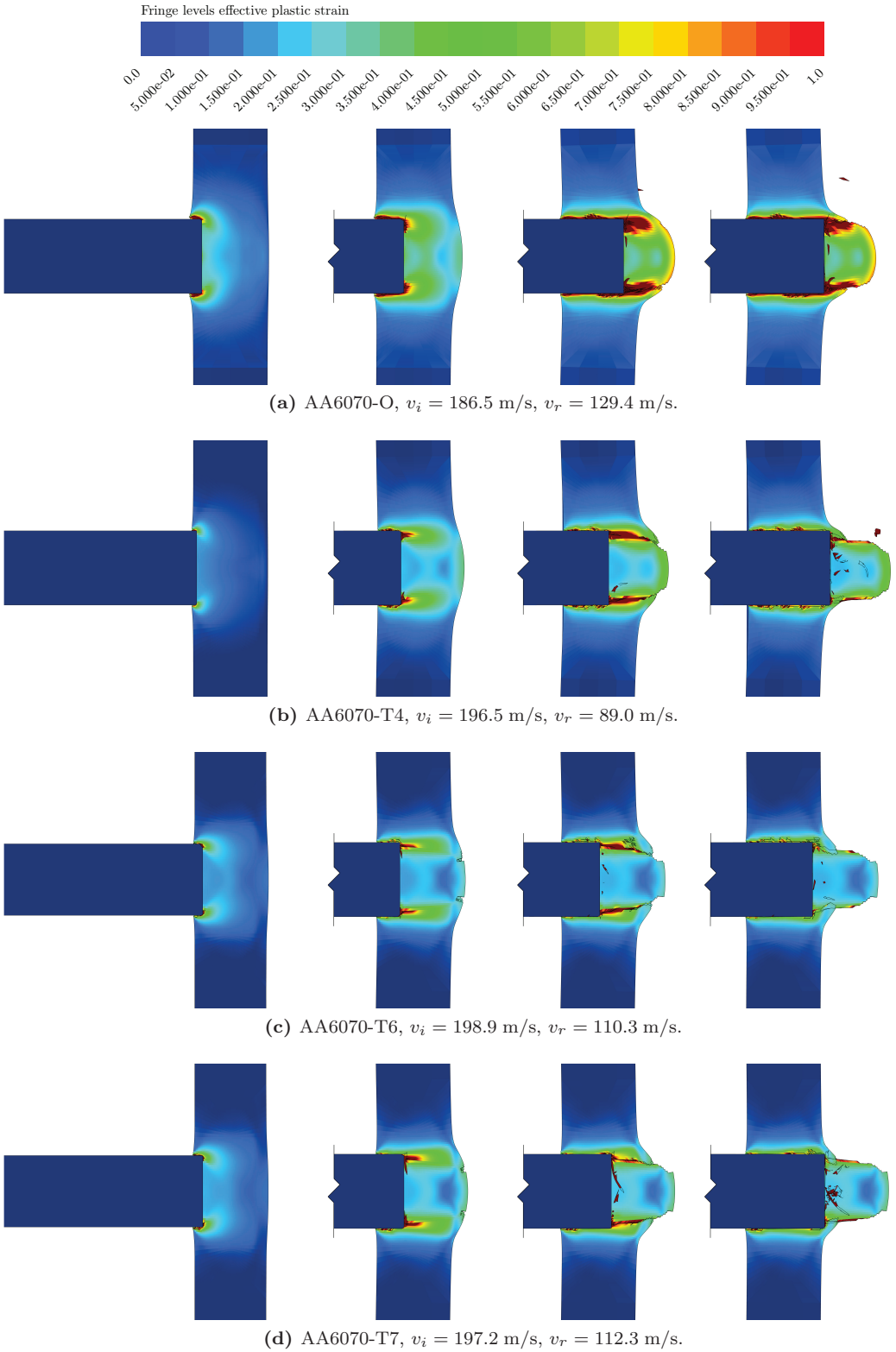

(a) AA6070-O, $v_i = 186.5$ m/s, $v_r = 129.4$ m/s.

(b) AA6070-T4, $v_i = 196.5$ m/s, $v_r = 89.0$ m/s.

(c) AA6070-T6, $v_i = 198.9$ m/s, $v_r = 110.3$ m/s.

(d) AA6070-T7, $v_i = 197.2$ m/s, $v_r = 112.3$ m/s.

Figure 8.6: Numerical simulations done with the IMPETUS Afea Solver, 20 mm blunt projectiles and 20 mm AA6070 plates.

8.2 Impacts with 20 mm Blunt Projectiles Analyzed in LS-DYNA

The amount of computational resources needed to analyze a plugging problem in 3D is large, so for completeness of the numerical study and to provide grounds of comparison to the IMPETUS simulations, previously tested axisymmetric computer models are used.

8.2.1 Procedure

The model used to analyze the ballistic experiments is adapted from a paper dealing with structural impact of AA7075-T651 plates by Børvik et al. [22]. Some keywords have been altered to fit the materials and the velocities needed for this thesis. This means that while maintaining the model geometry from the mentioned paper, the material card `*MAT_107` has been changed to the calibrated values in Table 6.2, and the initial velocity has been changed between numerical experiments in the card `*INITIAL_VELOCITY`. The mesh can be seen in Fig. 8.7.

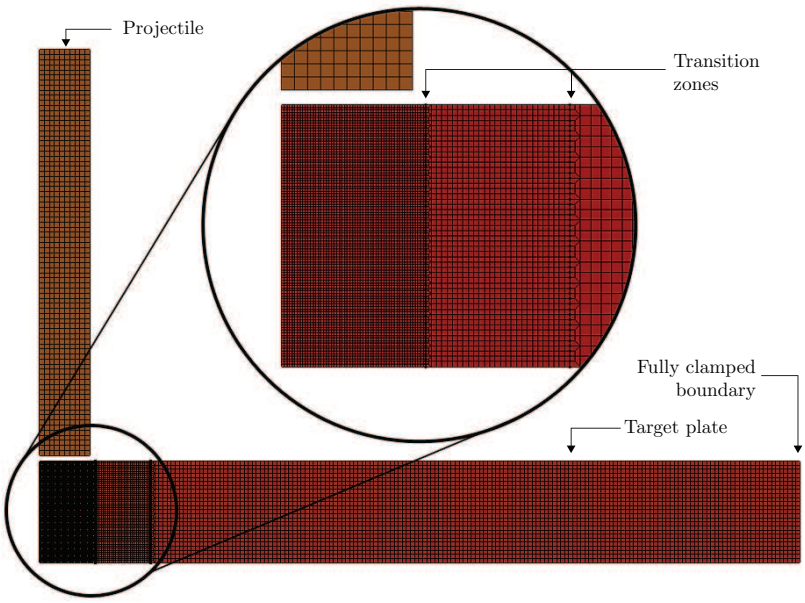

Figure 8.7: The axisymmetric model taken from Børvik et al. [22] used to simulate ballistic impact of blunt projectiles on the aluminium plates.

The model is axisymmetric and features four-node elements with one integration point, no friction, penalty formulated contact and stiffness-based hourglass control. In the impact region the model has quadratic elements with length 0.2 mm which gives 100 elements over the thickness. Towards the edges the mesh is gradually coarsened, the boundary is fully clamped.

Some things are worth noticing when it comes to an axissymmetric model like this: Firstly, the boundary conditions are not satisfied. In the ballistic experiments the top and bottom edges of the square target plates are clamped, but in the axissymmetric numerical analyses the plates are circular and completely clamped. However, some of the analyses reported in Table 8.2 were run with radiuses of both $r = 15$ mm and $r = 25$ mm. No deviation in residual velocity was observed. The analyses confirm the assumption that the response of a thin plate when impacted by a blunt nose projectile is very local. Secondly, an axissymmetric model will only be able to describe an axissymmetric response, so when one element fails (loses its ability to resist forces and movement), the response can be compared to a ring of failed elements in a 3D-model.

Some things are worth noticing when it comes to an axissymmetric model like this: Firstly, the boundary conditions are not satisfied. In the ballistic experiments the top and bottom edges of the square target plates are clamped, but in the axissymmetric numerical analyses the plates are circular and completely clamped. However, some of the analyses reported in Table 8.2 were run with radiuses of both $r = 15$ mm and $r = 25$ mm. No deviation in residual velocity was observed. The analyses confirm the assumption that the response of a thin plate when impacted by a blunt nose projectile is very local. Secondly, an axissymmetric model will only be able to describe an axissymmetric response, so when one element fails (loses its ability to resist forces and movement), the response can be compared to a ring of failed elements in a 3D-model.

Initially, the experiments from Chapter 5 are recreated, enabling a comparison of the numerical results to the real values. Subsequently, more simulations are done mostly at lower velocities to get enough results to create a reliable ballistic limit curve.

To confirm that the simulations are physically viable, energy balance checks have to be done. In LS-DYNA the checks are done by extracting the kinetic-, internal-, hourglass-, sliding-, and total energy from global ASCII-data named `glstat`. Two different plots are shown in Figs. 8.8a and 8.8b. It is seen that the kinetic and internal energies dominate the response while the sliding energy is close to zero. In the figures the hourglass energy is also very small, indicating that the energy lost in spurious modes because of the one-point underintegration is negligible [26]. In general the total energy gain for the analyses performed does not exceed 0.050%. For Figs. 8.8a and 8.8b the respective energy ratios are 1.00035 and 1.00030, giving total energy gains of 0.035% and 0.030%, meaning that the energy balances are satisfactory.

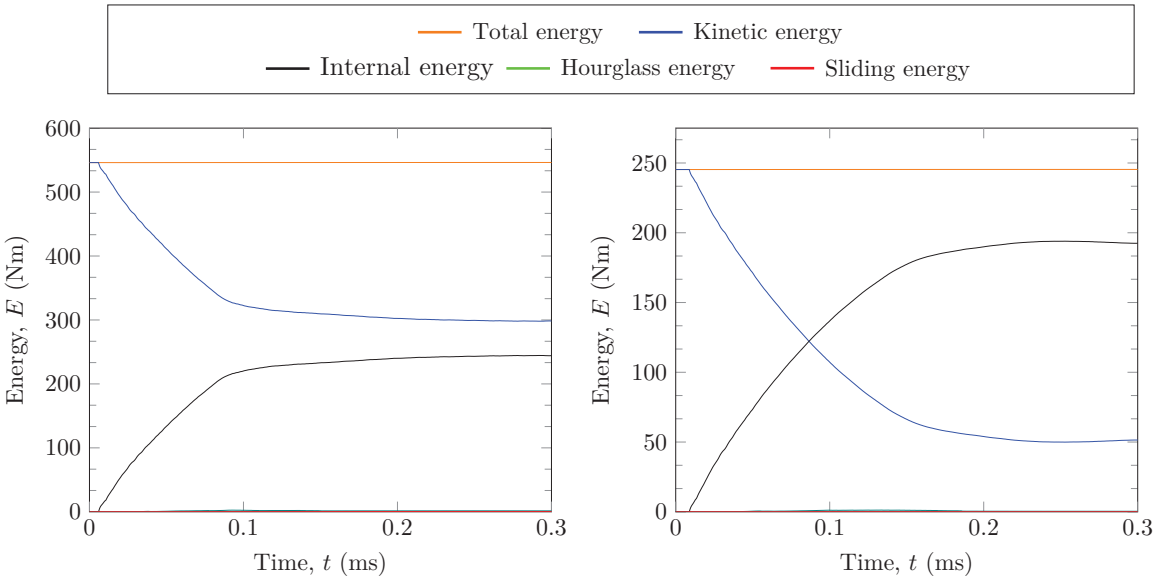

(a) $v_i = 186.5$ m/s **(b)** $v_i = 125$ m/s

Figure 8.8: Energy balance plots for the blunt projectile striking the O-temper with different initial velocities.

8.2.2 Results

Every initial/residual-velocity pair obtained from LS-DYNA that is directly comparable to experimental values is tabulated in Table 8.2 and plotted in Fig. 8.9 with all the numerical results. The ballistic limit velocity should in theory be calculated by averaging the highest velocity that gives embedment

and the lowest velocity providing penetration. However, due to the somewhat limited number of predictions done for each temper, v_{bl} is chosen as the value between the highest embedment velocity and lowest penetration velocity that minimizes the mean square error taken between the datapoints and the Recht-Ipson model stated in Eq. (2.20). Plastic deformation of the projectile is considered to be negligible, so $p = 2$ [22]. The factor that decides the slope of the curve at high velocities, a, is calculated from the experimental values by using the measured mass of the plug (m_{pl}) by using the following relationship: $a = \left(\frac{m_p}{m_p+m_{pl}}\right)$.

A mesh size sensitivity study of the configuration with the blunt projectiles (for LS-DYNA) has not been carried out in this thesis, albeit it has been done in Børvik et al [22]. Here it was found that the axisymmetric model experienced increased capacity when coarsening the mesh, meaning that the analyses run are less conservative when run with larger elements. It is unclear if this capacity increase is from a change in the failure mode. In any case the 2D axisymmetric mesh is sensitive to element size.

Table 8.2: Results from LS-DYNA and the experimental data for the corresponding impact test.

Temper	**Test**	$\boldsymbol{v_i}$ (m/s)	$\boldsymbol{v_r}$ (m/s)	$\boldsymbol{v_{r,\mathrm{EXP}}}$ (m/s)
AA6070-O	1	186.5	132	95.3
AA6070-T4	1	196.5	127	84.3
AA6070-T6	1	300.0	236	232.8
	2	250.0	188	177.8
	3	198.9	134	120.9
AA6070-T7	1	197.2	135	98.6

Screenshots from the numerical simulations are shown in Fig. 8.10. For all tempers the failure process begins around the circumference of the blunt projectile when shear bands initiates (shown in red in the figures). The O-, and T4-tempers get relatively clean fractures and plugs without mass-loss. While the T6- and T7-tempers eject plugs and experience some fragmentation on the rear side in the numerical analyses. The fracture shape of the O-, T4- and T6-tempers can, during penetration, be recognized in the experiments, but the T7-temper seems too brittle, i.e. it resembles the T6 more than the T4, as it does in the experiment and may explain why the numerical v_{bl} for T7 is low compared to the other tempers, see Table 8.3.

The estimated ballistic limit velocities obtained from LS-DYNA are from 23% to 33% lower than the ones calculated from the experimental results, thus we underestimated the ballistic performance of the aluminium plates. Taking into consideration the complexity of the problem and the simplicity of the axisymmetric model, some deviation from the experimental values is expected. In a previously mentioned study performed by Børvik et al. [22] the same model was used, and the results when simulating impacts with blunt projectiles also underestimated the ballistic limit velocity by about 20%. The plates do not dissipate enough energy to stop the bullet. As mentioned for the T7-temper this can come from premature fragmentation, while for the O- and T4-tempers it can be due to the lack of a hydrostatic pressure zone near the rear of the plate after impact.

Table 8.3: v_{bl} for blunt projectiles from experiments and LS-DYNA-analyses.

Temper	$\boldsymbol{v_{bl,\mathrm{EXP}}}$ (m/s)	$\boldsymbol{v_{bl,\mathrm{LS\text{-}DYNA}}}$ (m/s)	**Deviation**
AA6070-O	157.0	115.0	26.8%
AA6070-T4	175.7	135.8	22.7%
AA6070-T6	162.0	121.3	25.1%
AA6070-T7	166.0	111.5	32.8%

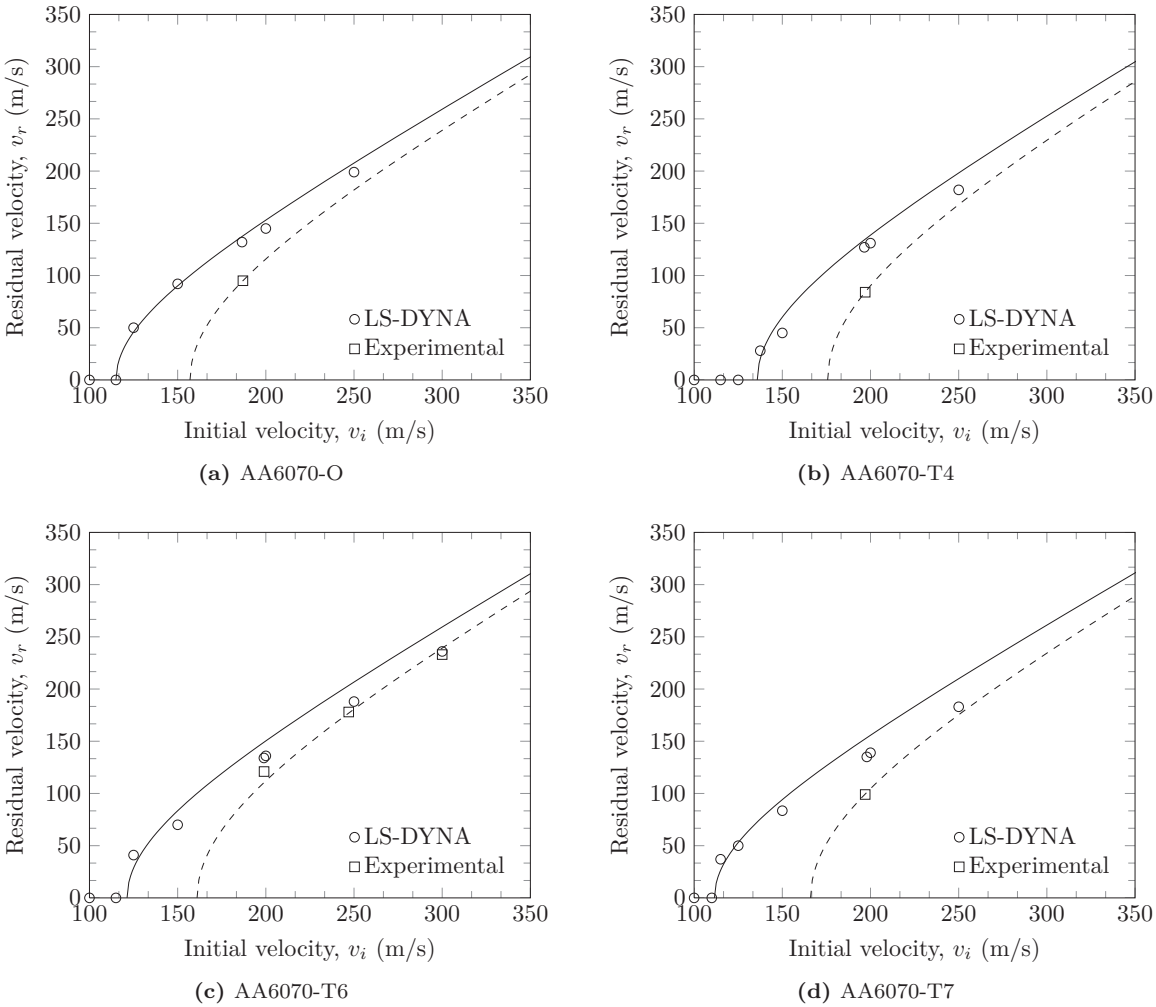

(a) AA6070-O **(b)** AA6070-T4

(c) AA6070-T6 **(d)** AA6070-T7

Figure 8.9: Ballistic limit curves for blunt projectiles from LS-DYNA compared to experimental values.

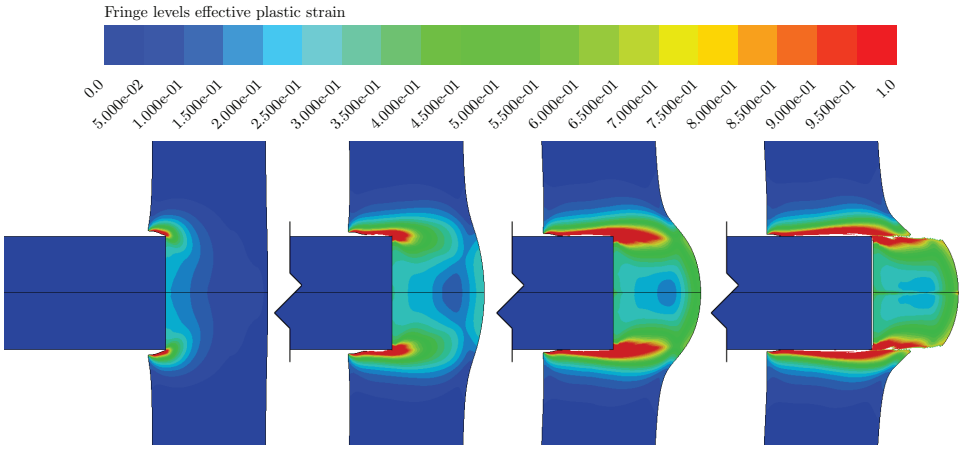

(a) O-temper: $v_i = 200$ m/s, $v_r = 145$ m/s.

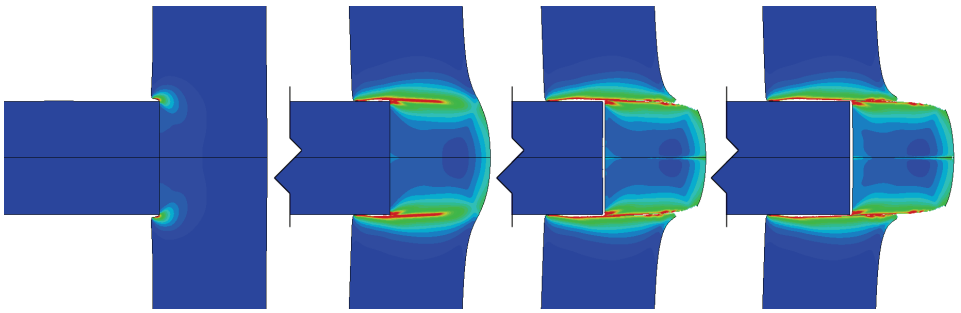

(b) T4-temper: $v_i = 200$ m/s, $v_r = 131$ m/s.

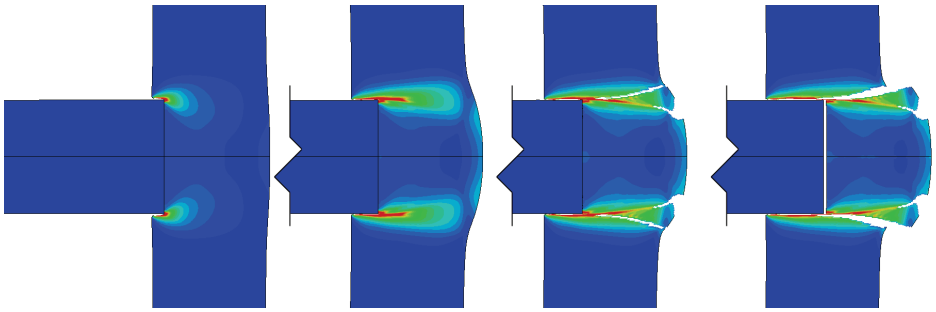

(c) T6-temper: $v_i = 200$ m/s, $v_r = 136$ m/s.

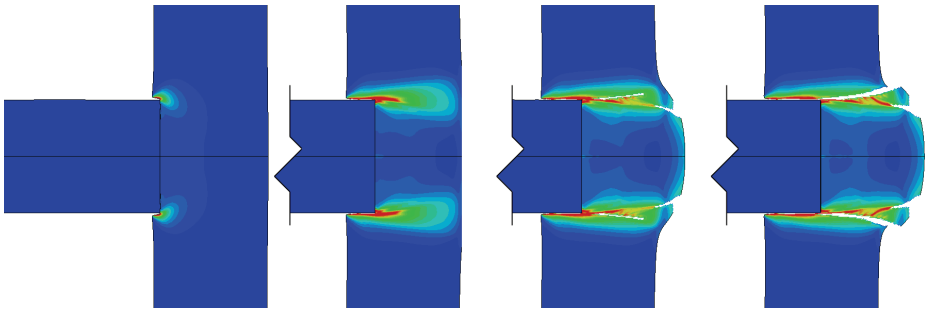

(d) T7-temper: $v_i = 200$ m/s, $v_r = 139$ m/s.

Figure 8.10: Numerical simulations done with an axisymmetric LS-DYNA model. 20 mm blunt projectiles, 20 mm AA6070 plates. The model has been reflected about a plane and rotated 90° counterclockwise to better visualize the results.

8.3 Impacts with 20 mm Ogival Projectiles Analyzed in IMPETUS

In this section, the goal is to recreate the ballistic experiments conducted with 20 mm ogival projectiles. Although the shape is comparable to the 7.62 mm APM2 bullets, the two projectile-types exhibit completely different sizes and weights, and thus the ballistic limit velocities are very different as already proven in Chapters 4 and 5.

8.3.1 Procedure

The input files used for these simulations are adapted from the input files created for the 7.62 mm bullets in Section 7.2. An assessment of the projectile's increased size and weight compared to the APM2 bullets led to a conclusion that a model featuring the entire target plate is needed for simulations with 20 mm ogival projectiles. The mesh can be seen Fig. 8.11; Abaqus CAE was used to create the geometry and generate the mesh. In the simulations carried out on APM2 bullets and blunt projectiles to save computational time only half the target plate was modeled, implementing the symmetry-plane through the `*BC_SYMMETRY` card in IMPETUS.

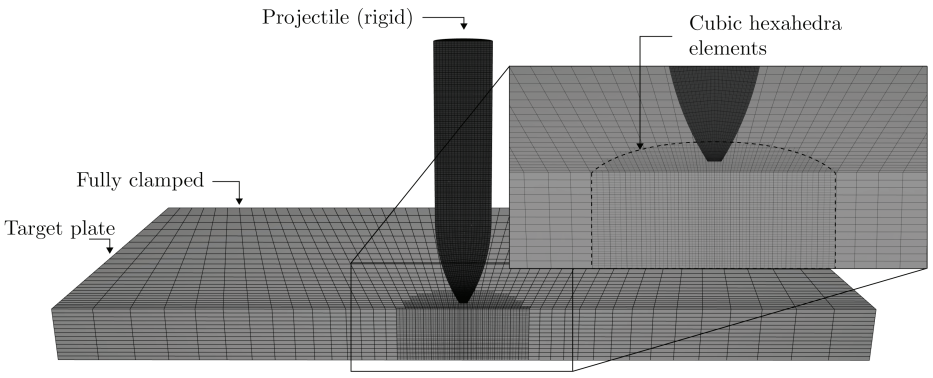

Figure 8.11: Mesh used in IMPETUS Afea analyses.

The bulk of the plate is modeled with 3D linear solid elements where the size of the elements gradually increase towards the periphery. In the impact zone itself the elements are cubic hexahedra and 13 cubic elements are chosen over the target plate thickness. Additionally, an analysis was also run with the same mesh used in Section 8.1, i.e. 60 3D linear solid elements over the thickness to see if a more physical fracture shape could be obtained.

An energy plot taken from the analysis of AA6070-T6 is included in Fig. 8.12 and the energy balance is considered satisfactory, as was also the case for the three other tempers.

8.3.2 Results

The first simulations we conducted with the IMPETUS Afea Solver did not look physically viable (see Fig. 8.13). By inspecting the time-lapse it can be seen that the plate encapsulates the projectile as the projectile exits the plate and that some plate material breaks the projectile-geometry boundary, indicating a serious contact problem. This has been seen before in other finite element codes and is a well-known numerical error that occurs when the projectile-tip-angle is extremely acute [14]. Seeing that the model was made with the exact geometry seen in Fig. 5.3, we had introduced a singularity in the mesh at the tip of the projectile, inevitably leading to contact problems in the simulation. We suspect that since the tip does not have a surface area of its own, contact between projectile and target

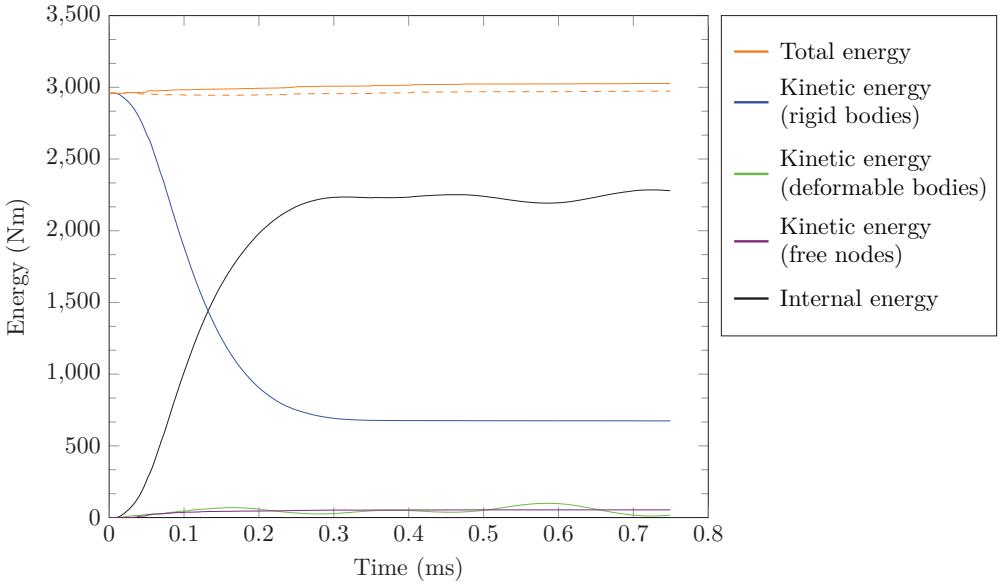

Figure 8.12: Energy balance of the AA6070-T6 temper, with inital velocity $v_i = 247.0$ m/s, and $v_r = 117.92$ m/s. The dashed line is the total energy without eroded kinetic energy.

plate cannot be established in a satisfactory way.

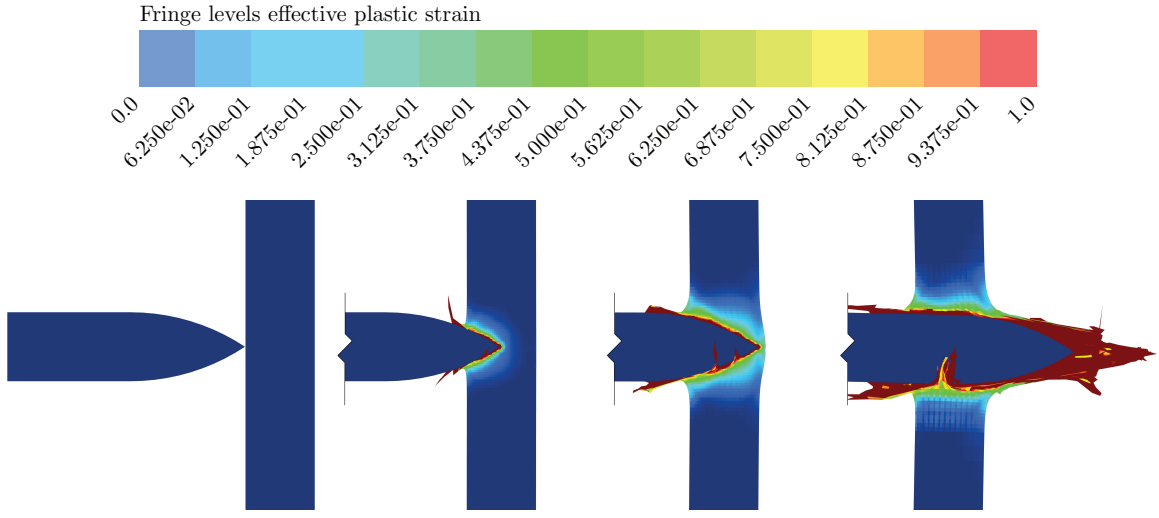

Figure 8.13: Time-lapse of perforation process of AA6070-T6, showing the problems with the initial projectile geometry. $v_i = 247.0$ m/s and $v_r = 152.0$ m/s.

The contact problem was easily fixed by flattening the tip of the 20 mm ogival projectile. The resulting time-lapses are shown in Fig. 8.14, in which all fractures seem somewhat ductile. However, the zone that experiences excessive plastic strain is bigger and evolves quicker and smoother when W_c is large (O- and T4-temper). Figs. 8.15 to 8.18 shows the entry- and exit holes of the different aluminium target plates where holes for AA6070-T6 and AA6070-T7 look less conformal than the holes for AA6070-O and AA6070-T4 indicating a more violent fracture.

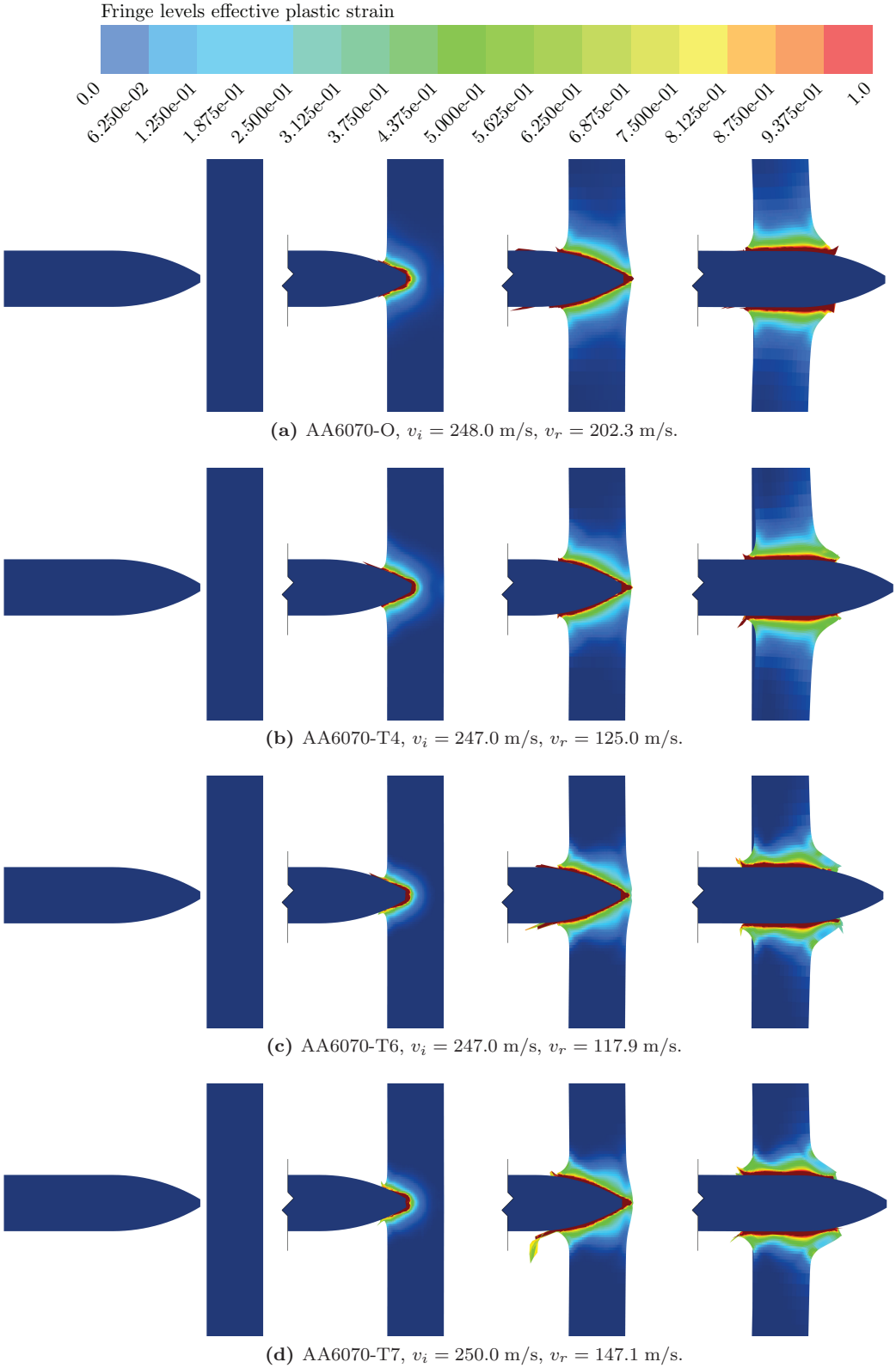

(a) AA6070-O, $v_i = 248.0$ m/s, $v_r = 202.3$ m/s.

(b) AA6070-T4, $v_i = 247.0$ m/s, $v_r = 125.0$ m/s.

(c) AA6070-T6, $v_i = 247.0$ m/s, $v_r = 117.9$ m/s.

(d) AA6070-T7, $v_i = 250.0$ m/s, $v_r = 147.1$ m/s.

Figure 8.14: Numerical simulations done with the IMPETUS Afea Solver, 20 mm ogival projectiles and 20 mm AA6070 plates. The colors are fringe levels of plastic strain.

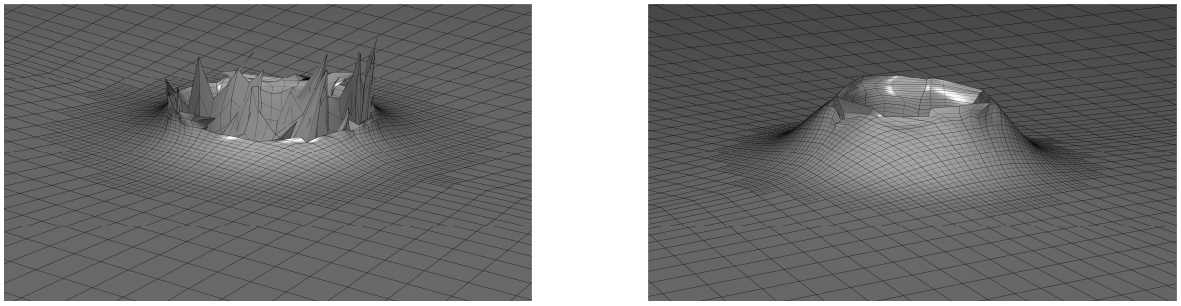

(a) Front **(b)** Back

Figure 8.15: Close-ups from IMPETUS Afea of entry and exit holes for AA6070-O aluminium target plates, $v_i = 248.0$ m/s, $v_r = 202.3$ m/s.

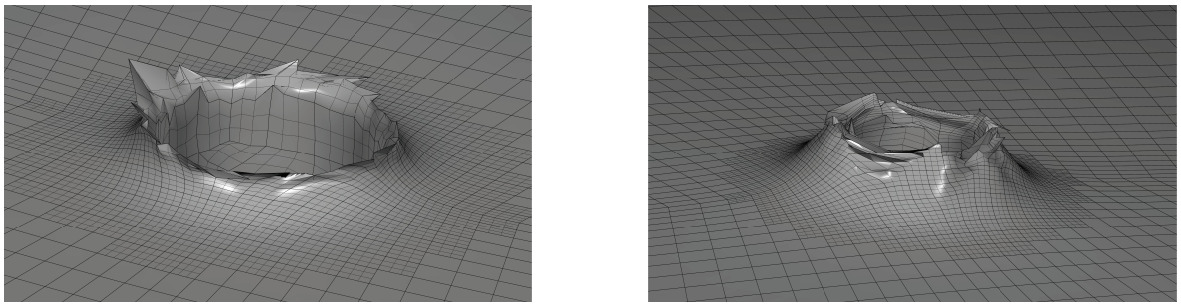

(a) Front **(b)** Back

Figure 8.16: Close-ups from IMPETUS Afea of entry and exit holes for AA6070-T4 aluminium target plates, $v_i = 247.0$ m/s, $v_r = 125.0$ m/s.

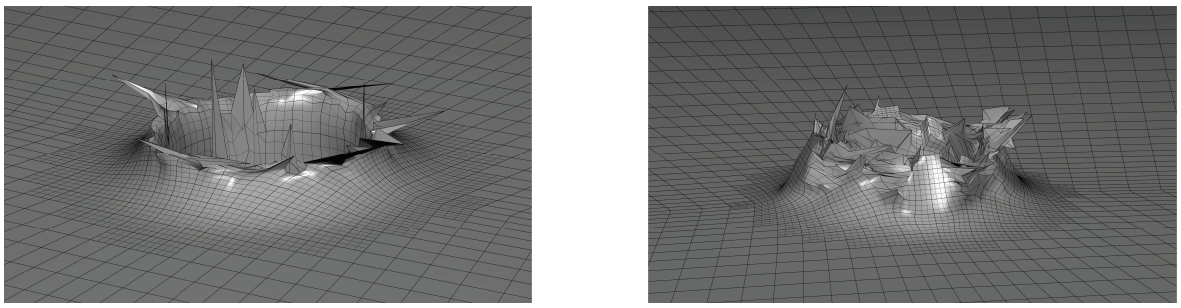

(a) Front **(b)** Back

Figure 8.17: Close-ups from IMPETUS Afea of entry and exit holes for AA6070-T6 aluminium target plates, $v_i = 247.0$ m/s, $v_r = 117.9$ m/s.

An additional simulation was carried out using the AA6070-T6 material parameters where 60 3D linear elements were used over the thickness of the plate. This was partially done to see if the fracture modes seen in Fig. 5.8 could be captured by IMPETUS, and partially to investigate how well the cubic elements measure up to the linear elements. Images from the simulation with linear elements can be seen in Fig. 8.19. When comparing this fracture-shape to the one for AA6070-T6 in Fig. 8.17, a more accurate fracture shape is seen, probably because the higher number of elements provide for more opportunities for fracture initiation and propagation. The residual velocity, on the other hand, is more accurate for cubic rather than for linear elements (see Fig. 8.20c).

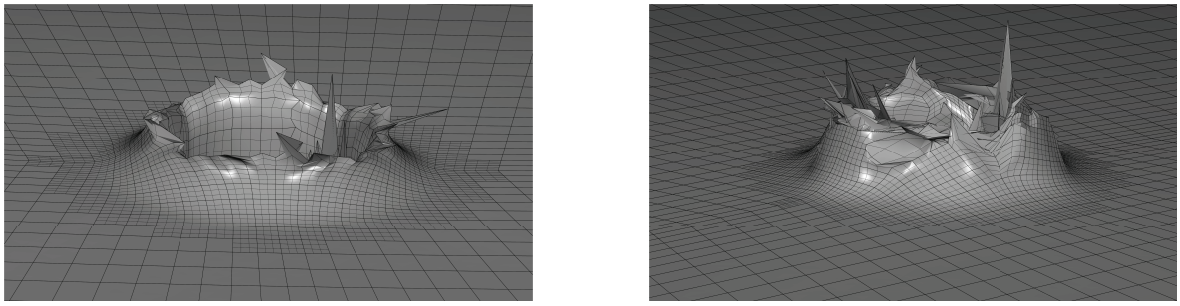

(a) Front **(b)** Back

Figure 8.18: Close-ups from IMPETUS Afea of entry and exit holes for AA6070-T7 aluminium target plates, $v_i = 250.0$ m/s, $v_r = 147.1$ m/s.

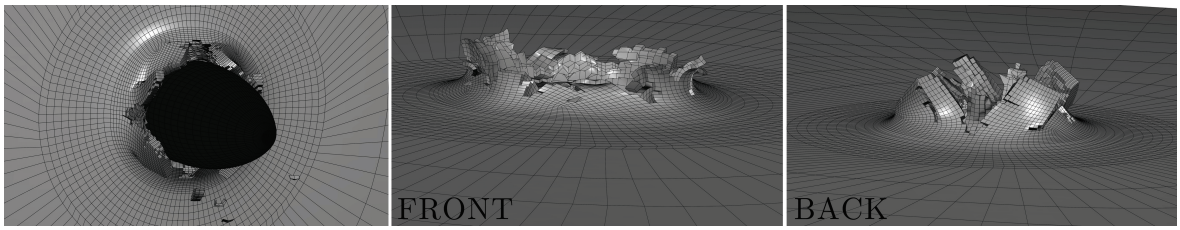

Figure 8.19: Screenshot from IMPETUS reflected about the symmetry-axis showing a post penetration image, the entry hole and the exit hole, respectively. $v_i = 247.0$ m/s and $v_r = 154.0$ m/s

In general,it is difficult to accurately describe fractures shapes seeing that a number of processes can take place during penetration and perforation of aluminium plates.

In Table 8.4 ballistic limit velocities obtained from numerical analysis in IMPETUS are compared to the ballistic limit velocities from the experimental ballistic tests in the laboratory. The parameters in the Recht-Ipson model used to calculate the ballistic limit velocites are $a = 1$ and $p = 2$. The ballistic limit curves from the simulations run with the IMPETUS Afea Solver are included in Fig. 8.20.

Table 8.4: v_{bl} for 20 mm ogival projectiles from experiments and IMPETUS analyses.

Temper	**Elements**	$\boldsymbol{v_{bl,\mathrm{EXP}}}$ (m/s)	$\boldsymbol{v_{bl,\mathrm{IMPETUS}}}$ (m/s)	**Deviation**
AA6070-O	Cubic	186.9	143.5	23.2%
AA6070-T4	Cubic	246.3	213.0	13.5%
AA6070-T6	Cubic	222.1	212.1	4.5%
AA6070-T6	Linear	222.1	193.1	13.1%
AA6070-T7	Cubic	246.9	202.2	18.1%

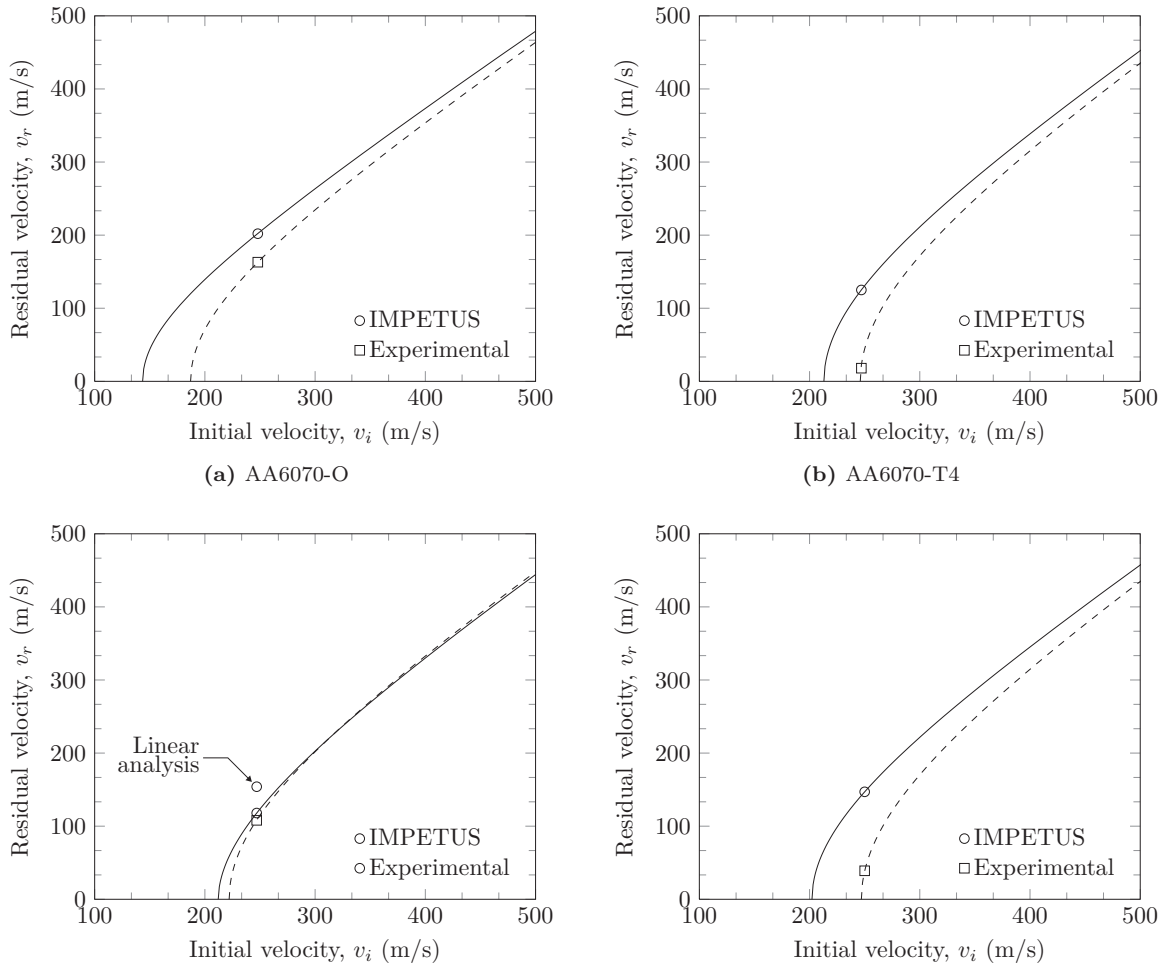

(a) AA6070-O

(b) AA6070-T4

(c) AA6070-T6

(d) AA6070-T7

Figure 8.20: Numerical results for ogival projectiles from IMPETUS compared to experimental values.

8.3.3 Sensitivity Studies

Due to the high demand of computational resources, only a limited sensitivity study of impacts with 20 mm ogival projectiles were run. High-speed video images from the ballistic experiments in the laboratory show that the aluminium target plates experienced some minor oscillation. To investigate the effect of these oscillations we have conducted a short study of the boundary conditions. In addition we carried out a simulation with a refined element mesh to get a feel of the mesh sensitivity.

Boundary Conditions

An extra analysis of the AA6070-O temper was run with clamping of all four plate edges in contrast to the initial model which included clamping only at the top and bottom edges of the plate. The extra clamping proved to have practically no effect on the residual velocity; the initial model gave a residual velocity of $v_r = 202.3$ m/s, and the model with clamping of all edges gave a residual velocity of $v_r = 202.1$ m/s, i.e. a deviation of 0.09%. The initial velocity in both cases was $v_i = 248.0$ m/s.

Mesh

Initially the target plates had 13 cubic elements over the thickness. A new simulation was run using AA6070-O material parameters with 20 elements over the thickness. The change in residual velocity was minimal. Residual velocity changed from $v_r = 202.3$ m/s to $v_r = 203.4$ m/s, indicating that to improve or change the results significantly, we will have to rely on substantially longer calculation times. Mesh size convergence cannot be ruled out either.

8.4 Impacts with 20 mm Ogival Projectiles Analyzed in LS-DYNA

For 20 mm ogival projectiles as well as for 20 mm blunt projectiles, the IMPETUS Afea Solver is used as the primary analysis tool in this thesis and LS-DYNA is run to get a basis of comparison for the IMPETUS results. Because ductile hole growth is expected to be the dominant mode of energy dissipation in this problem, the average element size can be increased for the ogival projectile analyses. The ballistic experiments from the laboratory are recreated when $v_i \approx 250$ m/s is used in one series of analyses, in addition an analyses series with $v_i = 200$ m/s is run.

8.4.1 Procedure

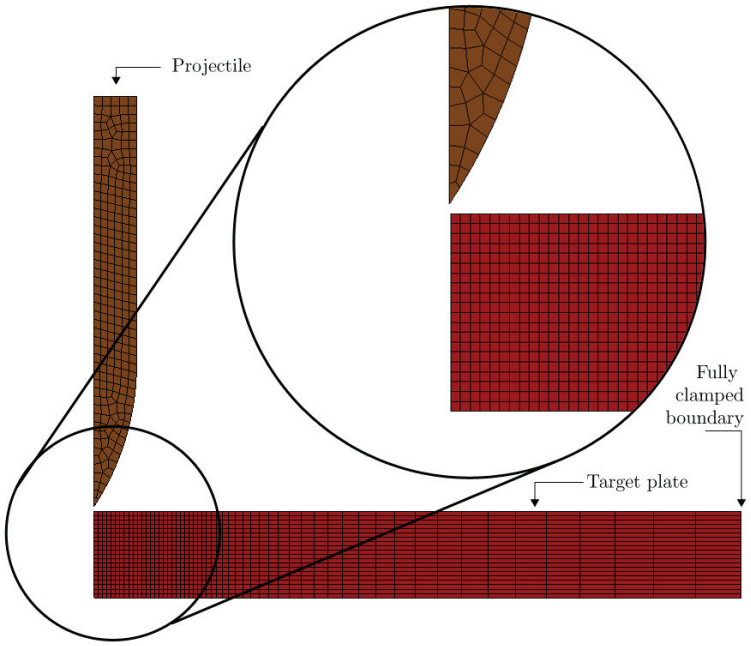

(a)

Figure 8.21: An example mesh used for the analyses involving 20 mm ogival projectiles in LS-DYNA.

Again it has to be mentioned that the implementation of a fracture criterion in an axisymmetric model may introduce errors because one element eroded in the model is equivalent to a ring of elements being eroded in a 3D setting. Initially, all the model-settings have been kept unchanged from the blunt nose projectile analysis except the geometry. But after encountering some problems with the contact algorithm, the scale factor for the penalty force stiffness in the card `*CONTACT_2D_AUTOMATIC_SINGLE_SURFACE` was increased from 2 to 5 to prevent unphysical penetration of the plate into the projectile. However this was only necessary to do for analyses where the shell elements in the plate were small, but it has been done on the other meshes as well to control that the solution is not significantly affected. All temper/initial velocity-configurations were run with 1 mm

elements and also with 0.5 mm elements in the area of interest, a selection of analyses were also done with 0.2 mm, 2 mm and 5 mm elements to get an indication of the mesh-sensitivity of the problem, see Fig. 8.25a. Pin-hole sensitivity and the effect of E_c in the Cockcroft-Latham criterion are examined. The orginal mesh uses a 0.2 mm pin-hole. Simulations using an adaptive mesh have not been conducted in this thesis.

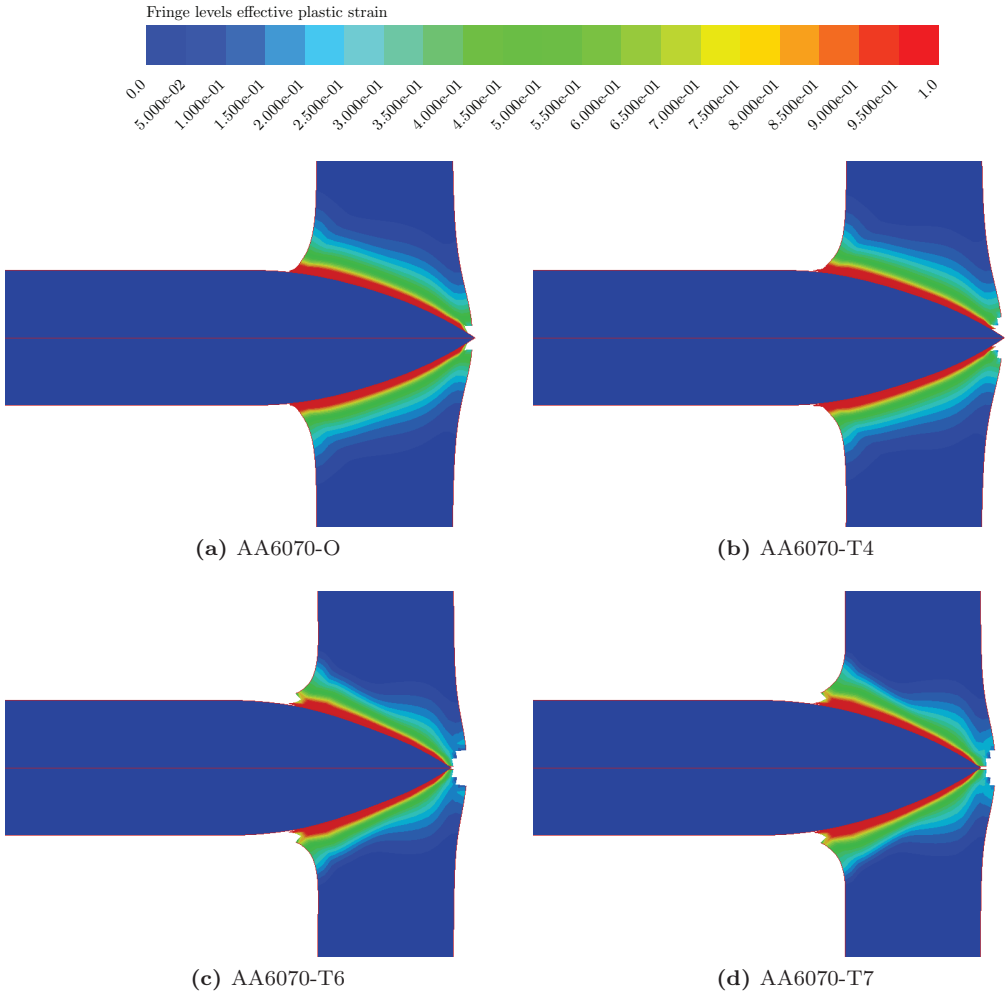

(a) AA6070-O **(b)** AA6070-T4

(c) AA6070-T6 **(d)** AA6070-T7

Figure 8.22: Screenshots of the plates impacted by ogival projectiles at incipient element erosion.

8.4.2 Results

After investigating the results from the analyses with 1 mm and 0.5 mm elements it is seen that the differences in residual velocities are less than 1%, so the reported results will be from the model with 1 mm elements. The estimated ballistic limit velocities from the experiments are compared to results from the analyses in LS-DYNA in Table 8.5 where the Recht-Ipson model has been used with $p = 2$ and $a = 1$.

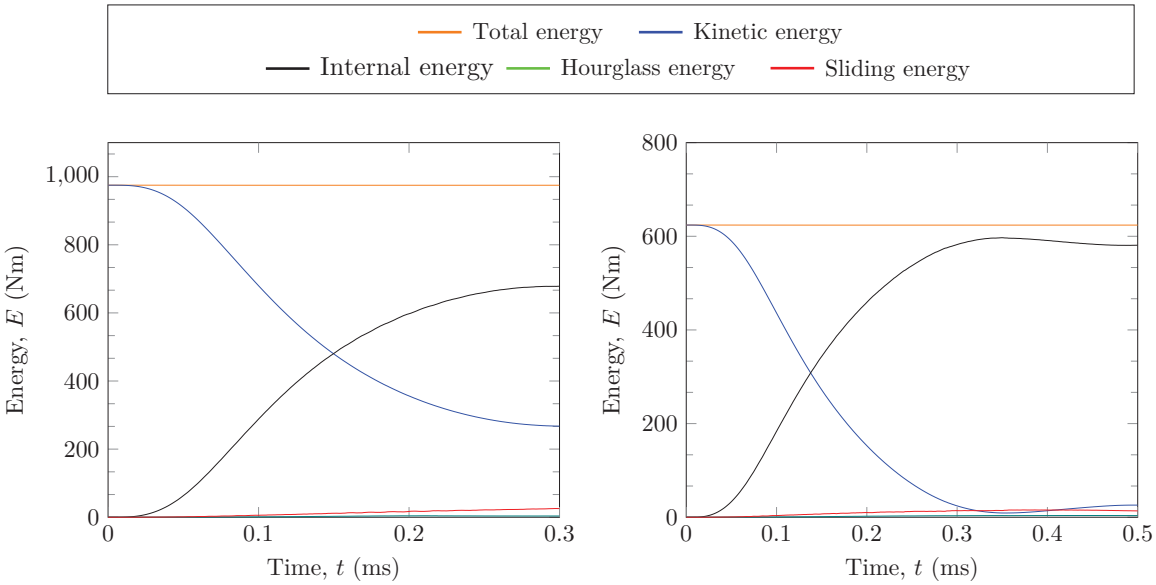

(a) $v_i = 250$ m/s **(b)** $v_i = 200$ m/s

Figure 8.23: Energy balance plots for the 20 mm ogival projectile striking the T7-temper with different initial velocities.

The ballistic limit velocity, v_{bl}, is underestimated for all the tempers when element erosion is present. This is clearly seen in Fig. 8.24 where the ballistic limit curves are reported from analyses where W_c is used. The capacities are underestimated by $0 - 21\%$. By inspecting the time-lapses from the experiments in Fig. 5.13 we can see that fragmentation takes place in the T6-temper and not in the others. On the other hand in the screenshots in Fig. 8.22 elements are eroded for T4, T6 and T7. The main reason for the general underestimation, is not clear to us; it may be because the pin-hole prevents the plate from developing a tensile zone at the back of the plate, but this is only speculative.

Table 8.5: v_{bl} for 20 mm ogival projectiles from experiments and LS-DYNA-analyses. $p = 2$ and $a = 1$.

Temper	$\boldsymbol{v_{bl,\mathrm{EXP}}}$ (m/s)	$\boldsymbol{v_{bl,\mathrm{LS\text{-}DYNA}}}$ (m/s)	**Deviation**
AA6070-O	186.9	147.7	21.0%
AA6070-T4	246.3	217.5	11.7%
AA6070-T6	222.1	221.4	0.3%
AA6070-T7	246.9	209.1	15.3%

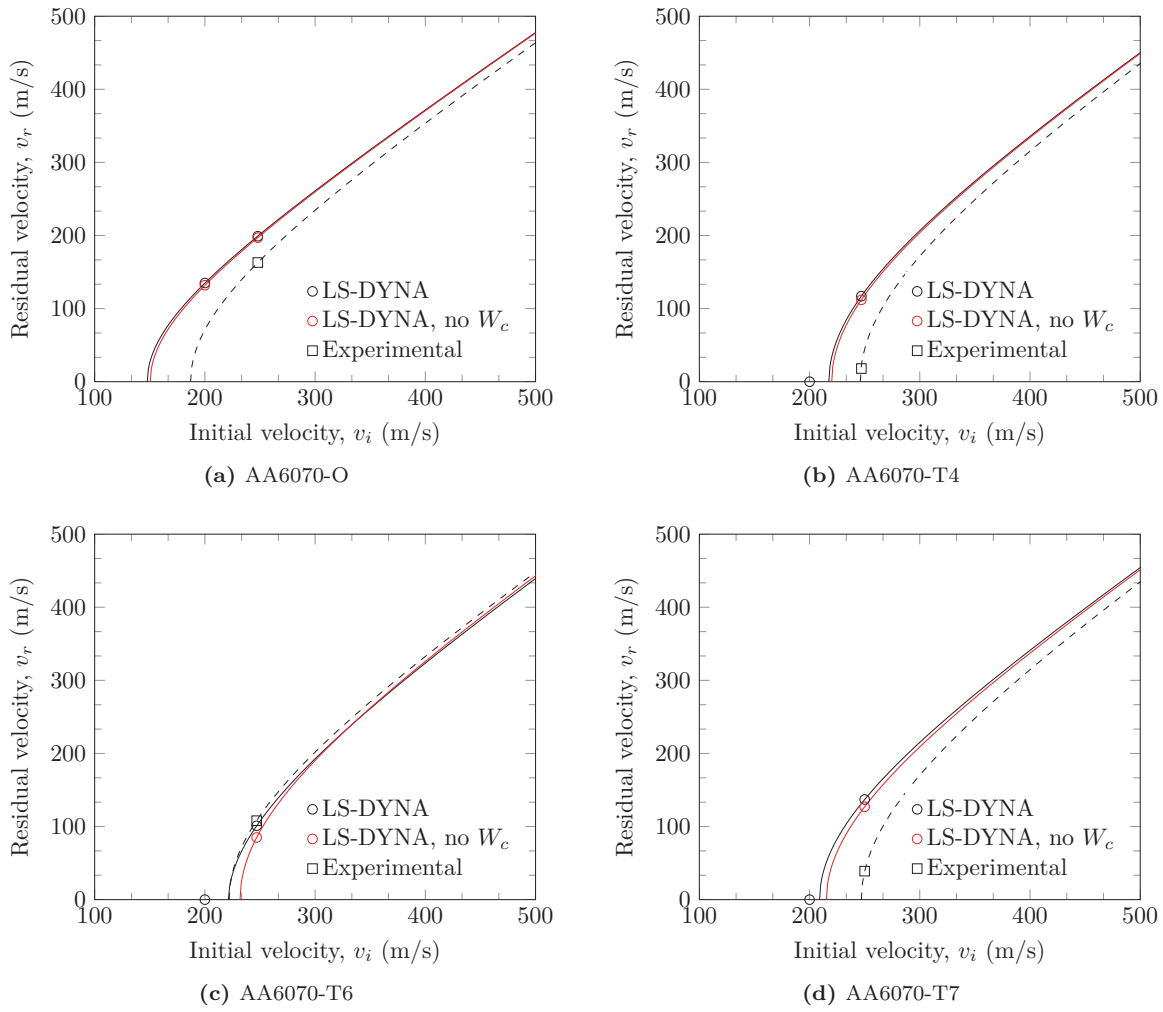

(a) AA6070-O

(b) AA6070-T4

(c) AA6070-T6

(d) AA6070-T7

Figure 8.24: Numerical results for 20 mm ogival projectiles from LS-DYNA (with 0.2 mm pinhole) compared to experimental values.

8.4.3 Sensitivity Study

The mesh sensitivity shown in Fig. 8.25a is almost negligible when more than 10 elements are used over the plate thickness, i.e. elements are smaller than 2 mm. It can also be seen that by omitting the W_c-number from the analyses all residual velocities decrease because of the aforementioned erosion of elements in axisymmetric models. With no element erosion, our conservative results will become less conservative, but the results for T6 (Fig. 8.24c) will become unconservative. The difference between the residual velocities calculated using element erosion and the residual velocities calculated without element erosion is found to be increasing with decreasing ductility (Fig. 8.25b). This is as expected after inspecting the high-speed video images in Fig. 5.13 where the O-temper experiences no fragmentation, and the T6-temper experiences excessive fragmentation. By using a 0.1 mm pinhole instead of a 0.2 mm pinhole the residual velocities drop by around 1 m/s so this has not been emphasized.

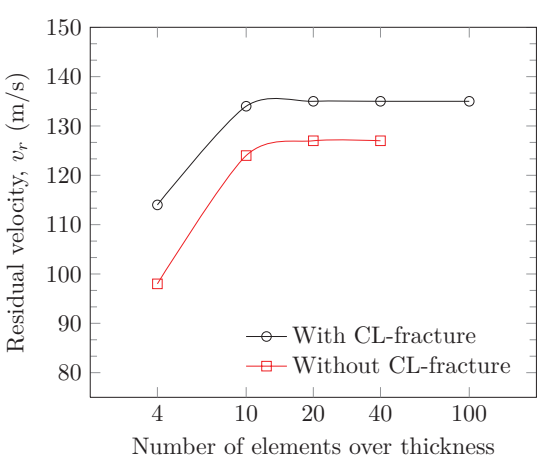

(a) Effect of element size on the residual velocity of a 20 mm ogival projectile striking a T7 plate at 250 m/s

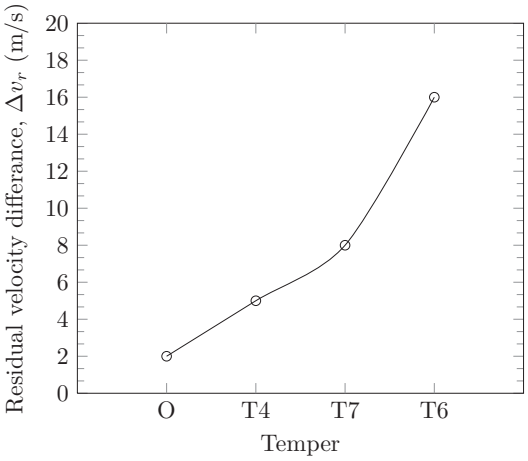

(b) Effect of fracture criterion on the residual velocity of a 20 mm ogival projectile striking the four tempers at 250 m/s described by the residual velocity differance between analyses with and without CL-fracture.

Figure 8.25: Results of the limited sensitivity study on 20 mm ogival projectiles.

Chapter 9

Analytical Methods

9.1 Cylindrical Cavity Expansion Theory

Post-experimental inspection of the targets (Fig. 4.3) indicate that the dominating mode of failure for several impacts is ductile hole growth. Even though no physical examination of the high-strength steel core of the APM2 bullet post perforation was carried out, high-speed videos from the ballistic experiments suggest that the core remains relatively undeformed through penetration and perforation, thus making the Cylindrical Cavity Expansion Theory (CCET) applicable.

The CCET was first developed by Hill [35], and the theory idealizes the target as thin, independent layers that are compressed normal to the penetration direction [32]. The cavity is expanded, from an initial radius of zero, at a constant velocity V, the material is modeled as elastic-plastic with power law work-hardening. A comprehensive step-by-step derivation of the equations stated by Forrestal et. al [31] will now be presented. We start by making the same assumption as Bishop et. al [10], namely that the octahedral stress τ_n is a definite function of the octahedral shear strain γ_n for all strain configurations. The octahedral stress τ_n is defined by [51]

$$\tau_n = \frac{1}{3}\left[(\sigma_1 - \sigma_2)^2 + (\sigma_2 - \sigma_3)^2 + (\sigma_3 - \sigma_1)^2\right]^{1/2} \tag{9.1}$$

and the octahedral strain γ_n is given by the equation

$$\gamma_n = \frac{2}{3}\left[(\epsilon_1 - \epsilon_2)^2 + (\epsilon_2 - \epsilon_3)^2 + (\epsilon_3 - \epsilon_1)^2\right]^{1/2} \tag{9.2}$$

An illustration of the cavity-expansion approximation along with the different response regions can be seen in Fig. 9.1.

9.1.1 Plastic Region

The plastic region is bounded by $r = Vt$ and $r = ct$ (see Fig. 9.1). Incompressibility is assumed for the material in the plastic region. Equations of momentum and mass conservation in Eulerian coordinates are given in [33]

$$\frac{\partial \sigma_r}{\partial r} + \frac{\sigma_r - \sigma_\theta}{r} = -\rho_t \left(\frac{\partial v}{\partial t} + v\frac{\partial v}{\partial r}\right) \tag{9.3}$$

$$\frac{\partial}{\partial r}\left[(r-u)^2\right] = 2r \tag{9.4}$$

where σ_r and σ_θ are the radial and tangential components of the Cauchy (true) stress taken positive in compression, ρ_t is density, and u and v are particle displacement and velocity, with outward motion considered positive. The particle velocity and displacement are related by

$$v\left(1 - \frac{\partial u}{\partial r}\right) = \frac{\partial u}{\partial t} \tag{9.5}$$

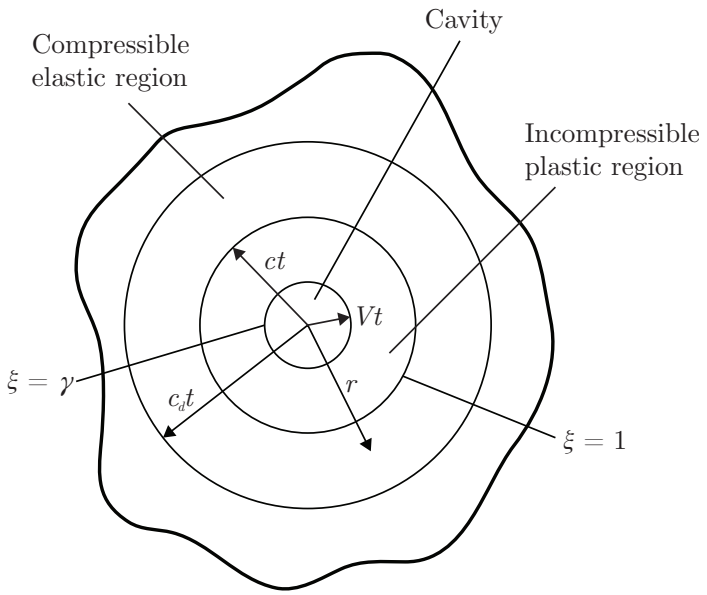

Figure 9.1: Cavity-expansion approximation and different response regions.

The logarithmic strain-displacement relations are defined as

$$\epsilon_r = \ln\left(1 - \partial u/\partial r\right) \tag{9.6}$$

$$\epsilon_\theta = \ln\left(1 - u/r\right) \tag{9.7}$$

both ϵ_r and ϵ_θ are taken as positive in compression.

Plastic flow is modelled with Power law work-hardening, i.e.

$$\sigma = \begin{cases} E\epsilon & \sigma \leq \sigma_0 \\ \sigma_0 \left(\frac{E\epsilon}{\sigma_0}\right)^n & \sigma > \sigma_0 \end{cases} \tag{9.8}$$

where σ is the true stress, ϵ is the logarithmic strain, E is the Young's modulus, σ_0 is yield stress, and n is the strain-hardening exponent.

For the uniaxial tensile test ($\sigma_2 = \sigma_3 = 0, \epsilon_2 = \epsilon_3 = -\epsilon_1/2$) Eqs. (9.1) and (9.2) reduce to

$$\tau_n = \frac{\sqrt{2}}{3}\sigma \tag{9.9}$$

$$\gamma_n = \sqrt{2}\epsilon \tag{9.10}$$

If Eqs. (9.9) and (9.10) are inserted into Eq. (9.8) we obtain

$$\frac{3\tau_n}{\sqrt{2}} = \sigma_0 \left[\frac{E\gamma_n}{\sqrt{2}\sigma_0}\right]^n \tag{9.11}$$

In the plastic region, we set σ_z by following Nadai [51]

$$\sigma_z = \frac{1}{2}(\sigma_r + \sigma_\theta) \tag{9.12}$$

This follows from the assumptions of plane strain and no volume change. Setting $\sigma_1 = \sigma_\theta$, $\sigma_2 = \sigma_r$, and $\sigma_3 = \sigma_z$ in Eq. (9.1), and $\epsilon_1 = \epsilon_r$, $\epsilon_2 = -\epsilon_r$ and $\epsilon_3 = 0$ in Eq. (9.2) we obtain:

$$\tau_n = \frac{1}{3}\sqrt{\frac{3}{2}}(\sigma_\theta - \sigma_r) \tag{9.13}$$

$$\gamma_n = 2\sqrt{\frac{2}{3}}\epsilon_r \tag{9.14}$$

The plastic flow of the cylindrical cavity expansion problem is obtained by substituting Eqs. (9.13) and (9.14) into Eq. (9.11), i.e.

$$\sigma_r - \sigma_\theta = \left[\frac{2}{\sqrt{3}}\right]^{1+n} E^n \sigma_0^{1-n} \epsilon_r^n, \quad \text{for} \quad \sigma_r - \sigma_\theta > 2\frac{\sigma_0}{\sqrt{3}} \quad (n = 0) \tag{9.15}$$

At the elastic-plastic interface there is no strain-hardening ($n = 0$), so Eq. (9.15) reduces to $\sigma_r - \sigma_\theta = 2\,\sigma_0/\sqrt{3}$ which is the usual von Mises yield criterion.

Now we seek to make the differential equations in Eqs. (9.3) and (9.4) dimensionless. We introduce the dimensionless variables, and their corresponding differentials

$$\begin{array}{cccc} S = \sigma_r/\sigma_0 & U = v/c & \overline{u} = u/ct & \gamma = V/c \\ \mathrm{d}S = \mathrm{d}\sigma_r/\sigma_0 & \mathrm{d}U = \mathrm{d}v/c & \mathrm{d}\overline{u} = \mathrm{d}u/ct & \mathrm{d}\gamma = 0 \end{array} \tag{9.16}$$

and the similarity transformation

$$\xi = r/ct \quad \mathrm{d}\xi = \mathrm{d}r/ct \quad \mathrm{d}\xi = \frac{\partial \xi}{\partial r}\mathrm{d}r + \frac{\partial \xi}{\partial t}\mathrm{d}t = \left(\frac{vt - r}{ct^2}\right)\mathrm{d}t \tag{9.17}$$

where c is the stress wave speed at the elastic-plastic interface. Now we premultiply Eq. (9.3) with ct/σ_0 and replace $(\sigma_r - \sigma_\theta)$ with the expression in Eq. (9.15), we get

$$\frac{\partial \sigma_r}{\partial r}\frac{ct}{\sigma_0} + \frac{ct}{r}\frac{1}{\sigma_0}\left[\frac{2}{\sqrt{3}}\right]^{1+n} E^n \sigma_0^{1-n}\epsilon_r^n = -\frac{\rho_t ct}{\sigma_0}\left(\frac{\partial v}{\partial t} + v\frac{\partial v}{\partial r}\right) \tag{9.18}$$

From Eqs. (9.16) and (9.17) we see that the first term becomes $\mathrm{d}S/\mathrm{d}\xi$. The last term on the right hand side is the total derivative of v with respect to t. Substituting ϵ_r with Eq. (9.6) we get:

$$\frac{\mathrm{d}S}{\mathrm{d}\xi} = -\left[\frac{2}{\sqrt{3}}\right]^{1+n}\left(\frac{E}{\sigma_0}\right)^n \frac{1}{\xi}\left[\ln\left(1 - \frac{\partial u}{\partial r}\right)\right]^n - \frac{\rho_t ct}{\sigma_0}\frac{\mathrm{d}v}{\mathrm{d}t}$$

where

$$\frac{\partial u}{\partial r} = \frac{\mathrm{d}\overline{u}}{\mathrm{d}\xi} \quad \text{and} \quad \frac{\mathrm{d}v}{\mathrm{d}t} = \frac{\mathrm{d}U}{\mathrm{d}\xi} \cdot \frac{(vt - r)}{t^2} \tag{9.19}$$

thus,

$$\begin{aligned} \frac{\mathrm{d}S}{\mathrm{d}\xi} &= -\left[\frac{2}{\sqrt{3}}\right]^{1+n}\left(\frac{E}{\sigma_0}\right)^n \frac{1}{\xi}\left[\ln\left(1 - \frac{\mathrm{d}\overline{u}}{\mathrm{d}\xi}\right)\right]^n - \frac{\rho_t ct}{\sigma_0}\left(\frac{vt - r}{ct^2}\right)\frac{\mathrm{d}U}{\mathrm{d}\xi} \\ \frac{\mathrm{d}S}{\mathrm{d}\xi} &= -\left[\frac{2}{\sqrt{3}}\right]^{1+n}\left(\frac{E}{\sigma_0}\right)^n \frac{1}{\xi}\left[\ln\left(1 - \frac{\mathrm{d}\overline{u}}{\mathrm{d}\xi}\right)\right]^n + \frac{\rho_t c^2}{\sigma_0}(\xi - U)\frac{\mathrm{d}U}{\mathrm{d}\xi} \end{aligned} \tag{9.20}$$

Similarly we obtain a new expression for Eq. (9.4) by introducing expressions in Eqs. (9.16) and (9.17) and premultiplying Eq. (9.4) with $1/ct$, we obtain

$$\frac{\mathrm{d}}{(ct)^2\mathrm{d}\xi}\left[(r - u)^2\right] = 2\frac{r}{ct} \quad \Rightarrow \quad \frac{\mathrm{d}}{\mathrm{d}\xi}\left[(\xi - \overline{u})^2\right] = 2\xi \tag{9.21}$$

The transformation of the relationship between particle velocity and displacement (Eq. (9.5)) is more elaborate. First we recognize that the equation may be rewritten to $v = \mathrm{d}u/\mathrm{d}t$. In order to make the derivation somewhat easier we rewrite the dimensionless variable $\overline{u} = u/ct$ to $u = \overline{u}r/\xi$, and then calculate the total derivative $\mathrm{d}u/\mathrm{d}t$ as

$$\begin{aligned}\frac{\mathrm{d}u}{\mathrm{d}t} &= \frac{\partial u}{\partial \overline{u}}\frac{\mathrm{d}\overline{u}}{\mathrm{d}t} + \frac{\partial u}{\partial r}\frac{\mathrm{d}r}{\mathrm{d}t} + \frac{\partial u}{\partial \xi}\frac{\mathrm{d}\xi}{\mathrm{d}t} \\ &= \frac{\partial u}{\partial \overline{u}}\frac{\mathrm{d}\overline{u}}{\mathrm{d}\xi}\frac{\mathrm{d}\xi}{\mathrm{d}t} + \frac{\partial u}{\partial r}\frac{\mathrm{d}r}{\mathrm{d}t} + \frac{\partial u}{\partial \xi}\frac{\mathrm{d}\xi}{\mathrm{d}t} \\ &= v\frac{\mathrm{d}\overline{u}}{\mathrm{d}\xi} - \frac{r}{t}\frac{\mathrm{d}\overline{u}}{\mathrm{d}\xi} + \frac{\overline{u}r}{\xi t}\end{aligned} \tag{9.22}$$

Premultiplying Eq. (9.5) with $1/c$ and inserting Eq. (9.22) yields:

$$U\left(1 - \frac{\mathrm{d}\overline{u}}{\mathrm{d}\xi}\right) = \overline{u} - \xi\frac{\mathrm{d}\overline{u}}{\mathrm{d}\xi} \tag{9.23}$$

The boundary condition at the cavity surface reads

$$\overline{u}(\xi = \gamma) = \gamma \tag{9.24}$$

For incompressible materials, stress and particle velocity are continuous at the elastic-plastic interface ($\xi = 1$), thus

$$S(\xi = 1) = S_1 \tag{9.25}$$

$$U(\xi = 1) = U_1 \tag{9.26}$$

where S_1 and U_1 are the radial stress and particle velocity respectively, in the elastic region at $\xi = 1$.

The solution for Eq. (9.21) that satisfies the boundary condition in Eq. (9.24) is

$$\overline{u} = \xi - \sqrt{\xi^2 - \gamma^2} \tag{9.27}$$

Inserting Eq. (9.27) into Eq. (9.23) gives

$$U = \frac{\gamma^2}{\xi} \tag{9.28}$$

Next substitute Eqs. (9.27) and (9.28) into Eq. (9.20), we get

$$\begin{aligned}\frac{\mathrm{d}S}{\mathrm{d}\xi} &= -\left[\frac{2}{\sqrt{3}}\right]^{1+n}\left(\frac{E}{\sigma_0}\right)^n\frac{1}{\xi}\left[\ln\left(\frac{\xi}{\sqrt{\xi^2-\gamma^2}}\right)\right]^n + \frac{\rho_t c^2}{\sigma_0}\left(\xi - \frac{\gamma^2}{\xi}\right)\left(-\frac{\gamma^2}{\xi^2}\right) \\ &= -\frac{2}{\sqrt{3}}\left[\frac{E}{\sqrt{3}\sigma_0}\right]^n\frac{1}{\xi}\left[\ln\left(\frac{\xi^2}{\xi^2-\gamma^2}\right)\right]^n + \frac{\rho_t c^2}{\sigma_0}(\gamma^2 - \xi^2)\frac{\gamma^2}{\xi^3}\end{aligned} \tag{9.29}$$

Integration gives the dimensionless radial stress $S(\xi)$:

$$\begin{aligned}\int \mathrm{d}S &= \int_\xi^1 \left(-\frac{2}{\sqrt{3}}\left[\frac{E}{\sqrt{3}\sigma_0}\right]^n\frac{1}{\xi}\left[\ln\left(\frac{\xi^2}{\xi^2-\gamma^2}\right)\right]^n + \frac{\rho_t c^2}{\sigma_0}(\gamma^2-\xi^2)\frac{\gamma^2}{\xi^3}\right)\mathrm{d}\xi \\ S(\xi) &= S_1 + \frac{2}{\sqrt{3}}\left[\frac{E}{\sqrt{3}\sigma_0}\right]^n\int_\xi^1\frac{1}{\xi}\left[\ln\left(\frac{\xi^2}{\xi^2-\gamma^2}\right)\right]^n\mathrm{d}\xi + \frac{\rho_t c^2}{\sigma_0}\left(-\frac{\gamma^4}{2\xi^2} - \gamma^2\ln\xi + \frac{1}{2}\gamma^2\right) \\ S(\xi) &= S_1 + \frac{2}{\sqrt{3}}\left[\frac{E}{\sqrt{3}\sigma_0}\right]^n I(\xi) + \frac{\rho_t V^2}{2\sigma_0}\left(\gamma^2 - 2\ln\xi - \frac{\gamma^2}{\xi^2}\right)\end{aligned} \tag{9.30}$$

where S_1 and c ($\gamma = V/c$) are to be determined in Sections 9.1.2 and 9.1.3.

9.1.2 Elastic Region

The elastic region is bounded by $r = c_d t$ and $r = ct$ (see Fig. 9.1). The following derivations are adapted from Dr. Forrestal's personal notes, given to us by Professore Tore Børvik [30]. For convenience strains in this section are taken positive in tension, which is opposite of the definition used in Section 9.1.1.

We start with the equation of motion, as previously described in Eq. (9.3), though the last term has been altered:

$$\frac{\partial \sigma_r}{\partial r} + \frac{\sigma_r - \sigma_\theta}{r} = \rho_t \frac{\partial^2 u}{\partial t^2} \tag{9.31}$$

Since we now are in the elastic regime, strains are given by:

$$\epsilon_r = \frac{1}{E}\left(\sigma_r - \nu(\sigma_\theta + \sigma_z)\right) \tag{9.32}$$

$$\epsilon_\theta = \frac{1}{E}\left(\sigma_\theta - \nu(\sigma_r + \sigma_z)\right) \tag{9.33}$$

$$\epsilon_z = 0 \quad \text{and} \quad \sigma_z = \nu(\sigma_r + \sigma_\theta) \tag{9.34}$$

Inserting the expression for σ_z in Eq. (9.34) into the strain expression in Eqs. (9.32) and (9.33), and premultiplying with E we obtain:

$$E\epsilon_r = (1-\nu^2)\sigma_r - \nu(1+\nu)\sigma_\theta \tag{9.35}$$

$$E\epsilon_\theta = (1-\nu^2)\sigma_\theta - \nu(1+\nu)\sigma_r \tag{9.36}$$

In the elastic regime the definitions of ϵ_r and ϵ_θ are given as:

$$\epsilon_r = \frac{\partial u}{\partial r} \tag{9.37}$$

$$\epsilon_\theta = \frac{u}{r} \tag{9.38}$$

Inserting the expressions from Eqs. (9.37) and (9.38) into Eqs. (9.35) and (9.36), and then subtracting Eq. (9.36) from Eq. (9.35) we obtain an expression for $\sigma_r - \sigma_\theta$:

$$\begin{aligned} E\left(\frac{\partial u}{\partial r} - \frac{u}{r}\right) &= (1-\nu^2)\sigma_r - \nu(1+\nu)\sigma_\theta - (1-\nu^2)\sigma_\theta + \nu(1+\nu)\sigma_r \\ &= (1-\nu^2)(\sigma_r - \sigma_\theta) + \nu(1+\nu)(\sigma_r - \sigma_\theta) \\ &= (1+\nu)(\sigma_r - \sigma_\theta) \end{aligned} \tag{9.39}$$

Solving Eq. (9.39) for $\sigma_r - \sigma_\theta$ gives:

$$\sigma_r - \sigma_\theta = \frac{E}{1+\nu}\left(\frac{\partial u}{\partial r} - \frac{u}{r}\right) \tag{9.40}$$

Now we want to eliminate σ_θ, this is done by multiplying Eq. (9.35) with $(1-\nu)$, and Eq. (9.36) by ν, subtracting the resulting expressions from each other we obtain:

$$\sigma_r = \frac{E(1-\nu)}{(1+\nu)(1-2\nu)}\frac{\partial u}{\partial r} + \frac{E\nu}{(1+\nu)(1-2\nu)}\frac{u}{r} \tag{9.41}$$

Differentiating Eq. (9.41) with respect to r gives:

$$\frac{\partial \sigma_r}{\partial r} = \frac{E(1-\nu)}{(1+\nu)(1-2\nu)}\frac{\partial^2 u}{\partial r^2} + \frac{E\nu}{(1+\nu)(1-2\nu)}\left(\frac{1}{r}\frac{\partial u}{\partial r} - \frac{u}{r^2}\right) \tag{9.42}$$

Addition of Eqs. (9.40) and (9.42) yields:

$$\frac{\partial \sigma_r}{\partial r} + \frac{\sigma_r - \sigma_\theta}{r} = \frac{E(1-\nu)}{(1+\nu)(1-2\nu)} \frac{\partial^2 u}{\partial r^2} + \frac{E(1-\nu)}{(1+\nu)(1-2\nu)} \left(\frac{1}{r} \frac{\partial u}{\partial r} - \frac{u}{r^2} \right)$$
$$= \frac{E(1-\nu)}{(1+\nu)(1-2\nu)} \left[\frac{\partial^2 u}{\partial r^2} + \frac{\partial}{\partial r} \left(\frac{u}{r} \right) \right] \tag{9.43}$$

Now the equation of motion (Eq. (9.31)) becomes

$$\frac{\partial^2 u}{\partial r^2} + \frac{1}{r} \frac{\partial u}{\partial r} - \frac{u}{r^2} = \frac{1}{c_d} \frac{\partial^2 u}{\partial t^2} \tag{9.44}$$

$$\text{where} \quad c_d = \frac{E(1-\nu)}{\rho_t (1+\nu)(1-2\nu)} \tag{9.45}$$

where c_d is the elastic dilatational wave speed. As was done in Section 9.1.1, we introduce the similarity transformation and the dimensionless variable:

$$\xi = \frac{r}{ct} \quad \text{and} \quad \bar{u}(\xi) = \frac{u}{ct} \tag{9.46}$$

where c is the wave speed at the plastic-elastic boundary. Now we need to express our differentials in terms of the new dimensionless variables in Eq. (9.46):

$$\frac{\partial u}{\partial r} = \frac{\partial u}{\partial \xi} \frac{\partial \xi}{\partial r} = \frac{1}{ct} \frac{\mathrm{d}u}{\mathrm{d}\xi}$$
$$= \frac{\mathrm{d}\bar{u}}{\mathrm{d}\xi} \tag{9.47}$$
$$\frac{\partial^2 u}{\partial r^2} = \frac{\mathrm{d}}{\mathrm{d}r} \left(\frac{\mathrm{d}\bar{u}}{\mathrm{d}\xi} \right) \frac{\mathrm{d}\xi}{\mathrm{d}r}$$
$$= \frac{1}{ct} \frac{\mathrm{d}^2 \bar{u}}{\mathrm{d}\xi^2} \tag{9.48}$$
$$\frac{\partial u}{\partial t} = \frac{\partial}{\partial t}(ct\bar{u}) = c\bar{u} + ct \frac{\mathrm{d}\bar{u}}{\mathrm{d}\xi} \frac{\mathrm{d}\xi}{\mathrm{d}t}$$
$$= c\bar{u} - c\xi \frac{\mathrm{d}\bar{u}}{\mathrm{d}\xi} \tag{9.49}$$
$$\frac{\partial^2 u}{\partial t^2} = c \frac{\mathrm{d}\bar{u}}{\mathrm{d}\xi} \frac{\mathrm{d}\xi}{\mathrm{d}t} - c \frac{\mathrm{d}\xi}{\mathrm{d}t} \frac{\mathrm{d}\bar{u}}{\mathrm{d}\xi} - c\xi \frac{\mathrm{d}^2 \bar{u}}{\mathrm{d}\xi^2} \frac{\mathrm{d}\xi}{\mathrm{d}t}$$
$$= \frac{c\xi^2}{t} \frac{\mathrm{d}^2 \bar{u}}{\mathrm{d}\xi^2} \tag{9.50}$$

Inserting the differentials in Eqs. (9.47) to (9.50) into Eq. (9.44) gives the differential equation:

$$\left(1 - \frac{c^2 \xi^2}{c_d^2} \right) \frac{\mathrm{d}^2 \bar{u}}{\mathrm{d}\xi^2} + \frac{1}{\xi} \frac{\mathrm{d}\bar{u}}{\mathrm{d}\xi} - \frac{1}{\xi^2} \bar{u} = 0 \tag{9.51}$$

Now we need to express $(\sigma_r - \sigma_\theta)$, and σ_r in terms of the dimensionless variables, inserting Eqs. (9.46) and (9.47) into Eqs. (9.40) and (9.41) gives:

$$\sigma_r - \sigma_\theta = \frac{E}{1+\nu} \left[\frac{\mathrm{d}\bar{u}}{\mathrm{d}\xi} - \frac{\bar{u}}{\xi} \right] \tag{9.52}$$
$$\sigma_r = \frac{E(1-\nu)}{(1+\nu)(1-2\nu)} \frac{\mathrm{d}\bar{u}}{\mathrm{d}\xi} + \frac{E\nu}{(1+\nu)(1-2\nu)} \frac{\bar{u}}{\xi}$$
$$\sigma_r = \frac{E(1-\nu)}{(1+\nu)(1-2\nu)} \left[\frac{\mathrm{d}\bar{u}}{\mathrm{d}\xi} + \frac{\nu}{1-\nu} \frac{\bar{u}}{\xi} \right] \tag{9.53}$$

To solve the differential equation in Eq. (9.51) we perform the substitution:

$$z = \alpha\xi \tag{9.54}$$

$$\frac{\mathrm{d}*}{\mathrm{d}\xi} = \frac{\mathrm{d}*}{\mathrm{d}z}\frac{\mathrm{d}z}{\mathrm{d}\xi} = \alpha\frac{\mathrm{d}*}{\mathrm{d}z} \tag{9.55}$$

Inserting Eqs. (9.54) and (9.55) into Eq. (9.51) gives:

$$z^2(1-z^2)\frac{\mathrm{d}^2\bar{u}}{\mathrm{d}z^2} + \frac{1}{z}\frac{\mathrm{d}\bar{u}}{\mathrm{d}z} - \bar{u} = 0 \tag{9.56}$$

To (eventually) reduce the differential equation (Eq. (9.51)) to first order, we introduce another substitution:

$$\bar{u} = z\phi \tag{9.57}$$

$$\frac{\mathrm{d}\bar{u}}{\mathrm{d}z} = \phi + z\frac{\mathrm{d}\phi}{\mathrm{d}z} \tag{9.58}$$

$$\frac{\mathrm{d}^2\bar{u}}{\mathrm{d}z^2} = 2\frac{\mathrm{d}\phi}{\mathrm{d}z} + z\frac{\mathrm{d}^2\phi}{\mathrm{d}z^2} \tag{9.59}$$

Substituting Eqs. (9.57) to (9.59) into Eq. (9.56) yields:

$$z(1-z^2)\phi'' + [2(1-z^2)+1]\phi' = 0 \tag{9.60}$$

Which can be separated into

$$\frac{\phi''}{\phi'} = \frac{-2}{z} - \frac{1}{z(1-z^2)} \tag{9.61}$$

Integration of both sides give:

$$\int\frac{\mathrm{d}^2\phi}{\mathrm{d}\phi} = -\int\frac{2}{z}\mathrm{d}z - \int\frac{\mathrm{d}z}{z(1-z^2)}$$

$$\ln\phi' + \ln C = -2\ln z - I_1 \tag{9.62}$$

To solve I_1 a series of manipulations have to be done. First a substitution; $u = z^2$:

$$I_1 = \frac{1}{2}\int\frac{\mathrm{d}u}{u(1-u)} \tag{9.63}$$

Second, partial fractions has to be used to split the integrand in Eq. (9.63) into two parts.

$$\frac{1}{u(1-u)} = \frac{A}{u} + \frac{B}{1-u}$$

which gives $A = B = 1$, now we may determine the integral I_1:

$$I_1 = \frac{1}{2}\left(\int\frac{\mathrm{d}u}{u} + \int\frac{\mathrm{d}u}{1-u}\right)$$

$$I_1 = \frac{1}{2}\ln\left(\frac{u}{1-u}\right) = \frac{1}{2}\ln\left(\frac{z^2}{1-z^2}\right) \tag{9.64}$$

Thus,

$$\ln\left(C\phi'\right) = \ln\frac{1}{z^2} - \frac{1}{2}\ln\left(\frac{z^2}{1-z^2}\right)$$

$$C\phi' = \frac{(1-z^2)^{1/2}}{z^3} \tag{9.65}$$

Another integration gives:

$$C\phi + D = \int \frac{(1-z^2)^{3/2}}{z^3}\mathrm{d}z = I_2 \tag{9.66}$$

The I_2 integral has to be integrated by parts, with $u' = 1/z^3$ and $v = (1-z^2)^{1/2}$, this gives:

$$I_2 = -\frac{(1-z^2)^{1/2}}{2z^2} - I_3 \tag{9.67}$$

$$I_3 = \frac{1}{2}\int \frac{\mathrm{d}z}{z(1-z^2)^{1/2}} \tag{9.68}$$

Another substitution is made: $y = (1-z^2)^{1/2}$, which yields:

$$I_3 = \frac{1}{2}\int \frac{\mathrm{d}y}{y^2-1} \tag{9.69}$$

The integrand in Eq. (9.69) is recognized as the derivative of $-\mathrm{arctanh}y$, so by the fundamental theorem of calculus I_3 becomes:

$$I_3 = -\frac{1}{2}\mathrm{arctanh}\left((1-z^2)^{1/2}\right) \tag{9.70}$$

In Rottmann [57] it is stated that

$$\mathrm{arctanh}x = \frac{1}{2}\ln\left(\frac{1+x}{1-x}\right)$$

I.e. Eq. (9.70) becomes:

$$I_3 = -\frac{1}{4}\ln\left(\frac{1+(1-z^2)^{1/2}}{1-(1-z^2)^{1/2}}\right) = -\frac{1}{2}\ln\left(\frac{1+(1-z^2)^{1/2}}{z}\right) \tag{9.71}$$

This gives the expression for I_2:

$$I_2 = -\frac{1}{2}\left[\frac{(1-z^2)^{1/2}}{z^2} - \ln\left(\frac{1+(1-z^2)^{1/2}}{z}\right)\right] \tag{9.72}$$

Inserting Eq. (9.72) into Eq. (9.66) gives the expression for ϕ:

$$\phi = A + \frac{B}{2}\left[\frac{(1-z^2)^{1/2}}{z^2} - \ln\left(\frac{1+(1-z^2)^{1/2}}{z}\right)\right] \tag{9.73}$$

Remembering the substitutions in Eqs. (9.54) and (9.57) ($z = \alpha\xi$, and $\bar{u} = z\phi$) we obtain the expression for $\bar{u}$:

$$\bar{u} = A\alpha\xi + \frac{B}{2}\left[\frac{(1-(\alpha\xi)^2)^{1/2}}{\alpha\xi} - \alpha\xi\ln\left(\frac{1+(1-(\alpha\xi)^2)^{1/2}}{\alpha\xi}\right)\right] \tag{9.74}$$

At the elastic wave front $\xi = 1/\alpha$ and $\bar{u}(\xi = 1/\alpha) = 0$:

$$\bar{u}(\xi = 1/\alpha) = A + B(0 - 1\ln 1) = 0 \quad \Rightarrow \quad A = 0$$

$$\bar{u}(\xi) = \frac{B\alpha\xi}{2}\left[\frac{(1-(\alpha\xi)^2)^{1/2}}{(\alpha\xi)^2} - \ln\left(\frac{1+(1-(\alpha\xi)^2)^{1/2}}{\alpha\xi}\right)\right] \tag{9.75}$$

From Eq. (9.65) we have:

$$\phi' = \frac{\mathrm{d}\phi}{\mathrm{d}z} = -B\frac{(1-z^2)^{1/2}}{z^3}, \quad \text{where} \quad B = 1/C \tag{9.76}$$

By inserting Eqs. (9.55) and (9.57) into Eq. (9.52) we may express $(\sigma_r - \sigma_\theta)$ in terms of ϕ and z:

$$\begin{aligned}
\sigma_r - \sigma_\theta &= \frac{E}{1+\nu}\left[\alpha\frac{\mathrm{d}(z\phi)}{\mathrm{d}z} - \alpha\phi\right] = \frac{E\alpha z}{1+\nu}\frac{\mathrm{d}\phi}{\mathrm{d}z} \\
\sigma_r - \sigma_\theta &= \frac{E\alpha(-B)}{1+\nu}\frac{(1-z^2)^{1/2}}{z^2}, \quad \text{where} \quad z = \alpha\xi \\
\sigma_r - \sigma_\theta &= \frac{E\alpha(-B)}{1+\nu}\frac{(1-(\alpha\xi)^2)^{1/2}}{(\alpha\xi)^2}
\end{aligned} \tag{9.77}$$

At the plastic-elastic interface ($\xi = 1$) the material yields, i.e. a von Mises yield criterion gives:

$$\sigma_r - \sigma_\theta = \frac{2\sigma_0}{\sqrt{3}} \tag{9.78}$$

where σ_0 is the yield stress. Inserting Eq. (9.78) into Eq. (9.77) with $\xi = 1$ gives:

$$\begin{aligned}
\frac{E\alpha(-B)}{1+\nu}\frac{(1-\alpha^2)^{1/2}}{\alpha^2} &= \frac{2\sigma_0}{\sqrt{3}} \\
-B &= \frac{2\sigma_0}{\sqrt{3}E}\frac{\alpha(1+\nu)}{(1-\alpha^2)^{1/2}}
\end{aligned} \tag{9.79}$$

Inserting Eq. (9.79) into Eq. (9.77) yields:

$$\sigma_r - \sigma_\theta = \frac{2\sigma_0}{\sqrt{3}}\frac{(1-(\alpha\xi)^2)^{1/2}}{\xi^2(1-\alpha^2)^{1/2}} \tag{9.80}$$

Now we seek to establish an expression for the dimensionless particle velocity:

$$U = \frac{v}{c} = \frac{1}{c}\frac{\partial u}{\partial t} \tag{9.81}$$

where v is the particle velocity. Inserting Eq. (9.49) into Eq. (9.81) gives:

$$U = \bar{u} - \xi\frac{\mathrm{d}\bar{u}}{\mathrm{d}\xi} = -\xi\left(\frac{\mathrm{d}\bar{u}}{\mathrm{d}\xi} - \frac{\bar{u}}{\xi}\right) \tag{9.82}$$

Combining Eqs. (9.52) and (9.80) yields:

$$\frac{\mathrm{d}\bar{u}}{\mathrm{d}\xi} - \frac{\bar{u}}{\xi} = \frac{1+\nu}{E}\left(\frac{2\sigma_0}{\sqrt{3}}\frac{(1-(\alpha\xi)^2)^{1/2}}{\xi^2(1-\alpha^2)^{1/2}}\right) \tag{9.83}$$

Inserting Eq. (9.83) into Eq. (9.82) gives an expression for U:

$$U = -\frac{2\sigma_0(1+\nu)}{\sqrt{3}E(1-\alpha^2)^{1/2}}\frac{(1-(\alpha\xi)^2)^{1/2}}{\xi} \tag{9.84}$$

And at the plastic-elastic interface

$$U(\xi = 1) = U_1 = -\frac{2\sigma_0(1+\nu)}{\sqrt{3}E} \tag{9.85}$$

Remembering that the strains are taken positive in this section explains the negative sign in Eq. (9.85). Using the same definition as in Section 9.1.1 (i.e. strains positive in compression) we obtain:

$$U_1 = \frac{2\sigma_0(1+\nu)}{\sqrt{3}E} \tag{9.86}$$

Now to calculate the radial stress σ_r we rewrite the expression in Eq. (9.53) so as the to avoid taking the derivative of $\bar{u}$, we obtain:

$$\sigma_r = \frac{E(1-\nu)}{(1+\nu)(1-2\nu)}\left[\frac{\mathrm{d}\bar{u}}{\mathrm{d}\xi} - \frac{\bar{u}}{\xi}\right] + \frac{E}{(1+\nu)(1-2\nu)}\frac{\bar{u}}{\xi} \tag{9.87}$$

The expression in the brackets in the first term of Eq. (9.87) is recognized as $-U/\xi$ (see Eq. (9.82)), inserting Eq. (9.84) multiplied with $-1/\xi$ gives:

$$\begin{aligned}\frac{E(1-\nu)}{(1+\nu)(1-2\nu)}\left[\frac{\mathrm{d}\bar{u}}{\mathrm{d}\xi} - \frac{\bar{u}}{\xi}\right] &= \frac{E(1-\nu)}{(1+\nu)(1-2\nu)}\frac{2\sigma_0(1+\nu)(1-(\alpha\xi)^2)^{1/2}}{\sqrt{3}E\xi^2(1-\alpha^2)^{1/2}} \\ &= \frac{2\sigma_0(1-\nu)(1-(\alpha\xi)^2)^{1/2}}{\sqrt{3}\xi^2(1-2\nu)(1-\alpha^2)^{1/2}}\end{aligned} \tag{9.88}$$

The second term in Eq. (9.87) may be rewritten by inserting Eq. (9.75):

$$\frac{E}{(1+\nu)(1-2\nu)}\frac{\bar{u}}{\xi} = \frac{E}{(1+\nu)(1-2\nu)}\frac{B\alpha}{2}\left[\frac{(1-(\alpha\xi)^2)^{1/2}}{(\alpha\xi)^2} - \ln\left(\frac{1+(1-(\alpha\xi)^2)^{1/2}}{\alpha\xi}\right)\right] \tag{9.89}$$

Inserting the expression for B in Eq. (9.79) into Eq. (9.89) and tidying up:

$$\begin{aligned}\frac{E}{(1+\nu)(1-2\nu)}\frac{\bar{u}}{\xi} = &\frac{-2\sigma_0(1-(\alpha\xi)^2)^{1/2}}{2\xi^2\sqrt{3}(1-2\nu)(1-\alpha^2)^{1/2}} \\ &+ \frac{2\sigma_0\alpha^2}{2\sqrt{3}(1-2\nu)(1-\alpha^2)^{1/2}}\ln\left(\frac{1+(1-(\alpha\xi)^2)^{1/2}}{\alpha\xi}\right)\end{aligned} \tag{9.90}$$

Finally the expression for σ_r is obtained by adding Eq. (9.88) to Eq. (9.90):

$$\sigma_r = \frac{\sigma_0(1-(\alpha\xi)^2)^{1/2}}{\sqrt{3}\xi^2(1-\alpha^2)^{1/2}} + \frac{\sigma_0\alpha^2}{\sqrt{3}(1-2\nu)(1-\alpha^2)^{1/2}}\ln\left(\frac{1+(1-(\alpha\xi)^2)^{1/2}}{\alpha\xi}\right) \tag{9.91}$$

Thus, at the plastic-elastic interface ($\xi = 1$) the dimensionless radial stress $S = \sigma_r/\sigma_0$ becomes:

$$S(\xi=1) = S_1 = \frac{1}{\sqrt{3}}\left[1 + \frac{\alpha^2}{(1-2\nu)\sqrt{1-\alpha^2}}\ln\left(\frac{1+\sqrt{1-\alpha^2}}{\alpha}\right)\right] \tag{9.92}$$

9.1.3 Response Equations

Now we can determine the elastic-plastic interface ($\xi = 1$) velocity c by combining Eqs. (9.26), (9.28) and (9.86):

$$\gamma = \frac{V}{c} = \sqrt{\frac{2(1+\nu)\sigma_0}{\sqrt{3}E}} \tag{9.93}$$

The S_1 parameter in Eq. (9.30) is now given by Eq. (9.92), substituting into Eq. (9.30) gives:

$$\begin{aligned}S(\xi) = &\frac{\overbrace{\alpha^2}^{A}}{\sqrt{3}(1-2\nu)\sqrt{1-\alpha^2}}\left[\frac{(1-2\nu)\sqrt{1-\alpha^2}}{\alpha^2} + \ln\left(\frac{1+\sqrt{1-\alpha^2}}{\alpha}\right)\right] \\ &+ \frac{2}{\sqrt{3}}\left[\frac{E}{\sqrt{3}\sigma_0}\right]^n I(\xi) + \frac{\rho_t V^2}{2\sigma_0}\left(\gamma^2 - 2\ln\xi - \frac{\gamma^2}{\xi^2}\right)\end{aligned} \tag{9.94}$$

$$\text{where}\quad \alpha^2 = \frac{c^2}{c_d^2} = \frac{V^2\rho_t(1-2\nu)\sqrt{3}}{2(1-\nu)\sigma_0} \tag{9.95}$$

Replacing A in Eq. (9.94) with Eq. (9.95) and tidying up a bit yields,

$$\begin{aligned} S(\xi) =& \frac{1}{\sqrt{3}}\left[1+2\left(\frac{E}{\sqrt{3}\sigma_0}\right)^n I(\xi)\right] \\ &+ \frac{\rho_t V^2}{2\sigma_0}\left[\frac{1}{(1-\nu)\sqrt{1-\alpha^2}}\ln\left(\frac{1+\sqrt{1+\alpha^2}}{\alpha}\right)+\gamma^2-2\ln\xi-\frac{\gamma^2}{\xi^2}\right] \end{aligned} \tag{9.96}$$

Now we are going to concentrate on the integral $I(\xi)$ (for convenience renamed $I_2(\xi)$), we start by doing the substitution $\zeta = (\gamma/\xi)^2 \;\Rightarrow\; \mathrm{d}\xi/\xi = -\,\mathrm{d}\zeta/2\gamma^2$:

$$\begin{aligned} I_2(\xi) &= \int_\xi^1 \frac{1}{\xi}\left[\ln\left(\frac{\xi^2}{\xi^2-\gamma^2}\right)\right]^n \mathrm{d}\xi \\ &= -\frac{1}{2}\int_{\gamma^2/\xi^2}^{\gamma^2} \frac{1}{\zeta}[-\ln(1-\zeta)]^n \mathrm{d}\zeta \end{aligned}$$

And the last substitution $x = 1-\zeta \;\Rightarrow\; \mathrm{d}x = -\mathrm{d}\zeta$ gives:

$$I(\xi) = 2I_2(\xi) = \int_{1-\gamma^2/\xi^2}^{1-\gamma^2} \frac{(-\ln x)^n}{1-x}\mathrm{d}x \tag{9.97}$$

This finally gives us the dimensionless radial stress $S(\xi)$ in the plastic region:

$$\begin{aligned} S(\xi) =& \frac{1}{\sqrt{3}}\left[1+\left(\frac{E}{\sqrt{3}\sigma_0}\right)^n I(\xi)\right] \\ &+ \frac{\rho_t V^2}{2\sigma_0}\left[\frac{1}{(1-\nu)\sqrt{1-\alpha^2}}\ln\left(\frac{1+\sqrt{1-\alpha^2}}{\alpha}\right)+\gamma^2-2\ln\xi-\frac{\gamma^2}{\xi^2}\right] \end{aligned} \tag{9.98}$$

where α is given in Eq. (9.95) and $I(\xi)$ is given in Eq. (9.97). We can now express the radial stress σ_r at the cavity surface ($\xi = \gamma$, see Fig. 9.1):

$$\begin{aligned} \sigma_r(\xi=\gamma) = S(\xi=\gamma)\sigma_0 =& \frac{\sigma_0}{\sqrt{3}}\left[1+\left(\frac{E}{\sqrt{3}\sigma_0}\right)^n I(\xi=\gamma)\right] \\ &+ \frac{\rho_t V^2}{2}\left[\frac{1}{(1-\nu)\sqrt{1-\alpha^2}}\ln\left(\frac{1+\sqrt{1-\alpha^2}}{\alpha}\right)+\gamma^2-2\ln\gamma-1\right] \end{aligned} \tag{9.99}$$

$$\sigma_r = \sigma_s + B\rho_t V^2 \tag{9.100}$$

$$\text{where}\quad \sigma_s = \frac{\sigma_0}{\sqrt{3}}\left[1+\left(\frac{E}{\sqrt{3}\sigma_0}\right)^n \int_0^{1-\gamma^2}\frac{(-\ln x)^n}{1-x}\mathrm{d}x\right] \tag{9.101}$$

$$\text{and}\quad B = \frac{1}{2}\left[\frac{1}{(1-\nu)\sqrt{1-\alpha^2}}\ln\left(\frac{1+\sqrt{1+\alpha^2}}{\alpha}\right)+\gamma^2-2\ln\gamma-1\right] \tag{9.102}$$

where σ_s is the quasi-static stress required to open the cavity, and ρ_t is the target density, α is given in Eq. (9.95), and γ is given in Eq. (9.93).

9.1.4 Perforation Model

It is now necessary to develop an expression for the ballistic limit velocity v_{bl}, and expressions for the residual velocity v_r as a function of initial velocity v_i and ballistic limit velocity v_{bl}. First off

the force acting on the projectile during perforation can be found by using an approximation of Eq. (9.100):

$$\sigma_r = \sigma_s + B_0 \rho_t V^2 \tag{9.103}$$

where B_0 is determined through curve fitting Eqs. (9.95), (9.100) and (9.102), the radial cavity-expansion velocity V is decomposed further into its z component; $V = V_z \frac{\mathrm{d}r}{\mathrm{d}z}$, see Fig. 9.2

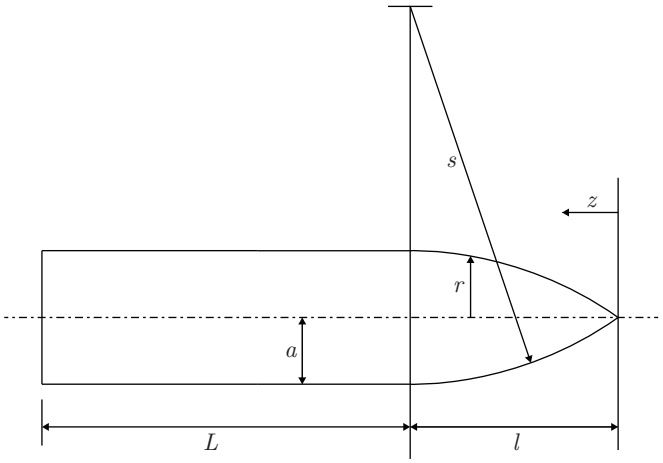

Figure 9.2: Ogival nose projectile with geometries.

By neglecting friction we obtain the force acting on the projectile:

$$\begin{aligned} F_z &= \int_0^{2\pi} \int_0^r \left[\sigma_s + B_0 \rho_t \left(V_z \frac{\mathrm{d}r}{\mathrm{d}z} \right)^2 \right] r \mathrm{d}r \mathrm{d}\theta \\ &= 2\pi \left(\int_0^l \sigma_s r \frac{\mathrm{d}r}{\mathrm{d}z} \mathrm{d}z + \rho_t B_0 \int_0^l \left(V_z \frac{\mathrm{d}r}{\mathrm{d}z} \right)^2 r \frac{\mathrm{d}r}{\mathrm{d}z} \mathrm{d}z \right) \qquad (9.104) \\ &= 2\pi (\sigma_s I_1 + \rho_t B_0 V_z^2 I_2) \qquad (9.105) \end{aligned}$$

where

$$r = (a - s) + \sqrt{s^2 - (l - z)^2} \tag{9.106}$$

$$\frac{\mathrm{d}r}{\mathrm{d}z} = \frac{l - z}{\sqrt{s^2 - (l - z)^2}} \tag{9.107}$$

We start by evaluating the integral I_1 in Eq. (9.105)

$$\begin{aligned} I_1 &= \int_0^l r \frac{\mathrm{d}r}{\mathrm{d}z} \mathrm{d}z = \int_0^l \left(a - s) + \sqrt{s^2 - (l - z)^2} \right) \frac{l - z}{\sqrt{s^2 - (l - z)^2}} \mathrm{d}z \\ &= \int_0^l \left[\frac{(a - s)(l - z)}{\sqrt{s^2 - (l - z)^2}} + (l - z) \right] \mathrm{d}z \\ &= \int_0^l \frac{(a - s)(l - z)}{\sqrt{s^2 - (l - z)^2}} \mathrm{d}z + \frac{1}{2} l^2 \qquad (9.108) \end{aligned}$$

using the substitution $u = s^2 - (l-z)^2$ gives:

$$I_1 = \frac{1}{2}\int_{s^2-l^2}^{s^2} \frac{a-s}{\sqrt{u}}\mathrm{d}u + \frac{1}{2}l^2 = (a-s)\left[\sqrt{u}\right]_{s^2-l^2}^{l^2} + \frac{1}{2}l^2$$
$$I_1 = \frac{1}{2}l^2 + (a-s)(s-\sqrt{s^2-l^2}) \tag{9.109}$$

in which $s = 2a\psi$, $l = a\sqrt{4\psi-1}$, and $(s-a) = a(2\psi-1)$. Inserting these expressions into Eq. (9.109) gives:

$$I_1 = \frac{a^2}{2} \tag{9.110}$$

For I_2 Eqs. (9.105) to (9.107) gives:

$$I_2 = \int_0^l \frac{(l-z)^3}{\sqrt[3]{s^2-(l-z)^2}}\left[(a-s) + \sqrt{s^2-(l-z)^2}\right]\mathrm{d}z$$
$$= \int_0^l \frac{(a-s)(l-z)^3}{\sqrt[3]{s^2-(l-z)^2}}\mathrm{d}z + \int_0^l \frac{(l-z)^3}{s^2-(l-z)^2}\mathrm{d}z \tag{9.111}$$

As for I_1 we use the substitution $u = s^2-(l-z)^2$, yielding

$$I_2 = \frac{(a-s)}{2}\left[\int_{s^2-l^2}^{s^2} s^2u^{-3/2}\,\mathrm{d}u - \int_{s^2-l^2}^{s^2} u^{-1/2}\,\mathrm{d}u\right] + \frac{1}{2}\int_{s^2-l^2}^{s^2}\frac{s^2}{u}\mathrm{d}u - \frac{1}{2}\int_{s^2-l^2}^{s^2}\mathrm{d}u$$
$$= (a-s)\left[-\frac{s^2}{\sqrt{u}} - \sqrt{u}\right]_{s^2-l^2}^{s^2} + \frac{1}{2}\left[s^2\ln u - u\right]_{s^2-l^2}^{s^2}$$
$$= (a-s)\left(-2s + \frac{s^2}{\sqrt{s^2-l^2}} + \sqrt{s^2-l^2}\right) + \frac{s^2}{2}\ln\left(\frac{s^2}{\sqrt{s^2-l^2}}\right) - \frac{1}{2}l^2 \tag{9.112}$$

And finally in terms of a and ψ:

$$I_2 = a^2\left[4\psi^2\ln\left(\frac{2\psi}{2\psi-1}\right) - (2\psi+\frac{1}{2})\right] \tag{9.113}$$

Inserting Eqs. (9.109) and (9.113) into Eq. (9.105) gives

$$F_z = 2\pi\sigma_s\frac{a^2}{2} + 2\pi\rho_t B_0 V_z^2 \cdot a^2\left[4\psi^2\ln\left(\frac{2\psi}{2\psi-1}\right) - (2\psi-\frac{1}{2})\right]$$
$$F_z = \pi a^2\left(\sigma_s + \rho_t B_0 N(\psi) V_z^2\right) \tag{9.114}$$

$$\text{where} \quad N(\psi) = 8\psi^2\ln\left(\frac{2\psi}{2\psi-1}\right) - (4\psi+1) \tag{9.115}$$

Newton's second law states

$$m\frac{\mathrm{d}V_z}{\mathrm{d}t} + F_z = mV_z\frac{\mathrm{d}V_z}{\mathrm{d}z} + F_z = 0 \tag{9.116}$$

$$\tag{9.117}$$

where m is the mass of the projectile given by [33]

$$m = \pi a^2\rho_p\left(L + \frac{k_1}{3}\right) \tag{9.118}$$

$$\text{where} \quad k_1 = \left(4\psi^2 - \frac{4\psi}{3} + \frac{1}{3}\right) - \frac{4\psi^2(2\psi-1)}{\sqrt{4\psi-1}}\arcsin\left[\frac{\sqrt{4\psi-1}}{2\psi}\right] \tag{9.119}$$

$$\text{and} \quad \psi = \frac{1}{4}\left[\left(\frac{l}{a}\right)^2 + 1\right] \tag{9.120}$$

ψ is the caliber radius-head (CRH) for the ogival nose, ρ_p is the projectile density, L is the projectile shank length, and l is the projectile nose length (see Fig. 9.2). Inserting Eqs. (9.114) and (9.118) into Eq. (9.116) yields

$$V_z \frac{\mathrm{d}V_z}{\mathrm{d}z} = A + BV_z^2 \tag{9.121}$$

$$\text{where} \quad A = \frac{-\sigma_s}{\rho_p(L + k_1 l)} \quad \text{and} \quad B = \frac{-\rho_t B_0 N(\psi)}{\rho_p(L + k_1 l)} \tag{9.122}$$

dividing Eq. (9.121) with its right hand side, and multiplying with $\mathrm{d}z$ gives

$$\frac{V_z}{A + BV_z^2}\mathrm{d}V_z = \mathrm{d}z \tag{9.123}$$

In order to obtain an expression for the ballistic limit velocity v_{bl} we integrate the left hand side from v_{bl} to 0 (recall that v_{bl} is the striking velocity giving 0 residual velocity v_r), and the right hand side over the plate thickness, i.e. from 0 to h. We get:

$$\int_{v_{bl}}^{0} \frac{V_z}{A + BV_z^2}\mathrm{d}V_z = \int_0^h \mathrm{d}z \quad \Rightarrow \quad I_1 = h \tag{9.124}$$

Implementing the substitution $u = A + BV_z^2$ yields

$$I_1 = \frac{1}{2B}\int_{A+Bv_{bl}^2}^{A} \frac{\mathrm{d}u}{u} = h$$

$$I_1 = \frac{1}{2B}\ln\left(\frac{A}{Bv_{bl}^2}\right) \tag{9.125}$$

Inserting Eq. (9.125) into Eq. (9.124) and solving for v_{bl} gives:

$$v_{bl} = \sqrt{\frac{\sigma_s}{\rho_t B_0 N(\psi)}\left(\exp\left[\frac{2\rho_t B_0 N(\psi)h}{\rho_p(L + k_1 l)}\right] - 1\right)} \tag{9.126}$$

Now we need to obtain an expression for the residual velocity v_r, this is done by integrating Eq. (9.123) from $z = 0$ to $z = h$, and $V_z = v_i$ to $V_z = v_r$, giving

$$\ln\left(\frac{A + Bv_r^2}{A + Bv_i^2}\right) = 2Bh \tag{9.127}$$

$$v_r^2 = \frac{A\left(\exp\left(2Bh\right) - 1\right)}{B} + v_i^2 \exp\left(2Bh\right) \tag{9.128}$$

Multiplying Eq. (9.128) with $\exp\left(-2Bh\right)$ gives:

$$v_r^2 \exp\left(-2Bh\right) = v_i^2 - v_{bl}^2$$

$$v_r = \sqrt{v_i^2 - v_{bl}^2}\sqrt{\exp\left[-\frac{2\rho_t B_0 N(\psi)h}{\rho_p(L + k_1 l)}\right]} \tag{9.129}$$

A power series expansion [43] of the last term on the right hand side of Eqs. (9.126) and (9.129) give the final expressions for v_{bl} and v_r:

$$v_{bl} = \left(\frac{\sigma_s}{\rho_t B_0 N(\psi)}\right)^{1/2} \left(1 + C + \frac{2}{3}C^2\right)^{1/2} \tag{9.130}$$

$$v_r = \left(v_i^2 - v_{bl}^2\right)^{1/2} \left(1 - C + \frac{1}{2}C^2\right)^{1/2} \tag{9.131}$$

$$\text{where} \quad C = \frac{h}{(L + k_1 l)} \frac{\rho_t}{\rho_p} B_0 N(\psi) \tag{9.132}$$

9.1.5 Results

All the equations needed to calculate the ballistic limit curves with CCET are now obtained. First we use Eq. (9.103) to approximate Eqs. (9.100) to (9.102) by conducting a curve fit in MATLAB. The value of B_0 found from this procedure is used in Eqs. (9.128) and (9.129) to calculate ballistic limit velocity v_{bl} and the ballistic limit curve. It is worth noticing that the integral in Eq. (9.101) is troublesome since the integrand goes to infinity for $x = 0$, this problem was solved by starting at a small x, and then applying Simpson's integration rule [43]. Since the shank of the APM2 bullet is truncated towards the end (Fig. 9.2), the shank length L and the nose length l have to be calculated from Eqs. (9.118) to (9.120). In Børvik et al. [18] different measurements of the 7.62 mm APM2 projectile were given; i.e. mass $m = 5.25$ g, diameter $2a = 6.17$ mm, and caliber radius head $\psi = 3.0$. This gives $L = 16.8$ mm and $l = 10.2$ mm. For the 20 mm ogival projectile measurements are given in Fig. 5.3a: $L = 62$ mm, $l = 33$ mm, and $a = 10$ mm.

Since the work-hardening law given in Eq. (9.8) lacks the constant term used in the previous calibration (see Section 6.1), another curve fit is performed. A script calculating new material constants and the ballistic limit curves is written in MATLAB (see Appendix E). The results can be seen in Table 9.1 and Figs. 9.3 and 9.4.

Table 9.1: Results obtained from MATLAB.

Temper	**Projectile**	n	B_0	C	$v_{bl,\text{CCET}}$ (m/s)	$v_{bl,\text{REAL}}$ (m/s)	**Deviation**
AA6070-O	APM2	0.2129	3.820	0.1503	357.58	348.0	2.75%
				0.0	331.24	348.0	4.82%
AA6070-T4	APM2	0.1664	3.168	0.1246	530.52	506.0	4.85%
				0.0	498.00	506.0	1.58%
AA6070-T6	APM2	0.0496	2.824	0.1111	595.18	563.0	5.72%
				0.0	562.56	563.0	0.08%
AA6070-T7	APM2	0.0364	2.868	0.1128	566.68	529.0	7.12%
				0.0	535.14	529.0	1.16%
AA6070-O	Ogival	0.2129	3.820	0.04218	178.90	186.9	4.28%
				0.0	175.14	186.9	5.93%
AA6070-T4	Ogival	0.1664	3.168	0.03498	267.96	246.3	8.79%
				0.0	263.29	246.3	6.90%
AA6070-T6	Ogival	0.0496	2.824	0.03119	302.14	222.1	36.04%
				0.0	297.44	222.1	33.92%
AA6070-T7	Ogival	0.0364	2.868	0.03167	287.49	246.9	16.44%
				0.0	282.94	246.9	14.60%

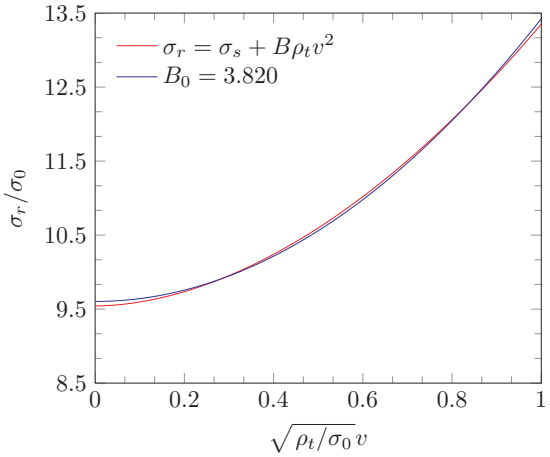

(a) AA6070-O

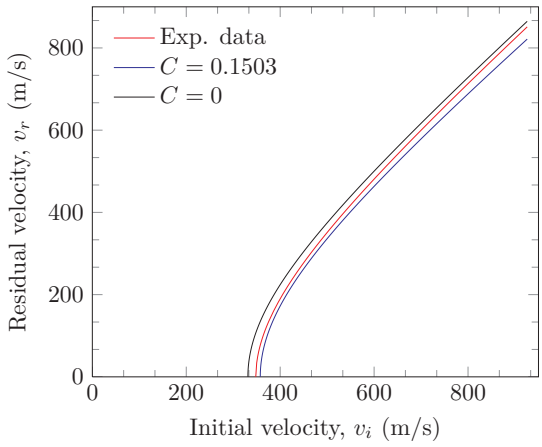

(b) AA6070-O

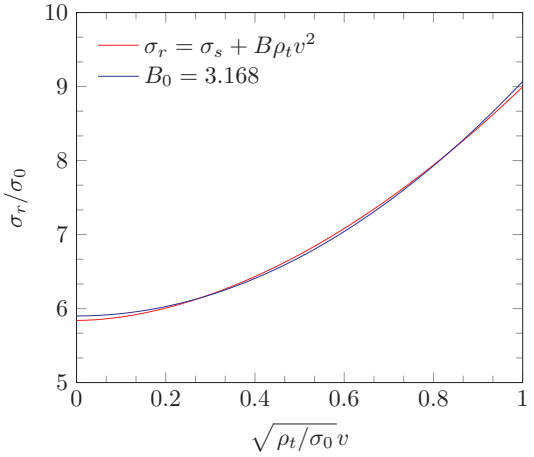

(c) AA6070-T4

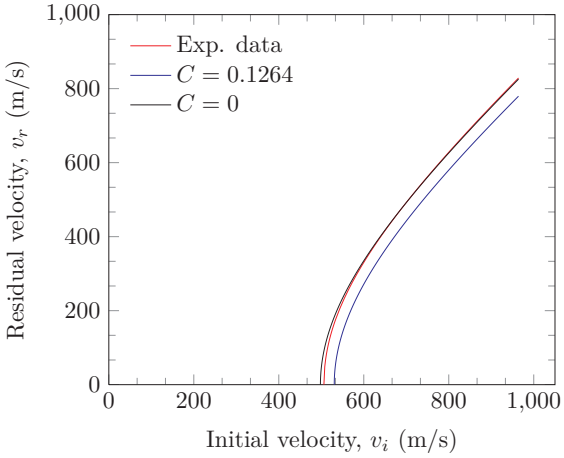

(d) AA6070-T4

Figure 9.3: Continues ...

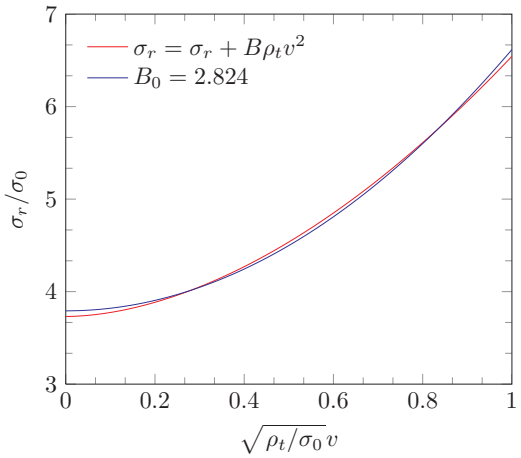

(e) AA6070-T6

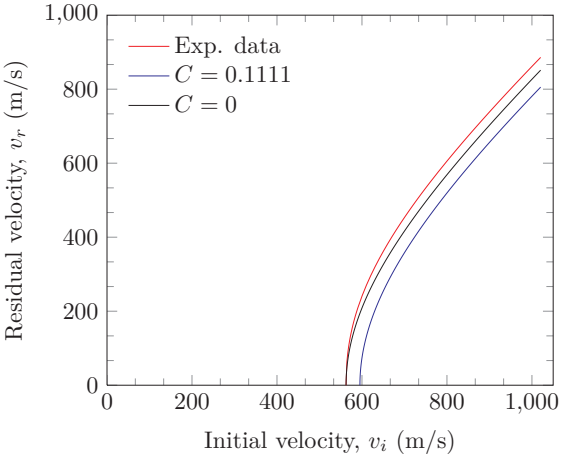

(f) AA6070-T6

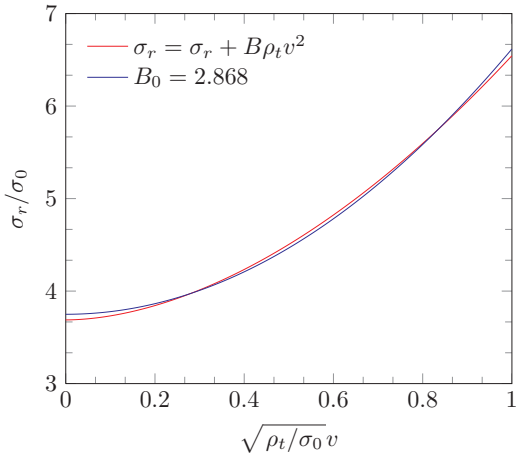

(g) AA6070-T7

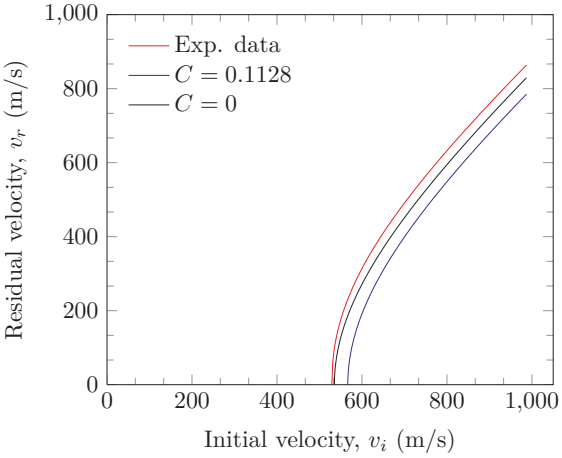

(h) AA6070-T7

Figure 9.3: Determination of ballistic limit curves for 7.62 mm APM2 bullets using CCET. Figures to the left illustrates curve fitting of Eqs. (9.93), (9.95) and (9.100) to (9.102), figures to the right displays the result.

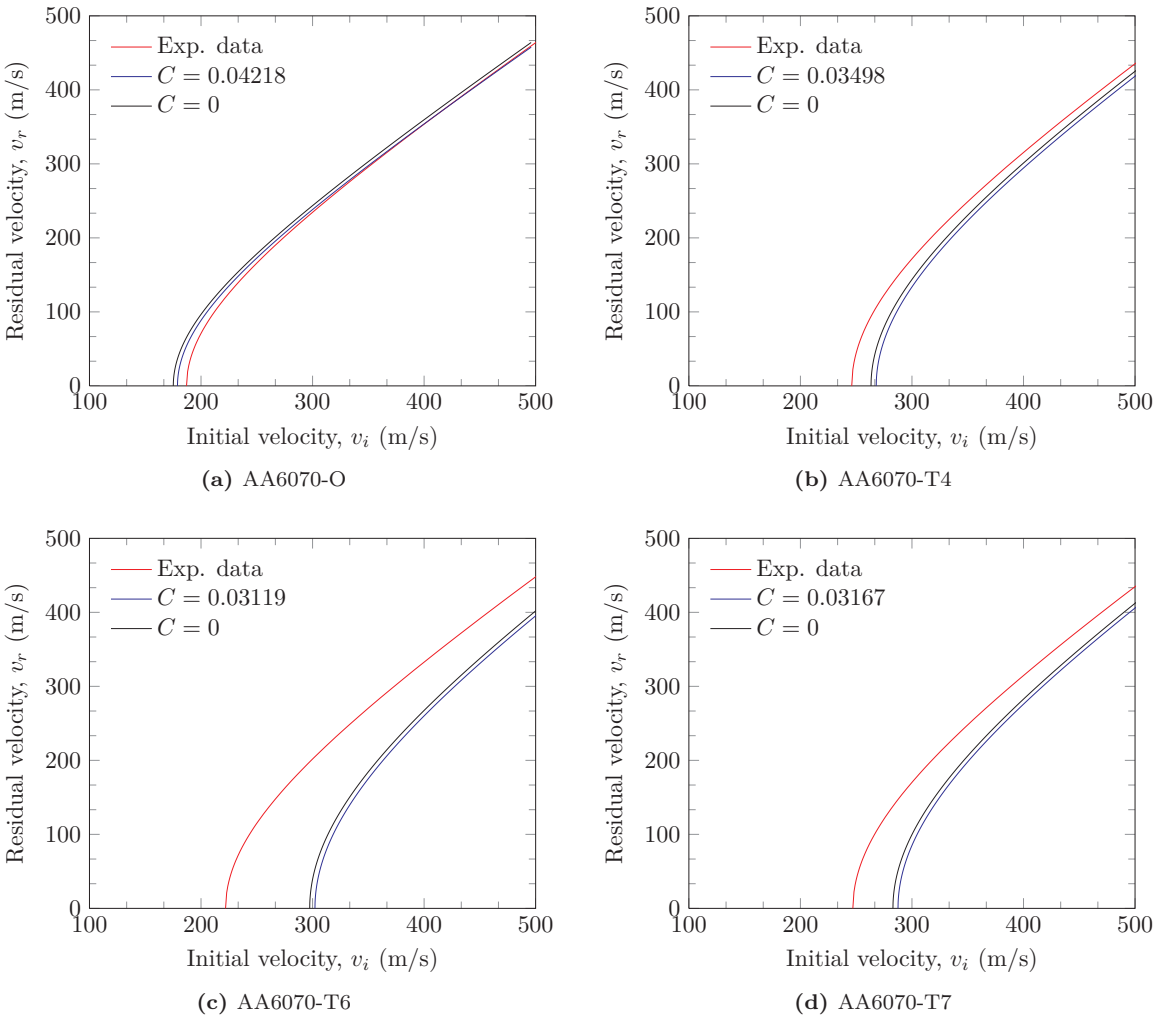

(a) AA6070-O **(b)** AA6070-T4

(c) AA6070-T6 **(d)** AA6070-T7

Figure 9.4: Determination of ballistic limit curves for 20 mm ogival projectiles using CCET.

When CCET is applied to the case with 20 mm APM2 bullets, the ballstic limit curves lie very close to the experimental results (Fig. 9.3). The results when 20 mm ogival projectiles are less accurate and even unconservative, specifically for the T6-temper. The Cylindrical Cavity Expansion Theory is, as the name implies, based on cylindrical ductile hole growth and cannot accurately describe the fragmentation that takes place in AA6070-T6 when impacted by ogival projectiles.

9.2 Estimation of Ballistic Limit Velocity for Blunt Projectiles

To get an initial estimate of what the ballistic limit velocity can be in the case of a blunt projectile hitting the aluminium alloy in question in this thesis, an analytical method based on conservation laws is given here (this entire section is based on derivations by Backman and Goldsmith [6] and Børvik [12]). Three fundamental conservation laws exist: conservation of mass Eq. (9.133), conservation of momentum Eq. (9.134), and conservation of energy Eq. (9.135)

$$m = \int_V \rho \mathrm{d}V = \text{constant} \tag{9.133}$$

$$\vec{p} = \int_V \vec{v}\rho \mathrm{d}V = \text{constant} \tag{9.134}$$

$$\Delta K = Q + W \tag{9.135}$$

If no heat transfer to the surroundings is assumed, then $Q = 0$ and $\Delta K = K_i - K_f = W$. This means that the change in kinetic energy is equal to the work done in the system. The change in kinetic energy when a projectile is slowed down from its ballistic limit velocity to a complete stop is expressed as

$$\Delta K = \frac{1}{2} m_p v_{bl}^2 \tag{9.136}$$

Where m_p is the mass of a plug, which is approximated to be the mass of a 20 mm long aluminium cylinder with diameter, d_p.

The plate does work to stop the projectile, and this work is carried out by several different mechanisms. Local work (W_l), global work (W_g), projectile work (W_p), elastic work (W_{el}) and frictional work (W_f) Eq. (9.137).

$$\Delta K = W_l + W_g + W_p + W_{el} + W_f = W \tag{9.137}$$

In this case, the plate is thick compared to the diameter of the projectile, $h_t/d_p \geq 1$, so the response of the system is dominated by the work done in a narrow shear band. As an approximation, the total work (W) is set to the local work (W_l) that can be expressed as the area of the walls of the cylindrical plug that is pushed away by the projectile multiplied with the shear strength of the target material at hand. The material tests conducted did not give the shear strength of each aluminium temper, so τ_0 can be estimated from the value of σ_0 directly

$$\tau_0 = \frac{\sigma_0}{\sqrt{3}} \tag{9.138}$$

or by incorporating the work under the true stress-strain curve [38]

$$\bar{\tau}_0 = \left(\frac{1}{\epsilon_f} \int_0^{\epsilon_f} \sigma_t \mathrm{d}\epsilon_l \right) \frac{1}{\sqrt{3}} \tag{9.139}$$

In either case the local shear work can now be found:

$$W_l = F_s h_t = \tau A_s h_t = 2\pi r_p h_t^2 \tau \tag{9.140}$$

By combining Eq. (9.136) and Eq. (9.140) an approximation of the ballistic limit velocity can be calculated

$$v_{bl} = \left(\frac{4\pi r_p h_t^2 \tau}{m_p} \right)^{1/2} \tag{9.141}$$

The values of the parameters used in Eq. (9.141) are given in Table 9.2.

Table 9.2: Material constants for use in analytical estimate for v_{bl}.

r_p (mm)	h_t (mm)	m_p (kg)
10	20	0.197

Table 9.3: τ_0 from Eq. (9.138) and Eq. (9.139)

Temper	τ_0 from Eq. (9.138) (MPa)	$\bar{\tau}_0$ from Eq. (9.139) (MPa)
AA6070-O	29	110
AA6070-T4	108	229
AA6070-T6	215	253
AA6070-T7	197	227

After estimating the ballistic limit velocity, v_{bl}, the expression proposed by Recht-Ipson (Eq. (2.18)) $v_r = \left[\frac{m_{pl}}{m_p+m_{pl}}\right]\left(v_i^2 - v_{bl}^2\right)^{1/2}$ can be used to find the relationship between v_i and v_r. The results are plotted in Fig. 9.5. The values obtained from this will most likely give unconservative results due to the fact that several energy dissipating mechanisms are omitted. Also, the shear strength of the material is calculated directly from σ_0 (and fracture strain). By comparing these results to values commonly found in literature it is seen that our residual velocity-values might be too small. The simple analytical method does not take into account delamination, spalling, fragmentation and other mechanisms that can be observed on the post-experiment photos of the bullet holes in Chapter 5.

The massive simplification that has been done in this section can to some extent be defended: a target thickness of 20 mm makes the local plastic work the dominant mechanism. Global work is negligible at target thicknesses of $h_t > 5$ mm. Plastic work in the projectile is negligible due to the high strength of the steel used compared to the aluminium. The effects of friction and elastic work is generally considered to be small in penetration problems, i.e they are negligible too [61].

By comparing the results in Table 9.4 and Fig. 9.5, we observe that τ_0 give conservative estimates for AA6070-O, OK for T4 and unconservative for -6 and T7; while $\bar{\tau}_0$ give estimates that are OK for AA6070-O, and unconservative for the remaining tempers, i.e. one should be careful designing protective structures based on this simplified method.

Table 9.4: v_{bl} for 20 mm blunt projectiles from experiments and the simplified analytical analyses.

Temper	$v_{bl,\mathrm{EXP}}$ (m/s)	v_{bl,τ_0} (m/s)	$v_{bl,\bar{\tau}_0}$ (m/s)
AA6070-O	157.0	124.7	20.6%
AA6070-T4	175.7	174.5	0.7%
AA6070-T6	162.0	161.5	0.3%
AA6070-T7	166.0	157.5	5.1%

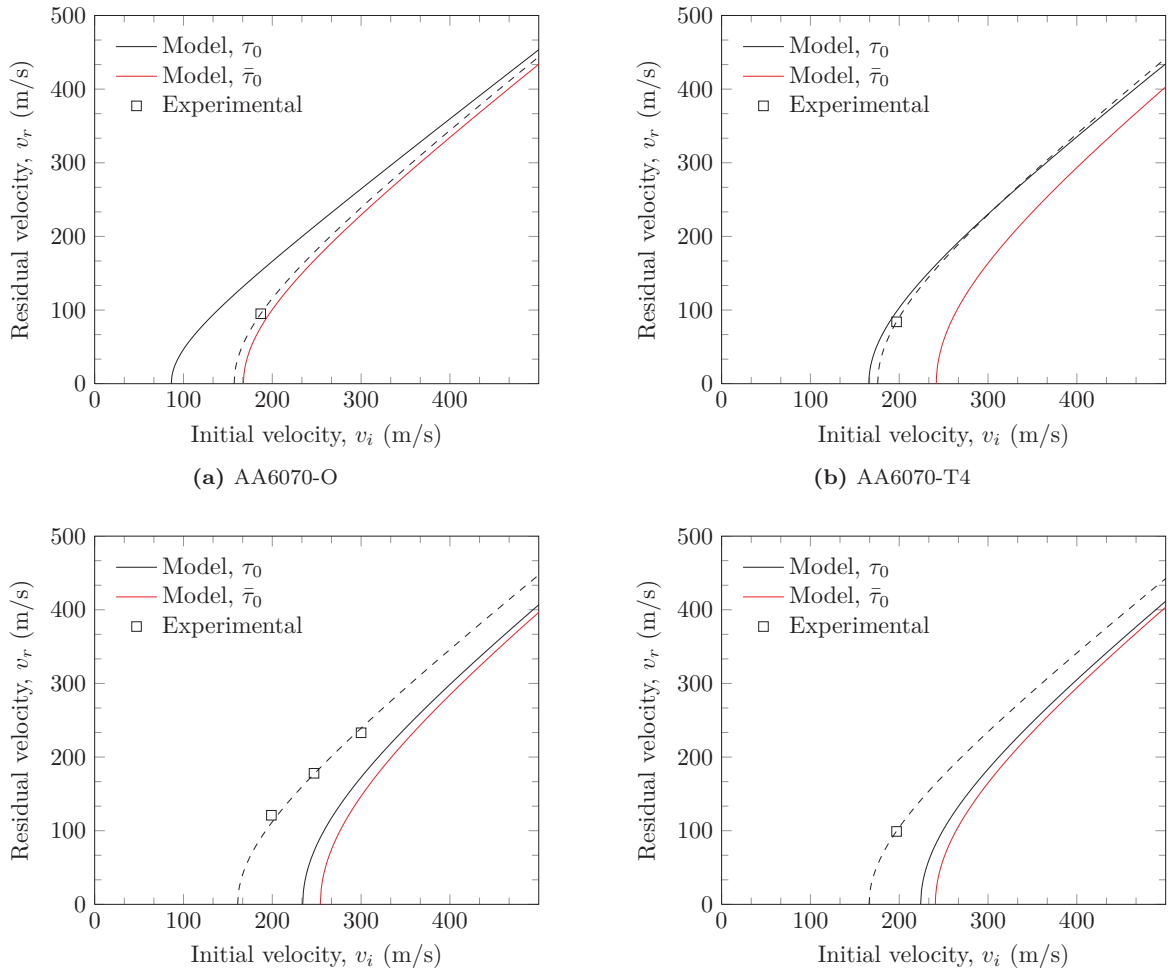

(a) AA6070-O

(b) AA6070-T4

(c) AA6070-T6

(d) AA6070-T7

Figure 9.5: Determination of ballistic limit curves for 20 mm blunt projectiles using a simplified analytical method with two different estimates for the shear strength.

Chapter 10

Case Study: NaMo

10.1 Introduction

Physical experimentation and testing are integral parts of evaluating new materials, but the process is time consuming and expensive. A method for designing new materials and structures with only numerical simulations would save both time and money, seeing that the ballistic properties of aluminium are dependent on both chemical composition and heat treatment, and that it is cumbersome to test the effect of these parameters thoroughly.

The Nanostructure Model, or NaMo, is a computer code that on the basis of the chemical composition and heat treatment of Al-Mg-Si-alloys can predict the stress-strain curve. This is done by using a precipitation model, a yield strength model and a work hardening model. The precipitation model calculates a particle size distribution that the yield strength model can use to find the room temperature yield stress and that the work hardening model can use to find the hardening curve [50].

Dr. Ole R. Myhr, Adjunct Professor at NTNU, received the composition for AA6070 and the heat treatment processes for the O-, T4-, T6- and T7-temper. In return he provided the true stress-plastic strain curves which he used NaMo to create.

10.2 Comparison to the Real Data

Fig. 10.1 show the true stress-plastic strain curves from NaMo and from the material tests. NaMo cannot describe the stadium 4 hardening, so the true stress-plastic strain curves are flat at high plastic strains [38]. Material failure is not a part of the model, so no fracture criterion can be calibrated from the NaMo-results; it is worth noticing that the hardening from NaMo stops at plastic strains approximately where the hardening stops (and fracture takes place) in experiments. However, in the following numerical simulations the infinite true stress-plastic strain curves displayed in Fig. 10.1 are used, because in this case study we are not supposed to know the exact point of failure.

10.3 Calibration of Material Parameters

Similar to the exercise carried out in Section 6.1 the material parameters of the Voce work-hardening law in the MJC constitutive relation were determined through a curve fitting procedure in MATLAB. The results of all the fits are excellent, and they are practically indistinguishable from the NaMo-curves shown in Fig. 10.1, the material model parameters from the Voce work-hardening law can be seen in Table 10.1.

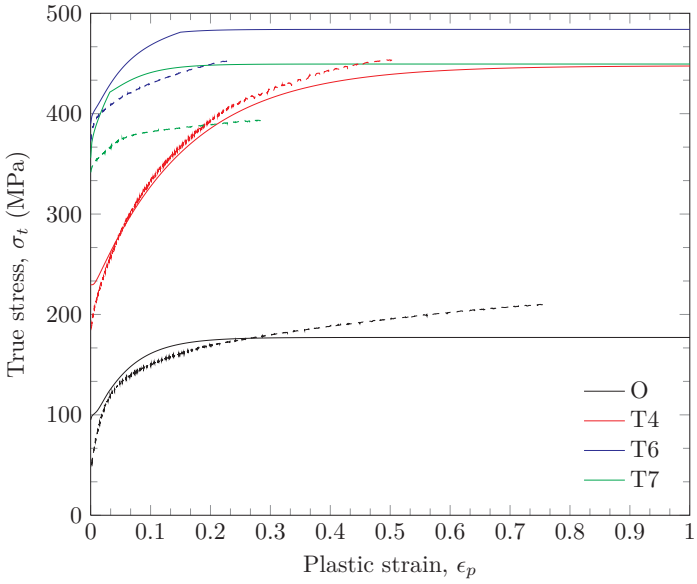

Figure 10.1: Results from NaMo-software in solid lines compared to experimental data in dashed lines.

Table 10.1: Material parameters obtained from direct calibration in MATLAB.

Temper	$\boldsymbol{A}$ (MPa)	$\boldsymbol{C_1}$	$\boldsymbol{C_2}$	$\boldsymbol{Q_1}$ (MPa)	$\boldsymbol{Q_2}$ (MPa)
AA6070-O	90.6	16.41	16.42	43.34	43.34
AA6070-T4	220.2	6.35	6.35	114.50	114.50
AA6070-T6	391.6	15.80	15.80	48.0010	48.29
AA6070-T7	360.1	17.098	82.66	49.063	40.70

10.4 Ballistic Analyses

As already mentioned, a fracture criterion cannot be calibrated from the Nanostructure Model. This means that ballistic experiments where fracture is a dominating part of the failure mode will be impossible to model correctly. The blunt projectile experiments where shearing is expected (and already proved by experimental work in Chapter 5 and with LS-DYNA Section 8.2) can not be appropriately recreated with input exclusively from NaMo. However, experiments where ductile hole growth dominate the response can be modeled with a pin-hole at the point of impact. This mode of failure is distinct in O, T4 and T7 with 20 mm ogival projectiles and 7.62 mm APM2 bullets. Despite the fragmentation that takes place in the T6 temper, simulations are conducted for this plate configuration too. By including a small pin-hole in the plate-mesh we can effectively remove the need for a fracture criterion; previous work has been done where the effect of a pin-hole is investigated, and in general the effect is seen to be very small [17]. Two limited penetration studies were performed: one with 20 mm ogival projectiles in an axisymmetric model in LS-DYNA, and one with 7.62 mm APM2 bullets in a 3D model in IMPETUS Afea. Ballistic limit velocities for both cases are given in Table 10.2

The ballistic tests conducted in LS-DYNA are done using the same model as in Section 8.4, an axisymmetric model with a 0.2 mm pinhole, 20 elements over the thickness (1 mm elements), and a fully clamped boundary. The material parameters from Table 10.1 are used. W_c is set to be 10^{20};

i.e. practically unbreakable. As expected the results are generally less conservative when the NaMo material data is used. The same tendency was seen when the real material data was used, but no fracture criterion was implemented in Section 8.4. In the case of T6 the results are unconservative, which might have resulted from the lack of fragmentation. The ballistic limit curves can be seen in Fig. 10.4

A new mesh was created for the IMPETUS analyses, see Fig. 10.2. Seeing that IMPETUS only supports 3D elements, the meshing around the pin-hole was a challenge. The solution was a square pin-hole with 1 mm edges. A 40x80 mm segment of the plate is modeled in the same fashion as in Section 7.2 with a symmetry constraint along the pin-hole edge. Only the steel core is used. In Fig. 10.3 some pictures from the penetration process are given, and from this we can see that the failure mechanism is forced to be ductile holegrowth.

$p = 2$ and $a = 1$ are used in the Recht-Ipson model because in this case study we have no experimentally determined values. By inspecting Fig. 10.5 it is clear that all the simulations are conservative, so all ballistic limit velocities are also conservative.

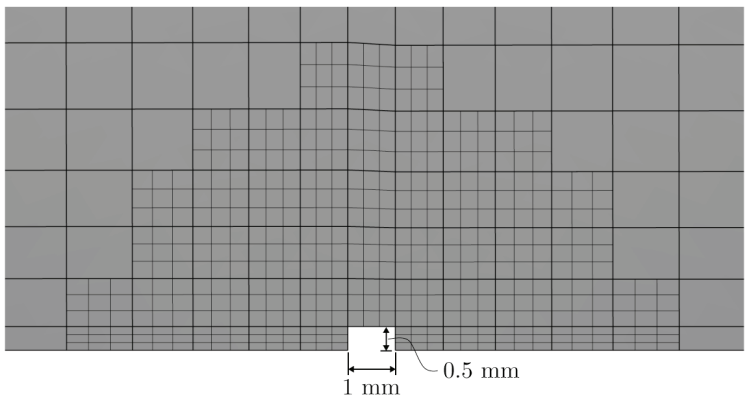

Figure 10.2: Overview of the impact area where cubic hexahedra elements are used and a 1 mm pin-hole is introduced.

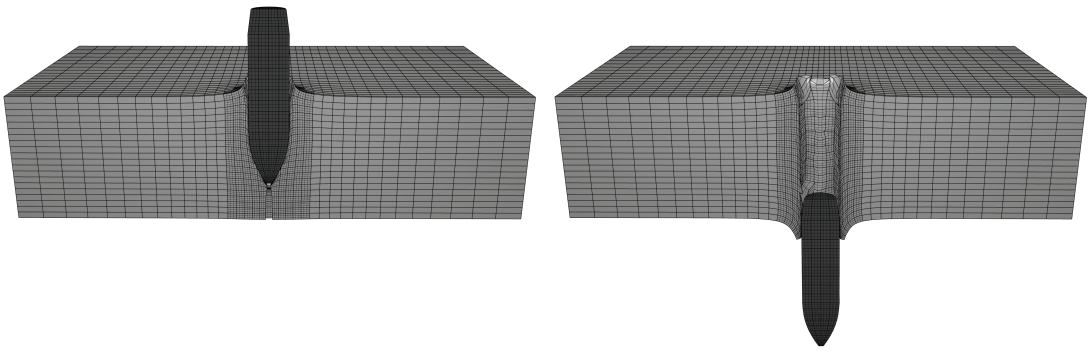

Figure 10.3: Pictures of the steel core penetrating the AA6070-O with $v_i = 549.3$ m/s and $v_r = 446.0$ m/s.

Table 10.2: Ballistic limit velocity, v_{bl}, for ogival projectile experiments compared to LS-DYNA and APM2 bullet experiments compared to IMPETUS with the NaMo material parameters.

Temper	20 mm Ogival			7.62 mm APM2		
	$v_{bl,\text{REAL}}$ (m/s)	$v_{bl,\text{LS-DYNA}}$ (m/s)	Dev.	$v_{bl,\text{REAL}}$ (m/s)	$v_{bl,\text{IMPETUS}}$ (m/s)	Dev.
AA6070-O	186.9	147.7	20.97%	348.0	320.6	7.87%
AA6070-T4	246.3	224.0	9.05%	506.2	452.0	10.71%
AA6070-T6	222.1	242.3	9.10%	562.5	504.3	10.35%
AA6070-T7	246.9	239.4	3.04%	529.1	490.2	7.35%

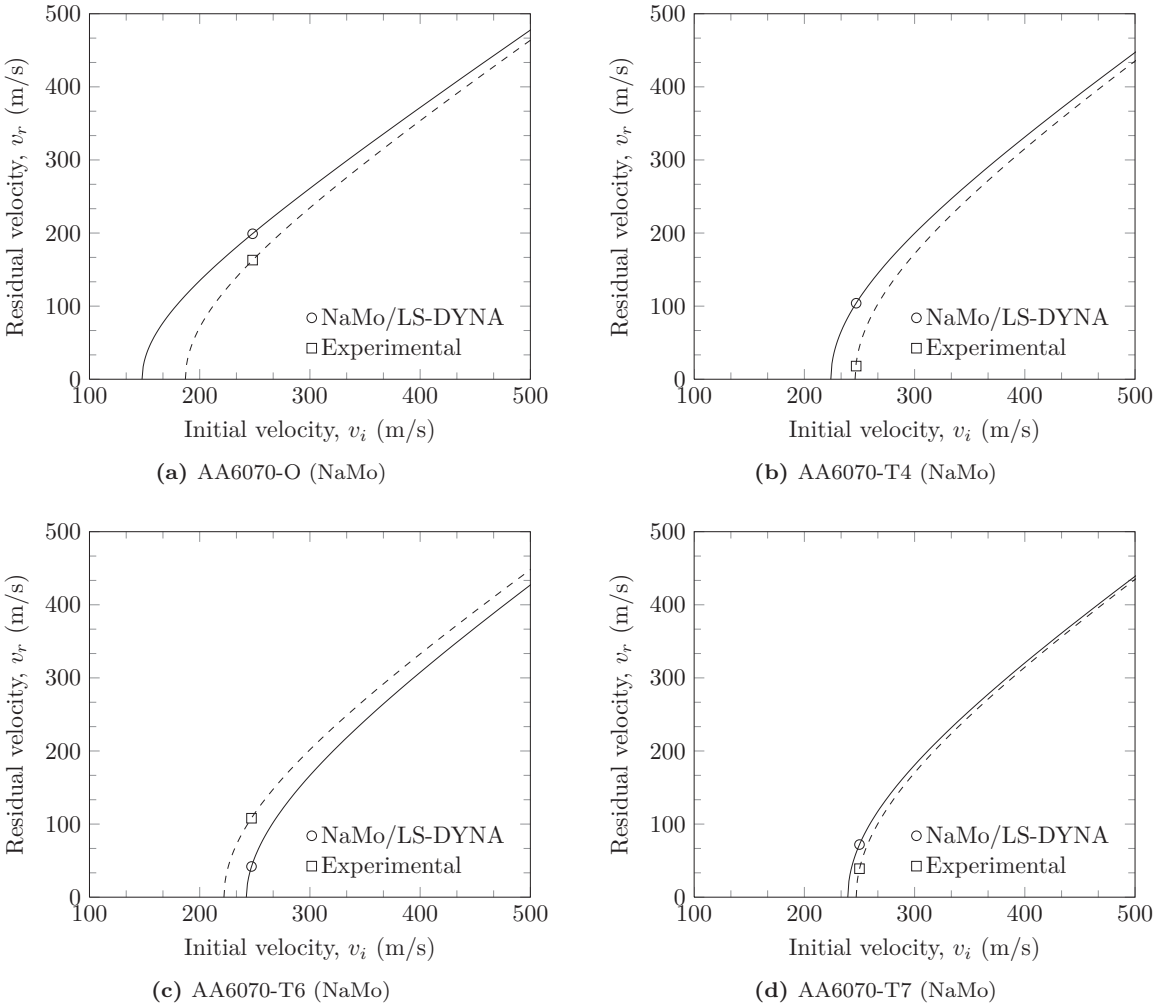

(a) AA6070-O (NaMo)

(b) AA6070-T4 (NaMo)

(c) AA6070-T6 (NaMo)

(d) AA6070-T7 (NaMo)

Figure 10.4: Numerical results for 20 mm ogival projectiles from LS-DYNA with material parameters from NaMo (using a 0.2 mm pin-hole) compared to experimental values.

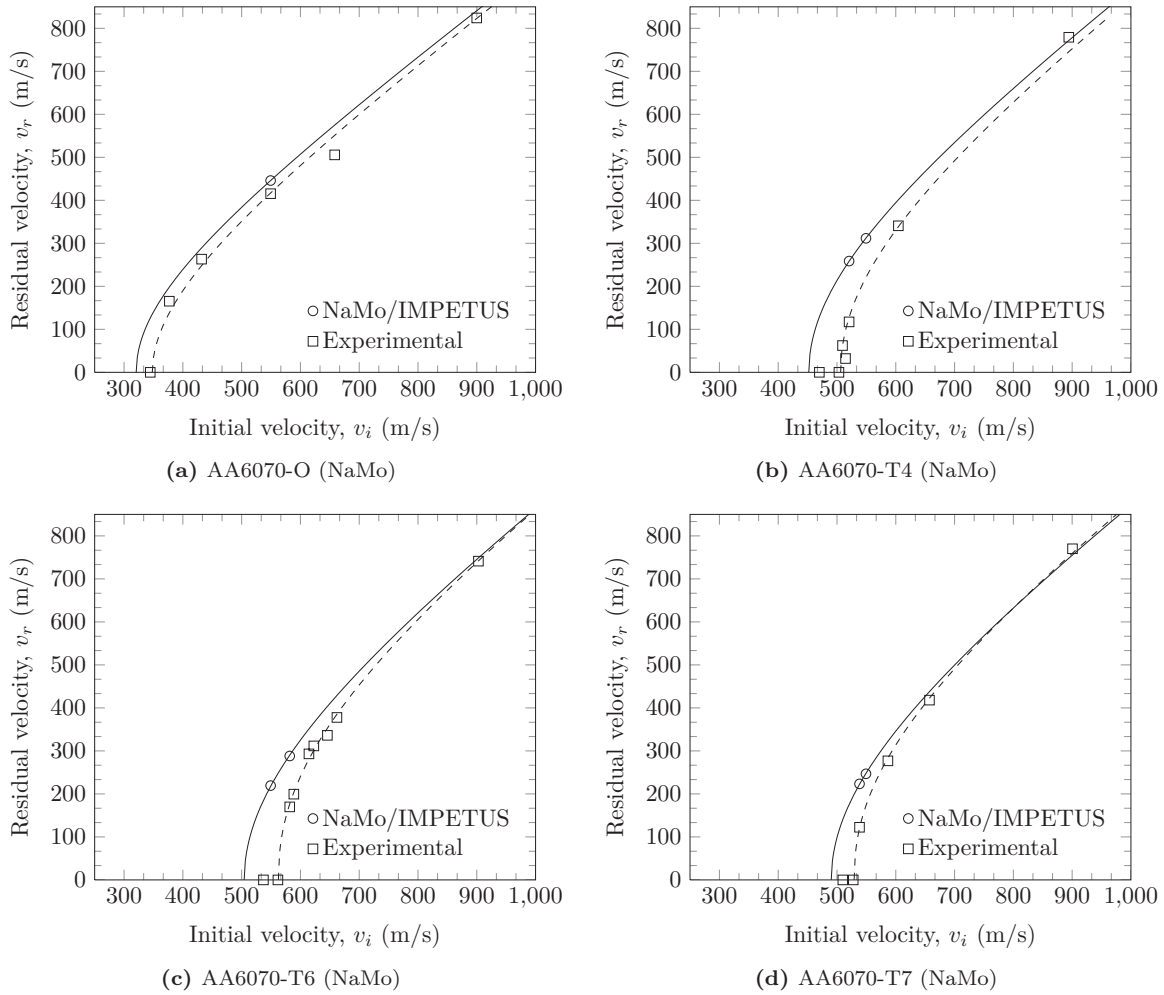

(a) AA6070-O (NaMo)

(b) AA6070-T4 (NaMo)

(c) AA6070-T6 (NaMo)

(d) AA6070-T7 (NaMo)

Figure 10.5: Numerical results for 7.62 mm APM2-bullets from IMPETUS with material parameters from NaMo (using a 1 mm pin-hole) compared to experimental values.

10.5 Conclusion

The general verdict from using the material parameters determined from the Nanostructure Model is that the results are good, taking into consideration that no physical experiments are carried out. However, it is unclear how much work and troubleshooting was needed to calibrate and use NaMo, since we were not a part of the process itself. In any case the results are promising, and it seems clear that the Nanostructure Model at this point in time can be used successfully in early design stages of Al-Mg-Si-alloys.

Chapter 11

Discussion

11.1 Fragmentation in Different Velocity Ranges

In the experimental work carried out for this thesis, ballistic tests in two velocity ranges have been conducted, namely the subordnance range ($25 - 500$ m/s) for the 20 mm blunt and ogival projectiles and the nominal ordnance range ($500 - 1300$ m/s) in which most of the experiments with 7.62 mm APM2 bullets can be classified. By choosing two velocities (one high and one low) for the APM2-bullets, and all experiments for the 20 mm projectiles, we can compare how the target plates respond to impacts within the different velocity regimes with different projectile shapes.

Table 11.1: Comparison of fragmentation that takes place in different tests.

Temper	**Projectile**	v_i	v_r	**Degree of fragmentation**	
		(m/s)	(m/s)	Front	Back
AA6070-O	7.62 mm APM2	899.9	824.1	Nothing	Many/Small
	7.62 mm APM2	377.0	165.4	Nothing	Nothing
	20 mm ogival	248.2	163.0	Nothing	Nothing
	20 mm blunt	186.5	95.3	Nothing	Nothing
AA6070-T4	7.62 mm APM2	894.3	779.2	Nothing	Many/Medium
	7.62 mm APM2	509.4	62.3	Nothing	Nothing
	20 mm ogival	246.5	18.2	Nothing	Very Few/Very Small
	20 mm blunt	196.5	84.3	Nothing	Some/Medium
AA6070-T6	7.62 mm APM2	902.8	741.3	Nothing	Many/Large
	7.62 mm APM2	614.5	293.1	Some/Small	Few/Small
	20 mm ogival	247.4	107.6	Few/Very Large	Some/Very Large
	20 mm blunt	198.9	120.9	Few/Very Large	Many/Large
AA6070-T7	7.62 mm APM2	900.6	780.1	Nothing	Many/Large
	7.62 mm APM2	538.3	122.4	Nothing	Few/Small
	20 mm ogival	250.0	39.4	Nothing	Very Few/Very Small
	20 mm blunt	197.2	98.6	Nothing	Some/Small

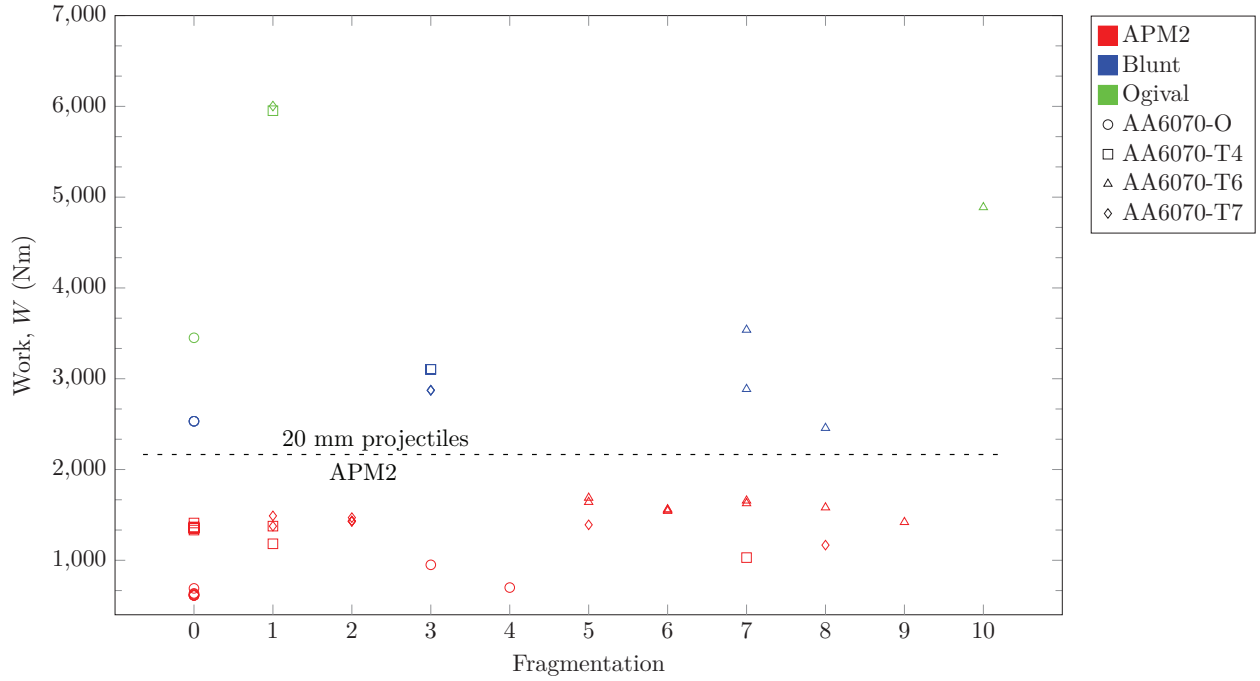

Figure 11.1: Work dissipated in the impact experiments plotted against a subjective measure of fragmentation for every ballistic tests conducted for this thesis.

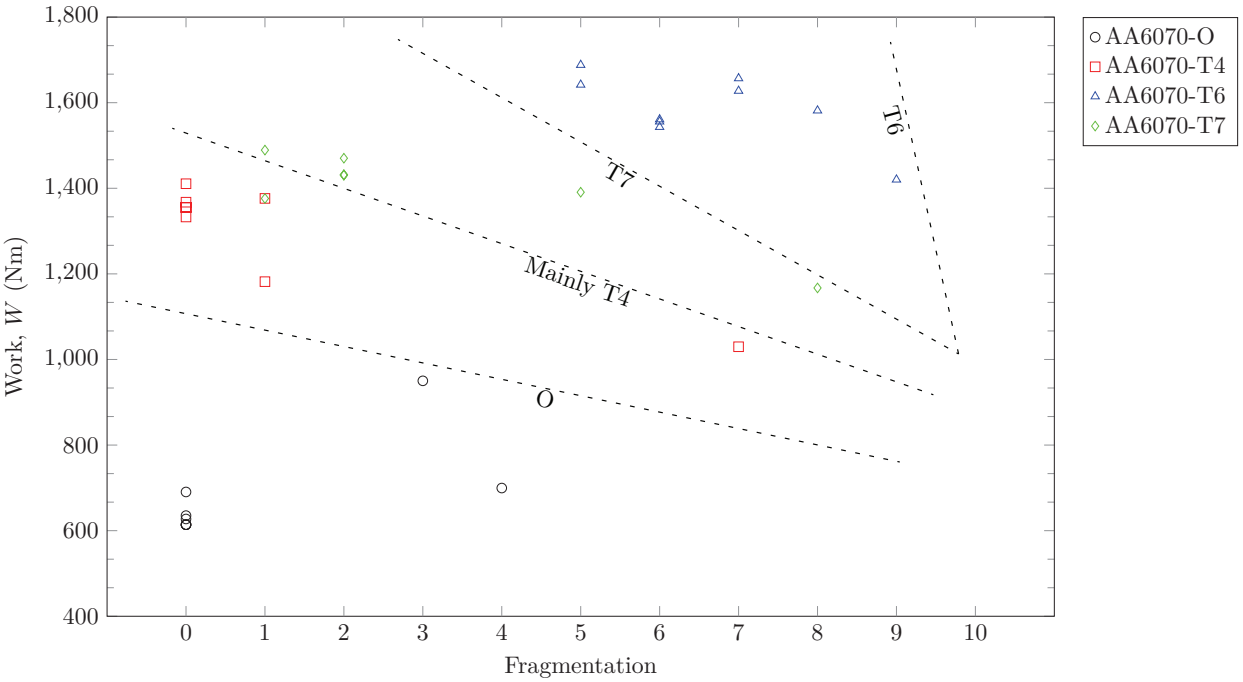

Figure 11.2: Work dissipated in the impact experiments for 7.62 mm APM2 bullets plotted against a subjective measure of fragmentation.

All experiments conducted in this thesis are shown in Fig. 11.1, and the experiments carried out with 7.62 mm APM2 bullets only are shown in Fig. 11.2. Here the work dissipated in each experiment

$$W = \frac{1}{2} m_p (v_i^2 - v_r^2) \tag{11.1}$$

is plotted against a quantitative and subjective measurement of fragmentation: a scale from 0 to 10, where 0 means no fragmentation, and 10 describes the fragmentation from AA6070-T6 impacted by a 20 mm ogival projectile (i.e. the maximum fragmentation seen in our experimental work). From these figures we can see that much fragmentation does not necessarily mean little energy dissipation under high impact velocities, instead when the weight of the projectile increases and the impact velocity decreases the energy dissipation is very dependent on degree of fragmentation. To design protective structures we have to be aware of the scale of the projectile relative to the protective material, seeing that excessive fragmentation can for some tempers, i.e. AA6070-T6 and AA7075-T651 lead to a drastic decrease in ballistic limit velocity. Ideally, a temper exhibiting low fragmentation and high strength would be optimal.

Table 11.1 shows the initial and residual velocities for a selection of the ballistic experiments and a short description of the fragmentation at both the front and rear. The description is subjective, of course, so high-speed images from the reported experiments are shown in Figs. 4.5, 4.7, 4.9, 4.11, 5.12 and 5.13. The T6-temper is the only temper that suffers fragmentation at the front of the plate, a few very large fragments for the 20 mm ogival projectile, and several small fragments when a 7.62 mm APM2 bullet was fired at a relatively low velocity. The back sides of the plates are more susceptible to fragmentation, and some of the plates more than others. Overall the O-temper experiences very little fragmentation, and the T6 experiences the most fragmentation. For the 7.62 mm APM2 bullets, high velocities means more fragmentation, and lower velocities means less fragmentation. The plate behavior in the experiments where the 20 mm ogival projectiles are used is somewhat more ductile for all tempers except T6. This might help explain why σ_0 can describe the internal ballistic ranking for the APM2-bullet but not for the ogival projectiles.

The plates experience no signs of fragmentation at the front of the plate when blunt projectiles are used. However, fragmentation takes place at the rear; excessively for T6 and more subtly for T4 and T7. By inspecting the high speed images for the two latter in Fig. 5.12 we can see that a small sheet of plate material is pushed out and separated from the plug.

11.2 Regarding the Boundary Conditions

A variety of boundary conditions have been used in this thesis, and they have been changed due to computational efficiency, model symmetry or for the sole purpose of investigating the effect boundary conditions have on the final results. Most of the time this final result is the residual velocity after penetration of the aluminium plate. In real life the target plates have been clamped by two crossover beams, which in turn are bolted to the rig, see Fig. 11.3.

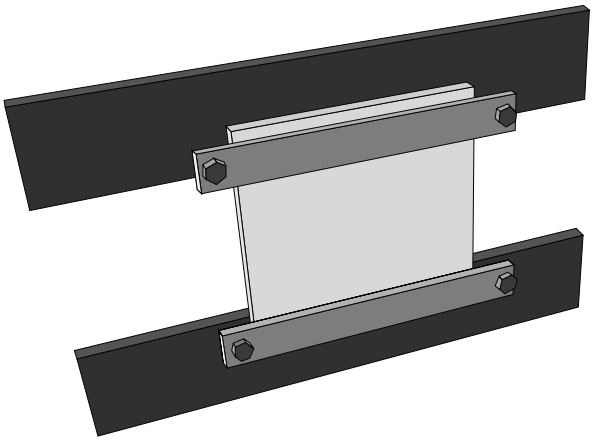

Figure 11.3: 3D-drawing of how the plate is attached to the rig.

11.2.1 IMPETUS

IMPETUS Afea has been used to analyze 7.62 mm APM2 bullets and 20 mm blunt and ogival projectiles. For the APM2-bullets three boundary conditions have been employed, see Fig. 11.4.

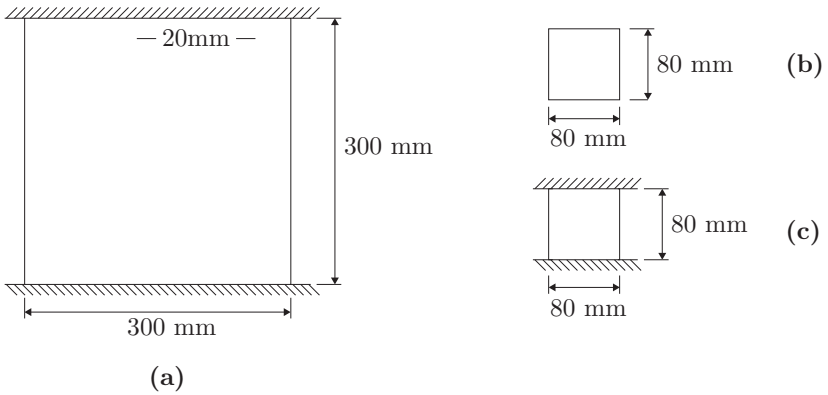

Figure 11.4: Idealized boundary conditions used in IMPETUS.**(a)** Full plate with clamped top and bottom. **(b)** Part of the plate without any boundary conditions. **(c)** Part of the plate with clamped top and bottom.

The results have shown that the effect of boundary conditions in high velocity, dynamic problems with mostly local deformation is small.

11.2.2 LS-DYNA

LS-DYNA has been used to analyze 20 mm blunt and ogival projectiles. In these analyses an axisymmetric mesh with a clamped boundary will represent the circular plates shown in Fig. 11.5. Many of the blunt simulations were run with the larger plate (Fig. 11.5a), absolutely no difference could be traced if an identical input-file was run with the smaller plate (Fig. 11.5b).

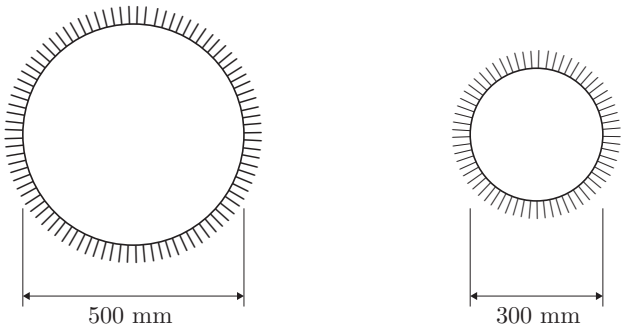

Figure 11.5: Idealized axisymmetric boundary conditions used in LS-DYNA. **(a)** $d = 500$ mm with clamped boudary, **(b)** $d = 300$ mm with clamped boundary.

11.3 Ballistic Performance Comparison

Earlier studies exist where the ballistic performance of various aluminium tempers and steel alloys are found, and in the following section we will investigate how AA6070-tempers compare to these studies.

11.3.1 Ballistic Performance Comparison: APM2 Bullets

As mentioned in the introduction, steel is often used in protective structures. Based on results available from past studies using 7.62 mm APM2 bullets, and results obtained in this study we will see how aluminium measures up to steel.

A direct comparison of the ballistic limit velocities will give biased results, seeing that high-strength steel generally is stronger than high-strength aluminium. On the other hand a big advantage for aluminium is its low weight. So by comparing the ballistic limit velocity divided by weight per m^2 for steel versus that of aluminium, we can get a feel of how the two materials behave relative to each other.

All the material results regarding steel is taken from Børvik et al. [16]. The ballistic limit velocities are found from experiments performed on 2×6 mm thick plates. The material parameters for AA6070 are taken from Chapter 3 in this thesis, while the other aluminium data is taken from the sources given in Table 11.2. All values are taken from the rolling direction.

Table 11.2 indicates that the ballistic limit when taking weight per m^2 into account is higher for aluminium than for steel. For aluminium the values are generally around 9, and for steel the values lie between 6 and 9. The results correspond to impacts of APM2-bullets with high striking velocity; under these conditions and including the factor of areal weight in the assessment, aluminium seems equal to or better than steel.

Results from this thesis and past work have shown that the yield stress is a decisive factor for v_{bl} when small-arms are fired at high velocities. Results shown in Table 11.2 do not contradict this statement.

Table 11.2: Parameters for steel and aluminium from this thesis and from literature using 7.62 mm APM2 projectiles. Please note that for the aluminium tempers v_{bl} is based on 20 mm plates, and that v_{bl} for the steel plates is found for 2×6 mm plates. Values from the rolling direction are used.

Designation	v_{bl} (m/s)	σ_0 (MPa)	ϵ_f	W_c (MPa)	ρ (kg/m^3)	**Weight** (kg/m^2)	v_{bl}/**Weight** (m^3/kg s)
AA5083-H116 [18]	492	244.0	0.16	47	2700	54.0	9.11
AA6070-O	348	50.5	0.84	151	2700	54.0	6.44
AA6070-T4	506	186.5	0.53	211	2700	54.0	9.37
AA6070-T6	563	372.5	0.26	115	2700	54.0	9.93
AA6070-T7	529	341.0	0.32	128	2700	54.0	9.80
AA6082-T4 [23]	414	195.0	0.53	199	2700	54.0	7.66
AA7075-T651 [19, 22]	628	520.0	0.11	106	2700	54.0	11.62
Weldox 500E	624	605.0	1.46	1516	7850	94.2	6.62
Weldox 700E	674	819.0	1.31	1486	7850	94.2	7.16
Hardox 400	741	1148.0	1.16	2013	7850	94.2	7.86
Domex Protect 500	837	1592.0	0.67	1484	7850	94.2	8.88
Armox 560T	871	1711.0	0.92	2310	7850	94.2	9.24

11.3.2 Ballistic Performance Comparison: Ogival Projectiles

As shown in Chapter 5 the T6-temper will lose its strength-advantage when a 20 mm ogival or blunt projectile is fired at lower velocities, which supports the findings of Børvik et al. [22] about AA7075-T651 and how delamination and fragmentation of the target takes place. The ballistic ranking of the tempers when impacted by 20 mm ogival projectiles is not the same as for 7.62 mm APM2 bullets, see Table 11.3.

The steels exhibit high yield strengths compared to the aluminium alloys. But when areal weight is considered the aluminium plates seem to perform better. (Please note the difference in yield stress for Weldox 700E between Table 11.2 and Table 11.3/Table 11.4).

Table 11.3: Parameters for some aluminium alloys and steels from previous studies compared to parameters from this thesis. 20 mm ogival projectiles striking 20 mm thick aluminium plates and 12 mm thick steel plates.

Designation	v_{bl} (m/s)	σ_0 (MPa)	**Weight** (kg/m^2)	v_{bl}/**Weight** (m^3/kg s)
AA5083-H116	244.0	244.0	54.0	4.52
AA6070-O	186.9	50.5	54.0	3.46
AA6070-T4	246.3	186.5	54.0	4.56
AA6070-T6	222.1	372.5	54.0	4.11
AA6070-T7	246.9	341.0	54.0	4.57
AA7075-T651	208.7	520.0	54.0	3.86
Weldox 460E [28]	295.9	515.0	94.2	2.76
Weldox 700E [28]	318.1	859.0	94.2	3.38
Weldox 900E [28]	322.2	995.0	94.2	3.42

11.3.3 Ballistic Performance Comparison: Blunt Projectiles

We found no ballistic limit using a blunt projectile for AA5083-H116 in the literature, but AA7075-T651 was found, and it seems that the tendencies found for the 20 mm ogival projectiles can not be directly transferred to the blunt projectiles. On the basis of the limited experimental data available, it appears that strength is the decisive factor with respect to ballistic limit velocity. However, additional experiments should be conducted.

The steels perform significantly worse than the aluminium under blunt nose impacts when areal weight is considered. It is unclear to us whether this behavior is caused by the steel plates being thinner than the aluminium plates. The ballistic limit velocity does not seem to be directly dependent on the yield stress for this configuration. It must be noted that the ballistic limit velocities found by Dey [28] are based on several experiments, and it was discovered that even though the ballistic limit velocity is higher for Weldox 460E than for Weldox 700E and 900E; the ballistic ranking is opposite at increased impact velocities.

Table 11.4: Parameters for some aluminium alloys and steels from previous studies compared to parameters from this thesis. 20 mm blunt projectiles striking 20 mm thick aluminium plates and 12 mm thick steel plates.

Designation	v_{bl} (m/s)	σ_0 (MPa)	**Weight** (kg/m^2)	v_{bl}**/Weight** (m^3/kg s)
AA6070-O	157.0	50.5	54.0	2.90
AA6070-T4	175.7	186.5	54.0	3.25
AA6070-T6	162.0	372.5	54.0	3.00
AA6070-T7	166.0	341.0	54.0	3.07
AA7075-T651	183.8	520.0	54.0	3.40
Weldox 460E [28]	184.5	515.0	94.5	1.95
Weldox 700E [28]	168.0	859.0	94.5	1.78
Weldox 900E [28]	161.0	995.0	94.5	1.70

Chapter 12

Concluding Assessment

12.1 Qualitative Summary

High-speed dynamic problems involve many insecurities and challenges. Firstly, the limited set of experimental results available can hardly be called statistically meaningful, seeing that material properties within a certain batch can vary significantly and that material properties between two batches can vary even more. The problem is referred to by Zukas et al. [62] as "one-shot statistics", where the cost of experimenting has to be measured up to the accuracy needed from the analyses. In short, the numerical results in this thesis are compared to a statistically limited number of experiments, and the conclusions drawn from the results should not be over-emphasized. This is also evident through the sensitivity studies carried out in this thesis: by changing some of the input-parameters, the results may vary significantly.

Heat treatment of aluminium can, as shown in this thesis, influence its ballistic properties and performance through material strength, local ductility and a temper's susceptibility to fragmentation. The latter is shown in Figs. 11.1 and 11.2 where energy dissipation is plotted against a subjective measure of fragmentation. These results indicate that to find an alloy with high strength and no fragmentation would be optimal. Tables 11.2 and 11.3 show that the high-strength tempers AA6070-T6 and AA7075-T651 perform badly compared to what their yield stresses predict. AA5083-H116 is not heat treatable, and thus does not have PFZs where fractures can propagate [47], as it seemingly does in AA6070-T6 and AA7075-T651, which seems advantageous with respect to fragmentation.

For high velocity impacts (i.e. 7.62 mm APM2 bullets) strength seems to be the decisive factor for perforation resistance. It has been shown that although the relationship between yield stress and ballistic limit velocity is not linear, it is very close to linear. High strength implies high ballistic limit velocity. However, when larger projectiles are fired at lower velocities (e.g. 20 mm blunt and ogival projectiles), local ductility is seen to influence the response more distinctly, and fragmentation of the target plate during penetration and perforation plays a huge part.

The simulations carried out with the IMPETUS Afea Solver on the 7.62 mm APM2 bullets gave conservative, but promising results considering the simplicity of the numerical model. The fragmentation seen in the experiments is not captured. This may be due to the relatively large cubic elements and plain fracture criterion (CL) limiting the initiation and propagation of fracture, thus favoring ductile hole growth. The sensitivity study on the mesh showed that the solution had not converged for the element sizes investigated, however for practical purposes the convergence is seen as good enough.

The IMPETUS Afea Solver managed to successfully predict the ballistic limit velocity curve for 20 mm blunt projectiles. The plug geometries are comparable to the ones obtained from experiments. Fragmentation in T4, T6 and T7 are to some extent seen in the simulations, although not as excessive as in the laboratory tests. The results for the O-temper are notably conservative in comparison to the other tempers, which might be because fragmentation is not present in the experiments to reduce the

conservativeness in numerical results. This implies that the great results for T4, T6 and T7 might be somewhat incidental in a physical sense.

The analyses carried out with 20 mm ogival projectiles in IMPETUS Afea has the same tendency as 20 mm blunt projectiles, i.e. the ballistic limit velocities are conservative for all tempers. However, the T6-temper that experienced excessive fragmentation in the experimental tests are less conservative than the three other tempers. When linear elements are used instead of cubic, the physical appearance of the post-perforation model is more consistent to the experimental tests, but the numerical results are less accurate.

Axisymmetric analyses run with blunt projectiles in LS-DYNA are consistent with previous results [22]. The 3D simulations run with the IMPETUS Afea Solver seem to provide better and more physical simulations. When ogival projectiles are used in an axisymmetric model the results are very conservative both with and without a fracture criterion; the results are very dependent on W_c for T6 and T7 (brittle tempers) but not for O and T4 (ductile tempers).

The Cylindrical Cavity Expansion Theory captures the ballistic limit velocity very well, particularly for 7.62 mm APM2 bullets. If the degree of fragmentation is large, as it is for the AA6070-T6 impacted by 20 mm ogival projectiles, it overestimates the amount of energy dissipated and consequently the results become non-conservative.

It appears that being able to describe fragmentation is of vital importance in penetration problems. Given ductile failure modes the models as used in this thesis seem to be conservative in nature and some energy dissipating effects are not adequately captured; however, when fragmentation takes place in experiments, the gap in energy dissipation between experimental and numerical tests evens out. The general trend of underestimating ballistic limit velocities might be a result of the shear fracture mode seen in many of the tensile tests, causing premature failure; consequently W_c will be too low [11].

The main explicit finite element code used in this thesis is the IMPETUS Afea Solver. It proved to be a user friendly tool, with some powerful features like the 64-node cubic hexahedron element, a streamlined set up with regards to fracture criterion, a single contact algorithm etc. It is also easy to implement personalized material models. The post-processor which is easy to use, gives relevant information in a logical way and provides convenient means of exporting data.

12.2 Quantitative Summary

Extensive experimental and numerical work have been presented throughout this thesis. To give the reader an overview of the results and maybe ease the use of this research in later literature-studies, some of the more important input and results are given here.

Table 12.1: General material constants used through the thesis.

Material	$\boldsymbol{E}$ (MPa)	$\boldsymbol{\nu}$	$\boldsymbol{\rho}$ (kg/m^3)	$\boldsymbol{C_p}$ (J/kg K)	$\boldsymbol{\chi}$	$\boldsymbol{T_r}$ (K)	$\boldsymbol{T_m}$ (K)	$\boldsymbol{m}$	$\boldsymbol{\dot{\epsilon}_{0_p}}$	$\boldsymbol{C}$
Aluminium	70 000	0.30	2700	910	0.9	293	893	1.0	$5.0 \cdot 10^{-4}$	0.001
Steel core[a]	210 000	0.33	7850	452	0.9	293	1800	1.0	$5.0 \cdot 10^{-4}$	0.0
Brass jacket	115 000	0.31	8520	385	0.9	293	1189	1.68	$5.0 \cdot 10^{-4}$	0.01
Lead filling[b]	10 000	0.42	10 660	124	0.9	293	760	1.0	$5.0 \cdot 10^{-4}$	0.1
Arne t.s.[a,c]	204 000	0.33	7850		.					

[a] Modeled as rigid in IMPETUS, only ρ is used. [b] Wrong Young's modulus in [23]. [c] $\sigma_0 = 1900$ MPa and $E_t = 15000$ MPa in LS-DYNA

Table 12.2: Material parameters for the target plate used throughout the thesis for Voce hardening and Cockcroft-Latham fracture.

Temper	**Mesh**	A (MPa)	C_1	C_2	Q_1 (MPa)	Q_2 (MPa)	W_c [a] (MPa)
AA6070-O	Coarse	38.80	4.00	56.89	88.17	79.51	151
AA6070-T4	Coarse	172.72	6.52	80.57	247.72	35.60	211
AA6070-T6	Coarse	350.00	185.92	7.70	30.12	72.82	115
AA6070-T7	Coarse	292.47	317.16	10.00	55.34	31.07	128

[a] Only from the rolling direction. Other directions may give considerable variation.

Table 12.3: Comparison of experimental ($v_{bl,\mathrm{E}}$) and IMPETUS-simulated ($v_{bl,\mathrm{I}}$) ballistic limit velocities.

Temper	7.62 mm APM2			20 mm blunt			20 mm ogival		
	$v_{bl,\mathrm{E}}$ (m/s)	$v_{bl,\mathrm{I}}$ (m/s)	**Dev.**	$v_{bl,\mathrm{E}}$ (m/s)	$v_{bl,\mathrm{I}}$ (m/s)	**Dev.**	$v_{bl,\mathrm{E}}$ (m/s)	$v_{bl,\mathrm{I}}$ (m/s)	**Dev.**
AA6070-O	348.0	296.0	14.9%	157.0	124.7	20.6%	186.9	143.5	23.2%
AA6070-T4	506.2	438.1	13.5%	175.7	174.5	0.7%	246.3	213.0	13.5%
AA6070-T6	562.5	480.6	14.6%	162.0	161.5	0.3%	222.1	212.1	4.5%
AA6070-T7	529.1	438.3	17.2%	166.0	157.5	5.1%	246.9	202.2	18.1%

Table 12.4: Comparison of experimental ($v_{bl,\mathrm{E}}$) and LS-DYNA-simulated ($v_{bl,\mathrm{LS}}$) ballistic limit velocities.

Temper	20 mm blunt			20 mm ogival		
	$v_{bl,\mathrm{E}}$ (m/s)	$v_{bl,\mathrm{LS}}$ (m/s)	**Dev.**	$v_{bl,\mathrm{E}}$ (m/s)	$v_{bl,\mathrm{LS}}$ (m/s)	**Dev.**
AA6070-O	157.0	115.0	26.8%	186.9	147.7	21.0%
AA6070-T4	175.7	135.8	22.7%	246.3	217.5	11.7%
AA6070-T6	162.0	121.3	25.1%	222.1	221.4	0.3%
AA6070-T7	166.0	111.5	32.8%	246.9	209.1	15.3%

Chapter 13

Further Work

Suggestions for further work are given here. Some of the proposals are natural prolongations of this thesis which we did not have time to perform and others require additional experimental work.

Mesh Sensitivity and Cubic Elements

A thorough analysis of the mesh sensitivity of the target plates perforated by blunt projectiles could be done. Although this has been done before with respect to 3D-simulations in LS-DYNA, the same thing would be informative to do in IMPETUS. In the simulations run in this thesis, linear elements are used; but how would the cubic elements available in the IMPETUS Afea Solver measure up to the linear ones?

In Fig. 7.19 it was shown that the meshes used in this thesis to analyze 7.62 mm APM2 bullets have not converged. This should be studied in depth.

Additional Experiments on AA6070

Only a limited experimental study on 20 mm ogival and blunt projectiles have been performed for this thesis. Additional testing could be valuable.

Investigate Other Alloys

Alloys with smaller (or no) precipitate free zones might prove to fragment less than AA6070 and should be looked into.

AA5083-H116 Impacted with Blunt Projectiles

An investigation of AA5083-H116 which exhibits high ballistic limits compared to its yield stress, for 20 mm blunt projectiles might be of interest.

Anisotropic Fracture Criterion

The AA6070 tempers proved to be anisotropic in fracture strain, and although this is often deemed negligible at high impact velocities, the effect of an anisotropic fracture criterion should be investigated. The IMPETUS Afea Solver includes a feature that can distribute flaws statistically in materials. This can be of interest in a study like this. Another way of capturing the anisotropy of fracture strain, which was discussed during sessions with our supervisors, is by scaling the plastic strain rate in different directions, i.e.

$$\dot{p} = \sqrt{\dot{\epsilon}^p_{ij} m_{ijkl} \dot{\epsilon}^p_{kl}} \tag{13.1}$$

where m_{ijkl} is a scaling tensor. Using the AA6070-T7 temper as an example, it would be desirable to scale up the plastic strains in the 45°- and 90° directions, causing $\epsilon_{f,45^\circ}$ and $\epsilon_{f,90^\circ}$ to reach $\epsilon_{f,0^\circ}$

sooner, causing fracture in these directions. This approach needs no further material testing, since all elements in m_{ijkl} can be directly obtained from results in Chapter 3. It would also be compatible with the Cockcroft-Latham fracture criterion.

Pressurized Tensile Testing

To obtain accurate estimates of W_c from tensile tests, that are not influenced by shear fracture. Conducting the tensile tests in a pressure chamber could be a possibility. Applying a hydrostatic pressure in order of magnitude of the peak true stress of the material, could prevent shear fracture. This has been done by Bridgman [11] and is expensive and difficult [14].

Boundary Condition

The boundary conditions from the experiments conducted in Chapters 4 and 5 are quite unorthodox, and no simulations are run in this thesis with exactly these conditions. Some numerical work incorporating the two bars locking the plate in place would put the boudary conditon uncertainty to rest.

Material Layering

Fragmentation has proved to be of integral importance to the perforation process. A three-layer plate consisting of a combination of ductile and brittle materials could be of interest to investigate. Studies have been conducted on plate layering before, but no emphasis was put on the fragmentation process [54]. In our case the ductile-brittle-ductile combinations (AA6070-O)-(AA6070-T6)-(AA6070-O) or (AA5083-H116)-(AA7075-T651)-(AA5083-H116) could be studied.

Bibliography

[1] T.L. Anderson. *Fracture Mechanics: Fundamentals and Applications*. Taylor & Francis Group, third edition, 2005.

[2] IMPETUS Afea AS. IMPETUS Afea Solver. http://www.impetus.no. [cited: 26.04.2012].

[3] IMPETUS Afea AS. IMPETUS Afea Solver: An introduction. [version: 16.02.2012].

[4] M.F. Ashby and D.R.H. Jones. *Engineering Materials 1: An Introduction to Properties, Applications and Design*. Elsevier Butterworth-Heinemann, third edition, 2005.

[5] M.F. Ashby and D.R.H. Jones. *Engineering Materials 2: An Introduction to Microstructures, Processing and Design*. Elsevier Butterworth-Heinemann, third edition, 2006.

[6] M.E. Backman and W. Goldsmith. The mechanics of penetration of projectiles into targets. *International Journal of Engineering Science*, 16(1):1 – 99, 1978.

[7] Y. Bai and B. Dodd. *Adiabatic Shear Localization: Occurrunce, Theories and Applications*. Pergamon Press, first edition, 1991.

[8] A. Benallal, T. Berstad, T. Børvik, and O.S. Hopperstad. Uniqueness, loss of ellipticity and localization for the time-discretized, rate-dependent boundary value problem with softening. *International Journal for Numerical Methods in Engineering*, 84:864 – 882, 2010.

[9] A. Benallal, T. Berstad, T. Børvik, O.S. Hopperstad, I. Koutiri, and R. Nogueira de Codes. An experimental and numerical investigation of the behaviour of AA5083 aluminium alloy in presence of the Portevin–Le Chatelier effect. *International Journal of Plasticity*, 24:1916 – 1945, 2008.

[10] R.F. Bishop, R. Hill, and N.F. Mott. The theory of indentation and hardness tests. *Proceedings of the Physical Society*, 57(3):147, 1945.

[11] P.W. Bridgman. *Studies in large plastic flow and fracture: with special emphasis on the effects of hydrostatic pressure*. Metallurgy and metallurgical engineering series. Harvard University Press, 1964.

[12] T. Børvik. An Introduction to Impact and Penetration Dynamics. SIMLab/Department of Structural Engineering, NTNU.

[13] T. Børvik. The tension test. 2011.

[14] T. Børvik. Oral information, 2012.

[15] T. Børvik, A.H. Clausen, M. Eriksson, T. Berstad, O.S. Hopperstad, and M. Langseth. Experimental and numerical study on the perforation of AA6005-T6 panels. *International Journal of Impact Engineering*, 32, 2005.

[16] T. Børvik, S. Dey, and A.H. Clausen. Perforation resistance of five different high-strength steel plates subjected to small-arms projectiles. *International Journal of Impact Engineering*, 36:948–964, 2009.

[17] T. Børvik, M.J. Forrestal, O.S. Hopperstad, T.L. Warren, and M. Langseth. Perforation of AA5083-H116 aluminium plates with conical-nose steel projectiles – Calculations. *International Journal of Impact Engineering*, 36(3):426 – 437, 2009.

[18] T. Børvik, M.J. Forrestal, and T.L. Warren. Perforation of 5083-H116 Aluminum Armor Plates with Ogive-Nose Rods and 7.62 mm APM2 Bullets. *Experimental Mechanics*, 50:969–978, 2010.

[19] T. Børvik, M.J. Forrestal, and T.L. Warren. Perforation of 7075-T651 Aluminum Armor Plates with 7.62 mm APM2 Bullets. *Experimental Mechanics*, 50:1245–1251, 2010.

[20] T. Børvik, O.S. Hopperstad, T. Berstad, and M. Langseth. A computational model of viscoplasticity and ductile damage for impact and penetration. *European Journal of Mechanics A/Solids*, 20:685–712, 2001.

[21] T. Børvik, O.S. Hopperstad, M. Langseth, and K.A. Malo. Effect of target thickness in blunt projectile penetration of Weldox 460 E steel plates. *International Journal of Impact Engineering*, 28(4):413–464, 2003.

[22] T. Børvik, O.S. Hopperstad, and K.O. Pedersen. Quasi-brittle fracture during structural impact of AA7075-T651 aluminium plates. *International Journal of Impact Engineering*, 37:537–551, 2010.

[23] T. Børvik, L. Olovsson, S. Dey, and M. Langseth. Normal and oblique impact of small arms bullets on AA6082-T4 aluminium protective plates. *International Journal of Impact Engineering*, 38(7):577 – 589, 2011.

[24] M.G. Cockcroft and D.J. Latham. Ductility and the Workability of Metals. *Journal of the Institute of Metals*, 96:33–39, 1968.

[25] Wikipedia contributors. Graphics processing unit. http://en.wikipedia.org/wiki/Graphics_processing_unit. [cited: 26.04.2012].

[26] R.D. Cook, D.S. Malkus, M.E. Plesha, and R.J. Witt. *Concepts and Applications of Finite Element Analysis*. John Wiley & Sons, Inc, fourth edition, 2002.

[27] Livermore Software Technology Corporation. LS-OPT. http://www.lstc.com/products/ls-opt. [cited: 05.03.2012].

[28] S. Dey. *High strength steel-plates subjected to projectile impact: An experimental and numerical study*. PhD thesis, Norwegian University of Science and Technology, 2004.

[29] X. Fang, M. Song, K. Li, and Y. Du. Precipitation Sequence of an Aged Al-Mg-Si Alloy. *Journal of Mining and Metallurgy*, 46(2):171 – 180, 2010.

[30] M.J. Forrestal. Personal notes.

[31] M.J. Forrestal, T. Børvik, and T.L. Warren. Perforation of 7075-T651 Aluminum Armor Plates with 7.62 mm APM2 Bullets. *Experimental Mechanics*, 50(8):1245–1251, 2010.

[32] M.J. Forrestal, V.K. Luk, and N.S. Brar. Perforation of aluminum armor plates with conical-nose projectiles. *Mechanics of Materials*, 10(1–2):97 – 105, 1990.

[33] M.J. Forrestal and T.L. Warren. Perforation equations for conical and ogival nose rigid projectiles into aluminum target plates. *International Journal of Impact Engineering*, 36(2):220 – 225, 2009.

[34] J.E. Hatch. *Properties and Physical Metallurgy*. American Society for Metals, firth edition, 1984.

[35] R. Hill. *The Mathematical Model of Plasticity*. Oxford University Press, 1998.

[36] J. Hodowany, G. Ravichandran, A. Rosakis, and P. Rosakis. Partition of plastic work into heat and stored energy in metals. *Experimental Mechanics*, 40:113–123, 2000. 10.1007/BF02325036.

[37] O.S. Hopperstad. Theory Manual: Models for metals and alloys. Still in progress at SIMLab/Department of Structural Engineering, NTNU.

[38] O.S. Hopperstad. Oral information, 2012.

[39] O.S. Hopperstad and T. Børvik. *Lecture Notes TKT4135 Mechanics of Materials, KT8306 Plasticity Theory*. Trondheim, December 2010.

[40] The International Aluminium Institute. The International Aluminium Institute. www.world-aluminium.org. [cited: 16.03.2012].

[41] ASM International. *Metals Handbook, Vol. 2 Properties and Selection: Non Ferrous Alloys and Special-Purpose Materials*. ASM Handbook Committee, tenth edition, 1990.

[42] G.R. Johnson and W.H. Cook. A constitutive model and data for metals subjected to large strains, high strain rates and high temperatures. *Proceedings of the 7th International Symposium on Ballistics*, 547(11):541–547, 1983.

[43] E. Kreyszig. *Advanced Engineering Mathematics*. John Wiley & Sons, Inc., ninth edition, 2006.

[44] P.S. Lee, H.R. Piehler, B.L. Adams, G. Jarvis, H. Hampel, and A.D. Rollet. Influence of surface texture on orange peel in aluminum. *Journal of MAterials Processing Technology*, 80-81:315–319, 1998.

[45] D.W. Marquardt. An algorithm for least-squares estimation of nonlinear parameters. *Journal of the Society for Industrial and Applied Mathematics*, 11(2):pp. 431–441, 1963.

[46] K.M. Mathisen. *Lecture notes: TKT4197 Nonlinear Finite Element Analysis*. Norwegian University of Science and Technology, Department of Structural Engineering, 2011. Lecture 12: Formulation of Geometrically Nonlinear FE.

[47] MATTER and the European Aluminium Association. aluMATTER. http://www.aluminium.matter.org.uk. [cited: 15.02.2012].

[48] P.G. McCormick, S. Venkadesan, and C.P. Ling. Propagative instabilities: An experimental view. *Scripta Metallurgica et Materialia*, 29(9):1159 – 1164, 1993.

[49] W.F. Miao and D.E. Laughlin. Precipitation Hardening in Aluminum Alloy 6022. *Scripta Materialia*, 40:873–878, 1999.

[50] O.R. Myhr. Lecture Notes for Dislocation Mechanics. Hydro Aluminium RTD.

[51] A. Nadai. Plastic behavior of metals in the strain-hardening range. part i. *Journal of Applied Physics*, 8(3):205 –213, 1937.

[52] L. Olovsson. Personal communication, 2012.

[53] C. Ostertag. Lecture Notes for Steel - Part 2. CE240 Advanced Civil Engineering Materials, Department of Structural Engineering, Mechanics and Materials, University of California, Berkeley.

[54] S. Oven. Design of lightweight protective structures. Master's thesis, Norwegian University of Science and Technology, 2010.

[55] K.O. Pedersen, T. Børvik, and O.S Hopperstad. Fracture mechanisms of aluminium alloy AA7075-T651 under various loading conditions. *Materials and Design*, 32(1):97 – 107, 2011.

[56] D.M. Riley and P.G. McCormick. The Effect of Precipitation Hardening on the Portevin-Le Chatelier Effect in an Al-Mg-Si Alloy. *Acta Metallurgica*, 25:181–185, 1976.

[57] K. Rottmann. *Matematisk Formelsamling*. BI-Hochschultaschenbücher. Spektrum Forlag, 10th edition, 2008.

[58] T.W. Wright. *The Physics and Mathematics of Adiabatic Shear Bands*. Cambridge University Press, first edition, 2002.

[59] Z. Zhao, R. Radovitzky, and A Cuitiño. A study of surface roughening in fcc metals using direct numerical simulation. *Acta Materialia*, 52:5791–5804, 2004.

[60] J.A. Zukas. *Impact Dynamics*. John Wiley & Sons, Inc., first edition, 1982.

[61] J.A. Zukas. *High Velocity Impact Dynamics*. John Wiley & Sons, Inc., first edition, 1990.

[62] J.A. Zukas and D.R. Scheffler. Practical aspects of numerical simulations of dynamic events: effects of meshing. *International Journal of Impact Engineering*, 24:925 – 945, 2000.

Appendix A

Load-Diameter Reduction Curves

The constitutive relations are calibrated using the data from the curves in Fig. A.1. This is also the original data obtained from the tensile tests described in Section 3.2 for the tests deemed typical. There are three curves in each plot: diameter reduction in thickness-direction (z), diameter reduction for the in-plane direction (y), and the average diameter reduction. The original diameter for all the the tensile specimens is approximately 6 mm.

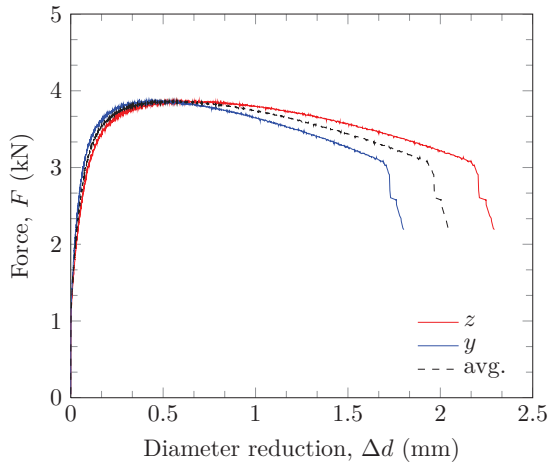

(a) Temper: O, Test orientation: 0°.

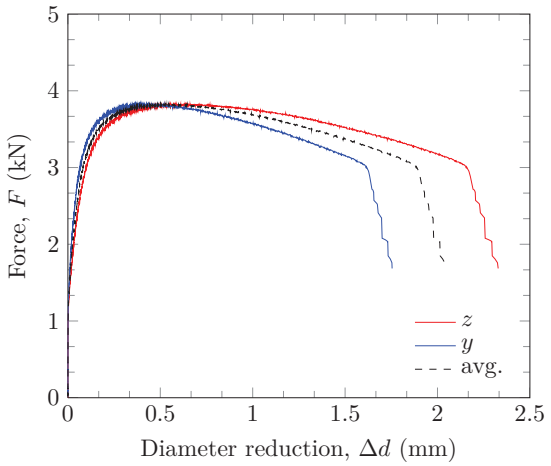

(b) Temper: O, Test orientation: 45°.

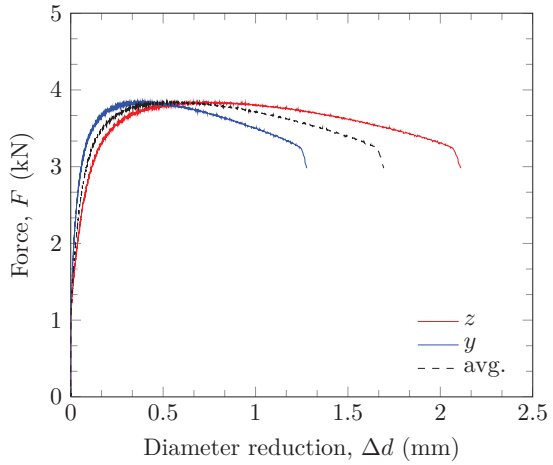

(c) Temper: O, Test orientation: 90°.

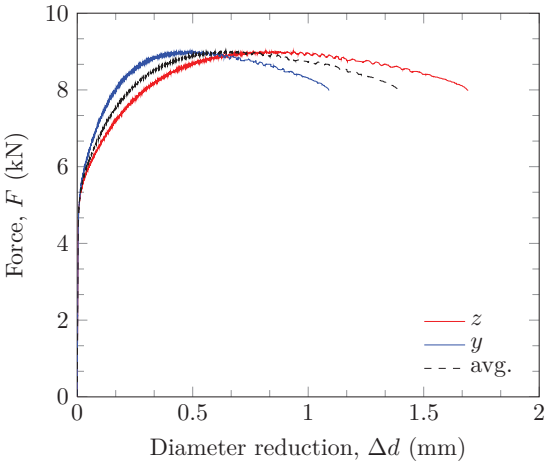

(d) Temper: T4, Test orientation: 0°.

Figure A.1: Continues..

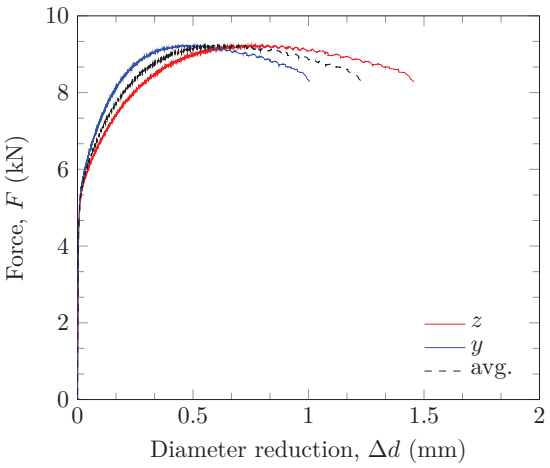

(e) Temper: T4, Test orientation: 45°.

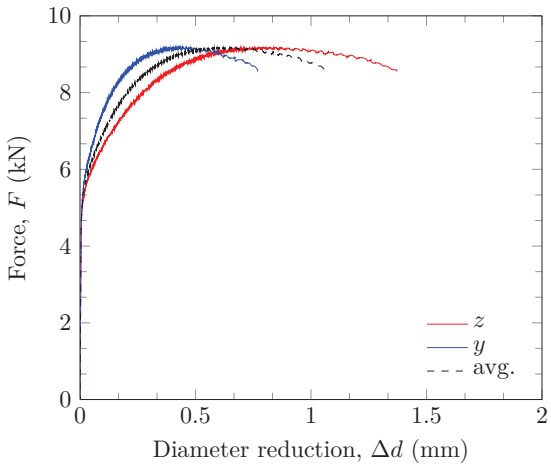

(f) Temper: T4, Test orientation: 90°.

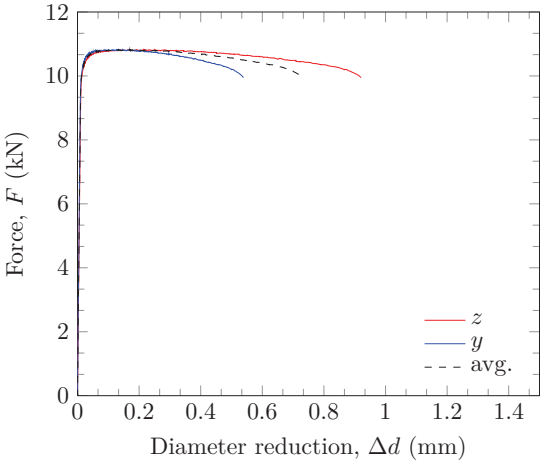

(g) Temper: T6, Test orientation: 0°.

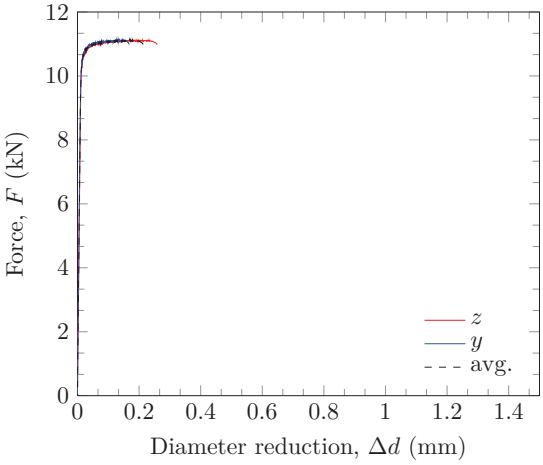

(h) Temper: T6, Test orientation: 45°.

Figure A.1: Continues..

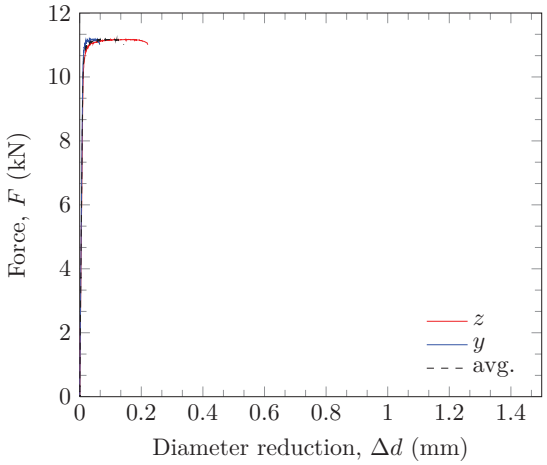

(i) Temper: T6, Test orientation: 90°.

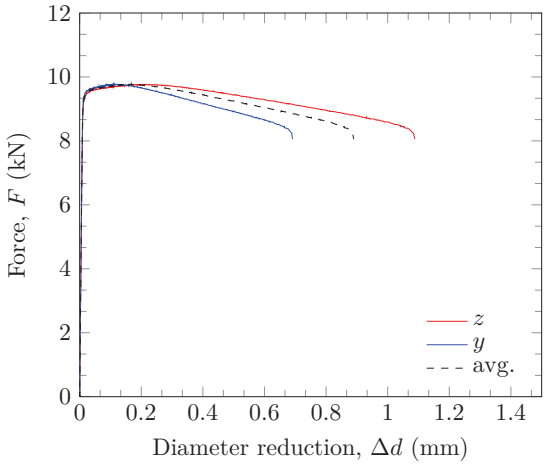

(j) Temper: T7 Test orientation: 0°.

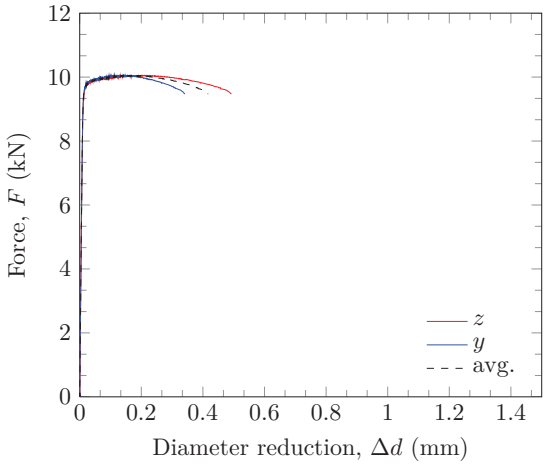

(k) Temper: T7, Test orientation: 45°.

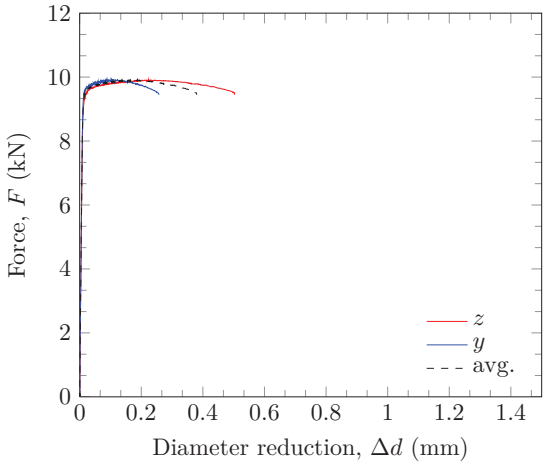

(l) Temper: T7 Test orientation: 90°.

Figure A.1: z denotes the direction of the plate thickness, y denotes the in-plane direction. Note the different scales.

Appendix B

True Stress-Strain Curves

True stress-strain curves for all 36 tensile tests.

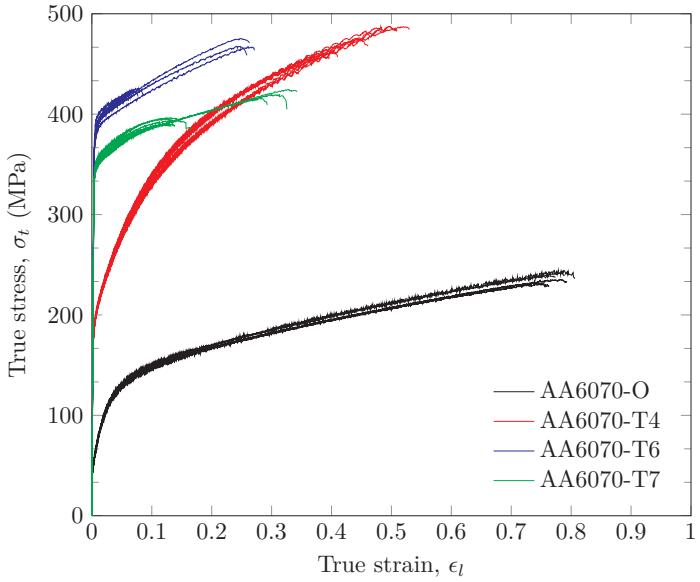

Figure B.1: An overview of all tensile tests.

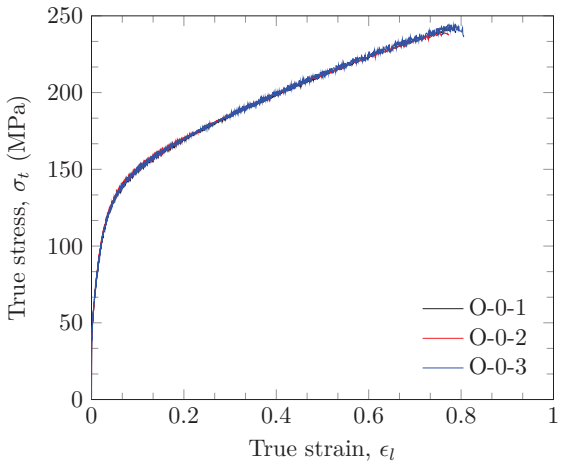

(a) O-0°

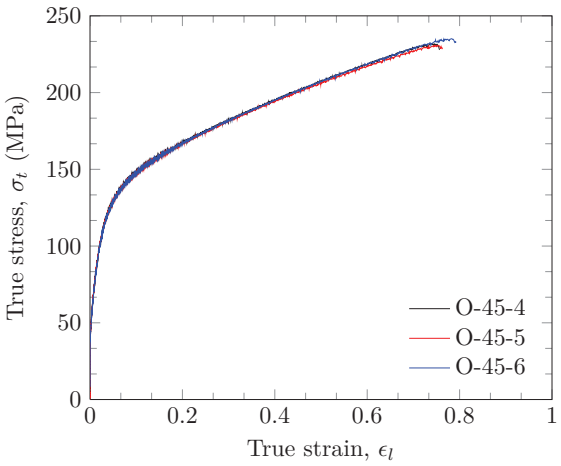

(b) O- 45°

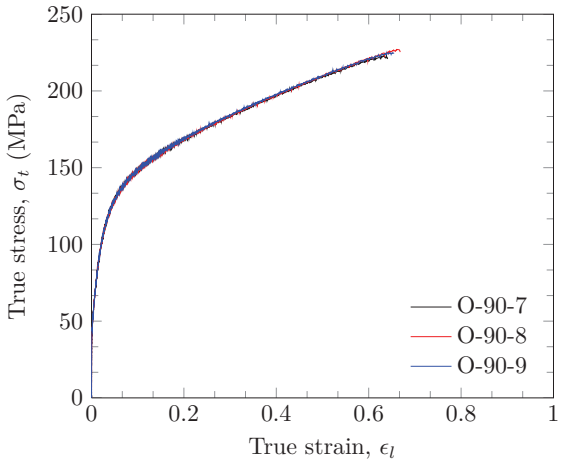

(c) O-90°

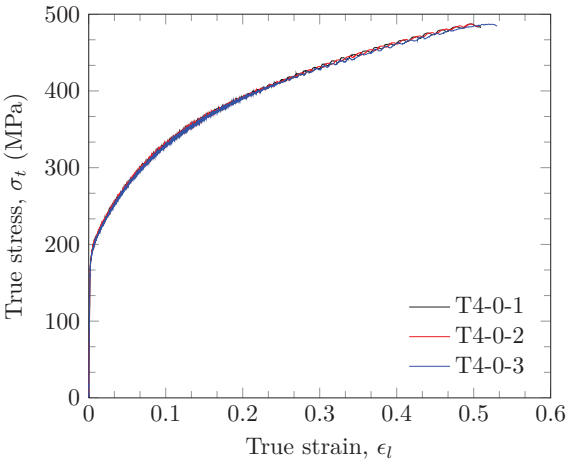

(d) T4-0°

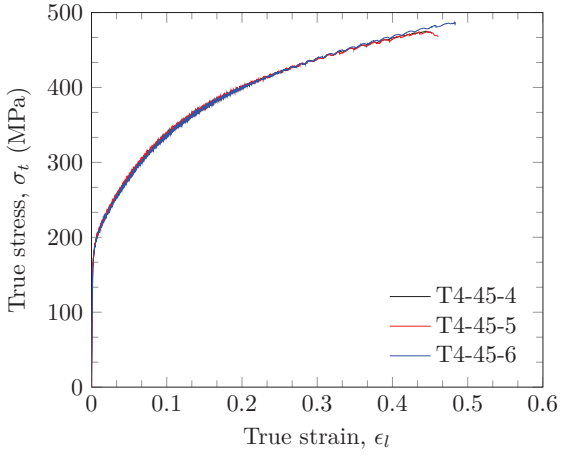

(e) T4-45°

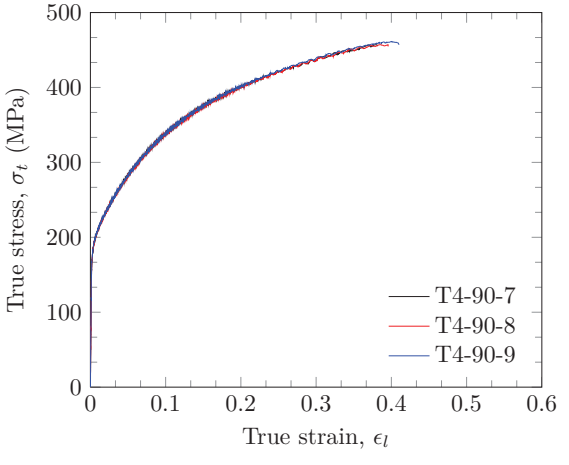

(f) T4-90°

Figure B.2: Continues...

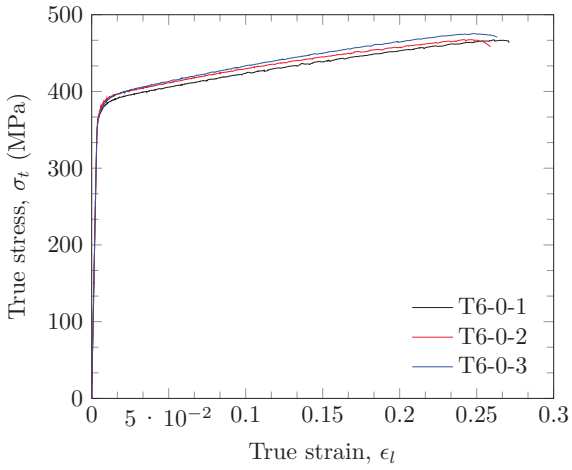

(g) T6-0°

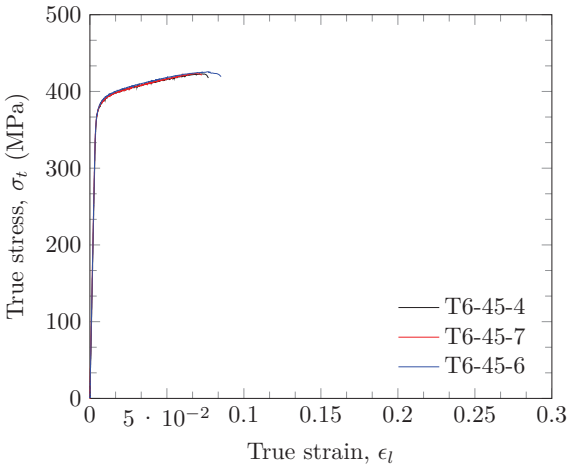

(h) T6-45°

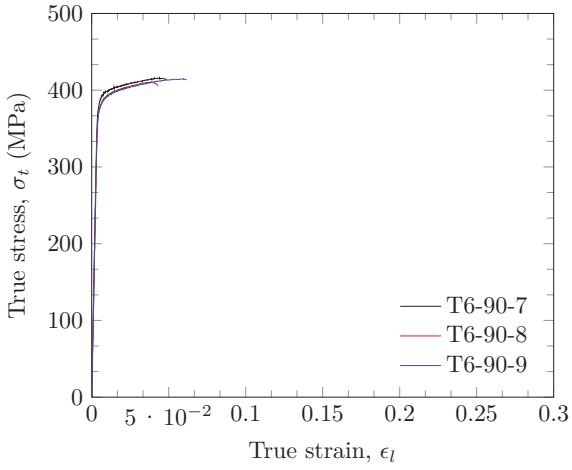

(i) T6-90°

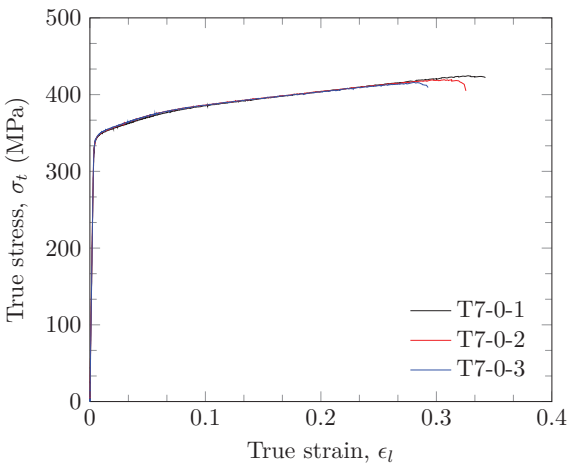

(j) T7-0°

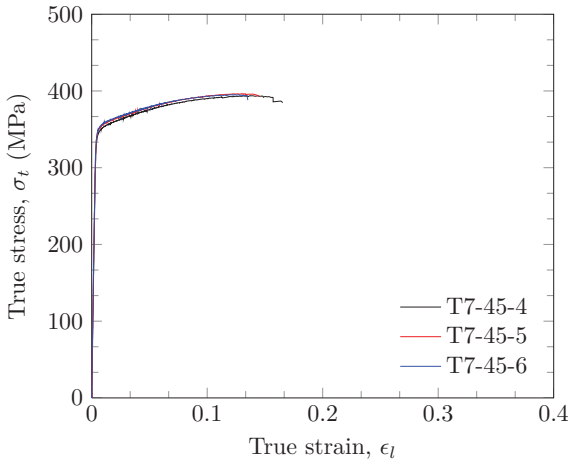

(k) T7-45°

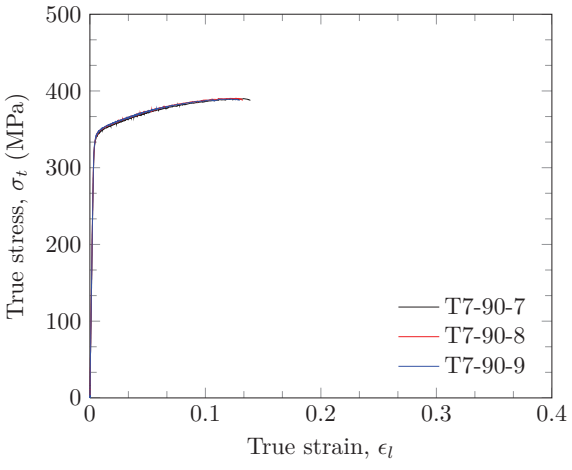

(l) T7-90°

Figure B.2: True stress-strain curves to fracture for all tensile tests. Note the different scales.

Appendix C

Calibration of Material Models

C.1 MATLAB Script

```
close all
clear all
clc

E = 70000; % Young's modulus (MPa)
yield = importdata('yieldstress.txt',' ',0);
wri = false;     % write text files
plotval = false; % create plot
truestrain_column = 16; % which column contains true strain
truestress_column = 14; % ......

% create blank matrices for coefficients from curve fit
voce_reg_coeff = zeros(7,length(yield));
voce_reg_coeff(1,:) = [1:length(yield)];
pwr_reg_coeff = zeros(3,length(yield));
pwr_reg_coeff(1,:) = voce_reg_coeff(1,:);
cet_reg_coeff = zeros(2,length(yield));
cet_reg_coeff(1,:) = pwr_reg_coeff(1,:);

% import data from laboratory work
% and start loop
temper = {'O' 't4' 't6' 't7'};
orientation = 45*[0 0 0 1 1 1 2 2 2];
nn = 1; % counting variable for index in yield vector

for i=1:length(temper)
for j=1:length(orientation)
eval([temper{i} '_' num2str(orientation(j)) '_' num2str(j) ' = importdata(''' ...
   temper{i} '-' num2str(orientation(j)) '-' num2str(j) '.txt''' ',' ''' ''' ',0'');']);
if (plotval == true)
    eval(['figure(''name'',''' temper{i} '-' num2str(orientation(j)) '-' num2str(j) ...
       ''',''numbertitle'',''off'');'])
end
eval(['mat = ' temper{i} '_' num2str(orientation(j)) '_' num2str(j) ';']);
epsi = mat(:,truestrain_column);
sigma = mat(:,truestress_column);

[a,b] = max(sigma);
sigma((b:length(sigma)),:) = [];
epsi((b:length(epsi)),:) = [];
sigma_n = sigma;
epsi_n = epsi;

% remove data points pre yield
jj=1;
while sigma_n(jj) < yield(nn)
```

```
45      sigma_n(jj,:) = [];
46      epsi_n(jj,:) = [];
47  end
48
49  % weight the last 20 data points 15 times more
50  % to make sure that the gradient of the regression line
51  % is consistent with laboratory data.
52  we = ones(1,length(epsi_n));
53  we(end-20:end) = 15*we(end-20:end);
54
55  % create voce law curve fitting function
56  g = fittype( @(c1,c2,q1,q2,x) yield(nn)+q1.*(1-exp(-c1.*x))+q2.*(1-exp(-c2.*x)));
57  f1 = fit(epsi_n,sigma_n,g,'startpoint',[1 1 1 1],'algorithm','Levenberg-Marquardt', ...
58      'Weights',we,'MaxIter',800,'MaxFunEvals',1000,'Robust','Bisquare');
59  df1 = differentiate(f1,epsi_n);
60
61  if (plotval == true)
62  subplot(2,1,1);
63  hold on
64  plot(epsi_n,f1(epsi_n),'r',epsi_n,df1,'b',epsi_n,sigma_n,'k')
65  legend('voce','deriv','data');
66  axis([0 1 0 500])
67  end
68
69  % calculate intersection between 'df1' and 'f1' as the mean value
70  % between the two data points closest to intersection
71  delta = df1-f1(epsi_n);
72  [neck1,index] = min(abs(delta));
73  delta(index)=1000;
74  [neck2,index2] = min(abs(delta));
75  neckstrain = 0.5*(epsi_n(index)+epsi_n(index2));
76  neckstress = 0.5*(sigma_n(index)+sigma_n(index2));
77
78  % calculate epsilon_lu,p, plastic strain eps_p, and Bridgman
79  % corrected flow stress
80  plu = neckstrain - neckstress/E;
81  epsi_p = epsi-sigma./E;
82
83  % check if computed neckstrain (including
84  if (plu < epsi_p(end))
85  b = 1.1.*(epsi_p-plu); %a/R
86  sigma_b = sigma./((1+2.*(1./b)).*log(1+0.5.*b));
87
88  % remove values pre necking from epsi_pb and sigma_b
89  l=1;
90  epsi_pb=epsi_p;
91  while epsi_pb(l) < plu
92      epsi_pb(l,:) = [];
93      sigma_b(l,:) = [];
94  end
95
96  % remove values pre yield from sigma, and epsi_p
97  jj=1;
98  while sigma(jj) < yield(nn)
99      sigma(jj,:) = [];
100     epsi_p(jj,:) = [];
101 end
102
103 % join Bridgman corrected flow stress post necking, to
104 % true stress pre necking
105 n_insert = length(epsi_p)-length(epsi_pb);
106 epsi_pb = [epsi_p(1:n_insert); epsi_pb];
107 sigma_b = [sigma(1:n_insert); sigma_b];
108 epsi_pb = abs(epsi_pb);
109 epsi_x = [0:0.001:1];
110
111 % create curve fitting functions for Bridgman corrected flow stress
112 % g = voce, h = power
113 if (temper{i} == 't7')
```

```
114     g = fittype( @(c1,c2,c3,q1,q2,q3,x) ...
            yield(nn)+q1.*(1-exp(-c1.*x))+q2.*(1-exp(-c2.*x))+q3.*(1-exp(-c3.*x)));
115 else
116     g = fittype( @(c1,c2,q1,q2,x) yield(nn)+q1.*(1-exp(-c1.*x))+q2.*(1-exp(-c2.*x)));
117 end
118 h = fittype(@(BB,n,x) yield(nn)+BB.*x.^n);
119 hh = fittype(@(n,x) yield(nn).*(E.*x./yield(nn)).^n);
120 % cap Bridgman corrected flow stress at maximum value
121 % ensures non-negative gradient
122 [mm ii] = max(sigma_b);
123 sigma_b = sigma_b(1:ii);
124 epsi_pb = epsi_pb(1:ii);
125
126 % weight the last 10 data points 15 times more than the rest
127 we = ones(1,length(epsi_pb));
128 we(end-10:end) = 15*we(end-10:end);
129 if (temper{i} == 't7')
130 f2 = fit(epsi_pb,sigma_b,g,'startpoint',[1 1 1 1 1 ...
        1],'algorithm','Levenberg-Marquardt', ...
131     'Weights',we,'Robust','Bisquare','maxiter',2000,'maxfunevals',2000);
132 else
133     f2 = fit(epsi_pb,sigma_b,g,'startpoint',[1 1 1 ...
            1],'algorithm','Levenberg-Marquardt', ...
134     'Weights',we,'Robust','Bisquare');
135 end
136 f3 = fit(epsi_pb,sigma_b,h,'startpoint',[1 1]);
137 f4 = fit(epsi_pb,sigma_b,hh,'startpoint',1);
138 voce_reg_coeff(2:length(coeffvalues(f2))+1,nn) = coeffvalues(f2)';
139 pwr_reg_coeff(2:end,nn) = coeffvalues(f3)';
140 cet_reg_coeff(2:end,nn) = coeffvalues(f4)';
141 if (plotval == true)
142     subplot(2,1,2)
143     plot(epsi_p,sigma,epsi_pb,sigma_b,epsi_x,f2(epsi_x),'--g',epsi_x,f3(epsi_x),'-.m');
144     xlabel('Plastic strain')
145     ylabel('Stress')
146     legend('data','bridgman','voce','pwr');
147 end
148
149 %print table in LaTeX format
150 fprintf('%s & %4.2f & %3.6f & %3.6f & %3.6f & %3.6f & %3.6f & %3.6f %1.3f ...
        \\tabularnewline\n',temper{i},yield(nn),pwr_reg_coeff(2,nn),pwr_reg_coeff(3,nn), ...

    151     voce_reg_coeff(2,nn),voce_reg_coeff(3,nn),voce_reg_coeff(4,nn),voce_reg_coeff(5,nn),plu);
152
153 %write data for use in pgfplot
154 if (wri == true)
155     data1 = [epsi_n sigma_n f1(epsi_n) df1 epsi_p sigma];
156     data2 = [epsi_x' f2(epsi_x) f3(epsi_x)];
157     data3 = [epsi_pb sigma_b];
158     eval(['fid = fopen(''' temper{i} '-' num2str(orientation(j)) '-' num2str(j) ...
            '-true.txt'',''w'');']);
159     eval(['fid2 = fopen(''' temper{i} '-' num2str(orientation(j)) '-' num2str(j) ...
            '-fit.txt'',''w'');']);
160     eval(['fid3 = fopen(''' temper{i} '-' num2str(orientation(j)) '-' num2str(j) ...
            '-bridgman.txt'',''w'');']);
161     fprintf(fid,'%.10f %.10f %.10f %.10f %.10f %.10f\n',data1');
162     fprintf(fid2,'%.10f %.10f %.10f\n',data2');
163     fprintf(fid3,'%.10f %.10f\n',data3');
164     ST = fclose('all');
165 end
166 nn = nn+1;
167 else
168     fprintf(' !! Neckstrain larger than maximum plastic strain, no Bridgman ...
            correction\n');
169 end
170     end
171 end
```

C.2 Calibration Results

Table C.1: Material parameters for MJC (Eq. (2.11)) and MJC with Voce hardening (Eq. (2.13))

Temper	A (MPa)	B (MPa)	n	C_1	C_2	Q_1 (MPa)	Q_2 (MPa)	$\epsilon_{lu,p}$
O-0-1	50.50	183.81	0.2907	2.57	41.45	90.34	80.95	0.188
O-45-5	51.00	177.13	0.2869	41.95	2.89	77.98	81.97	0.182
O-90-9	49.70	188.41	0.30167	3.47	43.64	84.82	75.85	0.199
T4-0-3	186.50	426.87	0.4790	6.057	40.61	240.082	37.37	0.231
T4-45-5	185.50	458.0064	0.4831	63.19	7.61	26.31	244.27	0.217
T4-90-8	187.00	487.42	0.5156	77.91	8.042	19.81	244.20	0.214
T6-0-3	372.50	149.88	0.4163	215.40	6.67	21.14	75.12	0.054
T6-45-5	377.80	165.62	0.4719	20.55	359.047	44.88	11.19	0.043
T6-90-7	387.40	116.87	0.4319	747.064	45.77	7.32	24.20	0.026
T7-0-2	341.00	86.20	0.3491	38.78	3.27	32.45	32.82	0.047
T7-45-5	346.30	141.36	0.487	667.96	23.52	5.16	41.43	0.049
T7-90-8	339.80	144.99	0.4841	672.78	25.06	4.81	42.41	0.050

C.3 Figures

In Fig. C.1 the position of the neck, and the Bridgman corrected stress are illustrated. In the figures showing neck position only the part after yield is plotted. This was done because a curve fit of the material data had to be done due to the scatter in our material data, which made plotting the gradient directly from experimental results impossible.

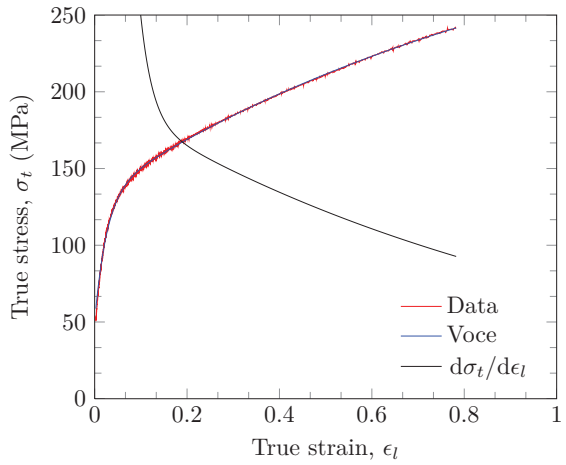

(a) AA6070-O-0°

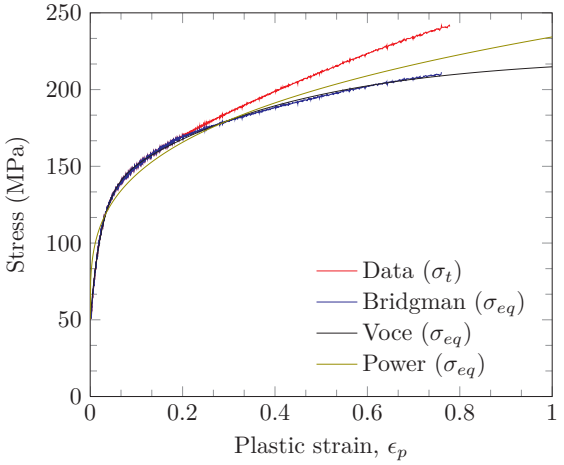

(b) AA6070-O-0°

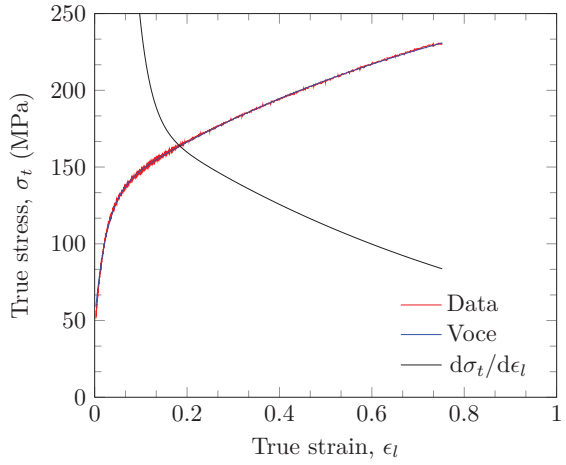

(c) AA6070-O-45°

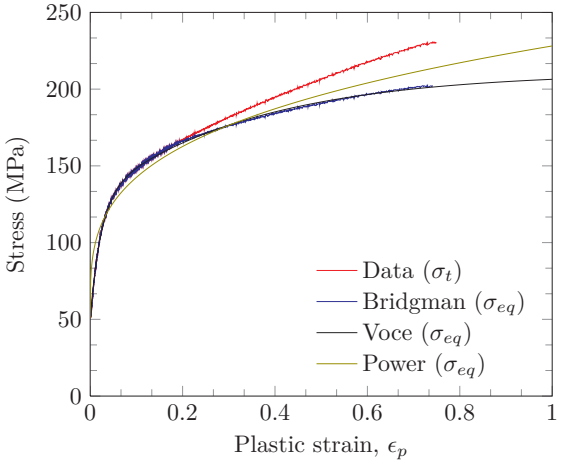

(d) AA6070-O-45°

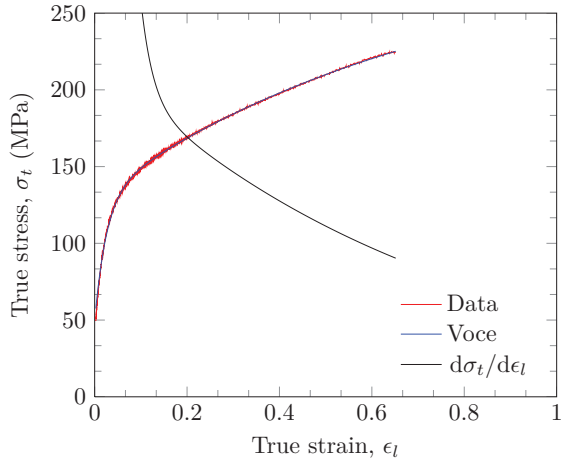

(e) AA6070-AA6070-O-90°

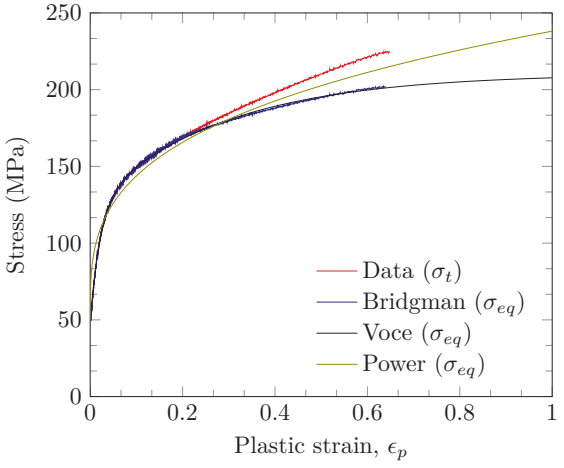

(f) AA6070-O-90°

Figure C.1: Continues...

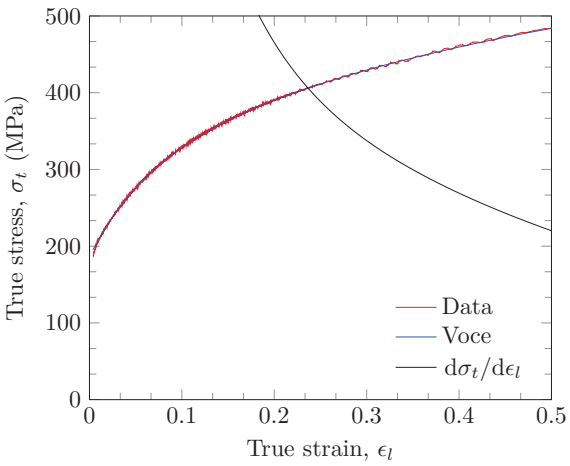

(g) AA6070-T4-0°

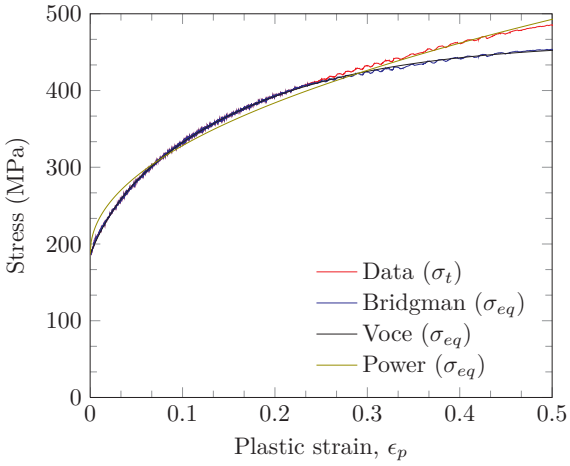

(h) AA6070-T4-0°

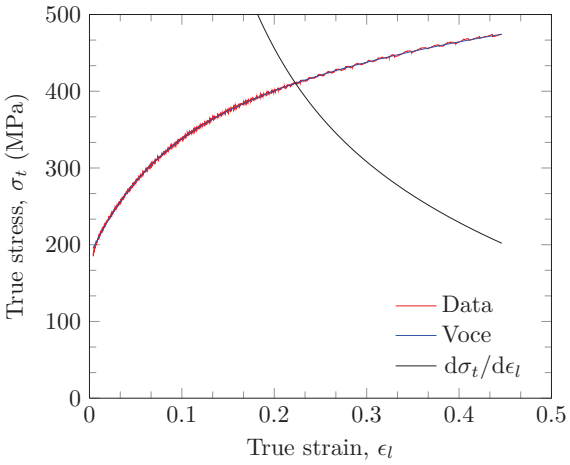

(i) AA6070-T4-45°

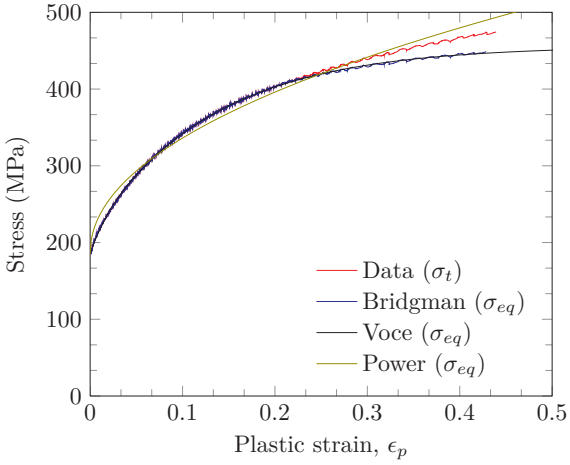

(j) AA6070-T4-45°

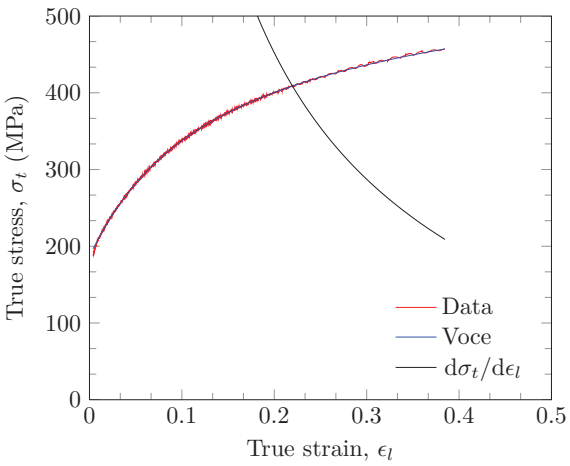

(k) AA6070-T4-90°

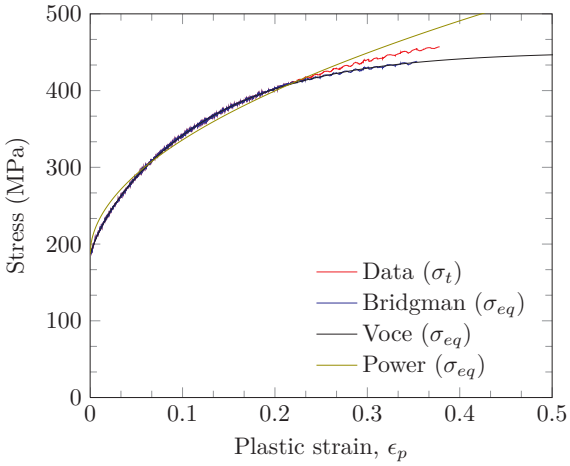

(l) AA6070-T4-90°

Figure C.1: Continues...

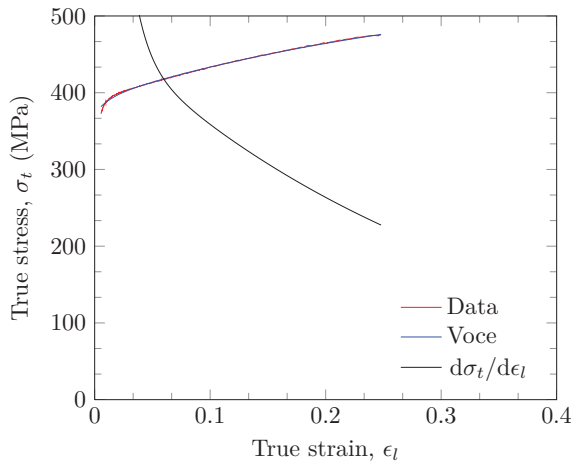

(m) AA6070-T6-0°

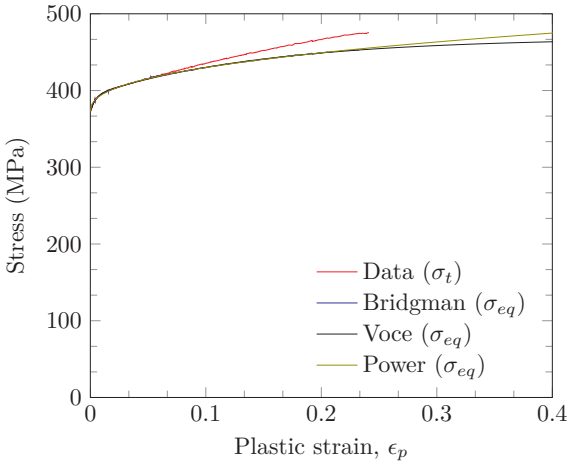

(n) AA6070-T6-0°

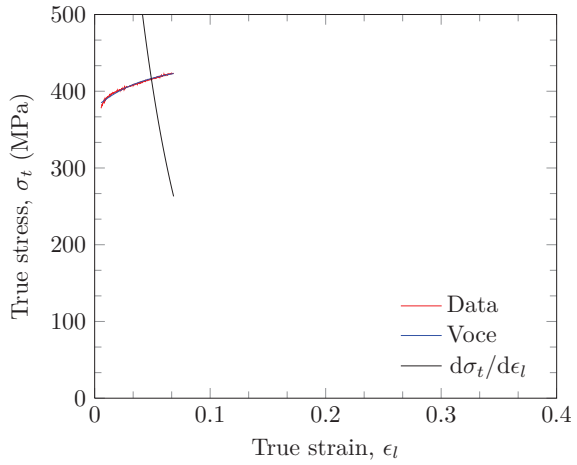

(o) AA6070-T6-45°

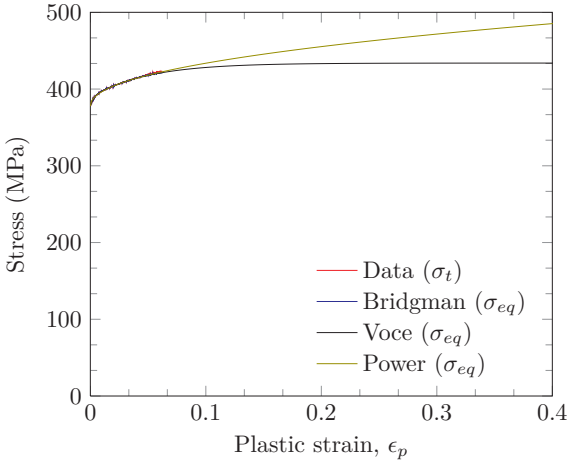

(p) AA6070-T6-45°

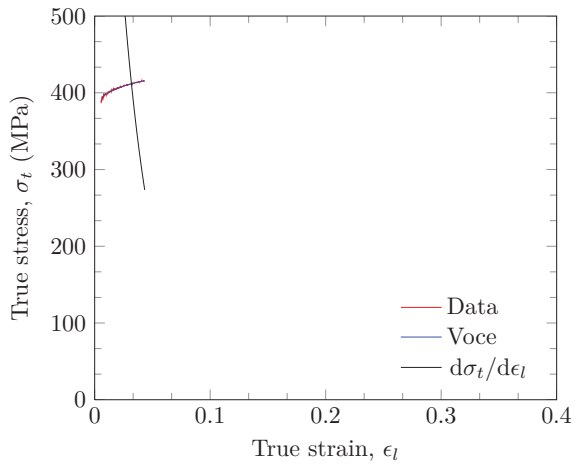

(q) AA6070-T6-90°

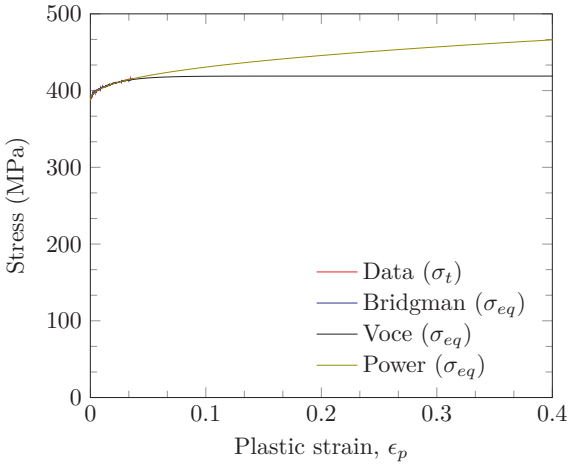

(r) AA6070-T6-90°

Figure C.1: Continues...

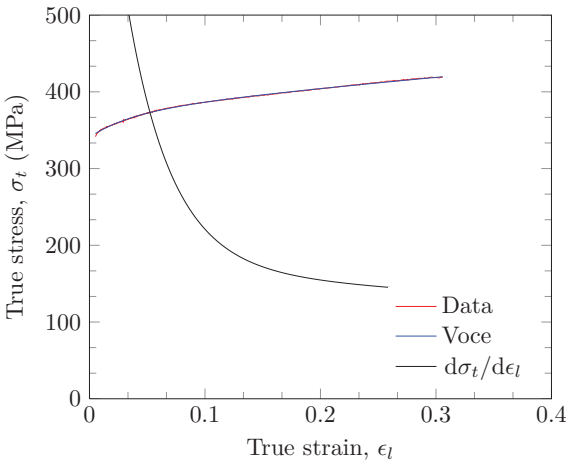

(s) AA6070-T7-0°

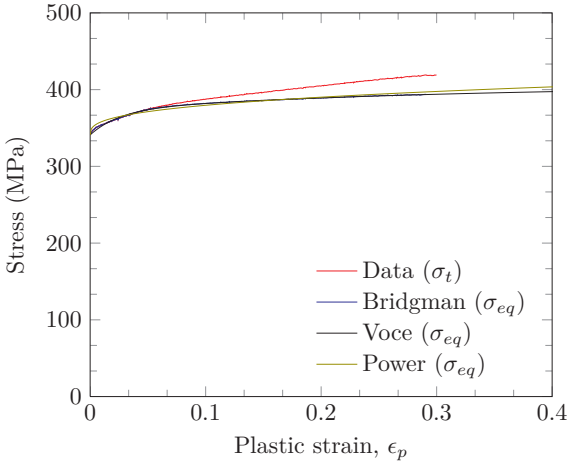

(t) AA6070-T7-0°

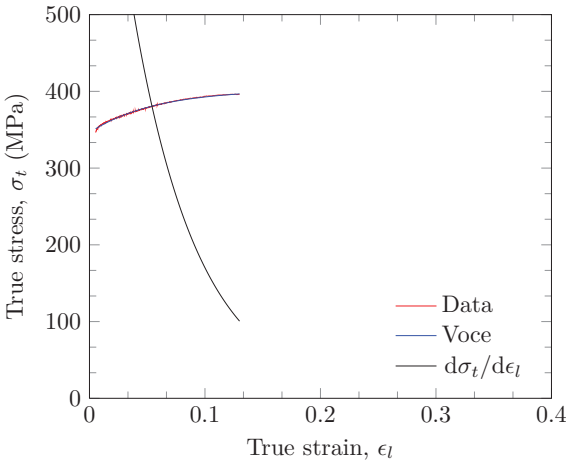

(u) AA6070-T7-45°

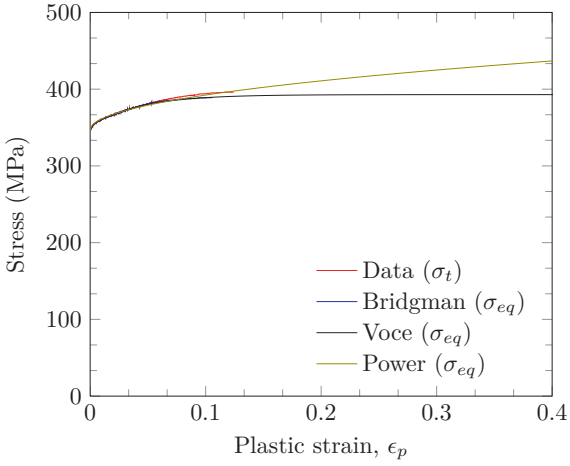

(v) AA6070-T7-45°

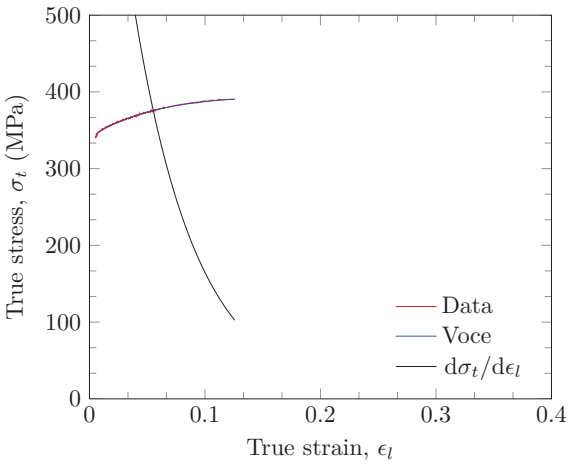

(w) AA6070-T7-90°

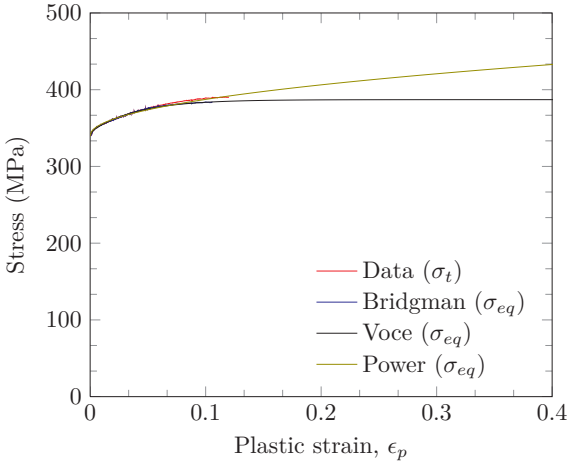

(x) AA6070-T7-90°

Figure C.1: Plots show identification of incipient neck and Bridgman corrected longitudinal tensile stresses for the **(a)-(f)** O, **(g)-(l)** T4, **(m)-(r)** T6, and **(s)-(x)** T7 tempers in the 0°, 45°, and 90° orientations.

Appendix D

Variation of Strain Ratio

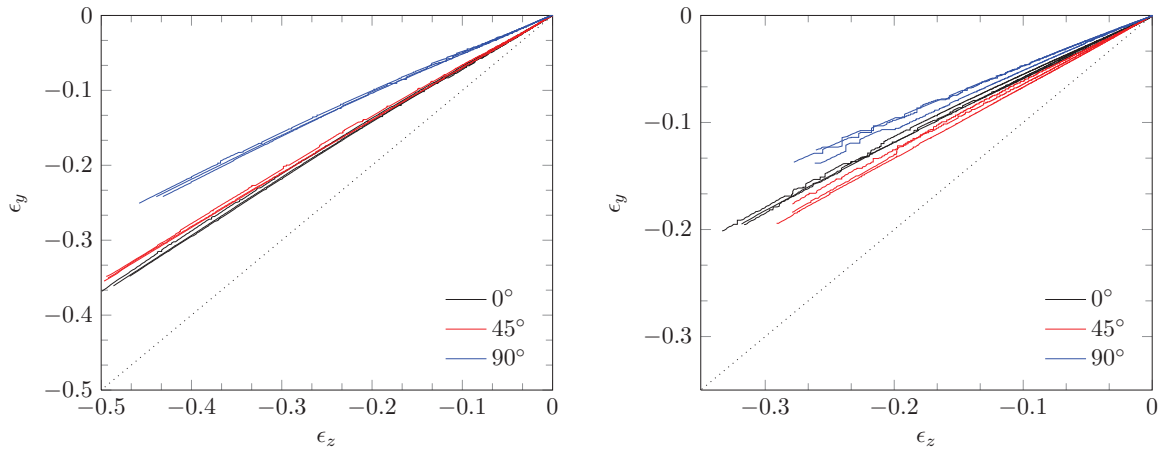

(a) AA6070-O

(b) AA6070-T4

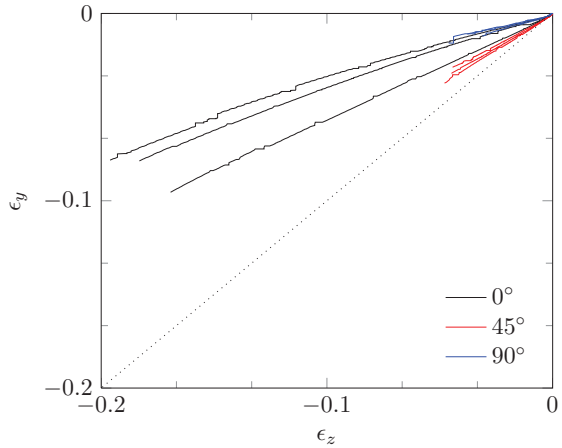

(c) AA6070-T6

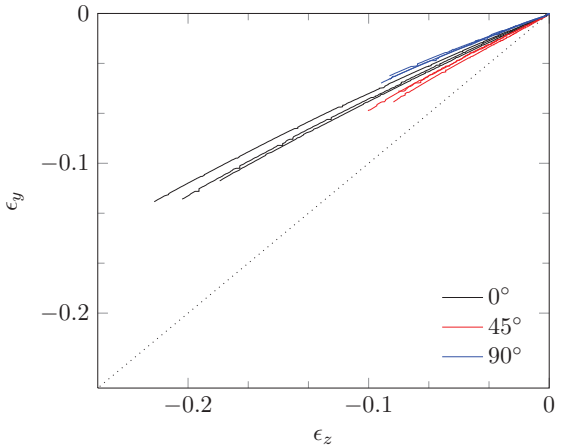

(d) AA6070-T7

Figure D.1: Strain in the longitudinal (y) and thickness-direction (z) plotted against each other.

Table D.1: Strain ratios r for every tensile test.

	0°			**45°**			**90°**		
	1	2	3	4	5	6	7	8	9
O	0.7265	0.7475	0.7436	0.7009	0.6900	0.7048	0.5446	0.5306	0.5385
T4	0.5916	0.5971	0.5806	0.6287	0.6342	0.6654	0.4844	0.5266	0.4833
T6	0.3699	0.4073	0.5575	0.7149	0.6631	0.7636	0.2854	0.3734	0.2956
T7	0.5551	0.5916	0.5976	0.6284	0.6647	0.6217	0.4799	0.4766	0.4588

Appendix E

Cylindrical Cavity Expansion Theory

E.1 MATLAB Script

The material constants n was taken from the calibration script in Appendix C.1, formulas used can be found in Section 9.1

```
clc
clear all
close all

% test of Cavity Expansion Theory

% constants

n = [0.2129 0.1664 0.0496 0.0364]; % O T4 T6 T7
Y = [50.5 186.5 372.5 341]*1e6;    % O T4 T6 T7
temper = {'O' 'T4' 'T6' 'T7'};
E = 70000e6;
ny = 0.3;
%
% 20mm projectile
%
a = 10.0e-3; % radius of projectile
rho_p = 7850;  % density of projectile
rho_t = 2700;  % density of target
l = 33.0e-3;   % nose length
L = 62.0e-3;   % shank length
h = 20e-3;     % target thickness
data = importdata('ogival-estimated-vbl.txt');
ogival = true;

%
% APM2
%
% a = 0.5*6.17e-3; % radius of projectile
% rho_p = 7850;  % density of projectile
% rho_t = 2700;  % density of target
% l = 10.2e-3;   % nose length
% L = 16.8e-3;   % shank length
% h = 20e-3;     % target thickness
% data = importdata('ballistic-tests.txt');
% ogival = false;
for i=1:4
V = [0.00001:0.1:1/sqrt(rho_t/Y(i))];
Vrdata = data(:,2*i);
Vidata = data(:,2*i-1);
psi = 0.25*((l/a)^2+1);
gamma2 = 2*(1+ny)*Y(i)/(sqrt(3)*E);
b = 1-gamma2;
k = @(x) (4*x^2-4*x/3+1/3)-4*x^2*(2*x-1)/sqrt(4*x-1)*asin(sqrt(4*x-1)/(2*x));
```

```
45 k1 = k(psi);
46 alpha2 = sqrt(3)*(1-2*ny)/(2*(1-ny)).*(rho_t.*V.^2./Y(i));
47 B = 0.5*(1./((1-ny).*sqrt(1-alpha2)).*log((1+sqrt(1-alpha2))./sqrt(alpha2)) ...
48     +gamma2-2*log(sqrt(gamma2))-1);
49 f = @(x) (-log(x)).^n(i)./(1-x);
50
51 sigma_s = (Y(i)/sqrt(3))*(1+(E/(sqrt(3)*Y(i)))^n(i)*quad(f,0.000001,b));
52
53
54 sigma_r = sigma_s + rho_t.*B.*V.^2;
55
56 Xdata = sqrt(rho_t/Y(i))*V;
57 Ydata = sigma_r/Y(i);
58 we = ones(1,length(Xdata));
59 we(1:20) = 10;
60 f1 = fittype(@(a,b,x) a+b.*x.^2);
61 g = fit(Xdata',Ydata',f1,'startpoint',[1 1],'algorithm','levenberg-marquardt');
62 x = [0:0.1:1];
63 aa = coeffvalues(g);
64 B0 = aa(2);
65 ff = @(x) Y(1)+B0.*x.^2;
66 figure(i)
67 subplot(2,1,1)
68 plot(Xdata,Ydata,Xdata,g(Xdata),'--r')
69 legend('Eq','Interpolant');
70 xlabel('$\sqrt{\frac{\rho_t}{Y}}V$','Interpreter','latex');
71 ylabel('$\frac{\sigma_r}{Y}$','Interpreter','latex');
72 v = length(Xdata)-length(coeffvalues(g));
73 RSS = sum((Ydata'-g(Xdata)).^2);
74 MSE = RSS/v;
75 text(0.2,g(0.9),['MSE =' num2str(MSE)]);
76 text(0.2,g(0.9)-0.5,['B = ' num2str(B0)]);
77
78 N = @(x) 8*x^2*log(2*x/(2*x-1))-(1+4*x);
79
80 C = h*rho_t*B0*N(psi)/((L+k1*l)*rho_p);
81
82 Vbl = @(C) (2*sigma_s*h/(rho_p*(L+k1*l)))^(0.5)*(1+C+2*C^2/3)^(0.5);
83
84 fprintf('-----------------------------------\n  %2s  |  C = %.3f   |  C = ...
     0\n-----------------------------------\n',temper{i},C);
85 fprintf('Vbl   |  %.2f      |  %.2f\n',Vbl(C),Vbl(0));
86
87 Vr = @(C,Vs,Vbl) Vbl.*((Vs./Vbl).^2-1).^(0.5).*(1-C+0.5.*C).^(0.5);
88
89 Vs = [Vbl(C):0.1:Vidata(end)];
90 Vs2 = [Vbl(0):0.1:Vidata(end)];
91 subplot(2,1,2)
92 plot(Vs,Vr(C,Vs,Vbl(C)),Vs2,Vr(0,Vs2,Vbl(0)),Vidata,Vrdata);
93 xlabel('$v_i$ (m/s)','Interpreter','latex');
94 ylabel('$v_r$ (m/s)','Interpreter','latex');
95 eval(['hh = legend(''C = ' num2str(C) ''','''C = 0''','''Data''');']);
96 plotdata = [Vs' Vr(C,Vs,Vbl(C))'];
97 plotdata2 = [Vs2' Vr(0,Vs2,Vbl(0))'];
98 plotdata3 = [Xdata' Ydata' g(Xdata)];
99 if (ogival == true)
100     eval(['fid = fopen(''CCET-ogival-' temper{i} '-1.txt'',''w'');']);
101     eval(['fid2 = fopen(''CCET-ogival-' temper{i} '-2.txt'',''w'');']);
102     eval(['fid3 = fopen(''CCET-ogival-' temper{i} '-3.txt'',''w'');']);
103 else
104     eval(['fid = fopen(''CCET-apm2-' temper{i} '-1.txt'',''w'');']);
105     eval(['fid2 = fopen(''CCET-apm2-' temper{i} '-2.txt'',''w'');']);
106     eval(['fid3 = fopen(''CCET-apm2-' temper{i} '-3.txt'',''w'');']);
107 end
108 fprintf(fid,'%.5f %.5f\n',plotdata');
109 fprintf(fid2,'%.5f %.5f\n',plotdata2');
110 fprintf(fid3,'%.5f %.5f %.5f\n',plotdata3');
111 end
```

Appendix F

Pictures of Tensile Tests Post Fracture

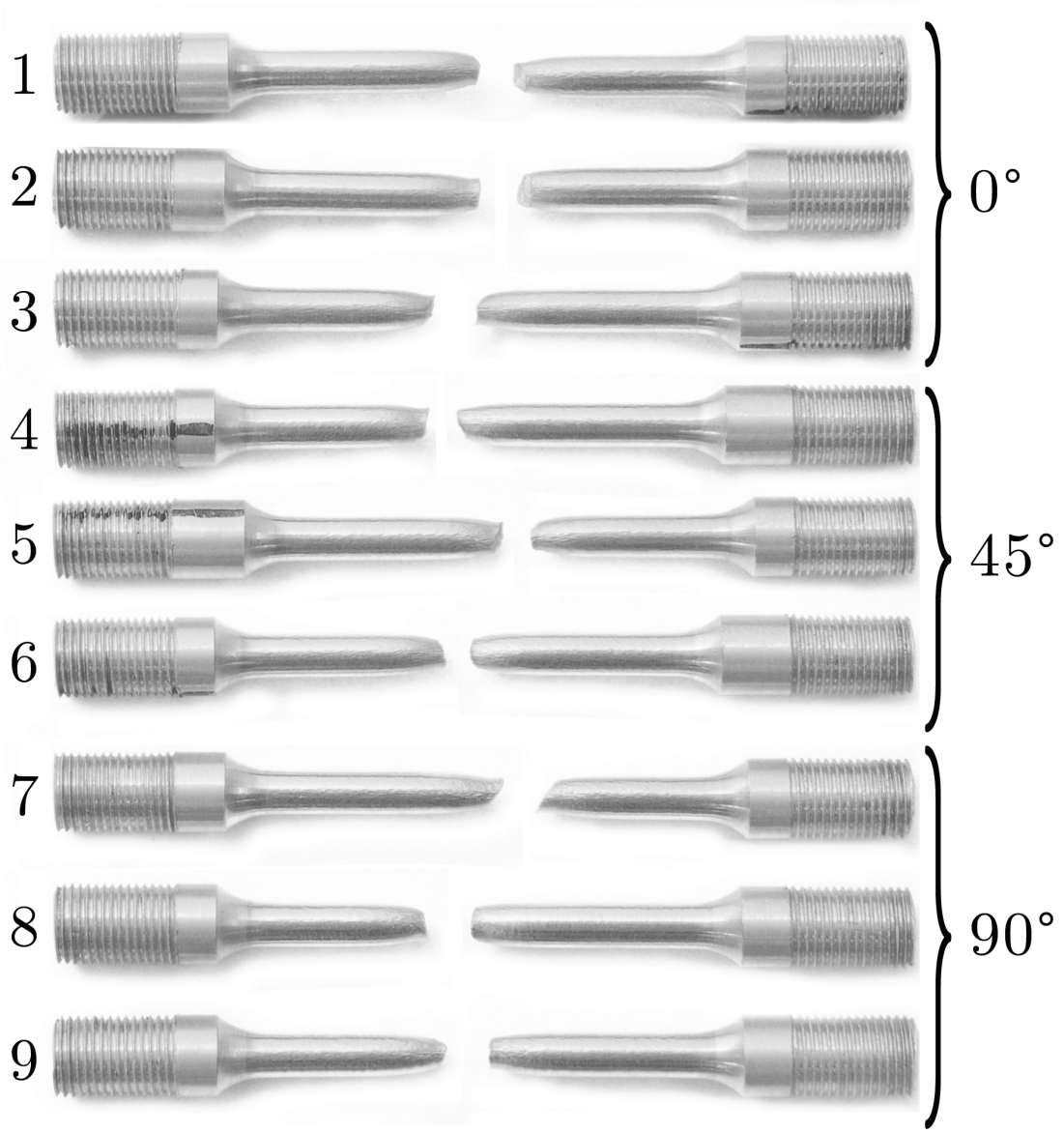

Figure F.1: Tensile specimens post fracture for all AA6070-O tests.

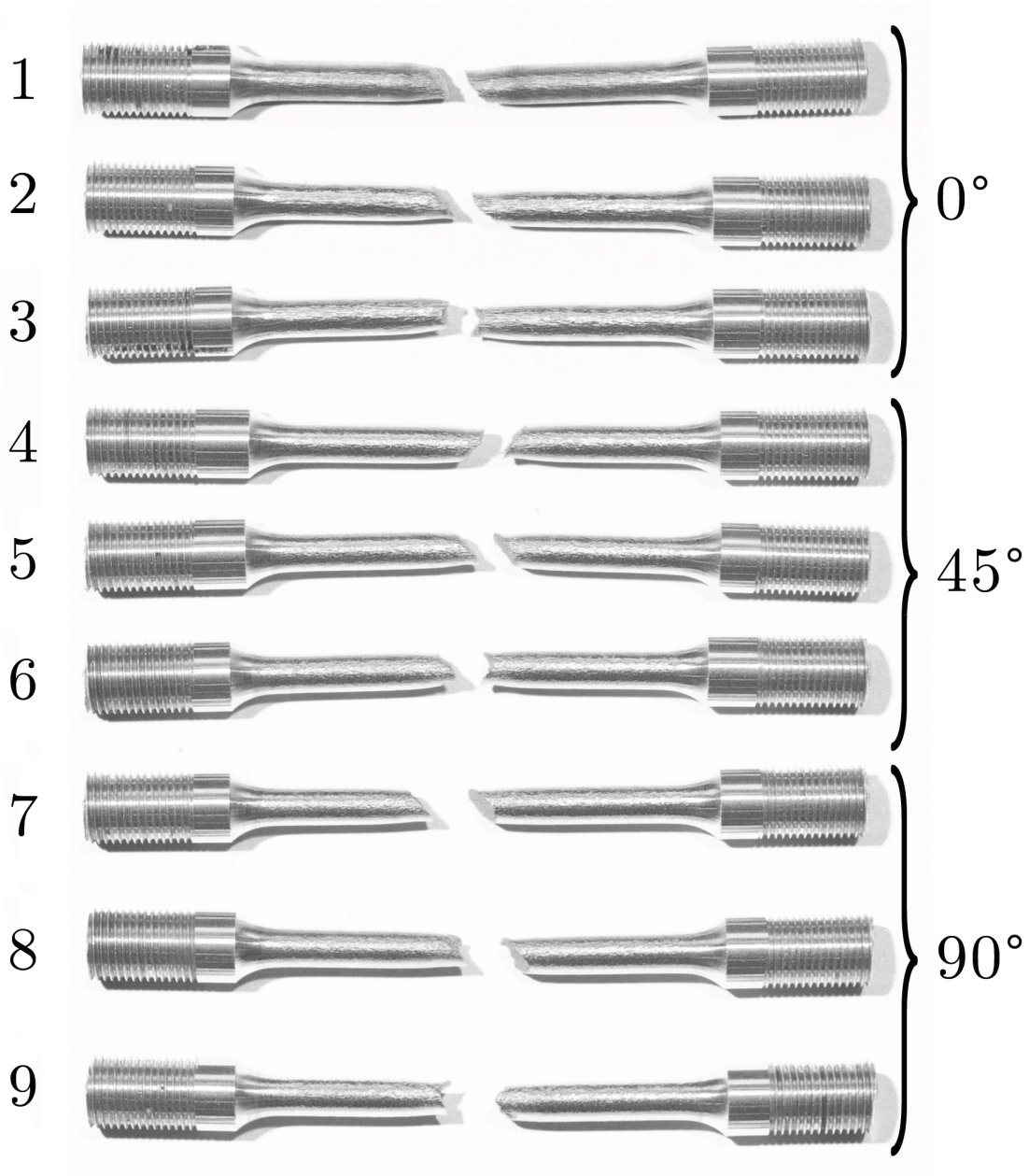

Figure F.2: Tensile specimens post fracture for all AA6070-T4 tests.

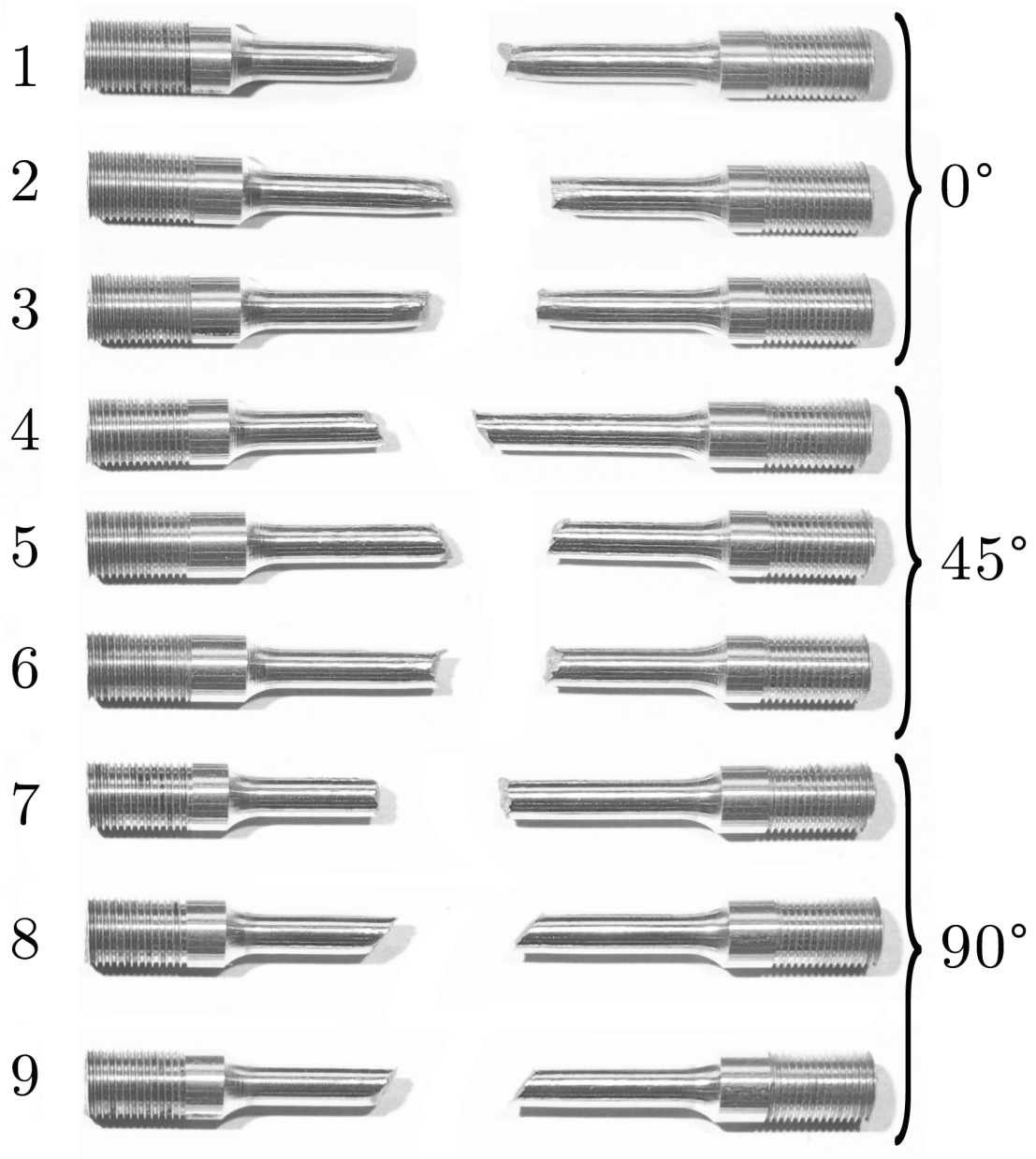

Figure F.3: Tensile specimens post fracture for all AA6070-T6 tests.

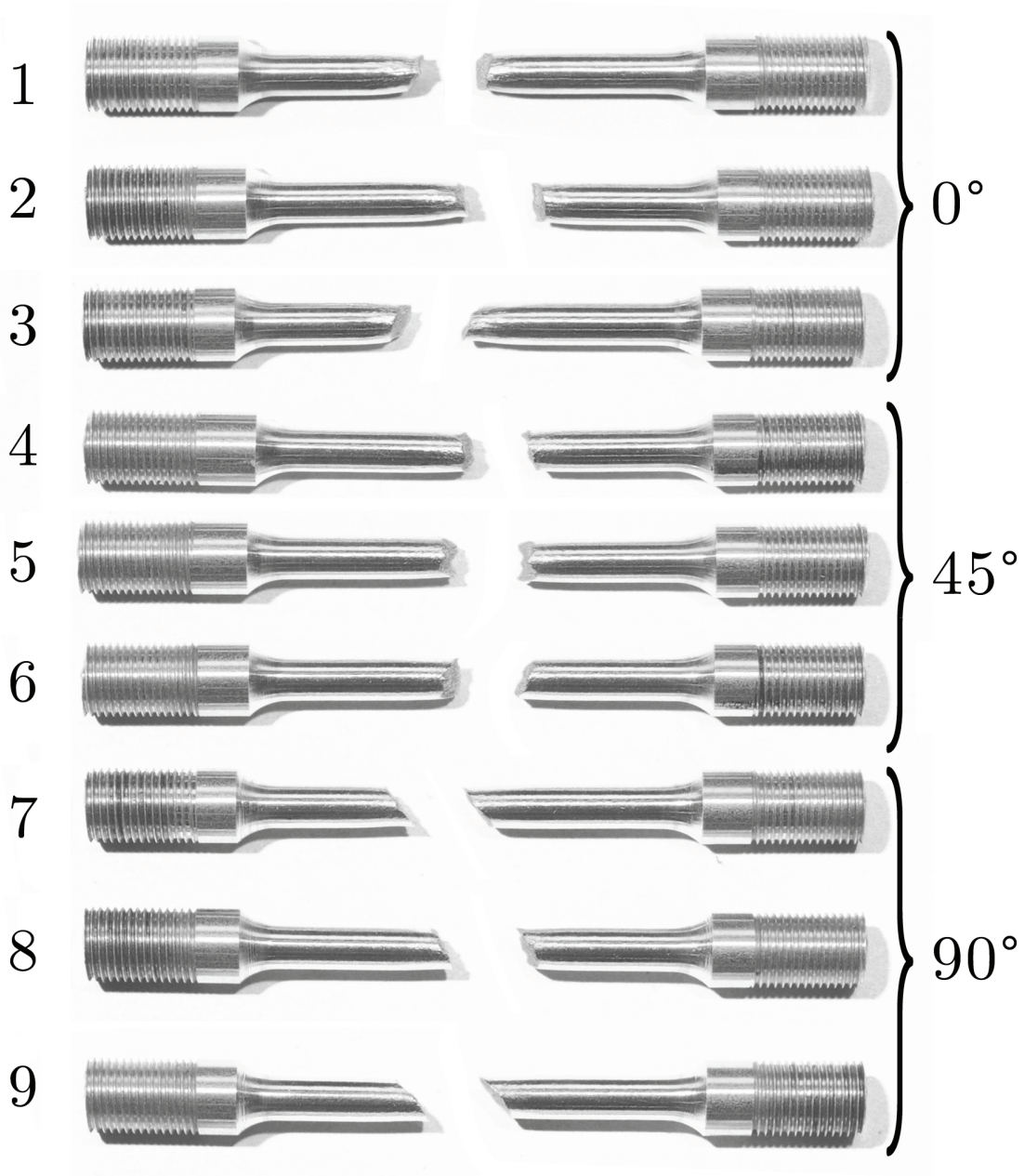

Figure F.4: Tensile specimens post fracture for all AA6070-T7 tests.

Appendix G

Script to Create Compatible Input-Files

The IMPETUS Afea Solver package does not come with a pre-processor. We used the Abaqus CAE pre-processor to mesh the projectiles and plates. To obtain compatible input-files the following script was written:

```
%% Clear workspace, command window and close figures
clc
clear all
close all

%% Read data from files
A = importdata('nodes.txt',',',0);
B = importdata('elements.txt',',',0);

%% Create files for formated data
fidnode = fopen('nodesstructured.k','w')
fidelem = fopen('elementstructured.k','w')

%% Print formated data to created files
fprintf(fidnode,'%i,%.13f,%.13f,%.13f,0\n',A')
fprintf(fidelem,'%i,1,%i,%i,%i,%i,%i,%i,%i,%i\n',B')
```

The nodal coordinates and properties were copied into the file *nodes.txt* and the element coordinates and properties were copied into *elements.txt*. Execution of the script sorted the information and added part-ID and desired boundary conditions before writing the results to *nodestructured.k* and *elementstructures.k*. Now the information is ready to be pasted into a .k-file, and the geometry can be used in IMPETUS.